MULTIFUNCTIONAL MICELLAR NANOMEDICINE FOR TARGETED CANCER THERAPY

By

Yichao Chen

B.S. in Phamracy, Shenyang Pharmaceutical University, 2012

Submitted to the Graduate Faculty of

School of Pharmacy in partial fulfillment

of the requirements for the degree of

Doctor of Philosophy

University of Pittsburgh

2017

UNIVERSITY OF PITTSBURGH

SCHOOL OF PHARMACY

This dissertation was presented

by

Yichao Chen

It was defended on

November 20, 2017

and approved by

Xiaochao Ma, Ph.D., Associate Professor
Center for Pharmacogenetics, Department of Pharmaceutical Sciences, School of Pharmacy, University of Pittsburgh

Raman Venkataramanan, Ph.D., Professor
Pharmaceutical Sciences, School of Pharmacy, University of Pittsburgh

Da Yang, Ph.D., Assistant Professor
Center for Pharmacogenetics, Department of Pharmaceutical Sciences, School of Pharmacy, University of Pittsburgh

Binfeng Lu, Ph.D., Associate Professor
Department of Immunology, School of Medicine, University of Pittsburgh

Dissertation Advisor: **Song Li**, M.D., Ph.D., Professor
Center for Pharmacogenetics, Department of Pharmaceutical Sciences, School of Pharmacy, University of Pittsburgh

MULTIFUNCTIONAL MICELLAR NANOMEDICINE FOR TARGETED CANCER THERAPY

Yichao Chen

University of Pittsburgh, 2017

Chemotherapy is frequently used in the treatment of cancer. However, their therapeutic outcome is compromised by the short circulation time and systemic toxicity. Nanomaterials have emerged as ideal platforms to circumvent these limitations and improve the therapeutic effect of anticancer agents.

We first developed a dual function carrier that is based on PEG-derivatized S-trans, trans-farnesylthiosalicylic acid (FTS) for delivery of curcumin. FTS is a potent nontoxic Ras antagonist and curcumin is a chemopreventive agent for cancers. Both curcumin and FTS have poor water solubility and limited bioavailability. The PEG_{5K}-FTS_2 led to a synergistic antitumor activity by co-delivery of curcumin. Next, we demonstrated that introduction of an Fmoc motif to PEG_{5k}-FTS_2 led to a significant improvement in the drug loading capacity and antitumor effect *in vitro* and *in vivo*.

Unfortunately, delivery of cytotoxic agents is often limited by various negative feedback mechanisms during cancer treatment. Immunochemotherapy represents a promising strategy to improve anti-cancer effect. Here we developed an immunostimulatory PEG-NLG nanomicellar carrier for delivery of paclitaxel (PTX). NLG is an indoleamine 2,3-dioxygenase (IDO) inhibitor, which can block tumor immune escape. *In vivo* delivery of

PTX using the PEG_{2k}-Fmoc-NLG nanocarrier leads to a significantly improved antitumor response in multiple mouse tumor models.

Although the PEG-NLG-based immunochemotherapy system achieved considerable antitumor effect, its efficacy was compromised by the accumulation of myeloid-derived suppressor cells (MDSCs). In order to solve this problem, an improved polymeric micelle system (PEG_{5k}-Fmoc-NLG_2) was developed to codeliver a multi-target receptor tyrosine kinase inhibitor, sunitinib (SUN) and PTX. SUN+PTX/PEG_{5k}-Fmoc-NLG_2 micelles could not only enhance *in vivo* antitumor activity but also decrease the recruitment and maturation of MDSCs in the tumor, too.

Tumoral expression of immune stimulating cytokines has been show to be an effective strategy to boost immunotherapy of cancer. This inspired us to develop a carrier system, which could codeliver both gene therapy and small molecule drug. We designed two polymeric conjugates POEG-*st*-Pmor and POEG-*st*-Ppipe for codelivery of IL-36γ plasmid DNA and Doxorubicin (Dox). Both carriers could achieve efficient Dox and pDNA co-delivery *in vitro* and *in vivo* and achieved lung-specific accumulation for treatment of lung cancer.

TABLE OF CONTENTS

LIST OF TABLES

LIST OF FIGURES

PREFACE

This Ph.D. dissertation is a summary of my research work accomplished in the Center for Pharmacogenetics, Department of Pharmaceutical Sciences, in University of Pittsburgh under the dedicated supervision and kind guidance of my advisor, Dr. Song Li.

First and foremost, I would like to express my deep and hearty thanks to my advisor, Dr. Song Li, who offered me this precious opportunity to work and study here and led me go through all of the toughness in life and research. It is my greatest luck to have his patient guidance, insightful suggestions and constant encouragement through the whole process of my long five-year study. This work would never be accomplished without his help, support, and encouragement.

During my Ph.D. study，my supervisor, Dr. Song Li, who has offered me numerous valuable comments and suggestions with incomparable patience throughout my work. I am so grateful that he is always there when I need help. I learned from him about his intelligence, diligence, patience and erudition through every conversation and discussion. He created a wonderful lab environment for us to grow and learn. He not only taught me how to conduct the experiments, but also equipped me with the ability and confidence to explore deeper in knowledge and to learn how to become a real scientist.

I would like to grant oceans of thanks to all my respected committee members, Dr. Xiaochao Ma, Dr. Raman Venkataramanan, Dr. Yang Da and Dr. Binfeng Lu for their numerous advices and help in my research. Their instructions have helped broaden my

horizon and their enlightening teaching has provided me with a solid foundation to accomplish my thesis work and will always be of great value for my future career and academic research.

I'd like to express my deep thanks to Dr. Jiang Li for his kind and patient guidance on my research and life. He taught me to how to conduct the cell culture work and numerous biological studies. I'd like to express my sincere thanks to Dr. Yixian Huang for his great help with chemical synthesis and for his selflessness help during all my works. I also want to show my great gratitude to Dr. Jingjing Sun for her great help in the polymer synthesis. I would like to extend my hearty thanks to all my family members in Dr. Li's Lab (Dr. Xiaolan Zhang, Dr. Yifei Zhang, Dr. Jianqin Lu, Dr. Peng Zhang, Dr. Mohammed Ghazwani, Jieni Xu, Yuan Wei, Zhuoya Wan, Zhangyi Luo, Pearl Moharil, Wuyueyang Liu, Yuqian Du, Dr. Gao Xiang, Dr. Yanhua Liu, Dr. Lei, Liang, Dr. Qiongfeng Liao, Dr. Min Zhao, Zuojun Li, Qianyu Zhai, Dr. Yan He), who inspired and helped me in every step forward.

Many thanks for all of faculties and members in Center for Pharmacogenetics. Special thanks to Dr. Wen Xie, Dr. Xiaochao Ma, Dr. Da Yang and Dr. Christian Fernandez who create such a great environment for us to study and learn. Great thanks for Mr. William C. Smith who help me to solve many problems during work.

Many thanks go to the faculties from School of Pharmacy at the University of Pittsburgh. Special thanks to Dr. Patricia Dowley Kroboth, Dr. Randall B. Smith, Dr. Samuel M. Poloyac, Dr. Barry Gold, Dr. Robert B Gibbs, Dr. Sean Xie, Dr. Maggie Folan, Lori M. Altenbaugh for their endless support and help all these years. Many thank to my classmates and friends in

School of Pharmacy, University of Pittsburgh.

This dissertation is dedicated to my father, Shiqiang Chen, for his endless love since I was born. Finally, I would like to express my deep gratitude to my dear boyfriend, Jiajun Ye, for his long-term support and love. They have been a constant motivation for me to achieve my goals and conquer every difficulty ahead of me.

1.0 INTRODUCTION

1.1 NANOPARTICLES FOR CANCER THERAPY

Cancer is defined as diseases involving uncontrolled growth of cells with the metastatic potential. It accounts for 15.7% of human deaths world-wide[1]. Conventional anti-cancer strategies include surgery, radiation, chemotherapy and targeted therapy agents[2, 3, 4]. Chemotherapy drugs are distributed nonspecifically in the systemic circulation and this lead to toxicities to normal cells and limited exposure in the tumor[5]. Cancer nanotherapeutics has emerged as an important approach to solve problems such as nonspecific toxicity in addition to low water solubility, low bioavailability, and poor therapeutic effect of certain chemotherapeutic agent. Nanoparticles, including polymeric nanoparticles, micelles, dendrimers, hydrogel nanoparticles, liposomes, metal and inorganic nanoparticles with the size around 3-200 nm are used as drug delivery systems[6, 7, 8, 9]. The optimal size and well-designed surface characteristics of the nanotherapeutic systems allow delivery of therapeutic agents to cancer cells by taking advantage of unique pathophysiology of the tumor, such as the hypoxia and the enhanced permeability and retention effect (EPR effect)[10, 11]. Tumor specific ligands or antibodies are also incorporated on the surface of the therapeutic nanoparticles to improve active targeting and overcome drug resistance, mediated by P-glycoprotein, via receptor-mediated endocytosis[7, 12].

1.1.1 POLYMERIC MICELLES DELIVERY SYSTEM IN ONCOLOGY

Polymeric micelles are colloidal nanoparticles with a size around 5-200 nm. Micelles consist of amphiphilic molecules, which have both a hydrophobic head and a hydrophilic tail. The well-designed hydrophilic shell of the micelle can stabilize the micelle, achieve prolonged circulation upon injection and thus avoid recognition by reticuloendothelial system (RES)[13]. The Poly(ethylene glycol) (PEG) is the most widely used hydrophilic structure due to its highly water solubility, low cytotoxicity and biocompatibility[14]. The hydrophobic structure should be able to interact with the loaded hydrophobic drug with a high drug loading capacity. Polyesters, polyethers, and polyamino acids are commonly used as hydrophobic core materials[15]. With increasing concentration of these amphiphilic molecules of polymer in an aqueous solution, the polymer can self-assemble to form micelles at the critical micelle concentration (CMC)[16]. The formation of micelles above the CMC is relied on the hydrophobic-hydrophobic interaction and/or π-π stacking inside the hydrophobic core of micelle or the hydrogen bonding between the hydrophilic motifs.

Micelle has gained increasing attention as carriers for hydrophobic drugs in anticancer therapy due to its structural simplicity, nano-scale sizes and targeted accumulation in the tumors[17, 18]. Currently, five anticancer micellar formulations have entered the clinical trials and among which, Genexol-PM for delivery of PTX has been approved by FDA for treatment of breast cancer[19, 20]. The Genexol-PM was effective and safe in treating metastatic breast cancer and advanced pancreatic cancer in phase II studies. Moreover, micelle formulation

allowed delivering higher doses of PTX compared to the Taxol formulation without significant toxicity in clinical study[21].

Although inspiring results have been achieved by micelle-based cancer therapy, there are still many ways to further improve the antitumor efficacy. Firstly, micelles can be modified with actively tumor targeting ligands to increase the tumor specific accumulation with reduced systemic toxicity[22]. Active ligands such as monoclonal antibodies and peptides allow the micelles bind to specific receptors on the cancer cell and thus increase the micelle endocytosis, achieving higher intracellular drug concentrations[22, 23]. Many reports have demonstrated the ligand modified micelles has shown superior antitumor activity compared to non-targeted micelles with higher cellular uptake, stronger cytotoxicity and more effective tumor regression[24]. Secondly, it is possible to improve the drug release profile of micelle by designing triggered release micelles based on the mechanisms such as pH-sensitive, thermo-sensitive, ultrasound-sensitive and light-sensitive linkers or structures[25, 26]. The rate of drug release from micelles is influenced by the micelle stability, polymer degradation rate and drug concentration. Drug release kinetics can be greatly enhanced by applying an internal or external trigger to the micelle formulations. For example, pH-sensitive polymer conjugates incorporating acid-labile bonds such as hydrazones have been demonstrated tumor specific release of loaded drug due to a more acidic condition in tumor (pH~6.8) than normal tissues (pH~7.4), which can trigger drug release through the pH-responsive structures in the micelles. Third, can incorporate bioactive components in to the carrier system by promoting potential synergistic effect or counteracting the side effects of loaded anticancer drugs[27, 28]. One

example of the dual functional micelle system is poly(ethylene glycol)$_{3500}$ embelin conjugation for PTX delivery that was developed in our lab[29]. Embelin induces antitumor activity by increasing cellular apoptosis, inhibiting tumor cell proliferation and suppressing cell proliferation pathway such as nuclear factor-kappa B (NF-κB). Data showed that PEG-derivatized embelin greatly enhanced the delivery of PTX and achieved better *in vivo* therapeutic effect than Taxol alone.

1.1.2 COMBINATIONAL CANCER THERAPY USING DUAL-FUNCTIONAL NANOCARRIER

Most of the micelles in drug delivery are using "inert" materials with no therapeutic activity, which will cause safety issues due to the large amount of carrier used in the treatment of cancer. It is a promising approach to develop biologically active nanocarriers for tumor therapy and at the same time, effectively incorporate and deliver hydrophobic drugs. One strategy is conjugating selected numbers of hydrophobic anticancer drugs to hydrophilic polymers yielding a prodrug, which can self-assemble into micelles in aqueous solution due to the interactions between the hydrophobic anticancer drugs[30, 31]. The hydrophobic core formed could be used to interact with incorporated drug to achieve simultaneous delivery of both drugs. The drug-formulated bioactive micelles can not only achieve enhanced therapeutic effect by targeting different signaling pathways and meanwhile, decrease the potential toxicity generated by the co-loaded antitumor drugs. In our lab, several dual-functional micelle delivery systems were developed for combinational cancer therapy

such as PEG_{2K}-Fmoc-Ibuprofen and PEG_{5K}-Fmoc-(vitamin $E)_2$ micelles for delivery of PTX[32].

1.1.3 PEG-FTS BASED DUAL-FUNCTIONAL NANOCARRIER

In our lab, we developed a dual functional PEG-FTS derivatized nanocarrier for delivery of PTX[33]. FTS is a synthetic nontoxic Ras proteins inhibitor[34]. Highly mutative Ras was constitutively active in promoting tumor cell proliferation by activating downstream pathways and was detected in ninety percent of pancreatic and fifty percent of colon cancers. FTS is a farnesyl mimetic anticancer drug and takes effect by competing with binding of active Ras proteins to cell memberane and further leads to the degradation of Ras protein in the cytoplasm[35]. FTS has been shown to have significant anticancer effect while using in combination with other anticancer agents such as gemcitabine or PTX[36, 37]. Recently, we found the FTS could synergize with curcumin in various types of cancers including breast and prostate cancer[33]. Both the FTS and other drugs such as curcumin are poorly water soluble with low bioavailability. A PEG-derivatized FTS prodrug based micelle formulation was developed and the antitumor activity of FTS was largely maintained upon conjugation. The PEG-FTS conjugation greatly enhanced the FTS solubility and could be used to formulate hydrophobic drug for targeted delivery. Our group previously demonstrated that the PTX formulated PEG_{5K}-FTS_2 micelles showed significantly higher antitumor activity compared to Taxol at the same dose of 10 mg PTX/kg in a mouse 4T1.2 mouse model. More biological active dual-functional nanocarriers were developed to achieve enhanced antitumor

activity such as PEG-derivatized embelin micelle or the camptothecin-tocopherol micelle system.

1.2 CANCER IMMUNOTHERAPY

Recently, increasing evicences have shown that cancer treatment with cytotoxic agents was often limited by various immunological negative feedback mechanisms[38, 39]. As a result, combing immunotherapy with other thrapeutic stratergy represents a promising approach to futher improve anti-cancer effect. Cancer immunotherapy refers to harnessing the power of immune system to cure and protect patients from cancer, which is based on the assumption that cancer cells are immunogenic and can be recognized and eliminated by the immune system[40, 41, 42]. Under ideal condition, tumor cell growth will disrupt the surrounding microenvironment and further induce local inflammation, which will stimulate antigen-presenting cells to engulf tumor-derived antigens and trigger activation of tumor-specific T cells in an adaptive immune response. However, tumor cells always find ways to interfere with the development of antitumor immune response, such as decreased expression of major histocompatibility complex or overexpressed immunosuppressive costimulatory proteins on the tumor cells, disrupted function of natural killer cells and increased expression of proteins that interfere antigen presentation and T cell proliferation[42, 43, 44]. As a result, development of strategies that effectively and safely augment antitumor responses remains a big challenge.

1.2.1 AN OVERVIEW OF CANCER IMMUNOTHERAPY

Over the past decade, immunotherapy in controlling tumor development and progression has been investigated intensively. Activation of innate and adaptive immune systems is a critical process for generating effective anticancer immune response[45]. Accumulating evidence shows a correlation between tumor-infiltrating lymphocytes in tumor tissue or tumor lymph nodes and favorable prognosis in various cancer types[46]. There are four essential steps to achieve effective tumor-specific immune response. Firstly, antigen presenting cells (mostly DCs) must engulf tumor specific antigens in order to initiate antitumor immune response, which can be achieved during tumor development or by stimulation of antitumor vaccines[47]. Secondly, the DCs would also have to undergo further maturation and differentiation processes to present tumor specific antigen-derived peptides. This can be achieved by activation of factors released by endogenous necrotic tumor cells or therapeutic approaches such as toll-like receptor (TLR) ligands. Third, the tumor antigen/DCs complexes need to initiate tumor-killing T cell immune responses such as the proliferation of tumor specific cytotoxic $CD8^+$ T cells[48]. Finally, the produced T cells must enter the tumor microenvironment to generate tumor specific cytotoxic effect.

Tumor cells are smart and may generate immunosuppressive micro-environment to avoid recognition of host immune system and inhibit T cell function through diverse mechanisms including upregulation of suppressive co-inhibitory receptors or ligands (eg, PD-1 and PD-L1) on the cellular surface, recruiting more suppressive regulatory cells (e.g., T_{reg} and MDSCs) or

consuming tryptophan to limits T cell proliferation by expressing indoleamine 2,3-dioxygenase (IDO) enzyme. Drugs or antibody against CTLA4, PD-1/PD-L1 axis or IDO may be a good choice to reverse the immunosuppressive status. Reciprocal to the blockade of co-inhibitory receptors, diverse strategies are developed to reverse the immunosuppressive status and stimulate the antitumor immune response, including immunogenic vaccines, immune stimulating antibodies, immunostimulatory cytokines, antitumor viruses, and adoptive T cell therapies. 1) vaccines: cancer vaccines are developed to generate and boost the body's natural defenses to fight a cancer by increasing the process of tumor antigen presentation, such as developing DNAs sequences that encode either tumor-specific or tumor-associated antigens that can stimulated T cell immune response[49]. Sipuleucel-T, is one of the therapeutic cancer vaccines approved by FDA for treatment hormone-refractory prostate cancer patients.[50] However, most of the cancer vaccines have limited efficacy and only work in selective patients due to the immune counteracting mechanisms engaged during cancer vaccine responses. Also it is very challenging and costly to develop high quality vaccine products for clinical use[51]. 2) cytokines: cytokines are small proteins (~5-20 kDa) that play a pivotal role in cell signaling. Nearly all cell types including tumor cells, immune cells and nonimmune stromal cells produce cytokines[52]. Together with cell surface adhesive molecules, cytokines mediate the activity of immune cells by altering cell signaling intensity and duration between cells and tissues[53]. Proinflammatory cytokines such as IFNs, IL-2, IL-4 and IL-15 are currently used to polarize the immune response against cancer through direct inhibit tumor cells growth or stimulation T-cell activation[54]. 3) antitumor virus therapy:

oncolytic virus are native or engineered viruses, which can preferentially replicate in cancer cells and kill infected cancer via direct oncolysis of tumor cells, targeting tumor vasculature and further stimulate immunogenic response towards tumors[55]. Currently, T-Vec is the only oncolytic virus approved by FDA for treatment of metastatic melanoma[56]. 4). adoptive T-cell therapy: adoptive T-cell therapy is a passive immunization strategy which involves the ex vivo selection and expansion of antigen-specific T cell clones, transfusion of specific T-cells which can recognize tumor associated antigens back to patients and trigger a cascade of antigen-specific immunity for treatment of cancer[57]. However, tumor-infiltrating lymphocytes are difficult to harvest and expand from the blood samples and the low expression of specific antigen on tumor cells limits the use of adoptive T-cell therapy.

Recent success of novel anticancer immunotherapies has led to a new era of cancer treatment. Immunotherapies have made clinically meaningful progress in multiple tumor types. Unfortunately, the patient responses to immunotherapy are still limited and more efforts are required to improve therapeutic outcomes with these treatments. Development of personalized treatment or combinational immunotherapy with other treatment strategies could help overcome some of these limitations.

1.2.2 THE BLOCKADE OF IMMUNE CHECKPOINTS IN CANCER IMMUNOTHERAPY

During long term development of cancer immunotherapy, advances have been made in the understanding of cancer development and progression, resulting in the availability of

promising novel therapeutic options, such as checkpoint inhibitors. Immune checkpoints are referred as stimulatory or inhibitory regulators in the immune system, which play important roles in modulating body immune tolerance, preventing autoimmunity and protecting tissues from damage for abnormal immune response. These checkpoint pathways are used as important immune resistance mechanisms for fast-growing tumor cells to protect themselves from immune system recognition and elimination. Blockade of immune checkpoints is thus a promising strategy for activating and restoring anti-tumor immune responses.

Many immune-checkpoint pathways were discovered as major mechanisms for tumor immune escape, such as CTLA-4, PD-1, TIM-3, IDO1 and LAG-3. Most of the immune checkpoint proteins mediate immune response by ligand-receptor interactions, so they can be readily blocked by antibodies and modulated by ligands. For example: CTLA-4 is an immune checkpoint protein expressed mainly on the surface of T cells and acts as a negative regulatory receptor in the antigen presentation process to T cells. Ipilimumab, antibodies against CTLA-4 were the first FDA approved immunotherapy for melanoma, worked by counteracting immune suppression in tumor microenvironment[58]. Another immune checkpoint pathway, PD-1/PD-L1 axis also plays a critical role in tumor immune escape. PD-1 is a co-inhibitory receptor expressed on several immune cells including activated T cells, NK) cells and MDSCs and PD-L1 has been found to be overexpressed in myeloid cells and various tumors types, including melanoma, non-small cell lung cancer and breast cancer[59]. Interaction between PD-1 and its ligands PD-L1 leads to effecter T-cell apoptosis and tumor immune resistance[60]. Blockade of the PD-1 or PD-L1 by monoclonal antibodies

produced both durable anti-tumor response and prolonged survival rate in patients with metastatic non-small cell lung cancer and melanoma[61].

Another category of immune-inhibitory molecules includes certain metabolic enzymes, such as indoleamine 2,3-dioxygenase (IDO). IDO is an enzyme catalyzes the first and rate-limiting step of tryptophan degradation[62]. IDO overexpression is observed in both tumor cells and tumor associated antigen-presenting cells[63]. Emerging evidence suggests that IDO becomes activated during tumor development, helping tumor cells escape the immune system through its ability to inhibit effector T cell proliferation and function[64]. IDO enzymes can be inhibited by small molecular analogues of their substrates such as 1-MT or NLG919[65].

1.2.3 RATIONALE OF COMBINATION USE OF CHEMOTHERAPY AND IMMUNOTHERAPY

The pre-existing antitumor immune responses are key factors for clinical response using the checkpoint inhibitors for IDO, CTLA-4 and PD-1/PD-L1[66]. Only a small potion of patients will benefit from immune therapy due to the complexity of immune suppressive mechanisms and the varying tumor immunogenicity. Even though the novel checkpoint inhibitors show impressive antitumor activity, their efficacy may be further enhanced in combination with other agents. In addition, combined treatment may reduce the resistance. Thus, drugs combinations therapies, which can target various mechanisms of immune tolerance, are being actively investigated[67].

Combination of chemotherapy and immune therapy has drawn increasing attention in treatment of cancer[68]. Chemotherapy drugs are generally believed to directly kill tumor cells. However, increasing evidence shows that chemotherapy also works through immune activation by either modifying the tumor microenvironment or directly stimulating anticancer immune response[69]. However, the chemotherapy induced immune response is restricted by various counteract mechanisms such as elevation of immune checkpoint proteins[70]. Combination of chemotherapy and checkpoint inhibitor represents one of the most promising strategies to treat cancer. For example, co-treatment of PD-1 antibody and chemotherapy such as platinum has been reported to have significant antitumor activity in both preclinical and clinical condition[71].

1.2.4 MULTIFUNCTIONAL MICELLE DELIVERY SYSTEM FOR CHEMOIMMUNOTHERAPY

Several IDO inhibitors have been reported, among which NLG919 is a highly IDO-selective inhibitor with an EC50 of 75 nM[72]. However, NLG919 has a poor water solubility and limited bioavailability, which presents a major challenge in the clinical use[73]. In addition, co-delivery of IDO inhibitors and chemotherapeutic agents faces many problems such as hydrophobicity and different pharmacokinetic profiles. To resolve these challenges, we synthesized a novel prodrug micellar system based on conjugation of PEG and NLG919. An Fmoc group was also introduced into the conjugate to improve drug carrier interactions. PEG-Fmoc-NLG could be further used as a carrier for co-delivery of chemotherapeutic drugs,

which represented an immunostimulatory dual-functional nanocarrier that improved cancer immunochemotherapy.

1.3 TARGETED CODELIVERY OF GRUG/GENE CONBINATION FOR CANCER THERAPY

Cancer cells contain various oncogenic and tumor suppressor mutations that enable tumor cells to evade programmed cell death and activate invasion and metastasis, thus making cancer treatment extremely challenging[74, 75]. Surgery and chemotherapy remain the mainstream of anti-cancer strategies. However, due to the complexity of cancer as a disease, it has become increasingly clear that small molecule drugs targeted to specific cellular pathways have limitations. Gene therapy involves the delivery of plasmid DNA (pDNA), small interfering RNA (siRNA), short hairpin RNA (shRNA) or micro RNA (miRNA) to modulate the expression of specific gene or proteins, which has the potential advantages to target any disease related gene[76]. Cancer gene therapy usually works through either upregulating apoptotic gene and cytotoxic immune cytokines or downregulating gene involved in tumor cell multidrug resistance[77, 78]. The use of combination therapy involving both gene therapy and chemotherapy has resulted in combinational effect and has become an increasingly important strategy for the future.

The usual strategy for co-delivery of drug and gene is using separate carriers, which have different pharmacokinetic and pharmacodynamics properties and can hardly achieve combinatory effects[79]. Co-delivery of two therapeutic agents by a single carrier offers several

advantages over using separate carriers and ensures the drug and genes are able to work synergistically within the same cell to produce an enhanced anti-cancer effect[80, 81]. However, the development of such carrier remains a significant challenge, due to the difference in hydrophobicity, molecular weight and release profiles of drug and genes[82]. Attempts have been made to deliver drugs and DNA/RNA simultaneously using nanocarriers such as liposomes, polymeric nanoparticles and micelles[83, 84]. Various functional groups were incorporated into the carriers for interaction and binding with drug and gene such as cationic quaternary amine groups for the electrostatic binding with DNA or RNA[85]. Here we report cationic micelle nanoparticles POEG-*st*-Pmor and POEG-*st*-Ppipe that were self-assembled from a biodegradable amphiphilic copolymer. These nanoparticles offered advantages over liposomes and other nanoparticles for their simplicity and flexibility in size and charge modulation. More importantly, they achieved high gene-transfection efficiency and the capability of co-delivering drugs and genes to tumor site. Enhanced gene transfection with the co-delivery of DOX had been demonstrated by *in vitro* and *in vivo* studies.

2.0 TARGETED DELIVERY OF CURCUMIN TO TUMORS VIA PEG-DERIVATIZED FTS-BASED MICELLAR SYSTEM

2.1 ABSTRACT

Curcumin and S-trans, trans-farnesylthiosalicylic acid (FTS) are two promising anticancer agents. In this study, we demonstrated that the two agents exerted significant synergy in antitumor activity in various types of cancer cells with combination indices ranging from 0.46 to 0.98 (a value of less than unity indicates synergism). We have further shown that synergistic-targeted co-delivery of the two agents can be achieved via formulating curcumin in polyethylene glycol (PEG)-derivatized FTS-based nanomicellar system. Curcumin formulated in PEG-FTS micelles had small size of around 20 nm. The nanomicellar curcumin demonstrated enhanced cytotoxicity towards several cancer cell lines *in vitro*. Intravenous application of curcumin-loaded micelle (20 mg/kg curcumin) led to a significantly more effective inhibition of tumor growth in a syngeneic mouse breast cancer model (4T1.2) than curcumin formulated in Cremophor/EL ($P<0.05$).

2.2 BACKGROUND

Curcumin, a hydrophobic polyphenol compound extracted from Curcuma longa, has a wide spectrum of pharmacological activities and holds promise in the management of various diseases, such as cancers, cardiovascular diseases, Alzheimer's disease, and diabetes[86, 87, 88].

Particularly, curcumin has drawn interests as a therapeutic and chemopreventive agent for cancers via suppressing multiple signaling pathways such as MAPKs, PI3K/AKT, and NF-κB and inhibiting tumor cell proliferation, invasion, metastasis, and angiogenesis with no obvious side effect[89, 90, 91]. Moreover, curcumin acts as a chemosensitizer that augments the cytotoxic effect of other chemotherapeutic drugs such as doxorubicin and cisplatin[92, 93, 94].

S-trans, trans-farnesylthiosalicylic acid (FTS) is a synthetic farnesylcysteine mimetic that acts as a potent and especially nontoxic Ras antagonist[95, 96]. Constitutively active Ras caused by mutation in the Ras family of proto-oncogenes is present in one third of human cancers, with the highest incidence of mutational activation of Ras being detected in pancreatic and colon cancers[97]. Ras is also activated in cancer cells by other mechanisms[98, 99]. FTS has been shown to cause significant reduction of Ras levels, showing antitumor activity in a wide range of human cancers without observable side effects[100, 101, 102]. FTS also can work in combination with other anticancer drugs, such as valproic acid and PKF115-584[103, 104]. Both curcumin and FTS have issues of poor water solubility and limited oral bioavailability despite their potentials as anticancer agents[105, 106]. We have recently shown that PEGylation of FTS led to significantly increased solubility of FTS in aqueous solution[107]. A conjugate of one molecule of PEG5000 (PEG_{5K}) with two molecules of FTS via a labile ester linkage (PEG_{5K}-FTS_2 (L)) well retained the FTS biological activity. Interestingly, polyethylene glycol (PEG)-derivatized FTS self-assembled to form small-sized micelles that are effective in solubilizing other hydrophobic drugs such as paclitaxel (PTX)[107]. In addition, PEG-FTS-based micelles demonstrated synergistic antitumor activity with co-delivered PTX

in vitro and *in vivo*[107]. In this study, we examined whether the combination of curcumin and FTS exerted a synergy in antitumor activity in various types of tumor cells. The potential of PEG-FTS-based micellar system in synergistic-targeted delivery of curcumin was also investigated.

2.3 EXPERIMENTAL PROCEDURES

2.3.1 Materials

Curcumin (synthetic) was purchased from TCI American (OR, USA). Dimethyl sulfoxide (DMSO), 3-(4,5-dimethylthiazol- 2-yl)-2,5-diphenyl tetrazolium bromide (MTT), trypsin-EDTA solution, Triton X-100, and Dulbecco's Modified Eagle's Medium (DMEM) were all purchased from Sigma-Aldrich (MO, USA). FTS was synthesized and purified following the published literature[96]. Antibodies against p-Akt (S473) and Akt were purchased from Santa Cruz Biotechnology. HRP-labeled goat antirabbit IgG was purchased from Amersham Biosciences (Piscataway, NJ, USA). Dulbecco's phosphate- buffered saline (DPBS) was purchased from Lonza (MD, USA). Fetal bovine serum (FBS) and penicillin−streptomycin solution were from Invitrogen (NY, USA).

2.3.2 Cell Culture

4T1.2 is a mouse breast cancer cell line, and Panc02-H7 (H7) is a mouse metastatic pancreatic cancer cell line. DU145 and PC3 are two human androgen-independent prostate

cancer cell lines. A549 is a human lung cancer cell line, and MCF7 is a human breast cancer cell line. All these cell lines were cultured in DMEM medium containing 10% FBS and 1% penicillin–streptomycin at 37°C in a humidified environment with 5% CO_2.

2.3.3 Animals

Female BALB/c mice (4–6 weeks) were purchased from Charles River Laboratories. All animals were housed at controlled temperature and humidity according to AAALAC guidelines. All animal-related procedures were performed by fully following the protocol guidelines approved by the Animal Use and Care Administrative Advisory Committee of the University of Pittsburgh.

2.3.4 Synthesis of PEG_{5K}-FTS_2 Conjugate

PEG_{5K}-FTS_2(L) is a conjugate of one molecule of PEG5000 (PEG_{5K}) with two molecules of FTS via a labile ester linkage. PEG_{5K}-FTS_2(S) is similar to PEG_{5K}-FTS_2(L) in structure but has a relatively stable amide linkage between PEG and FTS[108]. PEG_{5K}-FTS_2(L) and PEG_{5K}-FTS_2(S) conjugates were synthesized and chemically characterized as described previously[107]. Briefly, for the synthesis of PEG_{5K}-FTS_2(L), MeO-PEG_{5k}-OH (1 equiv.), succinic anhydride (5 equiv.), and 4-(dimethylamino) pyridine (DMAP, 5 equiv.) were mixed in DCM to yield carboxyl-terminated PEG monomethyl ether (MeO-PEG_{5k}-COOH). Diethanolamine (3 equiv.) was then coupled to the carboxylic group of MeO-PEG_{5k}-COOH (1 equiv.) using N-hydroxysuccinimide (NHS 3.6 equiv.) and dicyclohexylcarbodii- mide (DCC 3.6 equiv.). PEG monomethyl ether with two hydroxyl groups (MeO-PEG5k-(OH)2)

was purified by precipitation with ice-cold diethyl ether and ethanol respectively. PEG_{5K}-FTS_2(L) conjugate was obtained by coupling MeO-PEG_{5k}-$(OH)_2$ (1 equiv.) to FTS (5 equiv.) via DCC (3 equiv.) and DMAP (0.3 equiv.) in chloroform. The mixed solution was filtered, and the final product was purified by precipitation in cold diethyl ether and ethanol respectively. PEG_{5K}-FTS_2(S) was similarly synthesized except that MeO-PEG_{5K}-OH was first reacted with di-Boc lysine followed by deprotection of Boc using TFA. MeO-PEG_{5k}-$(NH2)_2$ was then reacted with FTS via DCC and DMAP, and the final product was similarly purified as described above. The structures of PEG_{5K}-FTS_2(L) and PEG_{5K}-FTS_2(S) were confirmed by NMR.

2.3.5 Preparation of Curcumin-Loaded Micelles

Curcumin (10 mM in chloroform) was mixed with PEG_{5K}-FTS_2(L) or PEG_{5K}-FTS_2(S) (10 mM in chloroform) at various carrier/drug molar ratios. The chloroform was removed by a stream of nitrogen to generate a thin film at the bottom of the glass tube, and the residual organic solvent was further removed under vacuum for 2 h. Subsequently, the thin film was hydrated and suspended in DPBS to form the curcumin-loaded micelles. The unincorporated curcumin was removed by filtration through a syringe filter (pore size, 0.22 μm). The drug-free micelles were similarly prepared as described above.

2.3.6 Characterization of Curcumin-Loaded Micelles

The average size and polydispersity index (PDI) of blank and curcumin-loaded micelles were measured by Zetasizer (Zetasizer Nano ZS instrument, Malvern, Worcestershire, UK) under room temperature.

The morphology of micelles was examined through transmission electron microscopy (TEM). Briefly, curcumin micelles were diluted with DPBS and placed on a copper grid covered with Formvar. Samples were stained with 1% uranyl acetate, and imaging was performed at room temperature using TEM (JEM-1011, JEOL, Japan).

The drug-loading capacity (DLC) and drug-loading efficiency (DLE) of curcumin micelles were determined by reverse phase HPLC (Alliance, 2695-2998 system). Briefly, curcumin- loaded micelles were prepared as described above and then filtered through a syringe filter (0.22 μm). Curcumin in the filtered and nonfiltered micelles was extracted with methanol and quantified by HPLC with a mobile phase consisting of methanol/0.3% acetic acid (80/20, v/v), a flow rate at 1 mL/min, and a UV detector. The DLC and DLE of curcumin micelles were calculated according to the following formula:

DLC(%)=[weight of drug used/(weight of polymer+drug used)]×100%

DLE (%)=[weight of loaded drug/weight of input drug]×100 %

The colloidal stability of curcumin micelles with various carrier/ drug molar ratios was evaluated by following the changes in sizes of the particles at different times following sample preparation.

2.3.7 Cytotoxicity Assay

Cytotoxicity assay was performed on 4T1.2, MCF7, A549, H7, DU145, and PC3 cell lines. All cells were plated at a density of 1,000 cells per well in 96-well plates and incubated for 24 h in DMEM with 2.5% FBS and 1% streptomycin/penicillin. Then, cells were treated with various concentrations of free FTS, free curcumin, and the combination of both respectively for 96 h. Viability of cells was evaluated by MTT assay as described[30].

To test the cytotoxicity of curcumin-loaded PEG_{5K}-FTS_2(L) or PEG_{5K}-FTS_2(S) micelles, cells were treated with indicated concentrations of free curcumin, drug-free micelles, and curcumin- loaded PEG_{5K}-FTS_2(L) or PEG_{5K}-FTS_2(S) micelles respectively for 96 h. MTT assay was then performed as described above.

2.3.8 Western Blot Analyses

Western blotting was performed to evaluate the protein expression levels of phospho-AKT in DU145 cells. Cells grown in six-wells plates with 80% confluency were treated with free PEG_{5K}-FTS_2(L) or PEG_{5K}-FTS_2(S) micelles, free curcumin, and curcumin-loaded micelles respectively for 12 h. Cells were washed twice with pre-cooled PBS and lysed in a buffer containing 0.2% Triton X-100 for 10 min on ice. Protein concentrations were determined, and equal amounts of total protein lysate were resolved on a 15% SDS-PAGE and subsequently transferred to a nitrocellulose membrane. Membranes were blocked with 5% nonfat milk in PBS for 1 h prior to incubation with rabbit p-Akt or Akt primary antibody dissolved in PBST (DPBS with 0.1% Tween 20) overnight at 4°C. The blots were washed with PBST and then

probed with goat antirabbit IgG for 1 h at room temperature followed by chemiluminescence detection. β-Actin was used as a loading control.

2.3.9 Transfection Assay

Transient transfections were performed on DU145 cells using the UF-2 transfection agent as described previously[109]. Briefly, the plasmid-UF2 complexes were formed by incubating 0.01 mg of NF-κB reporter gene and 0.04 mg of UF-2 transfection agent at room temperature for 20 min in a total volume of 400 μL of serum-free DMEM medium. The complexes were then mixed with freshly trypsinized cells in 5% FBS cell culture medium, and the cells were added to a 96-well plate at 50–70% confluency. After 12 h of incubation, the transfection medium was replaced with medium that contained 10% fetal bovine serum laced with the designated concentrations of free FTS, free curcumin, free PEG_{5K}-FTS_2(L) or PEG_{5K}-FTS_2(S) micelles, and curcumin- loaded PEG_{5K}-FTS_2(L) or PEG_{5K}-FTS_2(S) micelles respectively. Cells were lysed with 0.2% Triton X-100 12 h later and assayed for luciferase activities. Transfection experiments were per- formed on at least three occasions, and in each case, experiments were done in triplicate. Data were represented as fold induction over reporter gene alone.

2.3.10 *In Vivo* Therapeutic Study

The syngeneic mouse tumor model 4T1 was generated by s.c. injection of 2×10^5 cells in 100 μL PBS into the right flank of each female BALB/c mouse. When the tumors reached ~50 mm^3 in size, mice were randomized into four groups (N = 5) for treatment. Mice were injected intravenously every other day for six times with 200 μL saline, blank PEG_{5K}-FTS_2(L)

micelles, curcumin in Cremophor EL (20 mg/kg), and curcumin-loaded PEG_{5K}-FTS_2(L) micelles (20 mg/kg) respectively. Tumor sizes and body weights were monitored every 2 days. Tumor volume was calculated according to the formula: volume = (tumor length×tumor width^2)/2. To compare between groups, relative tumor volume (RTV=V/V_0, V_0 was the tumor volume prior to the first injection) was calculated for each measurement. The mice were sacrificed when the tumors became larger than 1.5 cm in diameter or developed ulceration.

2.3.11 Statistical Analysis

In all statistical analyses, the significance was set at a probability of $P<0.05$. All results were reported as the means ±standard deviation. Statistical analysis was performed by Student's t test for two groups and one-way ANOVA for multiple groups, followed by Newman-Keuls test if $P<0.05$.

2.4 RESULTS

2.4.1 Effect of FTS and Curcumin on Cancer Cell Growth

The growth inhibitory activity of curcumin and FTS was assessed in a broad range of cancer cell lines including DU145 and PC3 (prostate), A549 (lung), H7 (pancreas), and 4T1 and MCF7 (breast). Curcumin or FTS caused a concentration-dependent inhibition of proliferation in all six cell lines (Figure 1), which was consistent with literature reports

(3,20,30–32). When we fixed the concentration of curcumin and gradually increased the concen- tration of FTS in co-treatment, the inhibition effect was progres- sively increased with increasing FTS concentration, indicating more effective tumor-killing effect in the

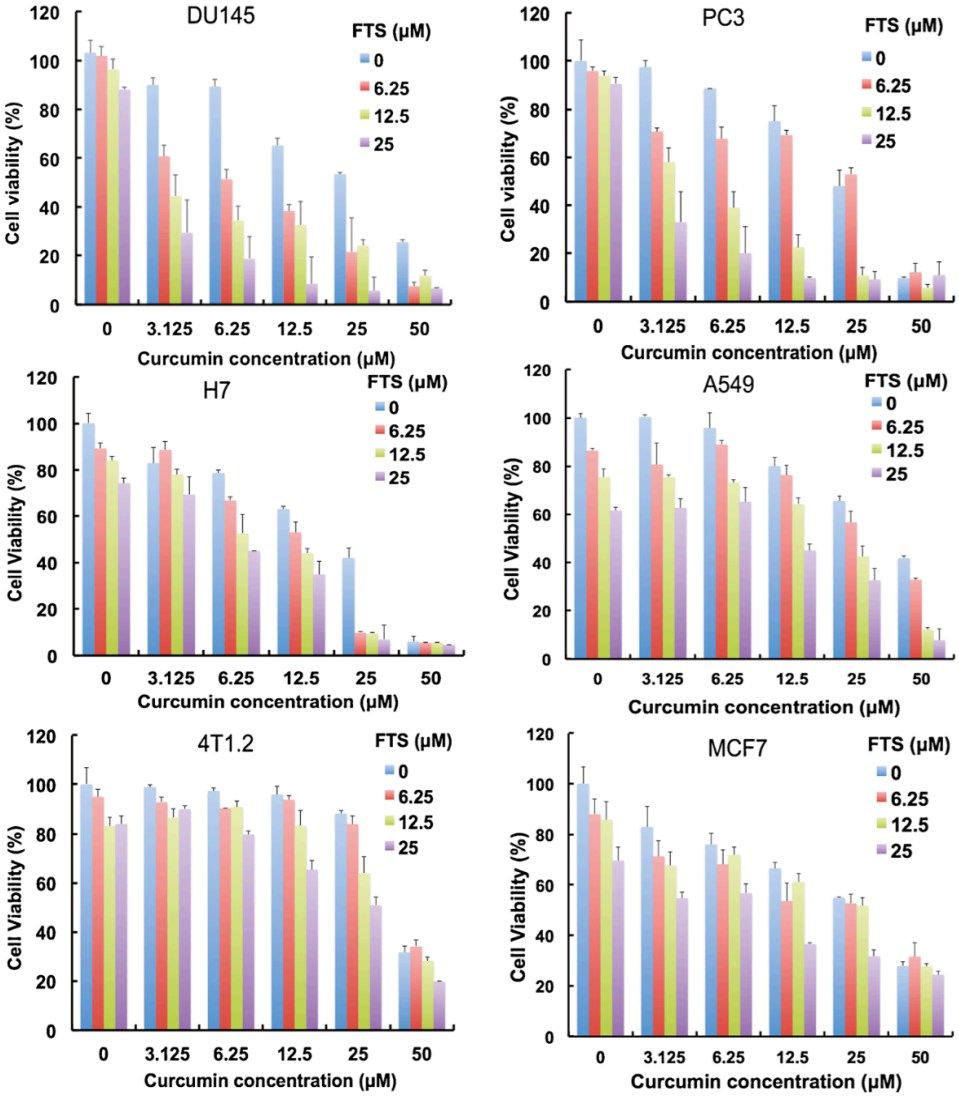

Figure 1. Synergistic action between FTS and curcumin in inhibiting the proliferation of tumor cells.

Various types of tumor cells including DU145, PC3, H7, A549, 4T1.2, and MCF7 cells were treated with various concentrations of free FTS, free curcumin, and combination of both respectively for 96 h, and the cytotoxicity was determined by MTT assay. The experiment was performed in triplicate and repeated three times. Data are presented as means ± standard deviation.

combination treatment (Figure 1). Table I compares the cytotoxicity of single treatment and that of combination treatment at a representative FTS concentration of 25 μM in combination with curcumin. We calculated the combination index (CI) after co-administration of FTS and curcumin to assess whether the combination could confer synergistic, additive, or antagonistic effects (Table 1). CI was calculated by the equation CI = (d1/D_{50}1)+(d2/D_{50}2), with D_{50}1 being the concentration of FTS producing 50% cell-killing effect in single treatment and d1 being the FTS concentration required to achieve the same 50% killing effect with d2 in co-treatment. Similarly, D_{50}2 is the concentration of curcumin producing 50% killing effect in single treatment, and d2 is the curcumin concentration required to obtain the same 50% cell-killing effect in combination with d1. A CI of <1, =1, and >1 is suggestive of synergism, additive effect, and antagonism, respectively. Data in Table I indicated that the combination of FTS and curcumin showed synergism in all of these examined cancer cell lines.

2.4.2 Characterizations of Curcumin-Loaded PEG_{5K}-FTS_2 Micelles

We have previously shown that a micellar system based on PEG_{5K}-FTS_2(L) retained the biological activity of FTS and was capable of synergistic delivery of paclitaxel. Following demonstration of synergy between curcumin and FTS in antitumor activity in various types of tumor cells, we then investigated whether curcumin can be formulated in PEG_{5K}-FTS_2(L) micelles, leading to effective co-delivery of PEG-derivatized FTS and curcumin and the subsequent synergistic action between the two at the tumor site.

Table 1. Synergistic Antiproliferative Activity of Curcumin and FTS in Cancer Cells

Drug combination	Cell line	d1 (μM)	$D_{50}1$	d2 (μM)	$D_{50}2$	CI
Curcumin+FTS	DU145	25	68.0±2.0	2.3±0.1	24.3±2.5	0.46
	PC3	25	75.3±4.6	2.5±1.2	29.0±1.3	0.42
	H7	25	70.5±0.7	9.6±0.2	22.5±4.7	0.78
	A549	25	58.0±2.3	20.3±1.4	42.2±3.5	0.91
	4T1.2	25	56.4±0.6	24.5±3.4	46.0±2.1	0.98
	MCF7	25	68.2±4.6	8.3±2.3	28.8±2.0	0.65

Combination Index (CI) of simultaneous treatment of curcumin and farnesylthiosalicylic acid (FTS) in DU145, PC3, H7, A549, 4T1.2, MCF7 cells. The CI values are interpreted as follows: <1.0, synergism; 1.0, additive; and >1.0, antagonism. Each experiment was done in triplicate

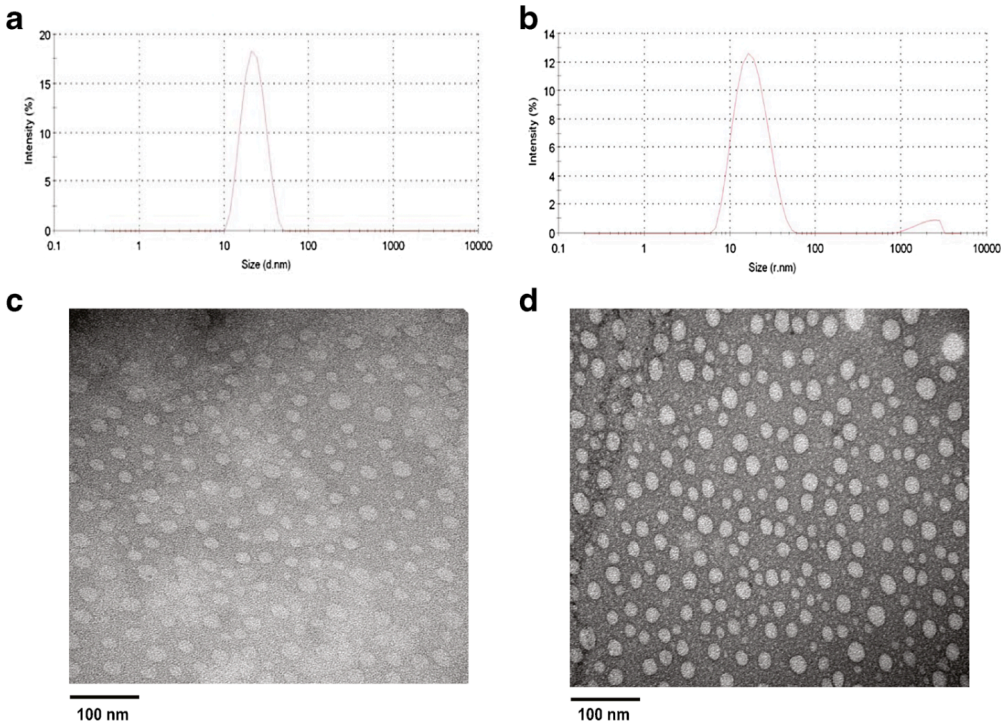

Figure 2. Particle size distribution and morphology of curcumin/PEG_{5K}-FTS_2 micelles. The average size and size distribution of drug-free micelles (a) and curcumin-loaded PEG_{5K}-FTS_2 micelles (b) were examined via DLS analysis. The morphology of drug-free micelles (c) and curcumin-loaded PEG_{5K}-FTS_2 micelles (d) was examined via EM following negative staining

Figure 2a shows that the particle size of PEG_{5K}-FTS_2(L) was around 20 nm, which was consistent with our previous report. Incorporation of curcumin into PEG_{5K}-FTS_2 (L) micelles had minimal impact on the average size and their size distribution (Figure 2b). TEM shows that both drug-free and curcumin-loaded PEG_{5K}-FTS_2(L) micelles had spherical shape and were homogenous in size distribution (Figure 2c, d), which was consistent with the result of DLS analysis (Figure 2a, b)

Table 2 shows the DLC and DLE at various carrier/drug molar ratios. Curcumin could be formulated in PEG_{5K}-FTS_2(L) micelles at a carrier/drug molar ratio as low as 0.5:1. However, the resulting mixed micelles were only stable for 2 h. Increasing the carrier/drug molar ratio was associated with an improvement in the colloidal stability of the curcumin-loaded micelles. Almost all of the input curcumin was loaded into the PEG_{5K}-FTS_2 micelles at a carrier/drug ratio of 2.5:1, and the resulting mixed micelles were stable for about 36 h. Curcumin/PEG_{5K}-FTS_2 mixed micelles prepared under this condition were used for all subsequent studies.

Table 2. Biophysical Characteristics of Curcumin-Loaded PEG_{5K}-FTS_2(L) Micelles and Free Micelles

Micelles	Molar ratio	Particle size (nm)	PDI	DLE (%)	DLC (%)	Stability (h)
PEG_{5K}-FTS_2(L)	-	19.8±0.1	0.266	-	-	-
PEG_{5K}-FTS_2(L): curcumin	0.5:1	24.2±0.6	0.139	75.2	11.8	2
	1:1	20.8±1.0	0.332	89.1	5.9	4
	2.5:1	19.0±1.3	0.239	98.5	2.4	36
	5:1	22.9±1.2	0.080	97.6	1.2	96
	10:1	21.3±0.3	0.145	98.2	0.6	180

Curcumin concentration in micelles was 1 mg/ml. Blank micelles concentration was 20 mg/ml. Values reported at the means±SEM PDI polydispersity index, DLE drug-loading efficiency, DLC drug-loading capacity

2.4.3 *In Vitro* Cytotoxicity of Curcumin/PEG_{5K}-FTS_2 Mixed Micelles

Curcumin was loaded into PEG_{5K}-FTS_2(L) and PEG_{5K}-FTS_2(S) micelles. Figure 3a shows the cytotoxicity of free curcumin and curcumin-formulated micelles in 4T1.2 cells. It was apparent that curcumin formulated in PEG_{5K}-FTS_2(L) micelles was more active than free curcumin in inhibiting the proliferation of tumor cells. Similar results were observed in DU145 (Fig. 3b) and PC3 (Figure 3c) cancer cells. Interestingly, curcumin formulated in PEG_{5K}-FTS_2(S) micelles was comparable to free curcumin among the three cell lines tested (Figure 3a–c).

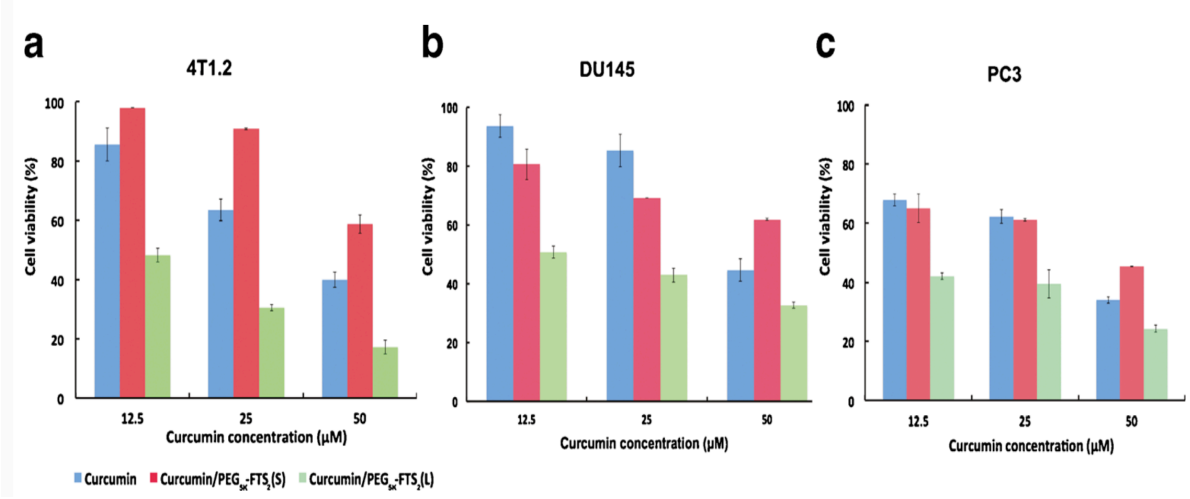

Figure 3 . Cytotoxicity of free curcumin, curcumin/PEG_{5K}-FTS_2 (L), and curcumin/PEG_{5K}-FTS_2 (S) against mouse breast cancer cell line, 4T1.2.
(a) and human prostate cancer cell lines, DU145 (b), and PC3 (c). Cells were treated for 96 h and cytotoxicity was determined by MTT assay. Values are reported as the means ± standard deviation for triplicate samples.

2.4.4 Effect of Curcumin/FTS Combination on AKT and NF-κB Pathways

To investigate the mechanism for the improved inhibitory effect of curcumin/ PEG_{5K}-FTS_2(L) mixed micelles on cancer cells, we examined their effect on AKT and NF-κB pathways in DU145 cells as the two signaling pathways are critically involved in the rapid proliferation of various types of cancer cells[89, 110, 111], and both FTS and curcumin have been shown to negatively regulate the two pathways[111]. As shown in Fig. 4, the level of pAKT was significantly downregulated following treatment with curcumin, which was consistent with previous reports[112]. The pAKT level was also decreased following treatment with either PEG_{5K}-FTS_2(L) or PEG_{5K}-FTS_2(S), although PEG_{5K}-FTS_2(L) was more effective compared to PEG_{5K}-FTS_2(S). It was also apparent that curcumin formulated in PEG_{5K}-FTS_2(L) micelles was more effective in inhibiting the phosphorylation of AKT compared to the treatment of either alone (Figure 4).

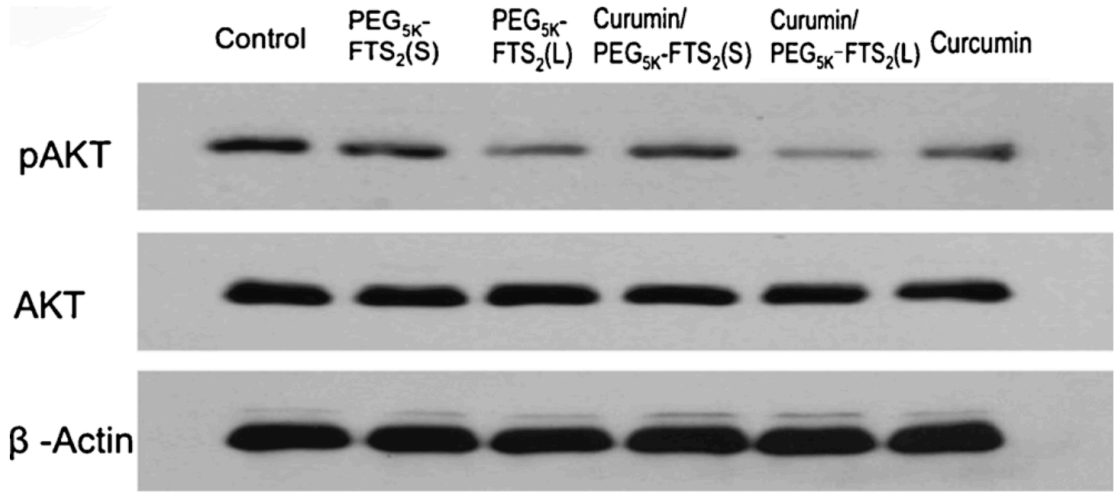

Figure 4. Inhibitory effect of micellar curcumin on AKT signaling in human prostate cancer cells, DU145.

Cells grown in medium containing 2.5% FBS were treated with 0.1% DMSO (control), PEG_{5K}-FTS_2(L), PEG_{5K}-FTS_2(S), curcumin/PEG_{5K}-FTS_2(L), curcumin/PEG_{5K}-FTS_2(S), and free curcumin respectively for 12 h. Western blotting was performed with total protein extracts using antibody against phospho-AKT. The same blot was reprobed with antibodies against total AKT as an internal control and β-Actin as a loading control.

Figure 5 shows the effect of FTS and curcumin on NF-κB signaling as examined in a NF-κB reporter assay. NF-κB activity was significantly inhibited by treatment with either curcumin or FTS alone. However, the inhibition of NF-κB activity was further enhanced by the combination treatment. It is also apparent that curcumin formulated in PEG_{5K}-FTS_2(L) micelles was more effective in inhibiting NF-κB signaling compared to PEG_{5K}-FTS_2(L) micelles alone or curcumin formulated in PEG_{5K}-FTS_2(S) micelles (Fig. 5).

2.4.5 *In Vivo* Therapeutic Study

A highly metastatic 4T1.2 model (s.c.) was used to evaluate the *in vivo* antitumor activity of curcumin formulated in PEG_{5K}-FTS_2(L) micelles. Curcumin formulated in Cremophor EL was used as a control. As shown in Figure 6a, treatment with curcumin/Cremophor EL (six times, every other day) led to a modest inhibition of tumor growth at the early stage. However, there is a rebound in the growth rate of tumor following discontinuation of the treatment after d10. At d20, the tumors in curcumin/Cremophor EL-treated group became comparable to the tumors in PBS group in size.

Curcumin formulated in PEG_{5K}-FTS_2(L) micelles was significantly more effective than curcumin/Cremophor EL in inhibiting the tumor growth. The growth of the tumors remained significantly retarded following the discontinuation of the treatment after d10. Figure 6b

shows the weights of the tumors collected at the end of the therapeutic study, which were consistent with the data of tumor growth curves (Figure 6a). All of the mice showed no signs of abnormal appearance, and no loss of body weight was found in these mice (Figure 6c).

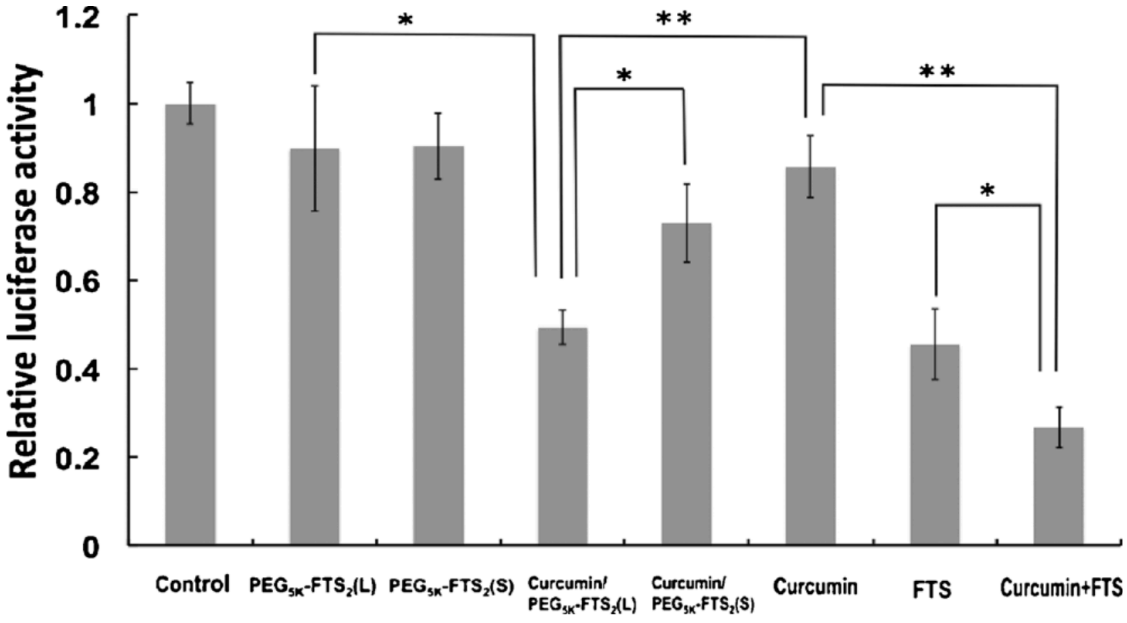

Figure 5. Inhibitory effect of micellar curcumin on NF-κB activity as determined in a NF-κB reporter assay.

DU145 cells were transfected with NF-κB reporter gene. At 12 h post-transfection, cells were treated with free PEG_{5K}-FTS_2, free curcumin, and curcumin-loaded PEG_{5K}-FTS_2 respectively for 12 h. The firefly luciferase activity was normalized and expressed as fold induction over untreated control. Results are presented as means ± standard deviation of the data from three independent experiments performed in triplicate. *P<0.05; **P<0.01.

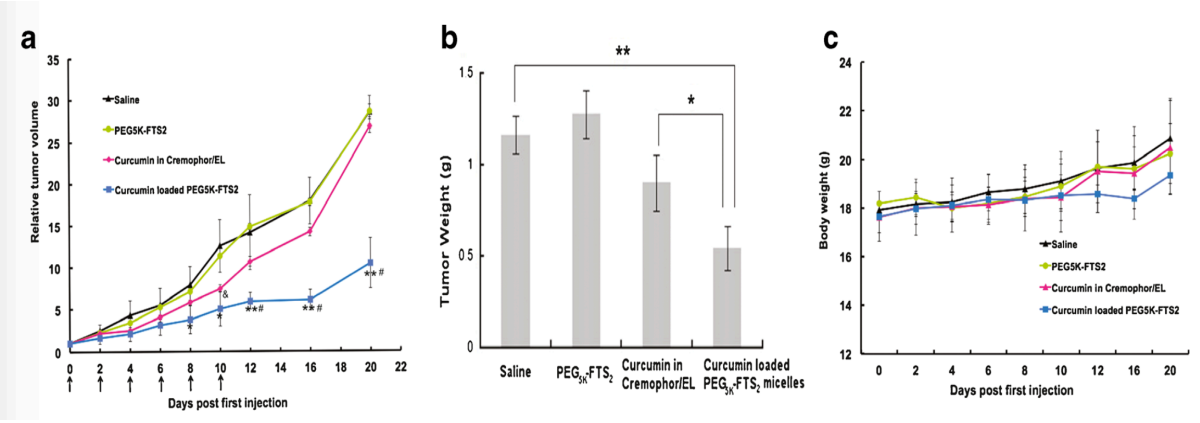

Figure 6. Enhanced antitumor activity of curcumin formulated in PEG_{5K}-FTS_2 (L) micelles.

BALB/c mice were inoculated s.c. with 4T1.2 cells (2×10^5 cells/mouse). Mice with palpable tumors received various treatments every other day and tumor growth and mouse body weight were followed. Tumors were collected at the end of the experiment and weighed. (a) Changes of relative tumor volume at different times following the first treatment. Significant improvement in antitumor activity was found for the curcumin-loaded PEG_{5K}-FTS_2 group compared with the control group (*P<0.05; **P<0.01; N=5) and the group of curcumin formulated in Cremophor/EL (#P<0.05; N=5). Curcumin formulated in Cremophor/EL had moderate tumor inhibitory effect at the early stage when compared to control group (&P<0.05; N=5). (b) Weights of tumors collected at the end of the experiment (*P<0.05; **P< 0.01; N=5). (c) Change of mouse body weight at different times following the first treatment

2.5 DISCUSSION

In this study, we have demonstrated for the first time significant synergistic effect between curcumin and FTS in various types of cancers. We have also shown that curcumin can be effectively formulated in PEG-FTS micellar system, leading to enhanced antitumor activity *in vitro* and *in vivo*.

Various systems have been developed for delivery of curcumin including polymeric micelles, liposomes, and hydrogels[113, 114, 115, 116, 117, 118, 119]. Several polymeric micellar

systems have been examined for delivery of curcumin including methoxy poly(- ethylene glycol)-zein, monomethyl poly(ethylene glycol)- poly(ε-caprolactone), methoxy-poly(ethylene glycol)-poly(- lactic acid)-tris-curcumin, methoxypoly(ethylene glycol)-b- poly(ε-caprolactone-co-p-dioxanone), poly(D,L-lac-tide-co-glycolide)-b-poly(ethylene glycol)-b-poly(D,L-lactide-co-gly- colide), and stearic acid-g-chitosan oligosaccharide micelle[119, 120, 121, 122]. Incorporation of curcumin into polymeric micelles led to enhanced antitumor activity in a number of tumor models including lung, breast, and colon cancers[116, 117]. Curcumin-loaded micelles have also been shown to effectively inhibit tumor angiogenesis[118]. However, most of the carrier materials in polymeric drug delivery systems do not have biological activity by themselves. PEG_{5K}-FTS_2(L)-based micelles are derived from a promising anticancer agent and have been demonstrated to well retain FTS-mediated antitumor activity[107]. FTS-derivatized system shall be particularly suitable for delivery of curcumin as curcumin and FTS demonstrated significant synergy in various types of cancers (Figure 1, Table 1). Indeed, curcumin formulated in PEG_{5K}-FTS_2(L) micelles was more active than free curcumin in several cancer cells tested including 4T1.2, DU145, and PC3 (Figure 3). The improved cytotoxicity of curcumin formulated in PEG_{5K}-FTS_2(L) micelles might be attributed to a synergistic action between the released curcumin and the free FTS that is cleaved from the PEG_{5K}-FTS_2(L) conjugate following intracellular delivery of the mixed micelles. Another important mechanism might involve the protection of curcumin from decomposition by the PEG_{5K}-FTS_2(L) micelles. Curcumin is known to undergo rapid degradation in a culture medium or buffer with physiological pH[123,

[124], and incorporation of curcumin into a delivery system has been shown to improve its bioavailability via slowing down the process of decomposition[125]. Interestingly, curcumin formulated in PEG_{5K}-FTS_2(S)-based micelles was compara- ble to or slightly less active than free curcumin in inhibiting the growth of cultured tumor cells (Figure 3). It might be due to the fact that PEG-FTS was largely designed for *in vivo* delivery and that *in vitro* cellular uptake of curcumin delivered via PEG-FTS micelles might be less efficient than that of free curcumin due to the steric hindrance imposed by PEG. This was supported by the data that the cytotoxicity of curcumin/ PEG_{5K}-FTS_2(L) mixed micelles is less active than the combination of free curcumin and FTS (Figure 1 and 3). It is possible that the PEG-FTS system can be further improved via incorporation of an active targeting ligand to facilitate intracellular delivery of curcumin/PEG-FTS mixed micelles.

The mechanism for the synergy between FTS and curcumin is not clearly understood at present. However, FTS and curcumin are known to inhibit both NF-κB and PI3K/AKT signaling pathways[89, 90]. Our preliminary data clearly showed a synergy between curcumin and FTS in inhibiting either PI3K/AKT or NF-κB signaling, which likely contributes to the synergistic antitumor effect of the combination treatment.

The *in vivo* antitumor activity of curcumin/PEG_{5K}-FTS_2(L) mixed micelles was examined in a syngeneic mouse tumor model, 4T1.2. 4T1.2 is an aggressive, metastatic breast cancer model. Although treatment with curcumin formulated in Cremophor/EL led to a modest inhibition of tumor growth at the early stage, there was a rapid rebound in the growth

rate of the tumor. In contrast, tumor growth was inhibited by curcumin/PEG_{5K}-FTS_2(L) mixed micelles in a more potent, sustained manner. A number of mechanisms are likely to be involved in the improved antitumor activity of curcumin formulated in PEG_{5K}-FTS_2(L) micelles. First, PEG-FTS formed very small-sized mixed micelles with curcumin. Such small sizes (20~30 nm) shall ensure effective penetration into various types of solid tumors including poorly vascularized tumors[126, 127]. In addition, the potential synergistic anti- tumor activity between curcumin and the freed FTS will contribute to the overall improved antitumor activity. More studies are currently underway in our laboratory to further improve the PEG-FTS-based delivery system and to better understand the molecular mechanism for the improved antitumor activity of the nanomicellar curcumin.

3.0 TARGETED CURCUMIN-LOADED PEGYLATED FTS-BASED NANOCARRIER FOR IMPROVED CANCER THERAPY *IN VIVO*

3.1 ABSTRACT

To improve the anti-tumor activity of curcumin, we have previously developed a dual-function carrier based on polyethylene glycol (PEG)-derivatized farnesylthiosalicylate (FTS). Despite the improved *in vivo* delivery, the application of this system is limited by a relatively low drug loading capacity (DLC). Here we report that incorporation of a drug-interactive motif (Fmoc) into PEG_{5k}-FTS_2 that led to further improvement in both drug loading capacity and formulation stability through the introduction of an additional mechanism of drug/carrier interaction. Curcumin could be effectively loaded into PEG_{5K}-Fmoc-FTS_2 micelles with a DLC of 37.6%. In addition, curcumin/PEG_{5K}-Fmoc-FTS_2 mixed micelles achieved a more sustained release of curcumin in comparison to the counterpart without Fmoc motif. *In vitro* cytotoxicity study showed that curcumin/PEG_{5K}-Fmoc-FTS_2 micelles exerted significantly higher levels of cell killing effect over free curcumin as well as curcumin/PEG_{5K}-FTS_2 in PC-3 and 4T1.2 cells, which might be due to improved cellular uptake of curcumin. Curcumin-loaded PEG_{5K}-Fmoc-FTS_2 micelles were also more effective in inhibiting colony formation by tumor cells. Finally, superior antitumor activity was demonstrated by curcumin/PEG_{5K}-Fmoc-FTS_2 in 4T1.2 mouse model compared to curcumin/Cremophr EL and curcumin/PEG_{5K}-FTS_2.

3.2 BACKGROUND

Curcumin is a natural polyphenol compound extracted from the plant Curcuma longa. Curcumin has various pharmacological activities including anti-inflammatory and anti-Alzheimer's. Recently, curcumin has been shown to be highly cytotoxic towards various cancer cell lines by blocking AKT and NF-κB pathway and inducing tumor cell apoptosis. In addition, curcumin has been under investigation in clinical trials and has shown clinical benefits in for patients with various types of cancers including colorectal cancer and pancreatic cancer without major side effects; however, its water-insolubility and instability make its poorly bioavailable and thus it demonstrates low *in vivo* anticancer activity in tumor bearing mouse model. Therefore, drug delivery systems with high loading capacity and tumor-specific distribution represent an attractive strategy for improving cancer treatment with curcumin.

Some attempts have been made to increase curcumin solubility and protect curcumin against degradation. Nanotechnology is one of the most promising methods for delivery of curcumin, which include liposomes, micelle, dendrimers and polymeric nanoparticles. Among these approaches, micelles have attracted increasing attentions as a nanocarrier in drug delivery and cancer treatment. Micelles are composed of amphiphilic molecules that can self-assemble into particles with a size ranging from 20 to 100 nm in aqueous solution. The hydrophobic core of micelle can accommodate hydrophobic drugs due to hydrophobic interactions between carrier and the loaded drug, which enable the water insoluble compound to stably and homogenously disperse in aqueous solution.

Besides, the flexible, hydrophilic PEG coating grafted onto the micelle surface acts as a steric barrier and it is effective in preventing rapid uptake of micelles by the RES, lengthens micelles circulation time in the blood. This together with small size (~20nm) gives micelles a better chance of extravasation through the leaky vasculature and slow accumulation in the tumor via the EPR effect. Therefore various polymeric micelles have been developed for solubilization and targeted delivery of curcumin. For example，Gou et al. demonstrated the encapsulation of curcumin into monomethoxy poly(ethylene glycol)-poly(3-caprolactone) (MPEG-PCL) micelles retained the *in vitro* cytotoxicity of curcumin on C-26 colon cancer cells and efficiently inhibited the tumor angiogenesis *in vivo*. Most recently, Gong et al. demonstrated curcumin -loaded mPEG-PCL-Phe(Boc) micelles significantly delayed tumor growth in an *in vivo* multidrug-resistant human erythroleukemia K562/ADR xenograft model. With assistance of micelle delivery system, curcumin can be completely dispersible in water for intravenous application. However, many polymer micelles can be dissociated by the blood components and lose the drug content right after administration. In addition, curcumin is quite unstable at physiological conditions. Thus, an efficient curcumin carrier should be able to retain it in blood circulation before it can access the tumor site. For most polymeric micelles, drug encapsulation is mainly based on carrier-drug hydrophobic interaction, which may not provide adequate compatibility for some drug molecules with different hydrophobicity. Therefore, it is critical to choose a suitable hydrophobic block to form the core.

In our previous work, we developed a derivatized FTS nano-carrier for delivery of hydrophobic drug including PTX or curcumin. FTS is a nontoxic and potent Ras antagonist for treatment of cancer. Ras gene mutations are widely found in different types of human cancers, with the highest incidence in pancreatic cancer and colon cancer. Continuously activated Ras protein caused by the gene mutations is highly involved in tumor maintenance and progression. FTS can effectively inhibit Ras-dependent signaling by causing dislodgement of actived Ras protein from the cell membrane and further lead to degradation of the protein. By conjugating FTS to PEG_{5k}, the PEG_{5k}-FTS_2 itself can maintain the antitumor activity of FTS and can be further used to load other anticancer drugs. In addition, curcumin and FTS combination has shown synergistic antitumor effect in several cancer cell lines and curcumin loaded PEG_{5k}-FTS_2 micelles were prepared and investigated for their therapeutic effect on mouse breast tumor. In order to further improve antitumor activity of our drug delivery system, an Fmoc group was introduced into the improved nanocarrier as we recently discovered Fmoc as a drug interactive motif, it can not only improve the DLC but also further increase the formulation stability via providing extra carrier-drug interaction. In this work, we formulated curcumin into PEG_{5k}-Fmoc-FTS_2 copolymer with a solid dispersion method to obtain micelles with improved drug loading, prolonged stability and enhanced *in vivo* antitumor activity. Our result indicated that improved curcumin/PEG_{5K}-Fmoc-FTS_2 micelles showed significantly enhanced anti-tumor activity both *in vitro* and *in vivo*, and may have potential clinical applications in breast cancer therapy.

3.3 EXPERIMENTAL PROCEDURES

3.3.1 Materials

Curcumin (synthetic) was purchased from TCI American (OR, USA). Poly(ethylene glycol) methyl ether (MeO-PEG-OH, MW = 5000 kDa), dimethyl sulfoxide (DMSO), 3-(4,5-dimethylthiazol-2-yl)-2,5-diphenyl tetrazolium bromide (MTT), trypsin-EDTA solution, Triton X-100, and Dulbecco's Modified Eagle's Medium (DMEM) were all purchased from Sigma-Aldrich (MO, USA). Dicyclohexylcarbodiimide (DCC) was purchased from Alfa Aesar (MA, USA). FTS was synthesized and purified following the published literature. Dulbecco's phosphate-buffered saline (DPBS) was purchased from Lonza (MD, USA). Fetal bovine serum (FBS) and penicillin−streptomycin solution were from Invitrogen (NY, USA). All solvents used in this study were HPLC grade.

3.3.2 Cell Culture

4T1.2 is a mouse breast cancer cell line, and PC3 is a human androgen-independent prostate cancer cell line. Both cell lines were cultured at 37°C cell incubator with 5% CO_2 in DMEM medium supplemented with 10% FBS and 1% penicillin–streptomycin.

3.3.3 Animals

Female BALB/c mice (4−6 weeks) were purchased from Charles River Company (Davis, CA, USA). All animals were housed in animal facility under pathogen-free conditions according to AAALAC guidelines. All animal-related experiments were performed in full compliance

with university guidelines and approved by the Animal Use and Care Administrative Advisory Committee at the University of Pittsburgh.

3.3.4 Synthesis of PEG_{5k}-Fmoc-FTS_2

PEG5k-Fmoc-FTS2 was prepared according to our previously published method. In brief, 1 equiv. of PEG methyl ether (Mw = 5000 Da, $mPEG_{5k}$−OH) was first reacted with 3 equiv. of a-Fmoc-e-Boc-lysine and DCC in dichloromethane (DCM) in the presence of DMAP for 2 days at room temperature (RT). The PEG derivative was filtered and precipitated twice with cold ether and ethanol. The Boc group was removed by treatment of DCM/TFA (1:1, v/v) for 2 h at RT and PEG_{5K}-lysine(Fmoc)-NH_2 was obtained by cold ether and ethanol precipitation. The PEG_{5K}-lysine(Fmoc)-NH_2 (1 equiv) was further reacted with succinate anhydride (2 equiv) in the presence of DMAP (2 equiv) overnight in CH_2Cl_2. The yielded crude, PEG_{5K}-lysine(Fmoc)-COOH was coupled with diethanolamine (3 equiv.) using N-hydroxysuccinimide (NHS 3.6 equiv.) and DCC (3.6 equiv.). PEG5K with two hydroxyl groups (MeO-PEG_{5k}-Fmoc-$(OH)_2$) was purified by precipitation with ice-cold diethyl ether and ethanol respectively. PEG_{5K}-Fmoc-FTS_2 conjugate was obtained by coupling PEG_{5k}-Fmoc-$(OH)_2$ (1 equiv.) to FTS (6 equiv.) via DCC (6 equiv.) and DMAP (0.6 equiv.) in chloroform. The pure PEG_{5k}-Fmoc-FTS_2 conjugate was obtained by filtration followed by precipitated in cold ether and ethanol twice. The dried powder was further purified by filtered the water solution through a 0.22 μm filter and lyophilization. PEG_{5K}-FTS_2 was synthesized following our reported method.

3.3.5 Preparation of Drug-Loaded and Drug-Free Micelles

Free curcumin (10 mM in chloroform) and PEG_{5k}-Fmoc-FTS_2 conjugate (10 mM in chloroform) were mixed at various carrier/drug ratios. The organic solvent was dried under pure nitrogen flow to obtain a thin film of carrier/drug mixture and the residue of solvent was further removed under vacuum for 1 h. curcumin -loaded micelles were obtained by adding DPBS to hydrate the thin film followed by filtration (0.22 μm) to remove the undissolved curcumin particles. The drug-free PEG_{5k}-Fmoc-FTS_2 micelles were similarly prepared as described above.

3.3.6 Characterizations of Curcumin/PEG_{5k}-Fmoc-FTS_2 Micelles

The particle size of drug-free and curcumin-formulated PEG_{5k}-Fmoc-FTS_2 micelles were measured by dynamic light scattering with a Zetasizer (Zetasizer Nano ZS instrument, Malvern, Worcestershire, UK). The micelle morphology was observed by transmission electron microscopy (TEM, JEOL JEM-1011, Japan) as described before. In brief, a small copper grid was fully immersed in the micelle sample solution and subsequently stained with 1% uranyl acetate solution. The morphology of micelle was examined by TEM at room temperature.

The curcumin loading efficiency was measured by high performance liquid chromatography (HPLC) (Alliance 2695- 2998 system). curcumin-loaded micelles were prepared and filtered through a 0.22 μm filter. Methanol was added to the micelles before and after filtration and extracted curcumin was quantified by HPLC (mobile phase: methanol/0.3%

acetic acid (80/20, v/v), flow rate: 1 mL/min, UV detector). The Drug loading capacity (DLC) and drug loading efficiency (DLE) were calculated by the following equation:

DLC (%) = [weight of drug loaded/(weight of carrier+ drug)] × 100

DLE (%) = (weight of loaded drug/weight of input drug) × 100

The micelle stability of curcumin/PEG_{5k}-Fmoc-FTS_2 micelles was followed and compared with previous curcumin/PEG_{5k}-FTS_2 formulation. Either drug precipitation or change of size was regarded as unstable.

3.3.7 *In Vitro* Curcumin Release Study

The *in vitro* curcumin release profile for the curcumin/PEG_{5k}-Fmoc-FTS_2 was investigated by a dialysis method according to our published paper. Curcumin/Cremophor EL or curcumin/PEG_{5k}-FTS_2 were added as control groups. Briefly, curcumin formulations at a concentration of 1 mg curcumin per mL were placed into a dialysis bag with a molecule weight cut off of 3500. The dialysis bag was clamped tightly on both ends and fully immersed in 200 mL DPBS containing 0.5% Tween 80 (w/v). The *in vitro* release studies were performed at 37 °C with gentle shaking. The concentration of curcumin remaining in the dialysis bag was measured at 0, 1, 2, 4, 8, 20, 40, 80 and 96 hours with HPLC. Cumulative percentage of drug released against time was plotted.

3.3.8 Fluorescence Quenching Studies

curcumin/PEG_{5K}-FTS_2 and curcumin/PEG_{5K}-Fmoc-FTS_2 were prepared at various carrier to drug molar ratio as described above. The micelles were placed in a 96-well plate and the

fluorescence intensity of the carriers or drug was recorded on a plate reader (Synergy H1 Hybrid reader, BioTek). To examine fluorescence quenching of the carriers, the molar concentrations of carrier were kept constant for comparison. The blank micelles and drug loaded micelles was excited at an excitation wavelength of 270 nm and emission spectrum from 300 to 500 nm was recorded. In another set of experiments, curcumin concentration in the micelle was kept constant to examine the fluorescence quenching of curcumin. The fluorescence intensity of curcumin was examined using an excitation wavelength of 480 nm and emission wavelength from 510 to 650 nm.

3.3.9 *In Vitro* Cytotoxicity Study

The cytotoxicity of curcumin-formulated PEG_{5K}-Fmoc-FTS_2 micelles was evaluated in 4T1.2 and PC3 cancer cell lines and compared to free curcumin in DMSO and curcumin /PEG_{5K}-FTS_2, respectively. Briefly, 4T1.2 (2000 cells/well) cells or PC3 cells (2000 cells/well) were placed in 96-well plates for overnight. After cells were attached, various concentrations of free curcumin, curcumin/PEG_{5K}-FTS_2 or curcumin/PEG_{5K}-Fmoc-FTS_2 were added to cells and incubated for 72h. Cell culture medium was removed and 100 μL of 3-(4,5-dimethylthiazol-2-yl)-2,5- diphenyltetrazolium bromide (MTT) solution (0.5 mg/mL in DPBS) was added to each well. After 2h of incubation，MTT solution was carefully removed and MTT formazan was solubilized by 100 μL of DMSO. The absorbance of each well at wavelength of 570 nm was measured by a plate reader. Untreated wells were used as

controls. Cell viability was calculated as [(ODtreated − ODblank)/(ODcontrol − ODblank) × 100%].

3.3.10 Colony Formation Assay

In order to determine the antitumor efficacy of the formulation, curcumin/PEG_{5K}-Fmoc-FTS_2 micelles were tested in an *in vitro* colony formation assay. 4T1.2 tumor cells were counted and seeded into a 6-well plate and incubated in 37 °C overnight. Cells were then treated with the free curcumin, curcumin/PEG_{5K}-FTS_2 or curcumin/PEG_{5K}-Fmoc-FTS_2 for 2 weeks, colonies consisting of >50 cells were counted. Colonies were washed with PBS and stained with 0.4% crystal violet for 1 min, rinsed in water and photographed under a microscope.

3.3.11 Intracellular Uptake

3×10^5 4T1.2 cells were seeded into each well of 6-well plates and incubated overnight to allow attachment. Then cells were treated with free curcumin, curcumin-loaded PEG_{5K}-FTS_2 and PEG_{5K}-Fmoc-FTS_2, respectively at a curcumin concentration of 10 μM for 2h, 4h and 8h at 37 °C. Subsequently, cells were washed three times with ice cold DPBS. The intracellular uptake of curcumin in various formulations was observed under confocal microscopy (CLSM, FluoView 1000, Olympus, Japan).

Quantitative cellular uptake of various curcumin formulations was evaluated by flow cytometry. Briefly, 4T1.2 cells in 6 well plates were prepared as described above. After incubation with various curcumin formulations at 37 °C for 4 h, cells were trypsinized,

washed thrice with cold DPBS and further resuspended in 0.5 mL of DPBS prior to the flow analysis. Curcumin were analyzed using a laser emitting at 488 nm wavelength and fluorescence was detected through a 575 nm band pass filter and quantified using flowjo Software. Triplicate assays were performed and results were calculated as percentage increase of the mean fluorescence intensity of the curcumin/PEG_{5k}-Fmoc-FTS_2 group compared to curcumin/PEG_{5k}-FTS_2 and free curcumin groups.

3.3.12 *In Vivo* Therapeutic Study

A syngeneic murine 4T1.2 breast cancer model was used to examine the therapeutic effect of different curcumin formulations. 2×10^5 4T1.2 tumor cells were inoculated subcutaneously at the right flank of female Balb/c mice. Treatments were initiated when tumors volume reached ~50 mm^3. Twenty mice were randomly divided into 4 groups and injected intravenously with PBS (control), curcumin/Cremophor EL, curcumin/PEG_{5K}-FTS_2 and curcumin/PEG_{5K}-Fmoc-FTS_2 at a Cur concentration of 25mg/kg, respectively on days 1, 3, 5, 8 and 11. Tumor sizes were measured with a digital caliper every three days since the start of treatment and tumor volume was calculated as $V=(L \times W^2)/2$ (L: longest tumor diameter, W: shortest tumor diameter). In order to better compare between groups, relative tumor volume (RTV) was calculated ($RTV=V/V_{day\ 1}$). Mice were sacrificed before the tumor reached 2000 mm^3 according to the university animal protocol. Body weighs and mouse survival was monitored during the therapeutic study.

3.3.13 Statistical Analysis

All results were reported as the mean ± standard deviation (SD). Statistical analysis was performed by Student's t test for two groups, and one-way ANOVA for multiple groups, followed by Newman−Keuls test if $P < 0.05$.

3.4 RESULTS

3.4.1 Synthesis of PEG_{5K}-Fmoc-FTS_2 Conjugates

PEG_{5k}-Fmoc-FTS_2 conjugate was synthesized by solution phase condensation reactions. Signals of Fmoc motif was at 7−8 ppm and methylene protons of PEG was located at 3.63 ppm. Signals of 1.5−2.2 ppm and 7−8 ppm were from carbon chain and benzene ring of FTS, respectively. We also synthesized PEG_{5K}-FTS_2 conjugates, which were confirmed by ^1H NMR spectra.

3.4.2 Biophysical Characteristic of Curcumin Formulated PEG_{5k}-Fmoc-FTS_2 Micelles

PEG_{2k}-Fmoc-FTS_2 could readily form micelles in aqueous solution with uniform size distribution around 20 nm at the concentration of 20 mg/mL (Figure 7a,c, Table 3). The spherical morphology observed by TEM showed good agreement with the DLS result (Figures 7a). Table 3 showed the sizes and PDIs of curcumin loaded PEG-FTS micelles at various carrier to drug ratios and PEG_{5k}-Fmoc-FTS_2 micelles were highly effective in solubilizing curcumin at a carrier to drug ratio as low as 0.1:1(molar ratio). The particle size

and shape were well retained following loading of curcumin into PEG_{5K}-Fmoc-FTS_2 micelles with a curcumin concentration of 1 mg/mL and a carrier/drug ratio of 2.5/1 (Figure 7b,d). At a carrier/drug ratio of 5/1, the curcumin formulated PEG_{5K}-Fmoc-FTS_2 micelles were stable for more than 1 month at room temperature compared to 4 days of curcumin/PEG_{5K}-FTS_2 micelles at the same carrier/drug ratio. The curcumin loading capacity and efficiency of PEG_{5K}-FTS_2 and PEG_{5K}-Fmoc-FTS_2 micelles with different carrier to drug molar ratios were determined by HPLC (Table 3). The curcumin formulated PEG_{5K}-Fmoc-FTS_2 micelles could achieve a DLC of as high as 37.6%, which was more than 3 fold that of curcumin/PEG_{5K}-FTS_2 micelles. Overall, the PEG_{5K}-Fmoc-FTS_2 conjugates worked better than the counterpart without Fmoc motif in both drug loading efficiency and micelle stability.

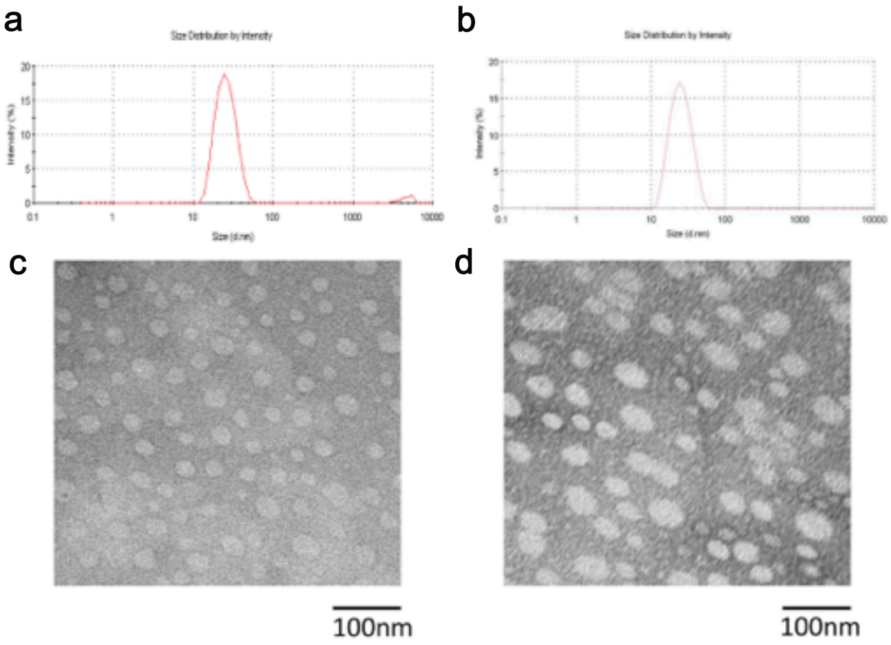

Figure 7. The size distribution of free (a) and curcumin loaded PEG_{5k}-Fmoc-FTS_2 micelles (b).
TEM morphology of free (c) and curcumin loaded PEG_{5k}-Fmoc-FTS_2 micelles (d).

3.4.3 *In Vitro* PTX Release Study

The profile of curcumin release from the curcumin/PEG_{5K}-Fmoc-FTS_2 mixed micelles was examined by a dialysis method. As shown in Figure 8, curcumin/Cremophor EL showed a relatively fast release of curcumin with greater than 60% of curcumin being released within 4 h and close to 90% of curcumin was released after 8 h. In contrast, the kinetics of curcumin release was significantly slower for either curcumin/PEG_{5K}-FTS_2 or curcumin/PEG_{5K}-Fmoc-FTS_2 formulation. In addition, curcumin/PEG_{5K}-Fmoc-FTS_2 mixed micelles showed a more sustained release of curcumin compared to curcumin/PEG_{5K}-FTS_2 mixed micelles. Less than 40% of curcumin in PEG_{5K}-Fmoc-FTS_2 micelles was released within 24 h and more than 45% of the curcumin remained associated with the micelles after 80 h compared to 65% and 80% released respectively in curcumin/PEG_{5K}-FTS_2 mixed micelles.

Table 3. Biophysical Characteristics of Anticancer Drug-loaded PEG_{2K}-Fmoc-NLG(L) Micelles and Blank Micelles.

Micelles	Molar Ratio	Particle Size (nm)	PDI	DLE (%)	DLC (%)	Stability (hours)
PEG_{5K}-Fmoc-FTS_2	—	20.5	0.175	—	—	—
PEG_{5K}-Fmoc-FTS_2: Curcumin	0.1:1	117	0.282	78.3	37.6	12
	0.5:1	30.9	0.255	82.2	10.7	17
	1:1	22.0	0.173	86.2	5.7	60
	2.5:1	19.9	0.369	97.5	2.4	840
	5:1	21.3	0.224	96.7	1.2	>840
PEG_{5K}-FTS_2	—	19.0	0.266	—	—	—
PEG_{5K}-FTS_2: Curcumin	0.5:1	22.2	0.214	75.2	11.8	2
	1:1	21.8	0.177	89.1	5.9	4
	2.5:1	25.9	0.239	98.5	2.4	36
	5:1	22.8	0.080	97.6	1.2	96

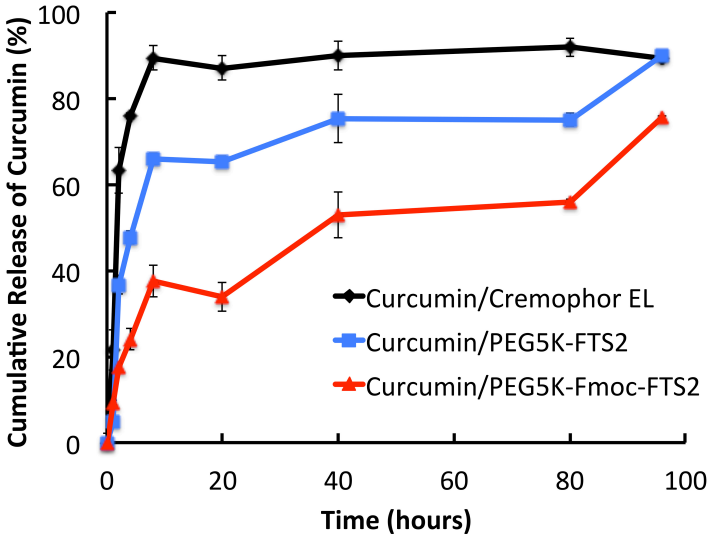

Figure 8. Cumulative release of curcumin from curcumin/Cremophor EL, curcumin-loaded PEG_{5K}-FTS_2 and PEG_{5K}-Fmoc-FTS_2 micelles.

3.4.4 Fluorescence Quenching Studies

The curcumin formulated PEG_{5K}-Fmoc-FTS_2 micelles exhibited a higher loading capacity and longer stability suggests that Fmoc groups may play an important role in interaction with loaded curcumin. A fluorescence quenching study was conducted to further examine the mechanism of drug-carrier interaction. The highest fluorescence intensity of Fmoc group in PEG_{5K}-Fmoc-FTS_2 alone was recorded at 310 nm at an excitation wavelength of 270 nm (Figure 9a). However, after the curcumin was loaded into the micelles, a dramatic fluorescence quenching was observed and the extent of fluorescence decrease was positively correlated to the amount of curcumin loaded in micelles. This phenomenon was likely due to the energy transfer between Fmoc groups and the loaded curcumin through the intermolecular π-π stacking interaction between aromatic rings. As a control, PEG_{5K}-FTS_2 alone and

curcumin/PEG_{5K}-FTS_2 showed minimum fluorescence at the wavelength range examined due to a lack of Fmoc groups (Figure 9a).

To further evaluate the mechanism of drug-carrier interaction between curcumin and PEG_{5K}-Fmoc-FTS_2 carrier, fluorescence quenching of curcumin was examined at an excitation wavelength of 460 nm (Figure 9b). Fluorescence emitted at a range of 490-700 nm was recorded. Neither PEG_{5K}-FTS_2 nor PEG_{5K}-Fmoc-FTS_2 carrier showed any fluorescence at this wavelength range. Interestingly, curcumin fluorescence intensity was increased with increased amount of PEG_{5K}-FTS_2 or PEG_{5K}-Fmoc-FTS_2 carrier and the curcumin/PEG_{5K}-Fmoc-FTS_2 showed ~3 folds of increase of curcumin fluorescence intensity over that of curcumin/PEG_{5K}-FTS_2 at the same concentration of curcumin. This may suggested the loaded curcumin had more drug-carrier interaction with PEG_{5K}-Fmoc-FTS_2 compared to PEG_{5K}-FTS_2.

Taking together, these data suggested curcumin/Fmoc interaction played an important role in the overall carrier/drug interaction and π-π stacking might be a major mechanism in this process besides the hydrophobic interaction and hydrogen bonding. The enhanced carrier-drug interaction may contribute to the improved drug loading capacity and micelle stability.

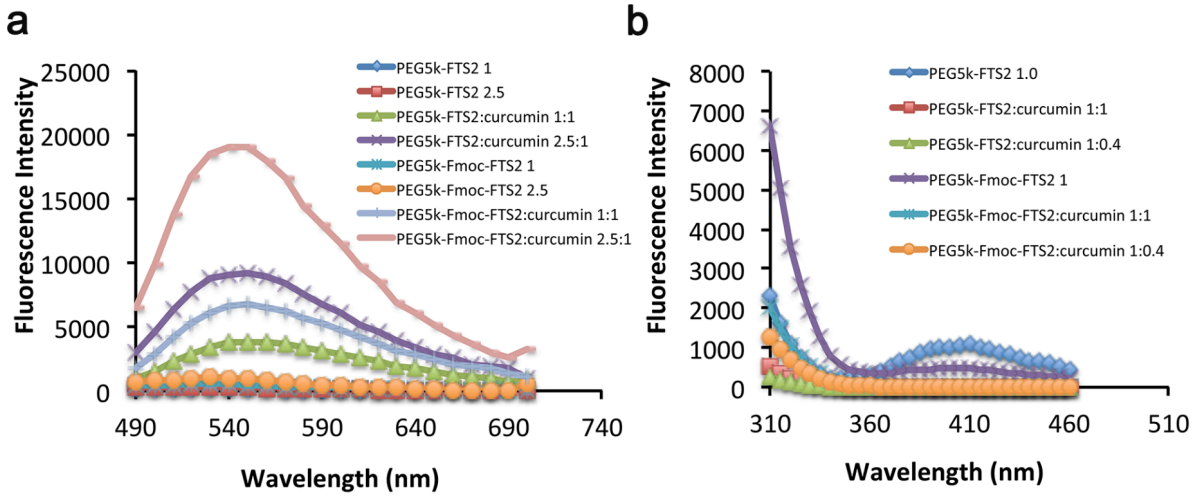

Figure 9. Fluorescence quenching of curcumin loaded PEG_{5k}-FTS_2 and PEG_{5k}-Fmoc-FTS_2 micelles.

(a) Curcumin loaded PEG_{5k}-FTS_2 and PEG_{5k}-Fmoc-FTS_2 micelle fluorescence intensity emitted between 310 and 460 was recorded with excitation wavelength at 270 nm. (b) The concentration of curcumin loaded in micelles was fixed at 1 mg/mL and intensity of fluorescence emitted between 490 and 700 nm was recorded with excitation wavelength at 460 nm.

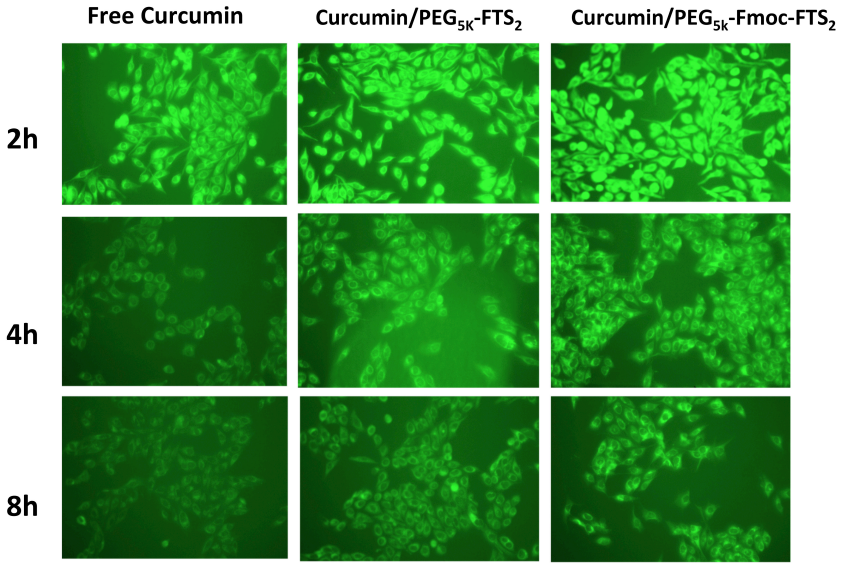

Figure 10. Improved celluar uptake of curcumin with micelle formulation.

4T1.2 cells were incubated with free curcumin, curcumin/PEG_{5k}-FTS_2 micelles or curcumin/PEG_{5k}-Fmoc-FTS_2 micelles for 2h, 4 h and 8h. Cellular uptake of curcumin was examined by confocal laser scanning microscope.

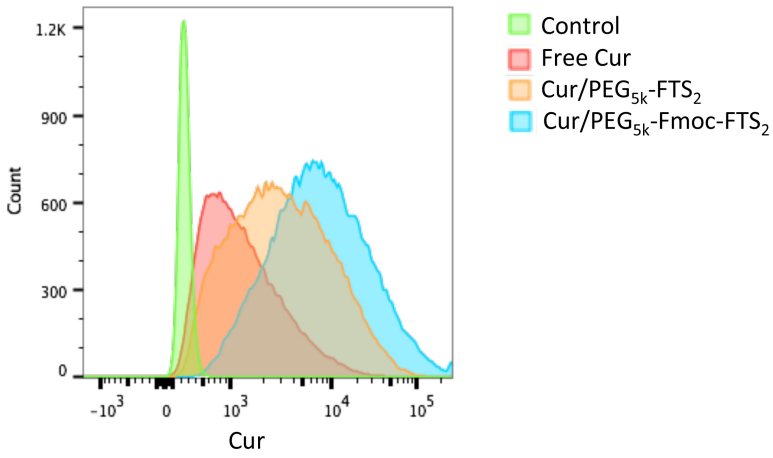

Figure 11. Cellular uptake study of curcumin quantified by flow cytometry.

3.4.5 Improved Intracellular Trafficking of Curcumin/PEG$_{5K}$-Fmoc-FTS$_2$ Micelles

Quantitative cellular uptake of various curcumin formulations was evaluated by flow cytometry. Cells without curcumin treatment were used as a control. As shown in Figure 10 and Figure 11, the curcumin formulated in PEG$_{5K}$-Fmoc-FTS$_2$ micelles showed higher uptake compare to curcumin loaed PEG$_{5K}$-FTS$_2$ and free curcumin after 6h of incubation, which was consistent with the imaging study.

3.4.6 Enhanced *In Vitro* Cytotoxicity of Curcumin-loaded PEG$_{5K}$-Fmoc-FTS$_2$ Micelles

Figure 12 showed the cytotoxicity of curcumin formulated in PEG$_{5K}$-Fmoc-FTS$_2$ micelles in 4T1.2 cell line, free curcumin and curcumin loaded PEG$_{5K}$-FTS$_2$ were used as control. Free curcumin inhibited the cell growth in a dose-dependent manner and delivery of curcumin via the PEG$_{5K}$-FTS$_2$ micelles led to a significant improvement of cell killing effect. Incorporation of an Fmoc group to the PEG$_{5K}$-FTS$_2$ resulted in further improvement in the *in vitro* antitumor activity. Table 2 summarizes the IC50s of three treatment groups in both 4T1.2 and

PC3 cell lines. The IC50 of curcumin/PEG_{5K}-Fmoc-FTS_2 on 4T1.2 cells was significant lower (15.8 μM) compared to 24.2 μM of curcumin/PEG_{5K}-FTS_2 and 45.3 μM of free curcumin. Similar result was obtained from PC3 human prostate cancer cell line.

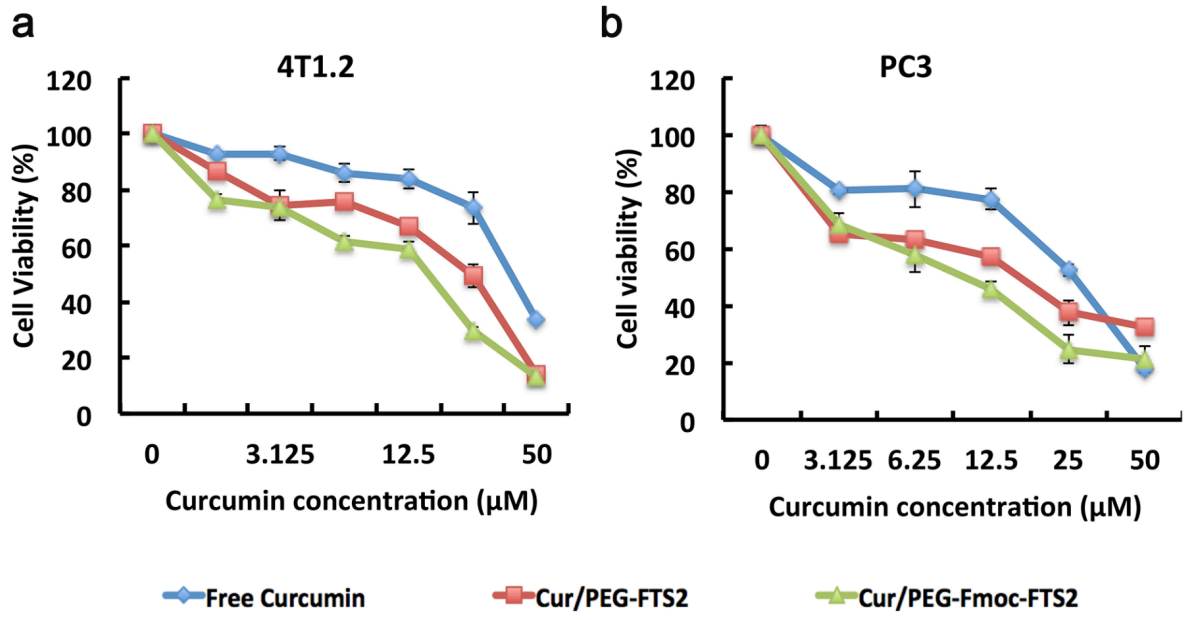

Figure 12. *In vitro* cytotoxicity of curcumin formulated PEG_{5k}-Fmoc-FTS_2 micelles.
(a) 4T1.2 mouse breast cancer cell line and (b) PC-3 human prostate cancer cell line were treated with free curcumin, curcumin loaded PEG_{5k}-FTS_2 micelle or curcumin loaded PEG_{5k}-Fmoc-FTS_2 micelle for 72 h and cell viability was examined by MTT assay. Results are reported as the means ± SD for triplicate samples.

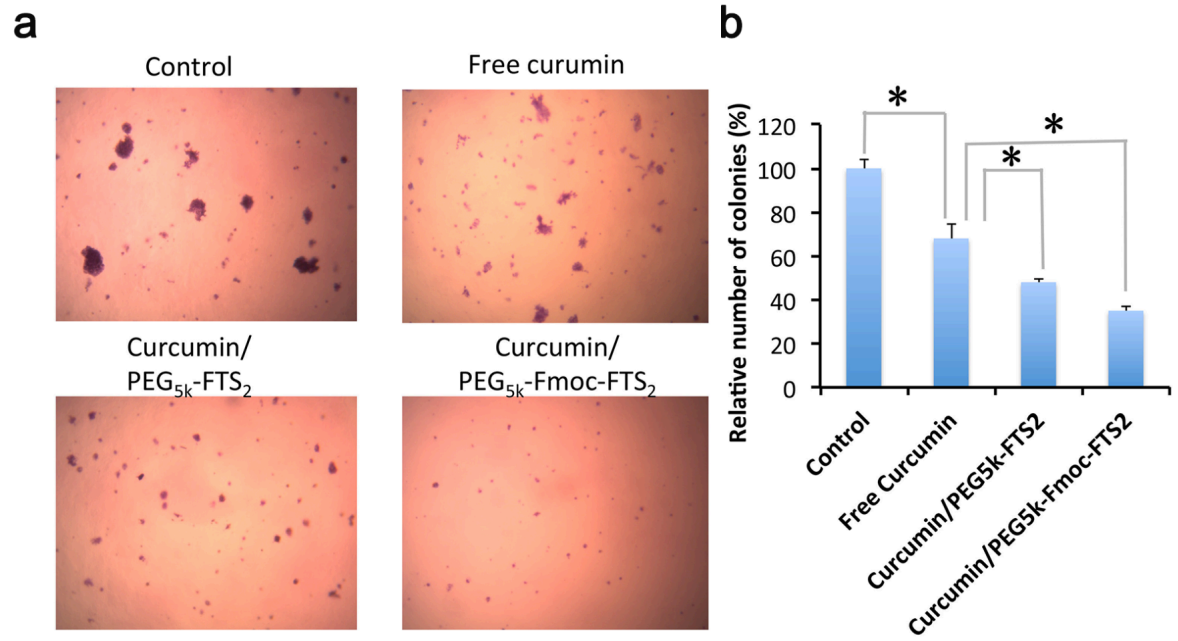

Figure 13. Improved inhibition of colony formation by cumumin formulated micelles.
(a) Effects of free curcumin, curcumin loaded PEG_{5k}-FTS_2 micelle or curcumin loaded PEG_{5k}-Fmoc-FTS_2 micelle on the colony formation and cell proliferation of 4T1.2 breast cancer cells. (b) Quantitative analysis of colony formation. The numbers of colonies in controls were set to 100%. Values are indicated as mean±SD from three experiments. *p<0.05.

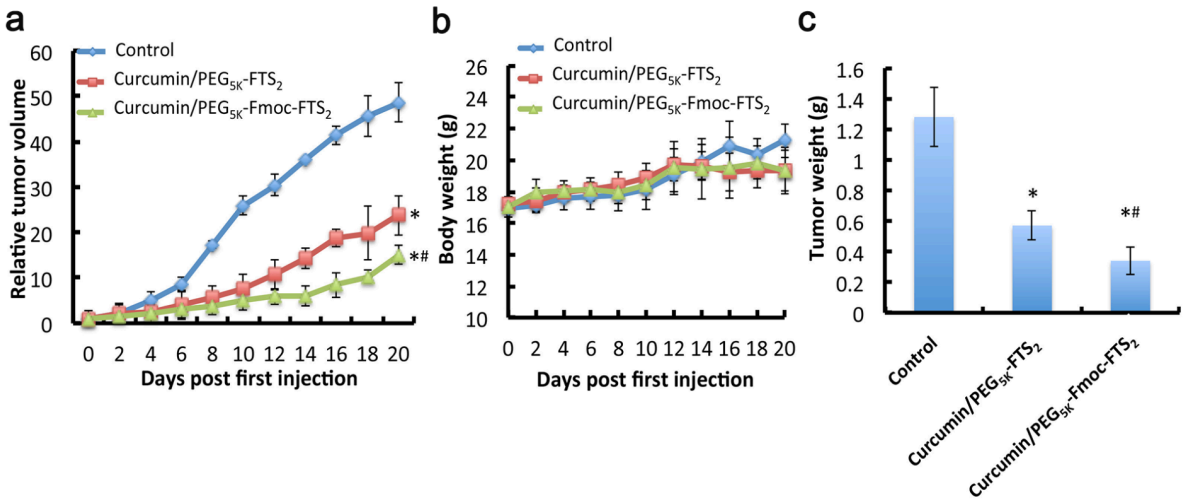

Figure 14. *In vivo* antitumor activity of curcumin/PEG_{5K}-Fmoc-FTS_2 in a 4T1.2 syngeneic breast cancer mouse model.
(a) Mice were inoculated with 2×10^5 cells and treatements were given every 2 days for 5 times when tumor volume reached ~50mm^3 *P < 0.05 (vs control) #P< 0.05 (vs curcumin/PEG_{5k}-FTS_2). (b) Mice body weight was followed during the therapeutic study. (c) Tumors were harvest at day 19 and weighted.

3.4.7 Curcumin/PEG_{5K}-Fmoc-FTS_2 Suppressed Cell Proliferation and Colony Formation

In vitro colony formation assay was performed to further examine the effects of the curcumin/PEG_{5K}-Fmoc-FTS_2 compared to free curcumin and curcumin/PEG_{5K}-FTS_2. Images of the colonies grown following various treatments were shown in Figure 13a. The numbers of colonies consisting of >50 cells were counted and normalized to untreated control groups (Figure 13b). As shown in figure 13, the curcumin/PEG_{5K}-Fmoc-FTS_2 could significantly decrease the colony formation compared with free curcumin and curcumin/PEG_{5K}-FTS_2, which was consistent with the result of MTT assay.

3.4.8 *In Vivo* Therapeutic Study

The *in vivo* therapeutic effect of curcumin formulated in PEG_{5K}-FTS_2 and PEG_{5K}-Fmoc-FTS_2 micelles was evaluated, respectively, in a syngeneic murine breast cancer model (4T1.2), and compared to curcumin/Cremophor EL. As shown in Figure 14a, Both curcumin-loaded PEG_{5K}-FTS_2 micelles and curcumin/PEG_{5K}-Fmoc-FTS_2 micelles exhibited a significantly enhanced antitumor activity compared to curcumin/Cremophor EL($P < 0.01$). Furthermore, curcumin formulated in PEG_{5K}-Fmoc-FTS_2 was more effective than curcumin formulated in PEG_{5K}-FTS_2 ($P < 0.05$). No significant changes in body weight were observed in all treatment groups compared to DPBS control group (Figure 14b). Tumors were harvested at the completion of the experiment and tumor weights were measured (Figure 14c).

3.5 DISCUSSION

Previously, we developed a polymeric micelle system PEG_{5K}-FTS_2, curcumin micelles had a stronger inhibitory effect on tumor cell proliferation than free curcumin. Furthermore, curcumin micelles were more effective in inhibiting *in vivo* tumor growth in subcutaneous metastatic 4T1.2 tumor models. However, the application of curcumin/PEG_{5k}-FTS_2 micelle was limited by its relatively low drug loading capacity and *in vivo* stability. In this work, an improved PEG_{5k}-Fmoc-FTS_2 system was developed for *in vivo* delivery of curcumin by adding an Fmoc drug interactive motif. Amphiphilic PEG_{5k}-Fmoc-FTS_2 polymer composed of hydrophilic PEG and hydrophobic FTS segments with Fmoc group at the interfacial layer and due to the hydrophobicity differences between FTS and PEG segments. The FTS segments, tangled with curcumin, serve as hydrophobic core, Fmoc group can provide extra interaction to further enhance the drug loading, PEG located at the micelle surface provides limited affinity among the particles to prevent the formation of aggregates. Accumulating data have demonstrated that the drug loading capacity and stability of micelles can be greatly improved by enhancing drug-carrier interaction between inner core segment of micelles and drugs. Our previous data showed that the PEG_{5k}-Fmoc-FTS_2 could not only greatly improve the drug loading capacity of seveal chemotherapy drug such as PTX, but also significantly enhanced the tumor inhibitory effect compared to PEG_{5k}-FTS_2 delivery system in tumor mouse models (4T1.2 and PC3).

Intracellular distribution of curcumin as free curcumin, curcumin /PEG_{5K}-FTS_2 or curcumin/PEG_{5K}-Fmoc-FTS_2 micelles was followed by confocal microscopy in 4T1.2 cells at

2, 4, 8 h after treatment, respectively (Figure 10). Of note, significantly greater amounts of curcumin were found inside of cells treated with curcumin/PEG_{5K}-Fmoc-FTS_2 after 4 h and 8 h of incubation compared to free curcumin or curcumin/PEG_{5K}-FTS_2, suggesting PEG_{5K}-Fmoc-FTS_2 help curcumin to stay longer inside cancer cells. This may be attributed to the prolonged release of curcumin and better protection of curcumin against inactivation from hydrolysis by the PEG_{5K}-Fmoc-FTS_2 micelle in the intracellular drug delivery.

In this study, our data showed that, by adding an extra drug interactive motif, Fmoc, the PEG_{5k}-Fmoc-FTS_2 is more effective in curcumin drug loading and delivery compared with PEG_{5k}-FTS_2 (Table 3, Figure 9,10). This may attributed to the improved micelle stability and drug carrier interactions. Firstly, Fmoc could enhance the micelle stability by promoting the carrier/carrier interaction. Our previous research showed that by incorporation of Fmoc to PEG_{5K}-VE_2, it could achieve lower CMC compared to the carrier without Fmoc. We noticed that the PEG_{5k}-Fmoc-FTS_2 had a CMC of 0.2μM, which was 4 times lower than that of PEG_{5k}-FTS_2. Due to the low CMC, the PEG_{5k}-Fmoc-FTS_2 polymeric micelles can remain stable in the blood stream at very low concentrations, which makes them relatively insensitive to blood dilution after i.v. administration, resulting in an prolonged circulation time compared to PEG_{5k}-FTS_2 micelles. This is likely due to the Fmoc incorporated may increased the balance between the hydrophobic head and hydrophilic tail of the carrier and may also contribute to the interaction between PEG_{5k}-Fmoc-FTS_2 molecules. The second mechanism involved in the carrier/drug interactions of curcumin-loaded PEG_{5k}-Fmoc-FTS_2 micelles. Besides the hydrophobic interaction and hydrogen bonding, the enhanced curcumin

loading capacity was most likely due to excellent Fmoc/curcumin interaction. Both Fmoc and curcumin had the structure of flat and rigid aromatic rings, which made them easily to interact with each other through a π-π stacking effect. This hypothesis was supported by Fmoc fluorescence intensity change in PEG_{5k}-Fmoc-FTS_2 micellar with loading of curcumin in Figure 9A and the decrease of Fmoc fluorescence intensity was likely resulted from the fluorescence quenching and energy transfer in the Fmoc/curcumin inter-moleculer interaction. This phenomenon was further supported by the increased curcumin fluorescence intensity when loaded into the PEG_{5k}-Fmoc-FTS_2 drug delivery system in Figure 9B. The application of Fmoc in the nanocarrier system may provide new thoughts for the design of novel polymeric nanocarriers for delivery of other therapeutic agents with various structures.

MTT assay and colony formation assay showed that the curcumin formulated in PEG_{5k}-Fmoc-FTS_2 micelles was more potent than free curcumin solubilized in DMSO in several cancer cells tested including 4T1.2 and PC3 (Figure. 12). The improved cytotoxicity of curcumin formulated in PEG_{5k}-Fmoc-FTS_2 micelles might be attributed to a synergistic action between the released curcumin and the free FTS that is cleaved from the PEG_{5k}-Fmoc-FTS_2 conjugate following intracellular delivery of the mixed micelles. In Figure 13, curcumin formulated in PEG_{5k}-Fmoc-FTS_2 micelles also showed enhanced cytotoxicity and more effective inhibition of cell colony formation compared to curcumin/PEG_{5K}-FTS_2 micelles. The fact that the cytotoxicity of curcumin-loaded PEG_{5k}-Fmoc-FTS_2 micelles was higher than that of curcumin-loaded PEG_{5k}-FTS_2 micelles suggests that the PEG_{5k}-Fmoc-FTS_2 not only retained the function of FTS, but also enhanced the cellular

uptake of curcumin into the cells and provided improved protection of curcumin from decomposition compared to PEG_{5k}-FTS_2 micelles. PEG_{5k}-FTS_2 is known to undergo rapid degradation in a physiological pH condition, and incorporation of PEG_{5k}-FTS_2 into PEG_{5K}-Fmoc-FTS_2 delivery system has been shown to improve its stability.

A highly metastatic 4T1.2 murine breast cancer mouse model was used to investigate the *in vivo* therapeutic efficacy of curcumin loaded PEG_{5K}-Fmoc-FTS_2 micelles. As shown in Figure 14, the PEG_{5k}-FTS_2/PEG_{5K}-FTS_2 micelles were significantly more effective than curcumin/Cremophor EL formulation, which is consistent with our previous report. It is also apparent that inclusion of an Fmoc motif into PEG_{5K}-Fmoc-FTS_2 micelle led to a further improvement in tumor growth inhibition at the same curcumin concentration (Figure 14). The overall improvement in antitumor activity is likely due to an improved stability of curcumin loaded micelle and an enhanced tumor accumulation of curcumin in the tumor site caused by the reduced CMC and improved carrier/drug interaction of the PEG_{5K}-Fmoc-FTS_2 delivery system. More studies are ongoing in our lab to better understand the underlying mechanisms for the improved performance of PEG_{5K}-Fmoc-FTS_2 micelles. Biodistribution and blood pharmacokinetics will be investigated whether the PEG_{5K}-Fmoc-FTS_2 can increase the curcumin blood circulation time and achieve tumor specific accumulation. Overall, our findings suggested that the prepared curcumin/PEG_{5K}-Fmoc-FTS_2 micelles reported in this study had excellent potential as an intravenous therapy for breast cancer.

3.6 CONCLUSION

In summary, we have extended and improved our previous formulation by introducing a drug-interactive motif at the interfacial region of conventional micellar system and demonstrated the biodegradable PEG_{5K}-Fmoc-FTS_2 polymeric micelles can effectively entrap curcumin and their excellent anti-tumor effects against 4T1.2 breast cancer cells *in vitro* and *in vivo*. In comparison with free curcumin and curcumin/PEG_{5K}-FTS_2, the prepared curcumin/PEG_{5K}-Fmoc-FTS_2 micelles showed enhanced the drug loading capacity of curcumin, increased cellular uptake, enhanced *in vitro* cytotoxicity, more sustained *in vitro* release kinetics, and better colony formation inhibitory effect. Moreover, with this improved FTS-based micellar carrier incorporated with Fmoc moiety, the curcumin/PEG_{5K}-Fmoc-FTS_2 micelles suppressed tumor growth in the 4T1.2 tumor model more effectively than free curcumin and curcumin formulated PEG_{5K}-FTS_2. Our strategy may represent an effective and general approach to improve the performance of various delivery systems including micelles.

4.0 AN IMMUNOSTIMULATORY DUAL-FUNCTIONAL NANOCARRIER THAT IMPROVES CANCER IMMUNOCHEMOTHERAPY

4.1 ABSTRACT

Immunochemotherapy that combines a chemotherapeutic agent with an immune checkpoint blocker represents an attractive approach to improve cancer therapy. However, the success of immunochemotherapy is hampered by the lack of a strategy to effectively codeliver the two therapeutics to the tumors. Here we report the development of the first dual-functional, immunostimulatory nanomicellar carrier that was based on a prodrug conjugate of PEG with NLG919, an indoleamine 2,3-dioxygenase (IDO) inhibitor currently used for reversing tumor immune suppression. An Fmoc group, an effective drug-interactive motif, was also introduced into the carrier to improve the drug loading capacity and formulation stability. We showed that PEG_{2k}-Fmoc-NLG alone was effective in enhancing T cell immune responses and exhibited significant antitumor activity *in vivo*. More importantly, systemic delivery of paclitaxel using the PEG_{2k}-Fmoc-NLG nanocarrier led to a significantly improved antitumor response in both breast cancer and melanoma mouse models.

4.2 INTRODUCTION

Chemotherapy remains a mainstay treatment for various types of cancers[128, 129]. It is generally believed that chemotherapeutics work through cytostatic and/or cytotoxic effects[130]. Accumulating evidence suggests that chemotherapy-elicited immune responses also

contribute significantly to the overall antitumor activity[131, 132, 133, 134]. Chemotherapeutic agents can modify the propensity of malignant cells to elicit an immune response and/or directly exert immunostimulatory effects[135]. However, the effectiveness of chemotherapy-elicited immune response as well as other types of immunotherapies is limited by various negative feedback mechanisms that are upregulated during tumor development and/or cancer treatment[136, 137]. Blockade of these immune checkpoints represents one of the most promising strategies to reactivate the immune response to cancer. Indeed, exciting preclinical and clinical anti-cancer results have been reported with the use of monoclonal antibodies against cytotoxic T-lymphocyte-associated protein 4 (CTLA-4) and programmed cell death protein 1(PD-1), two important immune checkpoints[137, 138, 139, 140, 141, 142, 143]. IDO is another important immune checkpoint protein involved in generating the immunosuppressive microenvironment that supports tumor cell growth[144, 145]. IDO is overexpressed in some cancer cells and functions as an enzyme that catalyzes the degradation of essential amino acid tryptophan (Trp) and accumulation of its metabolites[145, 146], resulting in cell cycle arrest and death of effector T cells, but increases in the number of regulatory T cells[147].

Consistent with previous findings, we have indeed shown that the mRNA expression of IFN-γ was significantly increased in 4T1.2 tumor tissues following treatment with Taxol® (Figure. 15a). We have also found that Taxol® treatment led to significant upregulation of IDO expression in tumor tissues (Figure. 15b), suggesting that IDO was induced, likely by IFN-γ, to counterbalance antitumor immune responses. Thus, strategies that are targeted at IDO represent an attractive approach for the treatment of cancer, particularly in combination

with chemotherapy[133].

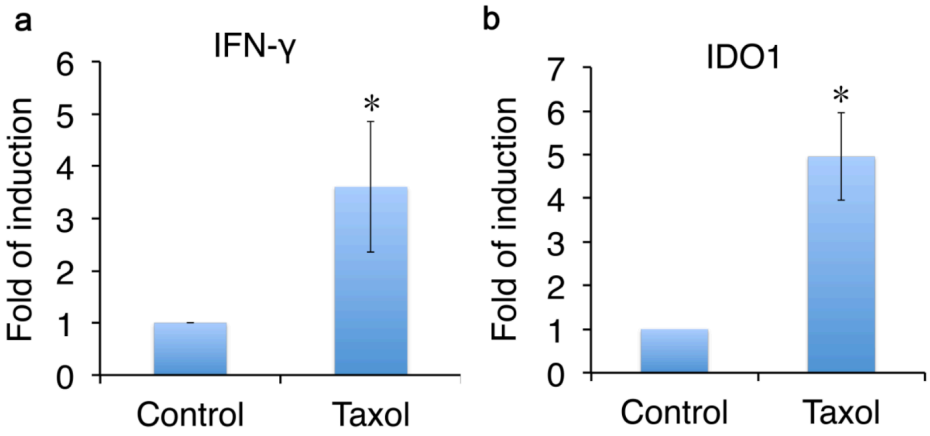

Figure 15. RT-PCR for (a) IFN-γ and (b) IDO1 RNA transcripts in tumor tissues following Taxol treatment.

Several IDO inhibitors have been reported, among which NLG919 is a highly IDO-selective inhibitor with an EC50 of 75 nM. However, most IDO inhibitors including NLG919 are poorly water soluble, which presents a major challenge in their therapeutic delivery and preclinical evaluations[73]. In addition, co-delivery of IDO inhibitors and chemotherapeutic agents to tumors remains a challenge due to their different physical and pharmacokinetic profiles. To resolve these challenges, we developed a novel micellar nanocarrier that was based on PEG-derivatized NLG919 prodrug. An Fmoc group was also introduced into the conjugate based on our recent discovery of Fmoc as a "formulation chemophor" or a structural unit capable of interacting with many pharmaceutical agents[148]. We have recently shown that incorporation of an Fmoc motif into a micellar system can not only improve the drug loading capacity and formulation stability but also broaden its utility in formulating various therapeutic agents of diverse structures[149, 150]. We hypothesized that

PEG-Fmoc-NLG represents an immunostimulatory dual-functional nanocarrier that facilitates synergistic delivery of chemotherapeutics and improves cancer immunochemotherapy.

4.3 EXPERIMENTAL PROCEDURES

4.3.1 Reagents

Paclitaxel (PTX, >99%) was purchased from TSZ Chem (MA, USA). Docetaxel (DTX, >99%) was obtained from LC Laboratories (MA, USA). α-Fmoc-ε-Boc-lysine, N, N'-dicyclohexylcarbodiimide (DCC), trifluoroacetic acid (TFA), and triethylamine (TEA) were purchased from Acros Organic (NJ, USA). Monomethoxy PEG_{2000}, 4-dimethylaminopyridine (DMAP), ninhydrin, and other unspecified chemicals were all purchased from Sigma Aldrich (MO, USA). Dulbecco's phosphate buffered saline (DPBS), Dulbecco's Modified Eagle's Medium (DMEM), fetal bovine serum (FBS), 100 penicillin-streptomycin solution were all purchased from Invitrogen (NY, USA). All solvents used in this study were HPLC grade.

4.3.2 Animals

Female BALB/c mice (4-6 weeks), female BALB/c nude mice (4-6 weeks) and C57BL/6 mice (4-6 weeks) were purchased from Charles River (Davis, CA). All animals were housed under pathogen-free conditions according to AAALAC (Association for Assessment and Accreditation of Laboratory Animal Care) guidelines. All animal-related experiments were

performed in full compliance with institutional guidelines and approved by the Animal Use and Care Administrative Advisory Committee at the University of Pittsburgh.

4.3.3 Cell Culture

4T1.2 murine breast cancer cells, B16 murine melanoma cells, Panc02 murine pancreatic ductal adenocarcinoma cells, HeLa human cervical cancer cells, and PC3 human prostate cancer cells were maintained in Dulbecco's Modified Eagle's Medium (DMEM) supplemented with 10% fetal bovine serum (FBS) and 1% penicillin-streptomycin at 37 °C in a humidified environment with 5% CO_2.

4.3.4 RNA Isolation and qRT-PCR

RNA extraction from cells and tissues were performed following our published protocols[151]. Briefly, TRIzol was used to extract RNA from cells and tissues, and the cDNA was synthesized with a high capacity cDNA reverse transcription kit (Applied Biosystems, CA). SYBR Green-based real-time PCR was performed with the ABI Prism 7300 Real-Time PCR System (Applied Biosystems, Foster City, CA). Data were normalized against the GAPDH. The relative transcript abundance was calculated based on three independent experiments.

4.3.5 Synthesis of PEG_{2k}-Fmoc-NLG Conjugate

Both PEG_{2k}-Fmoc-NLG(L) and PEG_{2k}-Fmoc-NLG(S) conjugates were synthesized by coupling NLG919 to PEG_{2k} with either ester linkage or ether linkage. PEG_{2k}-Fmoc-NLG(L) was synthesized as follow: 1 equiv. of monomethoxy PEG_{2000} was mixed with 3 equiv. of

α-Fmoc-ε-Boc-lysine and DCC in dichloromethane (DCM) in the presence of DMAP for 2 days at room temperature (RT). Purified PEG_{2K}-Fmoc-lysine-Boc was obtained by filtering the mixture and then ice-cold ether/ethanol precipitation twice. The Boc group was removed by treatment with DCM/TFA (1:1, v/v) for 2 h at RT and the deprotected PEG_{2K}-lysine(Fmoc)-NH_2 was obtained by ice-cold ether/ethanol precipitation. Finally, PEG_{2k}-Fmoc-NLG(L) was synthesized by mixing PEG_{2k}-lysine(Fmoc)-NH_2 with excess amount of NLG919, DCC, and small amount of DMAP in DCM at RT for 2 days. The mixture was filtered and the filtrate was precipitated by ice-cold ether/ethanol twice. The crude product was dissolved in water and filtered through a 450 nm filter, followed by lyophilization to yield the powder of purified PEG_{2k}-Fmoc-NLG(L). To synthesize PEG_{2k}-Fmoc-NLG(S), NLG919 was reacted with methyl 4-bromobutanoate to form ether bond under NaH condition. After column purification, the methyl ester was hydrolyzed by NaOH and the obtained compound (3 equiv.) was conjugated with PEG_{2k}-lys(Fmoc)-NH_2 (1 equiv.) using DCC (3 equiv.) and DMAP (0.3 equiv.). The mixture was filtered and the clear filtrate was precipitated by ice-cold ether/ethanol twice. The crude product was dissolved in water, filtered followed by lyophilization to obtain the purified PEG_{2k}-Fmoc-NLG(S).

4.3.6 Cell-based IDO Assays

The IDO inhibitory effect of PEG_{2k}-Fmoc-NLG was tested by an *in vitro* IDO assay[73]. Briefly, HeLa cells were seeded in a 96-well plate at a cell density of 5×10^3 cells per well and allowed to grow overnight. Recombinant human IFN-γ was then added to each well with a

final concentration of 50 ng/mL. At the same time, various concentrations of PEG_{2k}-Fmoc-NLG(L), PEG_{2k}-Fmoc-NLG(S) or free NLG919 (NLG919 concentrations: 50 nM-20μM) were added to the cells. After 48 h of incubation, 150μL of the supernatants per well was transferred to a new 96-well plate. Seventy-five μl of 30% trichloroacetic acid was added into each well and the mixture was incubated at 50 °C for 30 min to hydrolyze N-formylkynurenine to kynurenine. For colorimetric assay, supernatants were transferred to a new 96-well plate, mixed with equal volume of Ehrlich reagent (2% p-dimethylamino-benzaldehyde w/v in glacial acetic acid), and incubated 10 min at RT. Reaction product was measured at 490 nm by a plate reader. For HPLC-MS/MS detection (Wastes Alliance 2695 Separation Module combined with Waters Micromass Quattro Micro TM API MS detector), the plate was centrifuged for 10 min at 2500 rpm and 100 μl of the supernatants per well was collected for tryptophan and kynurenine assay.

4.3.7 T Cell Proliferation Study

A lymphocyte-Panc02 cell co-culture study was conducted to examine whether PEG_{2k}-Fmoc-NLG can reverse IDO1-mediated inhibition of T cell proliferation[73, 152]. Murine Panc02 cells were stimulated by IFN-γ (50ng/ml) to induce IDO expression and then irradiated (6000 rad) before coculture. Splenocyte suspensions were generated from BALB/c mice by passage through the nylon wool columns after lysing of red blood cells. IFN-γ-stimulated Panc02 cells (1×10^5 cell/well) were mixed with splenocytes (5×10^5 cells per well，pre-stained with CSFE) in a 96 well plate. Various concentrations of NLG919,

PEG_{2k}-Fmoc-NLG(L) or PEG_{2k}-Fmoc-NLG(S) were added to the cells. To measure the T cell proliferation, 100 ng/mL anti-CD3 and 10 ng/mL mouse recombinant IL-2 were added to the cocultures. The proliferation of $CD8^+$ and $CD4^+$T cells was measured by FACS after 3 days of coculture.

4.3.8 Measurements of Trp and Kyn in Plasma and Tumor Tissues

The kynurenine to tryptophan ratios in plasma or tumors in 4T1.2 tumor-bearing mice following different treatments were examined by LC-MS/MS as an indication of IDO enzyme activity[153]. BALB/c mice bearing 4T1.2 tumors of ~50mm^3 were treated with DPBS, TAXOL (10 mg PTX/kg), PEG_{2k}-Fmoc-NLG(L), or PTX/PEG_{2k}-Fmoc-NLG(L) (10 mg PTX/kg) via tail vein once every 3 days for 5 times. One day after the last treatment, the plasma and tumor samples were harvested. Plasma samples were mixed with methanol (plasma: methanol, 1:2.5, v/v) and centrifuged at 14,500 rpm for 15 min. Supernatants were collected for LC-MS quantification of kynurenine and tryptophan.

Tumor samples were homogenized in water and the homogenates were mixed with acetonitrile (1:1, v/v), centrifuged and supernatants were transferred to clean tubes. Equal volumes of methanol were added to precipitate proteins and supernatants were collected following centrifugation for HPLC-MS/MS measurement.

4.3.9 Quantification of Tumor-infiltrating Lymphocytes

BALB/c mice bearing 4T1.2 tumors of ~50mm^3 received various treatments via tail vein injection once every 2 days for 3 times. Tumors and spleen were harvested one day following

the last treatment. Single cell suspensions were prepared and costained for CD4, CD8 and Foxp3 for FACS analysis.

4.3.10 *In Vivo* Therapeutic Study of PEG_{2k}-Fmoc-NLG Micelles Alone in a Murine Breast Cancer Model (4T1.2)

To investigate whether IDO1 inhibition by PEG_{2k}-Fmoc-NLG micelles can suppress tumor growth, female BALB/c mice of 4-6 weeks old were s.c. inoculated with 4T1.2 tumor cells (2×10^5 cells/mouse)[147, 154]. Mice were randomly grouped (N = 5) when the tumor volume reached ~50 mm^3 and treated with PEG_{2k}-Fmoc-NLG(L) or PEG_{2k}-Fmoc-NLG919(S) once every 3 days for 5 times via tail vein injection. Tumor sizes were measured twice weekly in two dimensions using a caliper, and the tumor volumes were calculated with the formula: $V = (A \times B^2)/2$ (A and B are the long and short diameters of the tumor). Relative tumor volume was calculated to compare different treatment groups (relative tumor volume= tumor volume/tumor volume prior to first treatment). Mice were sacrificed when tumor volume reached ~2000 mm^3. The difference between different treatment groups was analyzed by ANOVA with significance defined as $P < 0.05$.

The above study was similarly performed in BALB/c nude mice to elucidate a role of T cell response in PEG_{2k}-Fmoc-NLG-mediated antitumor activity[73, 152].

4.3.11 Preparation and Characterizations of Drug-free or Drug-loaded PEG_{2k}-Fmoc-NLG Micelles

The drug-loaded micelles were prepared by mixing PTX (10 mM in chloroform) or DOX (10

mM in chloroform) with PEG_{2k}-Fmoc-NLG(L) or PEG_{2k}-Fmoc-NLG(S) (10 mM in chloroform) at various carrier/drug ratios. The solvent was removed by N_2 flow to form a thin film of drug/carrier mixture. The film was dried under vacuum for 1h and DPBS was added to form the drug-loaded micelles. The particle size and zeta potential of micelles were measured by a Zetasizer. The morphologies of both drug-free micelles and drug-loaded micelles were recorded under transmission electron microscopy (TEM). The critical micelle concentration (CMC) was determined by using nile red as a fluorescence probe following our published protocol[155].

4.3.12 *In Vitro* Cytotoxicity of PTX- and DOX-loaded PEG_{2k}-Fmoc-NLG(L) Micelles

4T1.2, PC3, Panc02, and B16 cells at 2000 cells/well were seeded in 96-well plates, respectively. After 12h incubation, the cell culture medium was removed and various concentrations of free PTX, free PEG_{2k}-Fmoc-NLG(L) micelles or PTX/PEG_{2k}-Fmoc-NLG(L) mixed micelles were added to the cells. After 3 days of incubation, 20μL of 3-(4, 5-dimethylthiazol-2-yl)-2,5-diphenyltetrazoliumbromide (MTT) in DPBS (5 mg/mL) was added to each well and cells were further incubated for 2 h. Medium was removed and MTT formazan crystals were solubilized by 100μL of DMSO per well. Absorbance of each well was measured with a microplate reader at wavelength of 550 nm. Untreated wells were used as controls. Cell viability was calculated as $[(OD_{treated}-OD_{blank})/(OD_{control}-OD_{blank}) \times 100\%]$. Cytotoxicity of DOX-loaded PEG_{2k}-Fmoc-NLG(L) micelles was similarly examined.

4.3.13 Intercellular Trafficking of DOX-loaded PEG_{2k}-Fmoc-NLG(L) Micelles

The intercellular trafficking of DOX-loaded PEG_{2k}-Fmoc-NLG(L) micelles was examined on 4T1.2 cells. DOX-loaded PEG_{2k}-Fmoc-NLG(L) micelles (carrier:drug, 5:1, m/m) were prepared as described above. PEG_{2k}-Fmoc-CBZ with a similar structure as PEG_{2k}-Fmoc-NLG(L) was used as control[156]. 4T1.2 cells were seeded in 29 mm glass bottom dishes (*In Vitro* Scientific, Sunnyvale, CA) at 5×10^4 cells per well in 2 mL optimal DMEM and cultured overnight. Cells were then treated for 4 h with free DOX, DOX/PEG_{2k}-Fmoc-CBZ or DOX/PEG_{2k}-Fmoc-NLG(L) mixed micelles at a DOX concentration of 10 nM. The nuclei of cells were stained with Hoechst and cells were observed under a confocal fluorescence microscope.

4.3.14 Plasma Pharmacokinetics and Tissue Distribution

Groups of 5 female CD-1 mice were i.v. administered with TAXOL or PTX/PEG_{2k}-Fmoc-NLG(L) mixed micelles at a dose of 10 mg PTX/kg. Blood samples of 50μL were withdrawn from the retro-orbital plexus/sinus of the mice from 3 min to 12 h (3 min, 10 min, 30 min, 1 h, 2 h, 4 h, 8 h, and 12 h). The blood collected in heparinized tubes was centrifuged at 2,500 rpm for 15 min. To 20μL of plasma, 350 μL of acetonitrile was added for protein precipitation and the resulting mixture was centrifuged at 12, 000rpm for 5 min. Three-hundred microliters of the supernatants were collected from each sample and dried under airflow. The residues were dissolved in 50 μL of methanol and analyzed by HPLC for PTX. The pharmacokinetic parameters were calculated based on a

noncompartment model by Phoenix WinNonlin.

For tissue distribution study, groups of 5 BALB/c mice bearing 4T1.2 tumors of 400–600 mm^3 were i.v. administered with PTX-loaded PEG_{2k}-Fmoc-NLG (L) micelles or TAXOL at a PTX dose of 10 mg/kg. Mice were sacrificed 24 h after injection. Major organs and tumor tissues were collected, weighed, and homogenized with 2 mL solvent (acetonitrile to H_2O=1:1, v/v). The samples were centrifuged at 4°C, 3,500 rpm for 15 min, and the supernatants were collected and dried under airflow. The residues were then dissolved in 200 μL solvent (Methanol to H_2O=1:1, v/v) and centrifuged at 4°C, 14,500 rpm for 10 min. The supernatants were mixed with equal volume of methanol and centrifuged again at 4°C, 14,500 rpm for 10 min. Twenty microliters of the clear supernatants were injected into HPLC system for detection of PTX.

4.3.15 *In Vivo* Antitumor Activity of PTX/ PEG_{2k}-Fmoc-NLG(L)

In vivo antitumor activity of PTX formulated in PEG_{2k}-Fmoc-NLG(L) micelles was similarly examined in 4T1.2 tumor model as described above. Controls included PEG_{2k}-Fmoc-NLG(L), TAXOL, and PTX/PEG_{2k}-Fmoc-NLG(S). The PTX dose was 10mg/kg and mice received the treatment once every 3 days for 5 times. The growth of tumors was followed every three days after initiation of treatment for 19 days and relative tumor volume was calculated. The difference between different treatment groups was analyzed by ANOVA with significance defined as $P < 0.05$. The tumors were harvested and weighted at the end of experiment. The relative expression of CD8a, CD4, Foxp3 and IFN-γ in tumor tissues was examined by

qRT-PCR[157].

Similarly, a dose escalation study (5, 10, and 20 mg PTX/kg) was conducted for PTX/PEG_{2k}-Fmoc-NLG(L) in 4T1.2 tumor model. The antitumor activity of PTX/PEG_{2k}-Fmoc-NLG(L) was further examined in a murine melanoma model, B16, as described above.

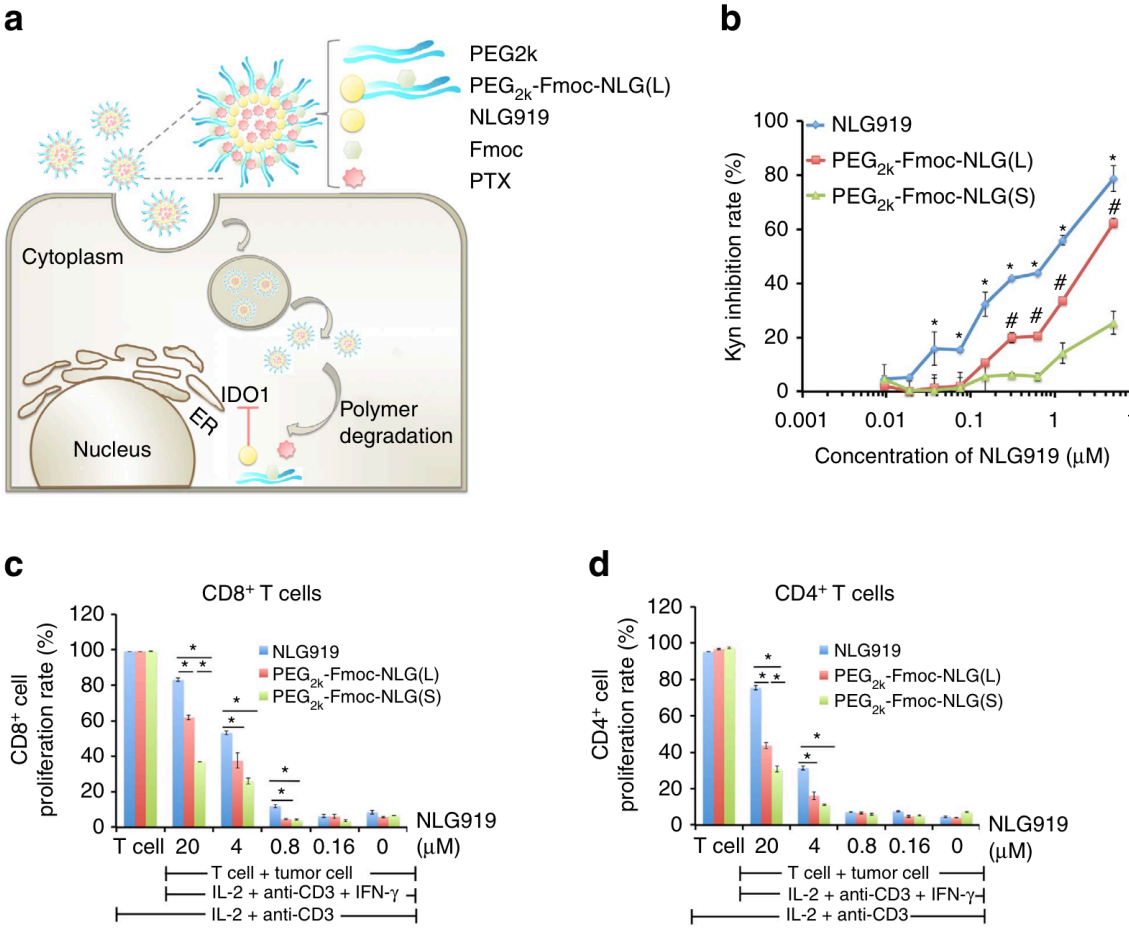

Figure 16. *In vitro* biological activities of PEG_{2k}-Fmoc-NLG.
(a) Schematic representation of self-assembled PTX/PEG_{2k}-Fmoc-NLG mixed micelles. (b) PEG_{2k}-Fmoc-NLG inhibited IDO enzyme activity *in vitro*. HeLa cells were treated with IFN-g together with free NLG919 or PEG-NLG conjugate. Kynurenine in supernatants was measured 2 days later. Data represent means±s.e.m. *P<0.05 (versus PEG_{2k}-Fmoc-NLG(L), N=3), #P<0.05 (versus PEG_{2k}-Fmoc-NLG(S), N=3). (c,d) IDO1 inhibition reversed T-cell suppression mediated by IDO-expressing mouse pancreatic cancer cells (Panc02). Panc02 cells and splenocytes were mixed and treated with IL-2, anti-CD3 antibody, IFN-g together with NLG919 or PEG-NLG conjugate for 3 days. (c) $CD4^+$ and (d) $CD8^+$ T-cell proliferation

was examined by FACS analysis. Representative data of three independent experiments are presented as means±s.e.m. *P<0.05.

4.3.16 Statistics

All data are presented as mean ± s.e.m. Differences between groups were assessed using ANOVA and P < 0.05 was considered statistically significant.

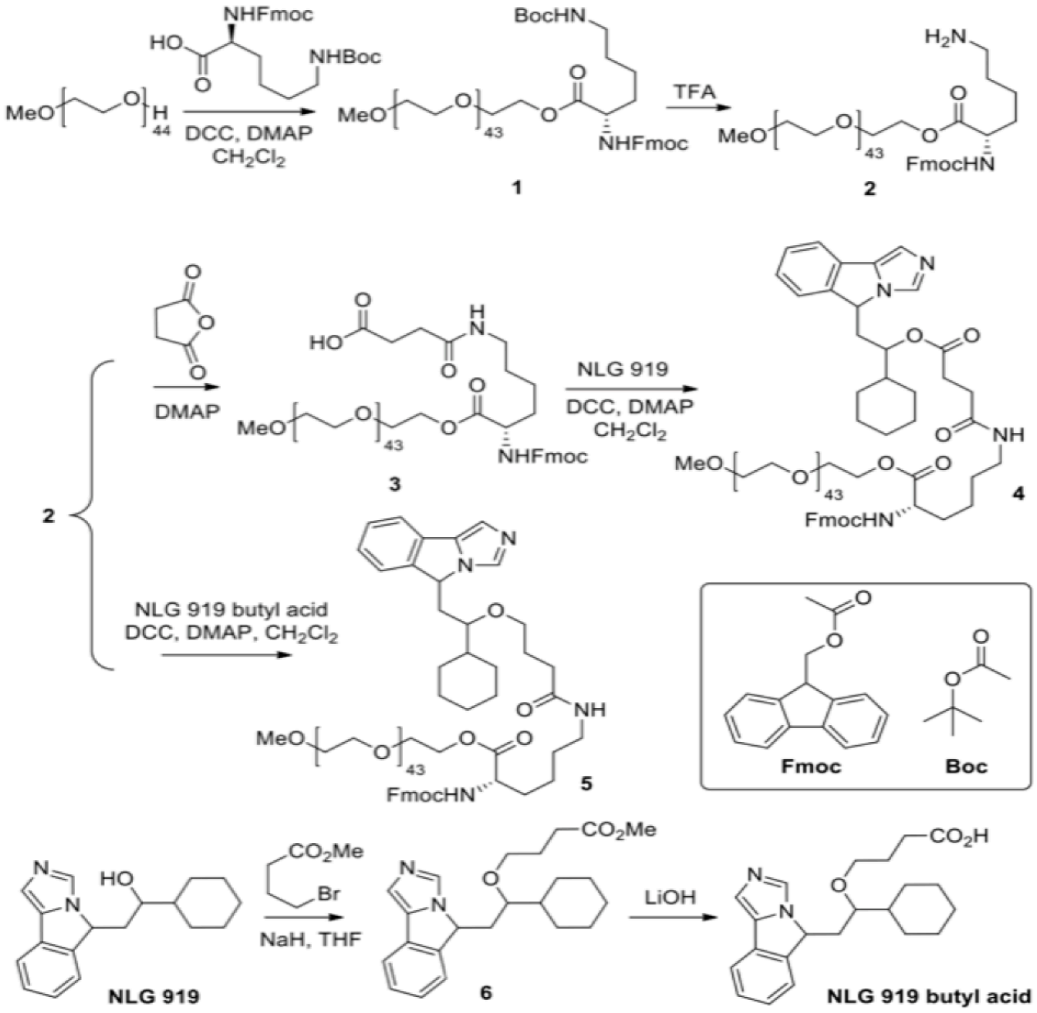

Figure 17. Synthesis schemes of PEG_{2K}-Fmoc-NLG(L) (4) and PEG_{2K}-Fmoc-NLG(S) (5) conjugates.

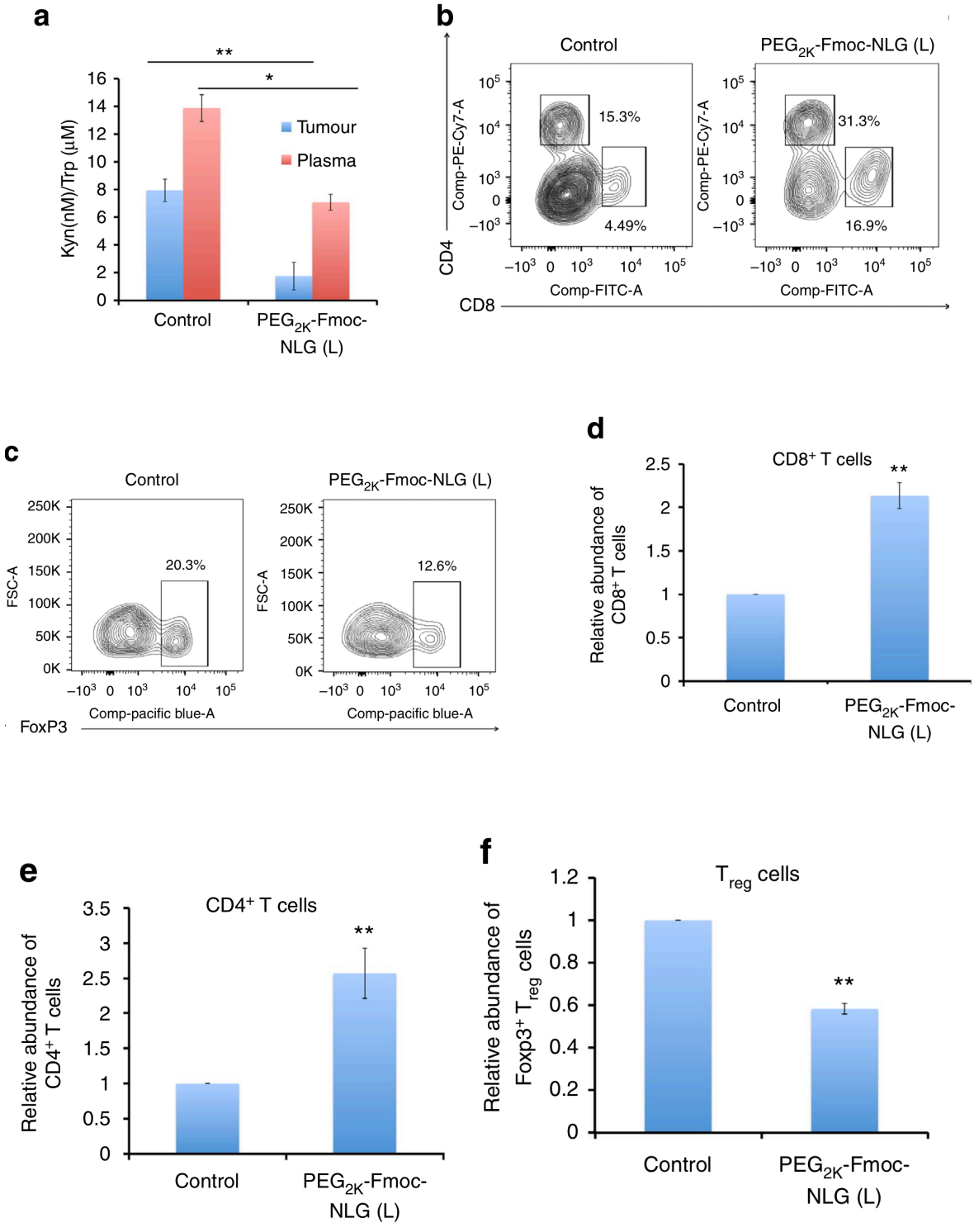
a
**
*
Kyn(nM)/Trp (μM)
Tumour
Plasma
Control
PEG2K-Fmoc-NLG (L)
b
Control
PEG2K-Fmoc-NLG (L)
CD4
CD8
Comp-PE-Cy7-A
Comp-FITC-A
15.3%
4.49%
31.3%
16.9%
c
Control
PEG2K-Fmoc-NLG (L)
FSC-A
FoxP3
Comp-pacific blue-A
20.3%
12.6%
d
CD8+ T cells
Relative abundance of CD8+ T cells
e
CD4+ T cells
Relative abundance of CD4+ T cells
f
Treg cells
Relative abundance of Foxp3+ Treg cells

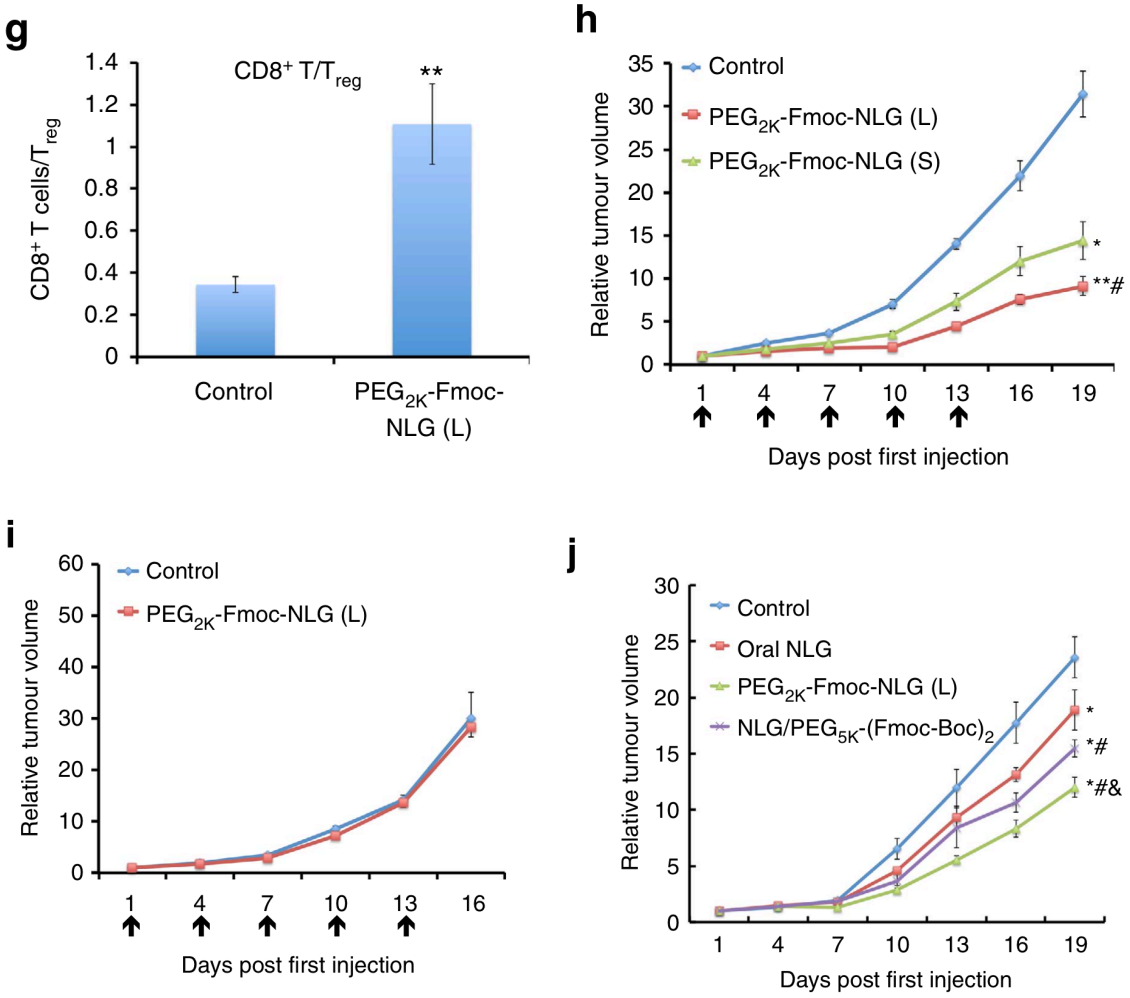

Figure 18. *In vivo* biological activities of PEG_{2k}-Fmoc-NLG.

(a) PEG_{2k}-Fmoc-NLG(L) treatment decreased kynurenine concentrations in plasma and tumours. BALB/c mice bearing s.c. 4T1.2 tumours of ~50 mm^3 received PBS or PEG_{2k}-Fmoc-NLG(L) i.v. once every 3 days for 5 times at a dose of 25 mgNLG919 per kg. Kynurenine/tryptophan ratios in plasma and tumours were determined by HPLC–MS one day following the last injection. Data are means±s.e.m. of 3 experiments. *P<0.05, **P<0.01. (b–g) IDO1 inhibition by PEG2k-Fmoc-NLG(L) increased $CD4^+$ and $CD8^+$ T cells, and decreased Treg cells in tumours. Tumour-bearing mice were treated as described above. (b) Gating of CD8 þ and $CD4^+$ T cells (marked with black boxes) as a percentage of $CD45^+$ lymphocytes. (c) Gating of T_{reg} ($CD4^+FoxP3^+$) cells (marked with black boxes) as a percentage of $CD4^+$ lymphocytes. (d,e) Relative number of intratumoural $CD8^+$ (d) and $CD4^+$ (e) T cells following different treatments. (f,g) Relative number of Treg cells (f) and $CD8^+$ T cells/T_{reg} (g) in tumour tissues. Data represent means±s.e.m. (**P<0.01, N=5). (h) PEG_{2k}-Fmoc-NLG maintained the tumour inhibitory effect. Mice bearing tumours of ~50 mm^3 received different treatments as indicated (black arrows). *P<0.05; **P<0.01 (versus control, N=5), #P<0.05 (versus PEG_{2k}-Fmoc-NLG(S), N=5). (i) Lymphocyte activities were required for the *in vivo* activity of PEG_{2k}-Fmoc-NLG(L) micelles. Female BALB/c-nu/nu mice bearing 4T1.2 tumour of B50 mm3 were similarly treated as described above. (**j**)

Enhanced *in vivo* antitumour activity of PEG_{2k}-Fmoc-NLG(L) compared with oral delivery of NLG (#P<0.05, N=5) or NLG formulated in PEG_{5k}-$(Fmoc\text{-}Boc)_2$ micelles (&P<0.05, N=5). *P<0.05 (versus control, N=5). Data represent means±s.e.m.

Table 4. Biophysical Characteristics of Anticancer Drug-loaded PEG_{2K}-Fmoc-NLG(L) Micelles and Blank Micelles.

Micelles	Molar ratio	Particle size (nm)†	DLC (%)
PEG_{2K}-Fmoc-NLG(L)	—	96.96	—
PEG_{2K}-Fmoc-NLG(L): Paclitaxel	1:1	96.57	24.7
PEG_{2K}-Fmoc-NLG(L): Doxorubicin	0.5:1	97.98	30.9
PEG_{2K}-Fmoc-NLG(L): Docetaxel	2.5:1	96.95	10.5
PEG_{2K}-Fmoc-NLG(L): Gefitinib	2.5:1	105.1	6.1
PEG_{2K}-Fmoc-NLG(L): Imatinib	2.5:1	102.1	6.7
PEG_{2K}-Fmoc-NLG(L): Curcumin	2.5:1	97.50	5.1

DLC, drug loading capacity. Drug concentrations in micelle were 1 mg/mL and blank micelle concentration was 20mg/mL. wMeasured by dynamic light scattering sizer.

4.4 RESULT

4.4.1 Characterization of PEG_{2k}-Fmoc-NLG

PEG_{2k}-Fmoc-NLG is an amphiphilic molecule that self-assembles into micelles in aqueous solutions. The self-assembly of PEG_{2k}-Fmoc-NLG and the loading of hydrophobic drugs into the PEG_{2k}-Fmoc-NLG micelles are illustrated in Fig. 16a. Fig. 17 shows the synthesis scheme of two PEG_{2k}-Fmoc-NLG conjugates, one with a relatively labile ester linkage (PEG_{2k}-Fmoc-NLG(L)) and the other one with a relatively stable amide linkage (PEG_{2k}-Fmoc-NLG(S)). The chemical structures of the two conjugates were confirmed by NMR and mass spectrometry (MS).

The inhibitory activity of PEG_{2k}-Fmoc-NLG(L) and PEG_{2k}-Fmoc-NLG(S) on IDO was evaluated by examining their potency in inhibiting the conversion of Trp to kynurenine (Kyn) in HeLa cells[73, 152]. HeLa cells were treated with IFN-γ to induce IDO expression and the amounts of Trp and Kyn in culture medium were determined by a colorimetric assay. As shown in Fig. 16b, free NLG919 inhibited the IDO activity in a concentration-dependent manner. PEG_{2k}-Fmoc-NLG(L) was only slightly less active in inhibiting IDO compared to free NLG919 while PEG_{2k}-Fmoc-NLG(S) was least active. Similar results were obtained when the Trp and Kyn concentrations were measured by LC/MS. We then examined if inhibition of IDO by PEG_{2k}-Fmoc-NLG(L) led to enhanced T cell proliferation in an *in vitro* lymphocyte and Panc02 (a murine pancreatic cancer cell line) coculture experiment. As shown in Fig. 16c, coculture of IDO^+ tumor cells with splenocytes isolated from BALB/c mice led to significant inhibition of T cell proliferation. This inhibition was significantly attenuated when the mixed cells were treated with NLG919. PEG_{2k}-Fmoc-NLG(L) was also active in reversing the inhibitory effect of tumor cells although slightly less potent than NLG919. PEG_{2k}-Fmoc-NLG(S) is less active compared to PEG_{2k}-Fmoc-NLG(L) (Fig. 16c).

The *in vivo* biological activity of PEG_{2k}-Fmoc-NLG(L) was evaluated in an aggressive murine breast cancer model, 4T1.2. As detailed later, PEG_{2k}-Fmoc-NLG(L) self-assembled to form nano-sized micelles (~90 nm) in aqueous solutions, which shall enable effective and selective delivery to tumors via enhanced permeation and retention (EPR) effect[158]. As shown in Fig. 18a, the ratios of Kyn (nM)/Trp (μM) in both blood and tumors were significantly reduced following the treatment of PEG_{2k}-Fmoc-NLG(L) while a more dramatic reduction

was observed in the tumor tissues, consistent with the intended specific targeting of IDO inhibitors to the tumor tissues. Fig. 18b-g shows multi-color flow cytometric analysis of tumor-infiltrating lymphocytes in 4T1.2 tumor-bearing mice with or without treatment of PEG_{2k}-Fmoc-NLG(L). It is clear that more $CD4^+$ and $CD8^+$ T cells were found in the tumors that received the treatment of PEG_{2k}-Fmoc-NLG(L). In addition, the number of regulatory T cells (Tregs) was significantly reduced in the tumors treated with PEG_{2k}-Fmoc-NLG(L).

Fig. 18h shows the *in vivo* antitumor activity of PEG_{2k}-Fmoc-NLG(L) and PEG_{2k}-Fmoc-NLG(S) in 4T1.2 tumor model. Significant antitumor responses were observed for both prodrugs. It is also apparent that PEG_{2k}-Fmoc-NLG(L) was more effective than PEG_{2k}-Fmoc-NLG(S) in inhibiting the tumor growth. We also showed that PEG_{2k}-Fmoc-NLG(L) was essentially not active in inhibiting the growth of 4T1.2 tumor in the immunocompromised nude mice that lack T and B cells (Fig. 18i), suggesting that the antitumor response was mediated via an enhanced T cell response. The above data clearly demonstrated that PEG-derivatized NLG919 prodrug well retained the pharmacological activity of NLG919 and that the cleavability of NLG919 from the conjugate affected its activity. We have further shown that i.v. PEG_{2k}-Fmoc-NLG(L) was more effective than NLG919 delivered orally or NLG919 formulated PEG_{5k}-$(Fmoc\text{-}Boc)_2$ micelles (Fig. 2j)

4.4.2 *In Vitro* Characterization of Drug-loaded PEG_{2k}-Fmoc-NLG Micelles

PEG_{2k}-Fmoc-NLG(L) readily formed small-sized (~90 nm) micelles in aqueous solutions as confirmed by DLS and TEM imaging (Fig. 19a). Loading of PTX into

PEG_{2k}-Fmoc-NLG(L) micelles resulted in minimal changes in the sizes of the particles and

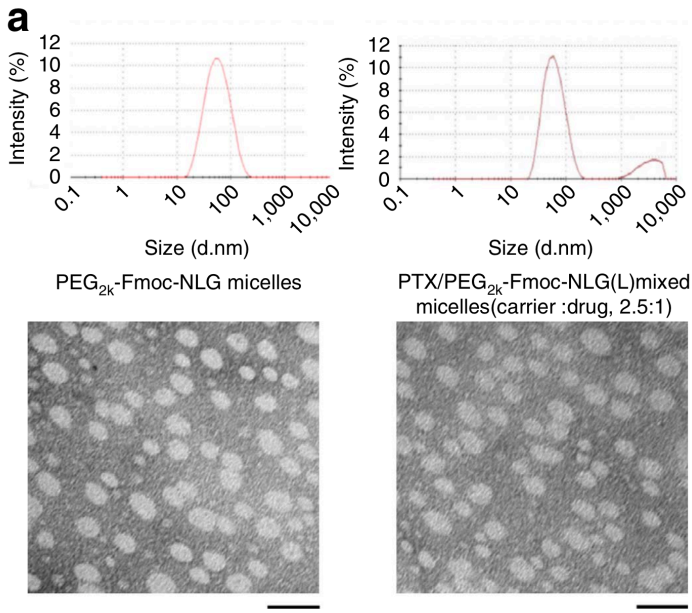

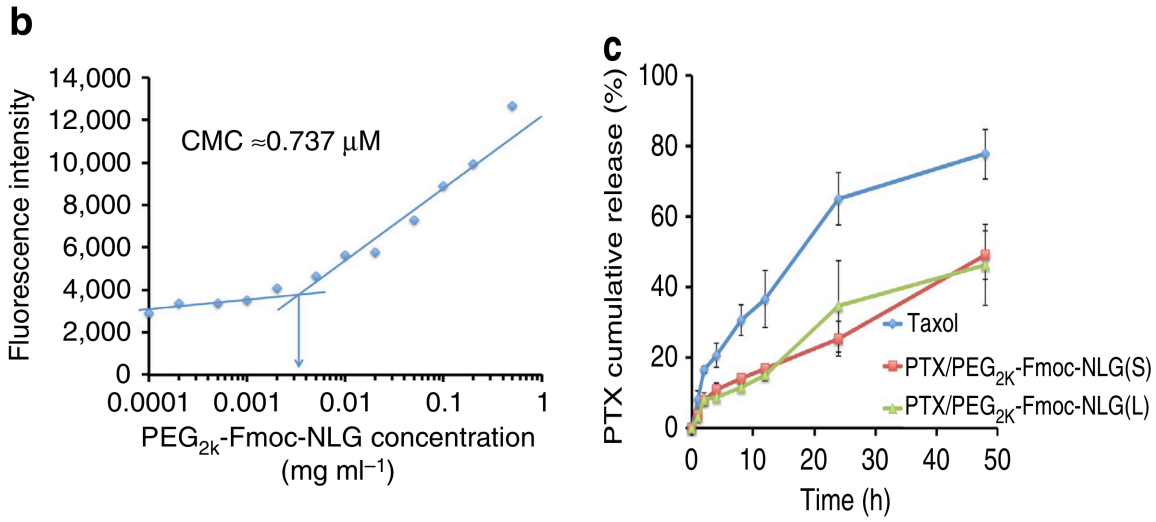

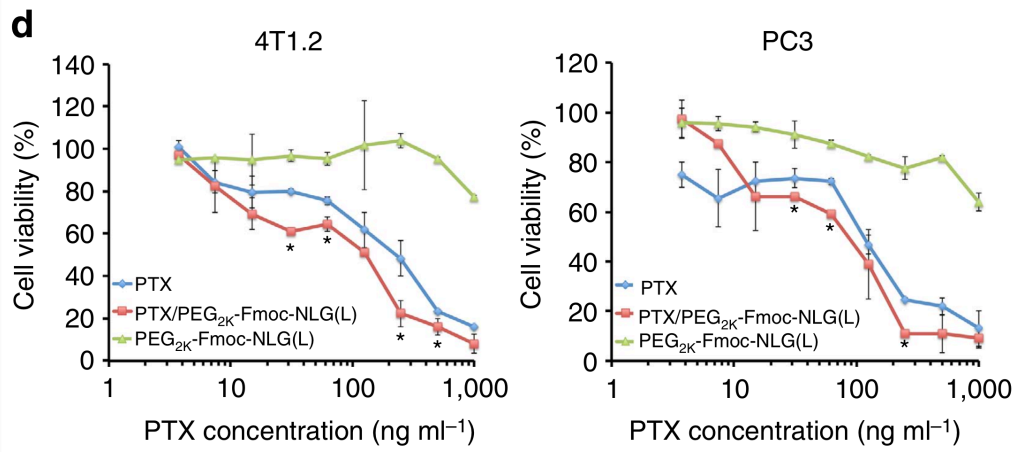

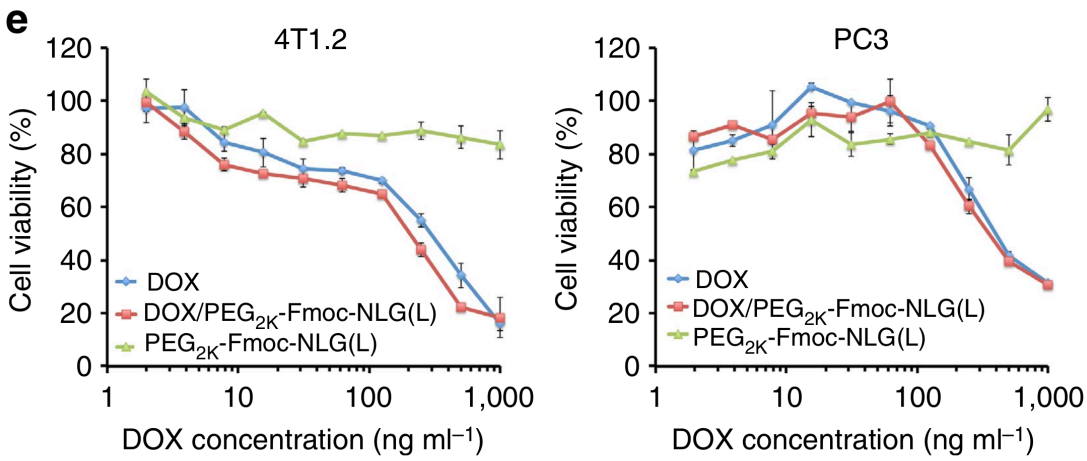

Figure 19. *In vitro* biophysical and biological characterizations of micelles.
(a) Size distribution and morphology of drug-free and PTX-loaded PEG_{2k}-Fmoc-NLG(L) micelles (carrier: drug, 2.5:1, m/m) were examined by dynamic light scattering and TEM, respectively. Drug concentration in micelles was kept at 1 mg ml^{-1}. Blank micelle concentration was 20 mg ml^{-1}. Scale bar, 100 nm. (b) Measurement of CMC of PEG2k-Fmoc-NLG(L) micelles. (c) PTX release kinetics of PTX/PEG_{2k}-Fmoc-NLG(L) examined via a dialysis method. PTX concentrations were kept at 1 mg ml1 in PTX/PEG_{2k}-Fmoc-NLG(S), PTX/PEG_{2k}-Fmoc-NLG(L) and Taxol. PTX concentrations were analysed at 0, 1, 2, 4, 8, 24 and 48 h by HPLC. (d) Cytotoxicity of PEG_{2k}-Fmoc-NLG(L) alone, free PTX, and micellar PTX against a mouse breast cancer cell line (4T1.2) and a human prostate cancer cell line (PC3). Cells were treated for 72 h and cytotoxicity was determined by MTT assay. *P<0.05 (PTX/PEG_{2k}-Fmoc-NLG(L) versus PTX), N=3. (**e**) Cytotoxicity of PEG_{2k}-Fmoc-NLG(L) alone, free DOX, and micellar DOX against a mouse breast cancer cell line (4T1.2) and a human prostate cancer cell line (PC3). Data represent means±s.e.m.

Table 5. IC50 of PTX or DOX in Different Formulation

Groups	IC50 (ng ml^{-1})	
	4T1.2	PC3
PTX	244.56 ± 21.05	101.30 ± 11.25
PTX/PEG_{2K}-Fmoc-NLG(L)	134.44 ± 21.81*	88.540 ± 6.431
DOX	268.60 ± 27.28	548.04 ± 58.93
DOX/PEG_{2K}-Fmoc-NLG(L)	178.53 ± 28.74	423.16 ± 38.15

Table 6. Pharmacokinetic Parameters of PTX in Different Formulations.

Groups	$T_{1/2}$(h)	$AUC_{0\text{-infinity}}$ (μg h ml^{-1})	C_{max} (μg ml^{-1})	CL (ml h^{-1} kg^{-1})	Vd (ml kg^{-1})
PTX/PEG_{2k}-Fmoc-NLG(L)	5.552	45.23	12.98	3.242	25.97
Taxol	1.434	4.313	9.912	46.09	95.33

The experiment was performed as described for Fig. 4e. The pharmacokinetic parameters were analysed by Phoenix WinNonlin.

their morphology (Fig. 19a). Similar results were obtained for PEG_{2k}-Fmoc-NLG(S) micelles (data not shown). Fig. 19b shows that the critical micelle concentration (CMC) of PEG_{2k}-Fmoc-NLG(L) was 0.737 μM. The relatively low CMC may render the micelles stable upon dilution in the blood, which is important for systemic delivery to tumors. Table. 4 shows the drug loading capacity (DLC) of PEG_{2k}-Fmoc-NLG(L) for several commonly used chemotherapeutic agents including paclitaxel (PTX), docetaxel, doxorubicin (DOX), gefitinib, imatinib, and curcumin.

Figure 19c shows the kinetics of PTX release from PTX/PEG_{2k}-Fmoc-NLG in comparison with Taxol. The kinetics of PTX release was significantly slower for either PTX/PEG_{2k}-Fmoc-NLG(L) or PTX/PEG_{2k}-Fmoc-NLG(S) formulation than Taxol. Fig. 19d shows the cytotoxicity of PTX-loaded PEG_{2k}-Fmoc-NLG(L) in 4T1.2 cells. PEG_{2k}-Fmoc-NLG(L) alone was not effective in inhibiting the tumor cell growth at the test concentrations. Free PTX inhibited the tumor cell growth in a concentration-dependent manner. PTX-loaded PEG_{2k}-Fmoc-NLG(L) micelles were more effective than free PTX in inhibiting the tumor cell growth (Fig. 19d). Similar results were found in the PC3 human

prostate cancer cell line (Fig. 19d). We also observed enhanced cytotoxicity for DOX following incorporation into PEG_{2k}-Fmoc-NLG(L) micelles (Fig. 19e). The IC50s of free drugs (PTX or DOX) and drug-loaded micelles are shown in Table 5.

4.4.3 Pharmacokinetics and Biodistribution of PTX-loaded Micelles

Figure 20a shows the kinetics of PEG-Fmoc-NLG in the blood in comparison to NLG loaded into PEG_{5k}-$(Fmoc\text{-}Boc)_2$ micelles. The concentrations of total NLG (intact PEG_{2k}-Fmoc-NLG plus released free NLG) in the blood were significantly higher than the blood concentrations of NLG delivered by PEG_{5k}-$(Fmoc\text{-}Boc)_2$ micelles at most time points examined. It is also apparent that very little free NLG was detected in the blood in the group treated with PEG_{2k}-Fmoc-NLG, suggesting the excellent stability of the conjugate in the blood.

Figure 20b shows the amounts of total NLG in the tumours at different time points following i.v. administration of either PEG_{2k}-Fmoc-NLG or NLG-loaded PEG_{5k}-$(Fmoc\text{-}Boc)_2$ micelles. The NLG concentrations in the tumours in NLG/PEG_{5k}-$(Fmoc\text{-}Boc)_2$ group reached the peak levels at 2 h and then quickly declined over time. In contrast, high concentrations of NLG (largely intact conjugate) were found in the tumours over the entire 48h in the mice treated with PEG_{2k}-Fmoc-NLG. It is also apparent that a relatively constant concentration of free NLG was detected in the tumours in this group, albeit at a low level, suggesting that NLG was slowly but continuously released from the conjugate over a prolonged period of time. Figure 20c,d shows the total amounts of NLG in tumours and other major organs/

tissues at various times following i.v. administration of either PEG2k-Fmoc-NLG or NLG/PEG_{5k}-$(Fmoc\text{-}Boc)_2$ mixed micelles.

Figure 20e shows the blood PTX kinetics in BALB/c mice as a function of time following i.v. bolus administration of PTX-loaded PEG_{2k}-Fmoc-NLG(L) and Taxol. It is apparent that PTX/PEG_{2k}-Fmoc-NLG(L) remained in the circulation for a significantly longer time compared with Taxol. The pharmacokinetic parameters are outlined in Table 3. Incorporation of PTX into PEG_{2k}-Fmoc-NLG(L) micelles resulted in significantly greater t1/2, area under curve (AUC), and Cmax over Taxol. Meanwhile, volume of distribution (Vd) and clearance (CL) for PTX/PEG_{2k}-Fmoc-NLG(L) were significantly lower than those for Taxol.

Figure 20f shows the biodistribution of PTX in 4T1.2 tumour-bearing mice 24h following i.v. administration of PTX-loaded PEG_{2k}-Fmoc-NLG(L) micelles or Taxol. Significantly greater amounts of PTX were found in tumour tissues for PTX-loaded PEG_{2k}-Fmoc-NLG(L) micelles in comparison with Taxol. In contrast, PTX-loaded PEG_{2k}-Fmoc-NLG(L) micelles showed significantly reduced accumulation than Taxol in liver, spleen and other organs/tissues. These data strongly suggest that PTX-loaded PEG_{2k}-Fmoc-NLG(L) micelles are stable in the blood and are highly effective in selective delivery to the tumour tissues. Figure 20g,h shows the amounts of PTX in tumours and other major organs/tissues at various times following i.v. administration of either PTX-loaded PEG_{2k}-Fmoc-NLG(L) micelles or Taxol.

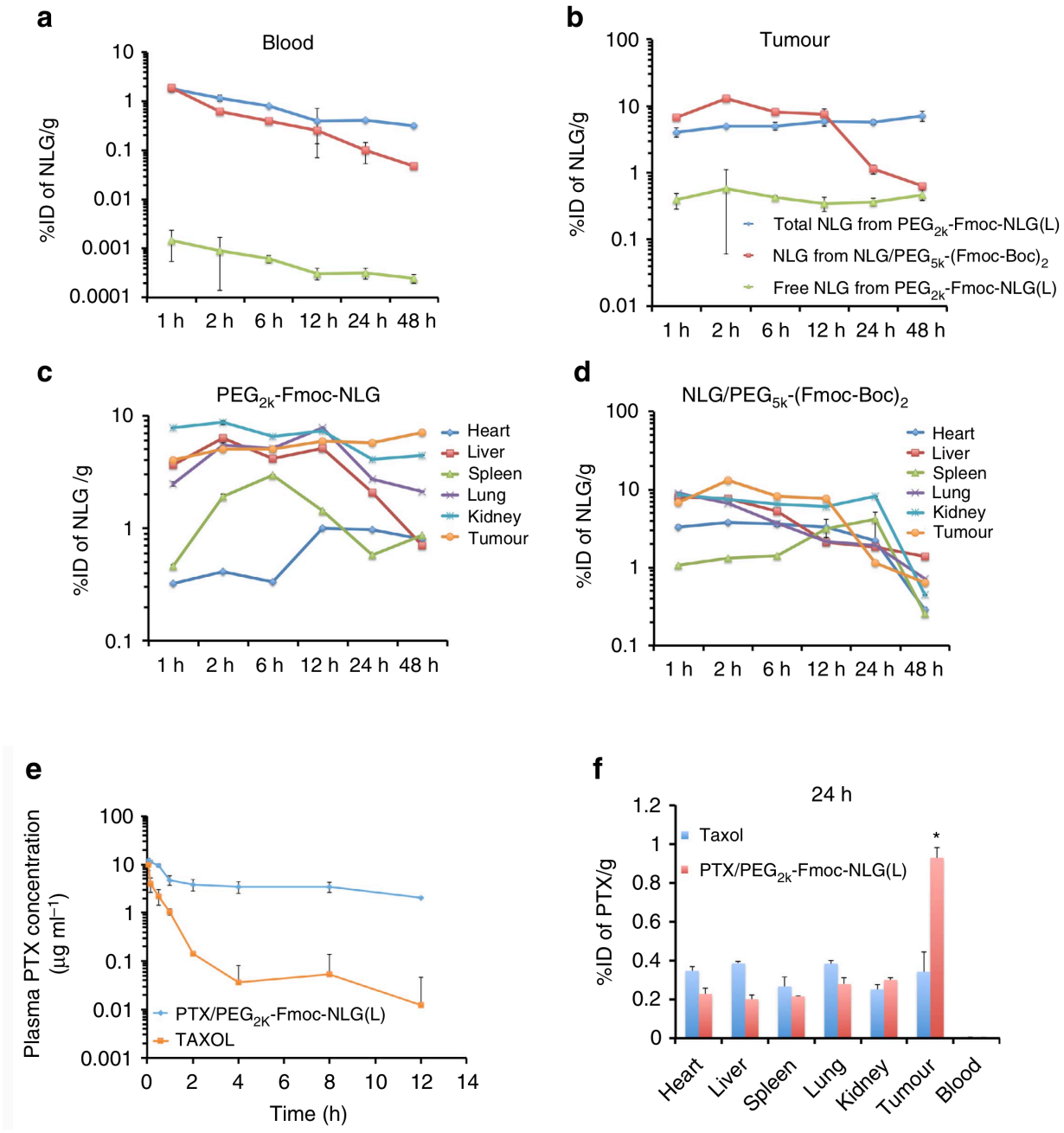
a
Blood
%ID of NLG/g
10
1
0.1
0.01
0.001
0.0001
1 h 2 h 6 h 12 h 24 h 48 h
b
Tumour
%ID of NLG/g
100
10
1
0.1
0.01
Total NLG from PEG2k-Fmoc-NLG(L)
NLG from NLG/PEG5k-(Fmoc-Boc)2
Free NLG from PEG2k-Fmoc-NLG(L)
1 h 2 h 6 h 12 h 24 h 48 h
c
PEG2k-Fmoc-NLG
%ID of NLG /g
10
1
0.1
Heart
Liver
Spleen
Lung
Kidney
Tumour
1 h 2 h 6 h 12 h 24 h 48 h
d
NLG/PEG5k-(Fmoc-Boc)2
%ID of NLG/g
100
10
1
0.1
Heart
Liver
Spleen
Lung
Kidney
Tumour
1 h 2 h 6 h 12 h 24 h 48 h
e
Plasma PTX concentration (μg ml−1)
100
10
1
0.1
0.01
0.001
PTX/PEG2K-Fmoc-NLG(L)
TAXOL
0 2 4 6 8 10 12 14
Time (h)
f
24 h
%ID of PTX/g
1.2
1
0.8
0.6
0.4
0.2
0
Taxol
PTX/PEG2k-Fmoc-NLG(L)
*
Heart
Liver
Spleen
Lung
Kidney
Tumour
Blood

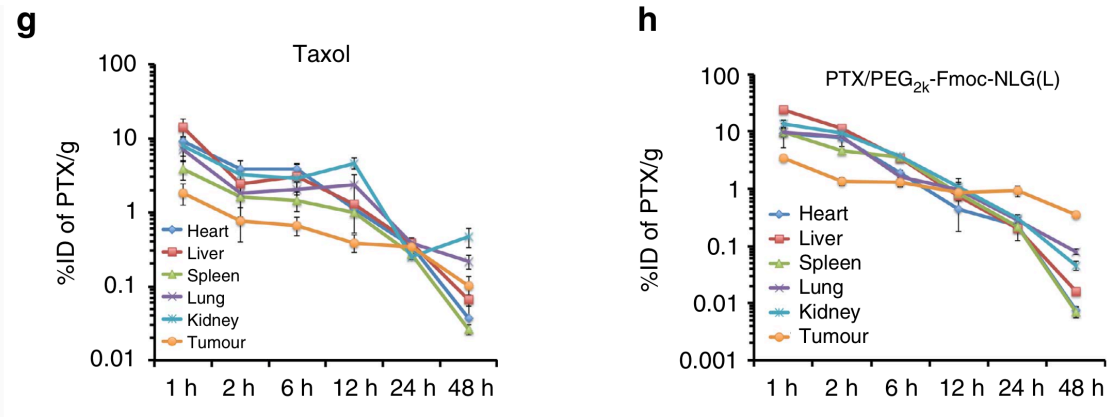

Figure 20. Pharmacokinetics and biodistribution of drug-free and PTX-loaded micelles. (a,b) The kinetics of NLG in blood (a) and tumour (b) in 4T1.2 tumour-bearing mice following i.v. administration of PEG_{2k}-Fmoc-NLG(L) in comparison to NLG-loaded PEG_{5K}-$(Fmoc\text{-}Boc)_2$ micelles (25 mg NLG per kg). (c,d) Tissue distribution of NLG in 4T1.2 tumour-bearing BALB/c mice following i.v. administration of PEG_{2k}-Fmoc-NLG(L) (c) or NLG-loaded PEG_{5K}-$(Fmoc\text{-}Boc)_2$ micelles (d) at a NLG dose of 25 mg kg-1. (e) Blood kinetics of PTX in BALB/c mice following i.v. administration of Taxol or PTX/PEG_{2K}-Fmoc-NLG(L) mixed micelles at a dose of 10 mg PTX per kg. (f) Tissue distribution of PTX in 4T1.2 tumour-bearing BALB/c mice 24 h following i.v. administration of Taxol or PTX/PEG_{2K}-Fmoc-NLG(L) mixed micelles at a PTX dose of 10 mg/kg. *$P<0.05$ (N=5). (g,h) Tissue distributions of PTX at various time points following i.v. administration of Taxol (g) or PTX/PEG_{2K}-Fmoc-NLG(L) mixed micelles (h) (10 mg PTX per kg). All data represent means±s.e.m.

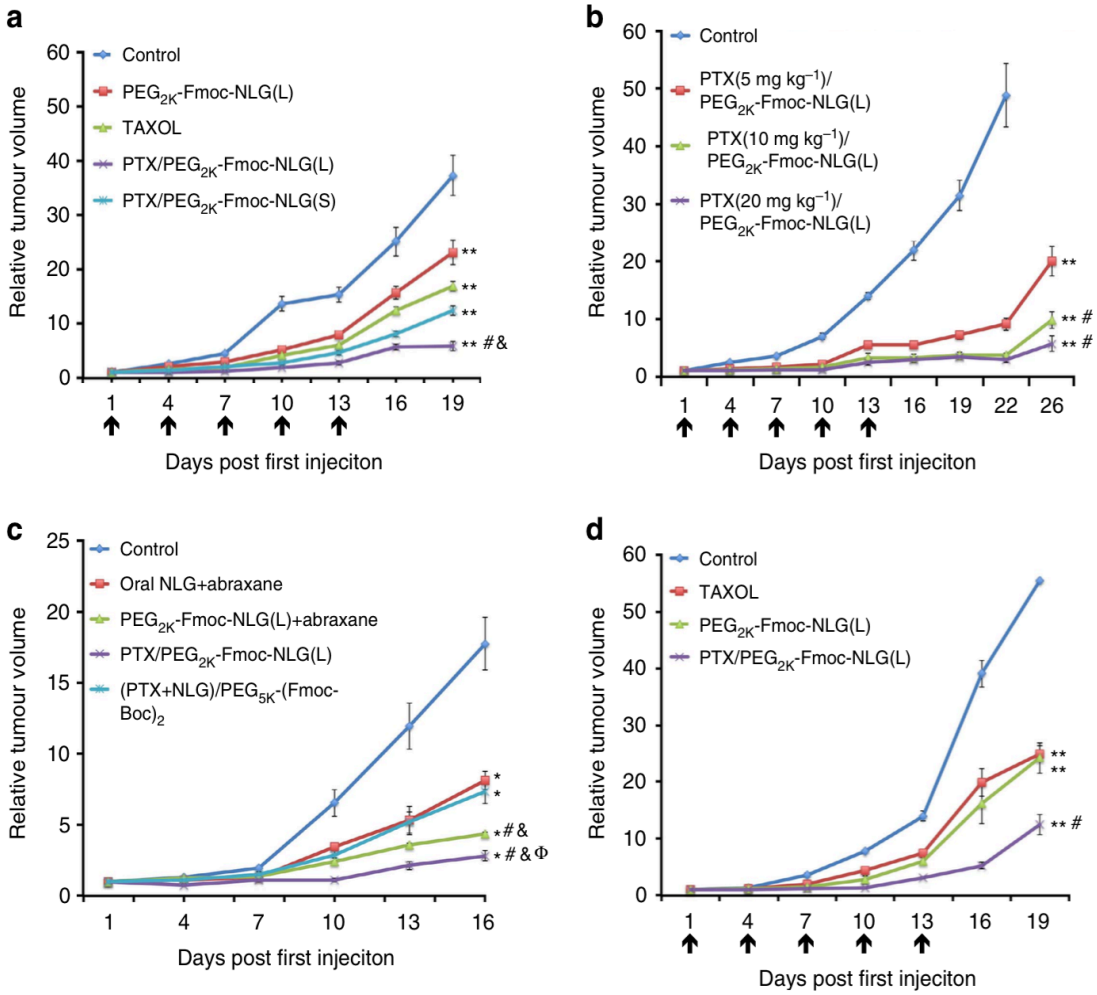

Figure 21. *In vivo* antitumour activity of PTX-loaded PEG_{2k}-Fmoc-NLG micelles.
(a) *In vivo* antitumour activity of various PTX formulations in 4T1.2 tumour model. PTX dose was 10 mg/kg. Tumour sizes were plotted as relative tumour volumes. **P<0.01 (all treatment groups versus control group), $^{\#}$P<0.05 (PTX/PEG_{2k}-Fmoc-NLG(L) versus Taxol), $^{\&}$P<0.05 (PTX/PEG_{2k}-Fmoc-NLG(L) versus PTX/PEG_{2k}-Fmoc-NLG(S)). N=5. (b) Dose-escalation study on the antitumour activity of PTX-loaded PEG_{2k}-Fmoc-NLG(L) micelles. PTX dose was 5, 10 and 20 mg/kg, respectively. **P<0.01 (all treatment groups versus control), $^{\#}$P<0.05 (10 mg, 20 mg PTX per kg versus 5 mg PTX per kg). N=5. (c) Antitumour activity of PTX/PEG_{2k}-Fmoc-NLG(L) in a 4T1.2 tumour model in comparison to a combination of oral NLG with i.v. Abraxane, PEG_{2k}-Fmoc-NLG(L) plus Abraxane or PEG_{5k}-$(Fmoc\text{-}Boc)_2$ micelles co-loaded with PTX and NLG. *P<0.01 (all treatment groups versus control), $^{\#}$P<0.05 (PTX/PEG_{2k}-Fmoc-NLG(L) or PEG_{2k}-Fmoc-NLG(L)+Abraxane versus oral NLG+Abraxane), $^{\&}$P<0.05 (PTX/PEG_{2k}-Fmoc-NLG(L) or PEG_{2k}-Fmoc-NLG(L)+Abraxane versus (PTX+NLG)/PEG_{5k}-$(Fmoc\text{-}Boc)_2$), (PTX/PEG_{2k}-Fmoc-NLG(L) versus PEG_{2k}-Fmoc-NLG(L)+ Abraxane), N=5. (d) Antitumour activity of PTX/PEG_{2k}-Fmoc-NLG(L) in a murine melanoma (B16) model. PTX dose was 10 mg/kg. **P<0.01 (all treatment groups versus control), $^{\#}$P<0.05 (PTX/PEG_{2k}-Fmoc-NLG(L) versus Taxol), N=5. All data represent means±s.e.m.

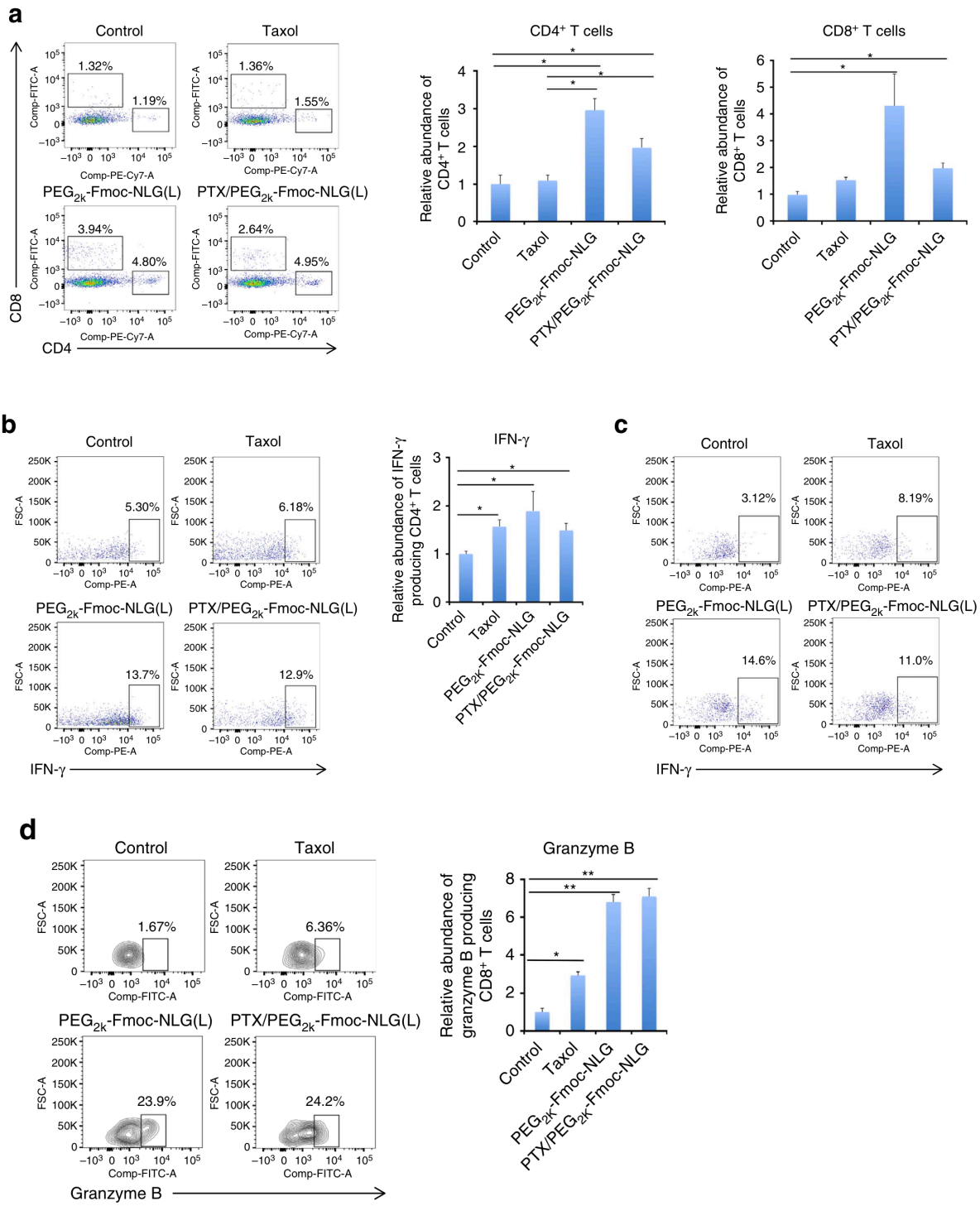
a
Control
Taxol
1.32%
1.19%
1.36%
1.55%
PEG2k-Fmoc-NLG(L)
PTX/PEG2k-Fmoc-NLG(L)
3.94%
4.80%
2.64%
4.95%
Comp-FITC-A
Comp-PE-Cy7-A
CD8
CD4
CD4+ T cells
CD8+ T cells
Relative abundance of CD4+ T cells
Relative abundance of CD8+ T cells
Control
Taxol
PEG2k-Fmoc-NLG
PTX/PEG2k-Fmoc-NLG
b
5.30%
6.18%
13.7%
12.9%
FSC-A
Comp-PE-A
IFN-γ
Relative abundance of IFN-γ producing CD4+ T cells
c
3.12%
8.19%
14.6%
11.0%
d
1.67%
6.36%
23.9%
24.2%
Granzyme B
Relative abundance of granzyme B producing CD8+ T cells

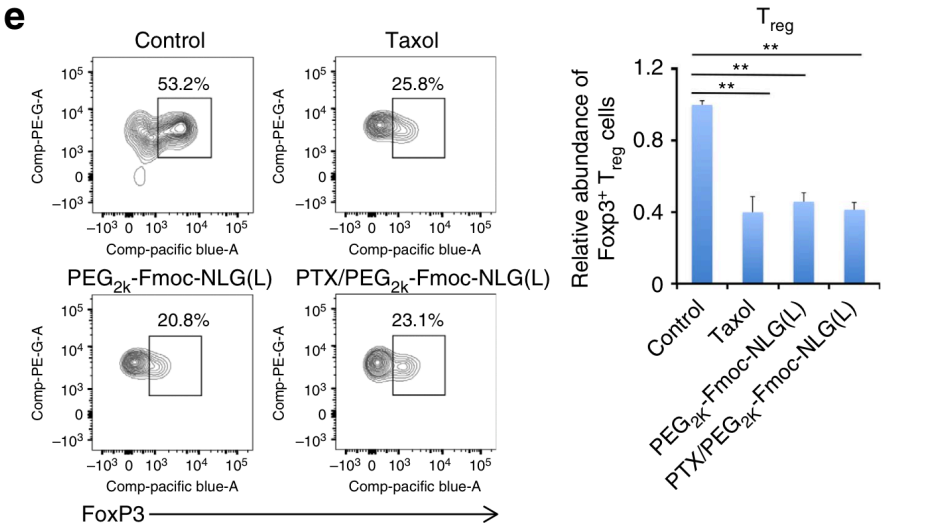
e
Control
Taxol
53.2%
25.8%
PEG2k-Fmoc-NLG(L)
PTX/PEG2k-Fmoc-NLG(L)
20.8%
23.1%
Comp-PE-G-A
Comp-pacific blue-A
FoxP3
Treg
Relative abundance of Foxp3+ Treg cells
Control
Taxol
PEG2k-Fmoc-NLG(L)
PTX/PEG2k-Fmoc-NLG(L)

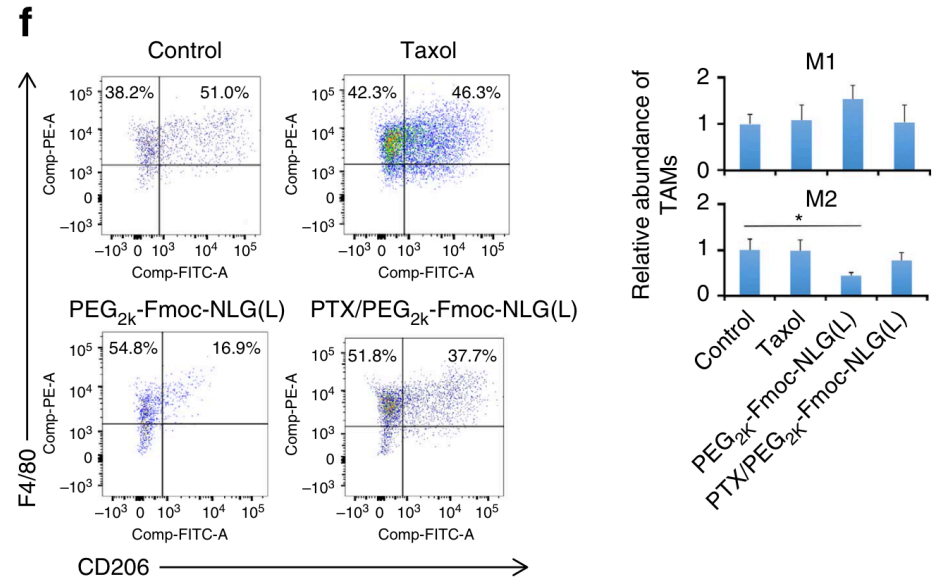
f
Control
Taxol
38.2%
51.0%
42.3%
46.3%
PEG2k-Fmoc-NLG(L)
PTX/PEG2k-Fmoc-NLG(L)
54.8%
16.9%
51.8%
37.7%
Comp-PE-A
Comp-FITC-A
F4/80
CD206
M1
M2
Relative abundance of TAMs
Control
Taxol
PEG2k-Fmoc-NLG(L)
PTX/PEG2k-Fmoc-NLG(L)

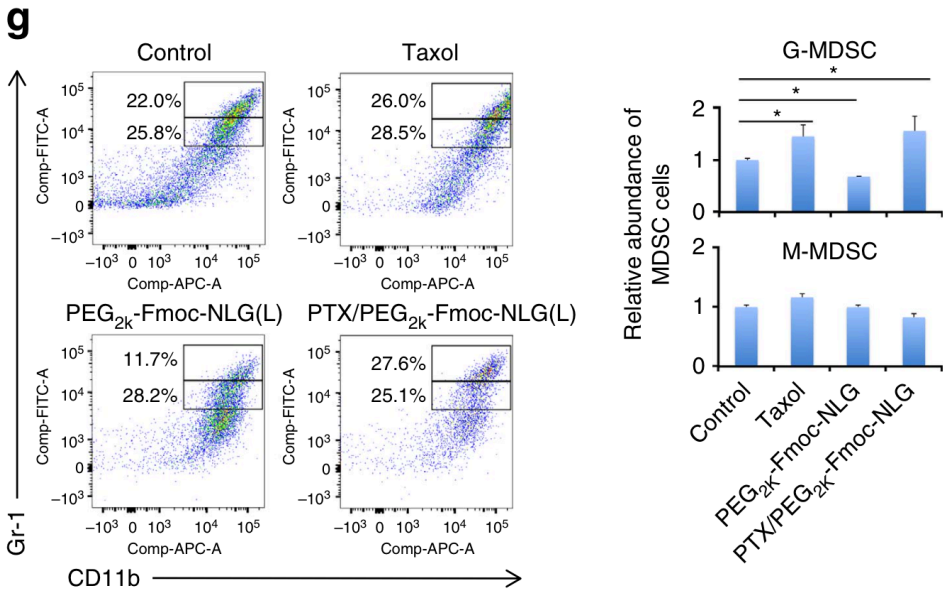
g
Control
Taxol
22.0%
25.8%
26.0%
28.5%
PEG2k-Fmoc-NLG(L)
PTX/PEG2k-Fmoc-NLG(L)
11.7%
28.2%
27.6%
25.1%
Comp-FITC-A
Comp-APC-A
Gr-1
CD11b
G-MDSC
M-MDSC
Relative abundance of MDSC cells
Control
Taxol
PEG2k-Fmoc-NLG
PTX/PEG2k-Fmoc-NLG

Figure 22. Flow cytometry analysis of immune cell subsets in tumour tissues.
(a–d) T-cell infiltration in mouse tumours treated with Taxol, PEG_{2k}-Fmoc-NLG(L) or PTX/PEG_{2k}-Fmoc-NLG(L) at a PTX dosage of 10mg/kg. The relative abundance of CD4,CD8 (a),IFN-g positive intratumoural CD4 T cells (b), IFN-g positive intratumoural $CD8^+$ T cells (c), and granzyme B-positive $CD8^+$ T cells (d) in tumour tissues were detected by flow cytometry. (e) Flow cytometry gating and histogram analysis of $FoxP3^+$T regulatory cells in mouse tumours. (f) Tumour-associated macrophages (TAMs) in mouse tumours. The percentages of TAM populations with specific macrophage markers (M1-type ($CD11b^+$/$F4/80^+$ /CD206-) and M2-type ($CD11b^+$/$F4/80^+$/$CD206^+$)) in tumour tissues were detected by flow cytometry. (g) Flow cytometry gating and histograms analysis of $CD11b^+$/$Gr\text{-}1^+$ MDSC cells in mouse tumours. Double positive cells contain two populations, including $Gr\text{-}1^{high}CD11b^+$granulocytic (G-MDSC) and $Gr\text{-}1^{int}CD11b^+$ monocytic (M-MDSC) MDSC subsets. The bars represent means±s.e.m. (*P<0.05, **P<0.01, N=3).

4.4.4 *In Vivo* Antitumor Activity of PTX-loaded Micelles

In vivo antitumour activity of PTX-loaded micelles. Figure 21a and Supplementary Fig. 10a show the *in vivo* antitumour activity of PEG_{2k}-Fmoc-NLG(L), Taxol, PTX/PEG_{2k}-Fmoc-NLG(S) and PTX/PEG_{2k}-Fmoc-NLG(L) at a PTX dosage of 10 mg kg 1. Taxol showed a modest effect in inhibiting the growth of 4T1.2 tumour, which was comparable to that of PEG_{2k}-Fmoc-NLG(L) alone. However, both PTX/PEG_{2k}-Fmoc-NLG(S) and PTX/PEG_{2k}-Fmoc-NLG(L) were more effective than Taxol or PEG_{2k}-Fmoc-NLG(L) in inhibiting the tumour growth. It is also apparent that PTX/PEG_{2k}-Fmoc-NLG(L) was more effective than PTX/PEG_{2k}-Fmoc-NLG(S), suggesting a role of released NLG919 in the overall antitumour activity of PTX/PEG_{2k}-Fmoc-NLG(L). The antitumour activity of the three PTX formulations follows the order of PTX/PEG_{2k}-Fmoc-NLG(L)>PTX/PEG_{2k}-Fmoc-NLG(S)>Taxol>PEG_{2k}-Fmoc-NLG(L).

The effective inhibition of tumour growth by PTX/PEG_{2k}-Fmoc-NLG(L) was associated with a significant survival benefit. The median survival time of mice in

PTX/PEG_{2k}-Fmoc-NLG(L) group is significantly longer compared with the mice treated with Taxol ($P<0.01$) or PEG_{2k}-Fmoc-NLG(L) ($P<0.01$).

Figure 21b show the antitumour activity of PTX/PEG_{2k}-Fmoc-NLG(L) at various doses of PTX. Tumour growth was well controlled at all dose groups at early time points. After the last treatment at day 13, the tumour growth was almost stalled until day 22 for the groups of 10 and 20 mg PTX per kg. After that, there was a rebound in tumour growth, particularly in the low-dose group.

Figure 21c and Supplementary Fig. 10c show that PTX/PEG_{2k}-Fmoc-NLG(L) was also more effective than a combination therapy that involves oral delivery of NLG together with i.v. administration of Abraxane. In addition, PTX/PEG_{2k}-Fmoc-NLG(L) was more active than a combination of i.v. Abraxane with i.v. PEG_{2k}-Fmoc-NLG(L). Furthermore, PTX/PEG_{2k}-Fmoc-NLG(L) was more active than an i.v. formulation of PEG_{5k}-$(Fmoc\text{-}Boc)_2$ that was co-loaded with PTX and NLG. Improved antitumour activity of PTX/PEG_{2k}-Fmoc-NLG(L) was also demonstrated in an aggressive B16 murine melanoma model (Fig. 21d).

All of the treatments were well tolerated by the mice and there were no abnormal physical signs in all treated mice. In addition, there were no obvious differences among all of the groups in body weights in all of the different therapy studies.

To delineate a role of immune response in PTX/PEG_{2k}-Fmoc-NLG(L)-mediated antitumour activity, the immune cell populations in the tumour tissues with various treatments were analysed by flow cytometry one day following five times of treatments.

Figure 22a shows infiltration of more $CD4^+$ T cells in the tumours treated with PTX/PEG_{2k}-Fmoc-NLG(L) compared with control or Taxol groups ($P<0.05$). There were also more $CD8^+$ T cells in the tumours treated with PTX/PEG_{2k}-Fmoc-NLG(L) compared with control group. It was also noted that the numbers of both $CD4^+$ and $CD8^+$ T cells in Taxol-treated tumours were lower than those in the tumours treated with carrier alone (Fig. 22a). Delivery of PTX via PEG_{2k}-Fmoc-NLG(L) was associated with a similar reduction in the numbers of $CD4^+$ and $CD8^+$ T cells (Fig. 22a).

Figure 22b,c shows that the numbers of IFN-g-positive $CD4^+$ or $CD8^+$ T cells were significantly increased in the tumours treated with Taxol, PEG_{2k}-Fmoc-NLG(L) or PTX/PEG_{2k}-Fmoc-NLG(L). The magnitude of increase was similar among all of the treatment groups.

The numbers of granzyme B-positive $CD8^+$ T cells were also significantly increased in all of the treatment groups (Fig. 22d). However, there were significantly more granzyme B-positive $CD8^+$ T cells in the tumours treated with PEG_{2k}-Fmoc-NLG(L) or PTX/PEG_{2k}-Fmoc-NLG(L) compared with Taxol-treated tumours (Fig. 22d). There were no differences between PEG_{2k}-Fmoc-NLG(L) and PTX/PEG_{2k}-Fmoc-NLG(L) groups in the numbers of granzyme B-positive $CD8^+$ T cells (Fig. 22d).

T_{reg} cells were significantly decreased in all treatment groups compared with control group ($P<0.01$) and there were no significant differences among these treatment groups ($P<0.05$) (Fig. 22e).

Figure 22f shows that the numbers of M2 ($CD11b^+F4/80^+CD206^+$) tumour-associated

macrophages were significantly reduced in the tumours treated with PEG_{2k}-Fmoc-NLG(L). Meanwhile, the numbers of M1 ($CD11b^{+}F4/80^{+}CD206^{-}$) tumour-associated macrophages were slightly increased. There were no significant changes in the numbers of either M1 or M2 macrophages in the tumours treated with Taxol or PTX/PEG_{2k}-Fmoc-NLG(L).

Figure 22g shows that the numbers of granulocytic myeloid-derived suppressor cells (G-MDSC) were significantly decreased in the tumours treated with PEG_{2k}-Fmoc-NLG(L) alone. This is consistent with the previous reports that inhibition of IDO leads to decreased MDSC in the tumours. Surprisingly, G-MDSC were significantly increased in the tumours treated with either PTX/PEG_{2k}-Fmoc-NLG(L) or Taxol. There were no significant differences among all of the groups in the numbers of monocytic MDSC (M-MDSC) in the tumours (Fig. 22g).

Overall, the above data suggest that the microenvironment in the tumours treated with PTX/PEG_{2k}-Fmoc-NLG(L) was more immune-active than that in Taxol-treated tumours. This is consistent with the data that the *in vivo* IDO activity was more effectively inhibited in mice treated with PTX/PEG_{2k}-Fmoc-NLG(L) compared with Taxol-treated mice.

4.5 DISCUSSION

PEG-NLG919-mediated co-delivery of PTX. Different from most drug carriers that are ‘inert’, PEG-Fmoc-NLG is a prodrug that exhibits immunostimulatory activity. Despite its reduced EC50 compared with free NLG with respect to the potency in inhibiting IDO in cultured cells, PEG-Fmoc-NLG was significantly more effective than NLG that was

formulated in a similar 'inert' nanocarrier without a NLG motif (PEG_{5k}-(Fmoc-Boc)$_2$) (Fig. 18j). In addition, i.v. PEG- Fmoc-NLG was more active than NLG delivered orally (Fig. 18j). This is likely due to the effective delivery of PEG-Fmoc-NLG to the tumours (Fig. 20b,c). The slow release of NLG from PEG-Fmoc-NLG in tumour tissues (Fig. 20b) may also play a role.

A major advantage of our approach is simultaneous delivery to the tumours of two agents of different mechanisms of action. In addition, this system could provide a programmable release of various drug components via both chemical conjugation and physical encapsulation. PTX and NLG showed different temporal release kinetics upon co-delivery to tumours. PTX has a much faster rate of release compared with that of NLG (Fig. 19c). PEG-Fmoc-NLG also has a longer retention time in the tumours (Fig. 20b), likely due to its macromolecule nature. Delivery of PTX via PEG-Fmoc-NLG was more effective in inhibiting the tumour growth than co-delivery of PTX and NLG via a similar 'inert' nanocarrier without a NLG motif (Fig. 21c). In addition, PTX/PEG_{2k}-Fmoc-NLG(L) was more effective than oral delivery of NLG together with i.v. administration of Abraxane (Fig. 21c). We hypothesize that the relatively rapid release of PTX will lead to the first round of antitumour response that will be further potentiated by the immune response that follows. The immune response could result from enhanced antigen presentation following PTX-mediated killing of tumour cells and/or direct effect of PTX on immune cells. Meanwhile, the slow release of active NLG919 from the prodrug helps sustaining or enhancing the magnitude of immune responses by reversing IDO-mediated immune suppression. As a result, the combined therapy has

produced a substantial inhibition of tumour growth. In fact, PTX/PEG_{2k}-Fmoc-NLG(L) outperformed most reported PTX formulations including PTX formulated in our non-immunostimulatory dual-functional carriers. It is possible that the carrier-mediated antitumour activity can be further improved via incorporation of a tumour microenvironment-responsive linkage to facilitate the NLG release. Another advantage of our strategy lies in the simplicity with respect to both the synthesis of dual-function carrier and the combination therapy protocol, which is expected to facilitate a rapid translation into clinic. In addition, our nanocarrier is versatile in formulating various anticancer agents of diverse structures (Table 4). Immunological analysis indicates that, compared with those tumours from the no-treatment group, tumour tissues isolated from mice treated with PEG_{2k}-Fmoc-NLG(L) are more immunoactive with more functional $CD4^+$ and $CD8^+$ T cells, decreased Treg and MDSC, and increased M1/M2 ratios. In addition, we showed a more immunoactive microenvironment within tumours treated with either Taxol or PTX/PEG_{2K}-Fmoc-NLG(L) compared with the no-treatment group in most of the parameters examined, indicating immunogenic function of these compounds. However, tumour tissues from Taxol or PTX/PEG_{2k}-Fmoc-NLG(L) groups had lower percentages of T cells including Treg, $CD4^+$ and $CD8^+$ T cells, but higher percentage of MDSC than the group treated with PEG2k-Fmoc-NLG(L) alone. The reduction in the percentage of total intratumoural T cells in the PTX/PEG_{2k}-Fmoc-NLG(L) group relative to the PEG_{2k}-Fmoc-NLG(L) group could be due to the cytotoxic effect of PTX treatment on these immune cells. Alternatively, it can also be attributed to the direct effect of PTX on tumour cells, leading to reduced production of

inflammatory factors. Nonetheless, when compared with PEG_{2k}-Fmoc-NLG(L) treatment, PTX/PEG_{2k}-Fmoc-NLG(L) does not significantly affect the percentage of T cells that produce IFN-g or Granzyme B, suggesting the antitumour effector function of intratumoural T cells is not affected by PTX. In addition, the cytotoxic effect of PTX might lead to reduced tumour burden, which can help enhance the overall efficacy of immunochemotherapy. Moreover, tumours treated with PTX/PEG_{2k}-Fmoc-NLG(L) had more granzyme B-producing $CD8^+$ T cells than the tumours treated with Taxol, suggesting IDO inhibition can still enhance antitumour T-cell immune responses in spite of repeated chemotherapy. Overall, our *in vivo* results show that the tumoricidal activity of PTX and the immune-enhancing function of NLG synergistically produced much more profound antitumour efficacy.

It should be noted that our strategy does not preclude the development of an oral NLG-based treatment. The purpose of our comparative study (Figs 18j and 21c) is to show the advantages of our strategy over other approaches at similar doses with respect to both the simplicity and potency as far as a combination therapy with a chemotherapeutic agent is concerned. Eventually, a therapeutic regimen that involves systemic immunochemotherapy followed by oral NLG-based sustained treatment can be developed to maximize the treatment outcome.

In summary, we have developed a simple and rational co-delivery approach that is effective in improving cancer immunochemotherapy. Although most of the works in this study are focused on PTX, it can be readily extended to immunochemotherapy with other anticancer agents such as DOX. Finally, such strategy can be employed in novel cancer

therapy combining chemotherapy drugs and other immune modulating agents such as small molecule inhibitors of PD-1.

5.0 PROGRAMMABLE CO-DELIVERY OF THE IMMUNE CHECKPOINT INHIBITOR NLG919 AND CHEMOTHERAPEUTIC DOXORUBICIN VIA A REDOX-RESPONSIVE IMMUNOSTIMULATORY POLYMERIC PRODRUG CARRIER

5.1 ABSTRACT

In order to achieve synergistic therapeutic efficacy and prevent cancer relapse, combination of chemotherapy and immunotherapy has been developed as a new modality for tumor treatment. In this work, we designed a redox-responsive immunostimulatory polymeric prodrug carrier PSSN10 for programmable co-delivery of immune checkpoint inhibitor NLG919 (NLG) and chemotherapeutics doxorubicin (DOX). NLG-containing PSSN10 prodrug polymers were self-assembled into nano-sized micelles which served as a carrier to load DOX. The particle size, morphology as well as drug loading capacity and *in vitro* release kinetics were evaluated. The pharmacokinetics and tissue biodistribution of DOX-loaded micelles were examined in murine breast cancer models. The synergistic antitumor activity of DOX formulated in the immunostimulatory nanocarrier and the underlying mechanism were investigated. DOX could be formulated into PSSN10 carrier to form DOX/PSSN10 micelles with size of ~170 nm. DOX/PSSN10 showed more accumulation of DOX and NLG in the tumor tissues compared with those in other organs. PSSN10 was effective in enhancing T-cell immune responses and inhibiting tumor growth *in vivo*. More importantly, DOX/PSSN10 exhibited significantly higher anti-tumor activity compared to that of DOX and PSSN10. Systemic delivery of DOX via PSSN10 nanocarrier results in synergistic anti-tumor activity.

5.2 INTRODUCTION

Chemotherapy is one of the most widely used treatments for cancers. Although chemotherapeutic agents kill tumor cells mainly through cytostatic and/or cytotoxic effects, a large body of evidence suggests that chemotherapy-elicited immune responses also contribute to the overall antitumor activity [159]. Nevertheless, various negative regulatory mechanisms such as inhibitory immune checkpoints are deployed by tumors to evade immune surveillance and suppress immune responses, which limits the overall effect of chemotherapy [160, 161]. For example, cytotoxic T-lymphocyte-associated protein 4 (CTLA-4) is an immune checkpoint receptor expressed by activated T cells and transmits an inhibitory signal to T cells [162]. Tumors exploit the CTLA-4 signaling to inhibit initiation of an immune response, resulting in decreased T-cell activation and proliferation [163]; Like CTLA-4, programmed cell death protein 1 (PD-1) receptor is also expressed on the surface of activated T cells. Its ligand PD-L1, overexpressed by tumor cells, can interact with PD-1, leading to inhibition of the cytotoxic T cells. Tumor cells utilize the PD-L1/PD-1 pathway to evade detection and inhibit the immune response [164, 165, 166]. To enhance anti-tumor immunity and prevent cancer relapse, combination of checkpoint blockade immunotherapy and chemotherapy has been developed as an attracting modality for cancer treatment [167, 168, 169].

Indoleamine 2, 3-dioxygenase-1 (IDO1) is another immunosuppressive protein that helps tumors evade the immune system and facilitates tumor growth and metastasis [170, 171, 172]. IDO1 is overexpressed by most tumors, which mediates the degradation of essential amino acid tryptophan (Trp) into kynurenine (Kyn) and other metabolites, resulting in suppression

of effector T cells, and promotion of the regulatory T cells proliferation [173]. Thus, blocking the function of IDO1 becomes a promising strategy to reactivate the immune response against cancer [174].

NLG919 is a nontoxic IDO1-selective inhibitor, which blocks IDO-mediated immune suppressive pathways and leads to tumor regression in preclinical models [175]. It has been shown that inhibition of IDO pathway can act synergistically with chemotherapy [176, 177]. However, the success of an immunochemotherapy that combines NLG919 with a chemotherapeutic drug is limited by the lack of a strategy to effectively co-deliver the two therapeutics to the tumors. Co-loading of the two agents into a nanocarrier may meet with limited success due to their differences in physiochemical properties. In addition, tempo-spatial control of the release of the different drugs is difficult as all of the loaded drugs are often released at the same time.

To solve these problems, our group previously developed PEG-NLG conjugate (PEG2k-Fmoc-NLG) as a prodrug carrier for co-delivery of NLG919 and chemotherapeutic drug paclitaxel (PTX) [178]. It was found that the immune-enhancing function of NLG and the tumor killing effect of PTX synergistically contributed to the increased anti-tumor efficacy. In this work, we further improved the NLG-based prodrug system by increasing the units of NLG per prodrug molecule via reversible addition-fragmentation chain transfer (RAFT) polymerization technology. The new PSSN10 system consists of a POEG hydrophilic block and a PNLG hydrophobic block with a number of NLG919 motifs attached via redox-sensitive linkage (Fig. 1). PNLG hydrophobic block in the polymeric carrier not only

provides immunostimulatory property, but also facilitates the encapsulation of doxorubicin (DOX), a potent chemotherapeutic agent that induces immunogenic tumor cell death [179]. NLG919 and DOX are incorporated into this system through chemical conjugation and physical "loading", respectively, which allows the programmed release of DOX and NLG919 in the tumors. Besides, disulfide linkage was introduced between NLG919 and polymer backbone to facilitate the cleavage of NLG919 from the polymeric carrier at tumor sites. The effect of the PSSN10 polymer on IDO activity and T cell proliferation was tested. The efficiency of the nanocarrier in selective delivery of DOX to tumors was examined. The synergistic antitumor activity of DOX formulated in the immunostimulatory nanocarrier and the underlying mechanism were also investigated.

5.3 EXPERIMENTAL PROCEDURES

5.3.1 Materials

DOX·HCl were purchased from LC Laboratories. 4-nitrophenyl chloroformate was purchased from Acros. Dulbecco's Modified Eagle's Medium (DMEM), trypsin-EDTA solution, 3-(4, 5-dimethylthiazol-2-yl)-2,5-diphenyl tetrazolium bromide (MTT), Triton X-100 and Hoechst 33342 were purchased from Sigma-Aldrich. Penicillin-streptomycin solution and fetal bovine serum (FBS) were purchased from Invitrogen. 2-Azobis(isobutyronitrile) (AIBN, Sigma-Aldrich) was purified by recrystallization in anhydrous ethanol [180]. *N*-methacryloyl-*N*′-(*t*-butyoxycarbonyl)cystamine (MBC) [181] and POEG macroCTA [182] were prepared according to the literatures. All other reagents were of

N, N-Diisopropylethylamine (DIPEA) were dissolved in 8 mL anhydrous dichloromethane (DCM), and stirred overnight at room temperature. The product (NLG-NO_2) was obtained by column chromatography purification.

5.3.2 Synthesis of POEG-*b*-PMBC Polymers

MBC monomer (144 mg，0.45 mmol), POEG macroCTA (175 mg，0.0194 mmol), AIBN (1 mg, 0.0062 mmol) and 1 mL 1, 4-dioxane were added into a Schlenk tube, and deoxygenated by free-pump-thawing for three times. Then the Schlenk tube was immersed into an oil bath at 90°C. After 24 h, the mixture was precipitated in diethyl ether for 3 times to yield the POEG-*b*-PMBC polymers.

5.3.3 Synthesis of PSSN10 Polymers

POEG-*b*-PMBC polymers were deprotected in a mixture of TFA/DCM (1/1, v/v) at room temperature for 2 h, and then precipitated in cold diethyl ether for 3 times and dried in vacuum to give the Boc-deprotected polymer products. Then, the as-synthesized Boc-deprotected polymers (118 mg, 0.01 mmol) and NLG-NO_2 (179 mg, 0.4 mmol) were dissolved in 2 mL DMF with 200 μL DIPEA. After stirring at room temperature for 24 h, the reaction mixture was precipitated in diethyl ether for 3 times. The final products PSSN10 were obtained after vacuum drying.

5.3.4 Preparation of Blank and DOX-loaded Micelles

The blank and DOX-loaded PSSN10 micelles were prepared through a dialysis method. DOX·HCl was first dissolved in methanol at a concentration of 5 mg/mL containing triethylamine (3 equiv.) to remove HCl. PSSN10 polymer was dissolved in THF at a concentration of 50 mg/mL. Then, the DOX solution was mixed with the PSSN10 polymer solution at a DOX/polymer mass ratio of 1: 20, followed by the dropwise addition of 0.5 mL of PBS. After removing solvent under reduced pressure, the solution was dialyzed against PBS overnight (MWCO 3.5 KDa). Blank micelles were similarly prepared except that no DOX was added. For determination of DOX concentration, DOX-loaded micelles were dissolved in DMSO and detected by fluorescence spectroscopy with excitation at 490 nm. Drug loading capacity (DLC) and drug loading efficiency (DLE) were calculated according to the following formula:

DLC (wt%) = (weight of loaded drug/weight of input polymer +drug) × 100%

DLE (%) = (weight of loaded drug/weight of drug in feed) × 100%

5.3.5 Critical Micelle Concentration (CMC) Measurement

The CMC value of PSSN10 micelles was measured using nile red as a fluorescence probe [183]. Briefly, 10 μL of a 0.05 mg/mL stock solution of nile red in DCM was added to each tube. After the solvent was completely evaporated, PSSN10 solution in PBS ranging from 1.0×10^{-4} to 5×10^{-1} mg/mL was added. The mixtures were kept overnight and then evaluated by fluorescence spectrometry.

5.3.6 Polymers and Micelles Characterization

^{1}H NMR spectrum was performed on a Varian-400 FT-NMR spectrometer (400.0 MHz) with $CDCl_3$ and DMSO-d_6 as the solvent. Molecular weight (M_n and M_w) and distribution (M_w/M_n) of the synthesized polymers were measured by gel permeation chromatography (GPC) with a Waters 2414 refractive index detector. A series of polystyrene standards with narrow molecular weight distribution were applied to calibrate the GPC elution traces. Tetrahydrofuran (THF) was used as the eluent at a flow rate of 1.0 mL/min at 35°C and a series of commercial polystyrene standards were used for the calibration. The size distribution and morphology of blank and drug-loaded micelles were examined by dynamic light scattering (DLS, Malvern Zeta Nanosizer) and transmission electron microscopy (TEM, negative staining method), respectively.

5.3.7 *In Vitro* DOX Release

The *in vitro* DOX release profiles of DOX-loaded PSSN10 micelles were examined under different GSH concentrations (0, 10 μM, 10 mM). DOX-loaded micelles with a DOX concentration of 0.25 mg/mL were transferred into a dialysis bag (MWCO = 3.5kDa, Spectrum Laboratories), and immersed into a tank with 50 mL DPBS (PH =7.4) with different GSH concentrations (0, 10 μM, 10 mM) with gentle shaking at 37 °C. At specific time intervals, 4 mL PBS solution outside of the dialysis bag was withdrawn and displaced with 4 mL fresh solution. The amount of DOX released was determined by fluorescence spectrometry as described above.

5.3.8 Cell Culture

Mouse metastatic breast cancer cells (4T1.2), human prostatic carcinoma cells (PC3) and human cervical cancer cells (HeLa) were cultured in DMEM culture medium, containing 10% (v/v) fetal bovine serum and 100 IU/mL penicillin and 100 μg/mL streptomycin at 37 °C in a humidified 5% CO_2 atmosphere.

5.3.9 *In Vitro* IDO Inhibition

The IDO inhibitory activity of PSSN10 was tested by an IDO assay [184]. Briefly, HeLa cells were plated in a 96-well plate (5×10^3 cells/well) and allowed to grow overnight. Recombinant human IFN-γ (50 ng/mL) was then added to each well. At the same time, various concentrations of PSSN10 or free NLG919 (NLG919 concentrations: 50 nM ~ 20 μM) were added to the cells. After incubation for 48 h, 150 μL of the supernatants was transferred to a new 96-well plate. Then 75 μL of 30% trichloroacetic acid was added and the mixture was incubated at 50 °C for 30 min to hydrolyze N-formylkynurenine to kynurenine. For colorimetric assay, supernatants were transferred to a new 96-well plate and incubated with equal volume of Ehrlich reagent (2% p-dimethylamino-benzaldehyde in glacial acetic acid, w/v) for 10 min at room temperature. Reaction product was measured at 490 nm by a plate reader. For HPLC-MS detection (Wastes Alliance 2695 Separation Module combined with Waters Micromass Quattro Micro TM API MS detector), the plate was centrifuged for 10 min at 2,500 r.p.m. and 100 μL of the supernatant per well was collected for tryptophan and kynurenine assay.

5.3.10 T-cell Proliferation Study

A lymphocyte-Panc02 cell co-culture experiment was performed to determine whether PSSN10 can reverse IDO1-mediated inhibition of T-cell proliferation [185]. Murine Panc02 cells were stimulated by IFN-γ (50 ng/mL) to induce IDO expression and then irradiated (6,000 rad) before coculture. Splenocyte suspensions were generated from BALB/c mice by passing through the nylon wool columns after lysis of red blood cells. IFN-γ stimulated Panc02 cells (1×10^5 cells/well) were mixed with splenocytes (5×10^5 cells/well, pre-stained with 5-(and 6)-carboxyfluorescein diacetate (CFSE)) in a 96-well plate. Various concentrations of PSSN10 and NLG919 were added to the cells. Then 100 ng/mL anti-CD3 (clone 2C11) and 10 ng/mL mouse recombinant IL-2 were added to the cocultures. The proliferation of $CD8^+$ and $CD4^+$T cells was measured by flow cytometric analysis after 3 days of coculture.

5.3.11 *In Vitro* Cytotoxicity Assay

4T1.2 and PC3 cancer cell lines were used for *in vitro* cytotoxicity study. Cells were seeded in 96-well plates at a density of 1.5×10^3 (4T1.2) and 3×10^3 (PC3) cells/well. After incubation for 24 h, cells were treated with free DOX, PSSN10 and DOX/PSSN10 micelles in a gradient concentration. After incubation for 72 h, the cell viability was measured via MTT assay as reported before [186]. Untreated cells were included as a control.

5.3.12 Cell Uptake and Intracellular Trafficking

4T1.2 cells were cultured in glass bottom dishes (1×10^5 cells/dish) for 24 h and then treated

with DOX/PSSN10 micelles and free DOX (DOX concentration: 20 μg/mL) in FBS-free culture medium. After 4 h, the cells were stained with Hoechst 33342 for 20 min and washed with PBS for 3 times. The fluorescence images were obtained using a confocal laser scanning microscope (CLSM, FluoView 1000, Olympus, Japan).

5.3.13 Animals

Female BALB/c mice (6~8 weeks) and C57BL/6 mice (4~6 weeks) were purchased from Charles River (Davis, CA). All animals were housed under pathogen-free conditions according to AAALAC guidelines. All animal-related experiments were performed in full compliance with institutional guidelines and approved by the Animal Use and Care Administrative Advisory Committee at the University of Pittsburgh.

5.3.14 Quantification of Trp/Kyn Ratio in Plasma and Tumor Tissues

The kynurenine to tryptophan ratios in plasma or tumors in 4T1.2 tumor-bearing mice were examined by HPLC-MS/MS as an indication of IDO enzyme activity [187]. BALB/c mice bearing 4T1.2 tumors of ~50mm^3 were treated with DPBS, DOX, DOXIL, PSSN10, DOX/PSSN10 at a DOX dosage of 5 mg/kg via tail vein once every 3 days for 3 times. One day after the last treatment, the plasma and tumor samples were harvested. Plasma samples were mixed with methanol (plasma: methanol, 1:2.5, v/v) and centrifuged at 14,500 r.p.m. for 15 min. Supernatants were collected for HPLC-MS quantification of kynurenine and tryptophan.

Tumor samples were homogenized in water and the homogenates were mixed with acetonitrile (1:1, v/v), centrifuged and supernatants were transferred to clean tubes. Equal volumes of methanol were added to precipitate proteins and supernatants were collected for HPLC-MS measurement.

5.3.15 Plasma Pharmacokinetics and Tissue Distribution

Female BALB/c mice (5 mice/group) were *i.v.* administered with DOX·HCl and DOX-loaded PSSN10 micelles at a DOX dose of 5 mg/kg. Blood samples were collected at different time points (3 min, 10 min, 30 min, 1 h, 2 h, 4 h, 8 h and 12 h) and centrifuged at 2,500 r.p.m. for 15 min. 350 μL acetonitrile was added to the plasma and centrifuged at 12,000 r.p.m. for 5 min. Then, the supernatants were collected and dried under airflow. DOX concentrations in the samples were analyzed by HPLC. The pharmacokinetic parameters were calculated based on a noncompartment model by Phoenix WinNonlin.

For tissue distribution study, DOX·HCl and DOX/PSSN10 micelles were *i.v.* injected into female BALB/c mice bearing 4T1.2 tumors at a DOX dose of 5 mg/kg. At 24 h post injection, mice were sacrificed and the major organs were excised. The tissues were weighted and homogenized with 2 mL solvent (acetonitrile: H_2O = 1:1, v/v). The samples were centrifuged at 3,500 r.p.m. for 10 min, and the supernatants were collected and dried under airflow. The residues were then dissolved in 200 mL solvent (methanol: H_2O = 1:1, v/v) and centrifuged at 14,500 r.p.m. for 10 min. DOX concentrations in the clear supernatants were detected by HPLC.

5.3.16 *In Vivo* Therapeutic Efficacy

Female BALB/c mice bearing 4T1.2 tumors were *i.v.* administered with saline, free DOX, blank PSSN10 micelles and DOX/PSSN10 mixed micelles (5 mg DOX/kg) once every two days for 3 times respectively. Tumor volumes were calculated according to the formula: $(L \times W^2)/2$, in which L is the longest and W is the shortest tumor diameter (mm), and presented as relative tumor volume (the tumor volume at a given time point divided by the tumor volume prior to first treatment). Besides, changes in body weights of all mice were monitored. At the completion of the experiment, tumor tissues were excised and fixed with 10% formaldehyde and embedded in paraffin. The sliced tissues at 5 μm were stained by hematoxylin and eosin (H&E) and observed by a Zeiss Axiostar plus Microscope (PA, USA). The Kaplan-Meier survival of the tumor-bearing mice (n = 8) was followed within 45 days. Mice were considered to be dead either when the mice died during treatment or when the tumor volume reached ~1000 mm^3.

5.3.17 Quantification of Tumor-infiltrating Lymphocytes

The immune cell populations in the tumors following various treatments were measured by flow cytometry[188]. One day after the last treatment, cell suspensions from the spleens or tumors were filtered and red blood cells were lysed. For extracellular staining, cells were co-incubated with combinations of antibodies (CD8, CD4, CD11b, Gr-1, CD45, F4/80 and CD206). For intracellular staining, cells were fixed immediately after cell surface staining following the manufacturer's description (eBioscience). Then the combinations of antibodies

(IFN-γ, FoxP3 and granzyme B) were added into cells in permeabilization buffer. For IFN-γ staining, cells were stimulated with PMA (5 ng/mL) and ionomycin (500 ng/mL) in presence of 10 mg/mL BFA for 4 h followed by extracellular and intracellular staining. The data were analyzed using the FlowJo software (Tree Star Inc.).

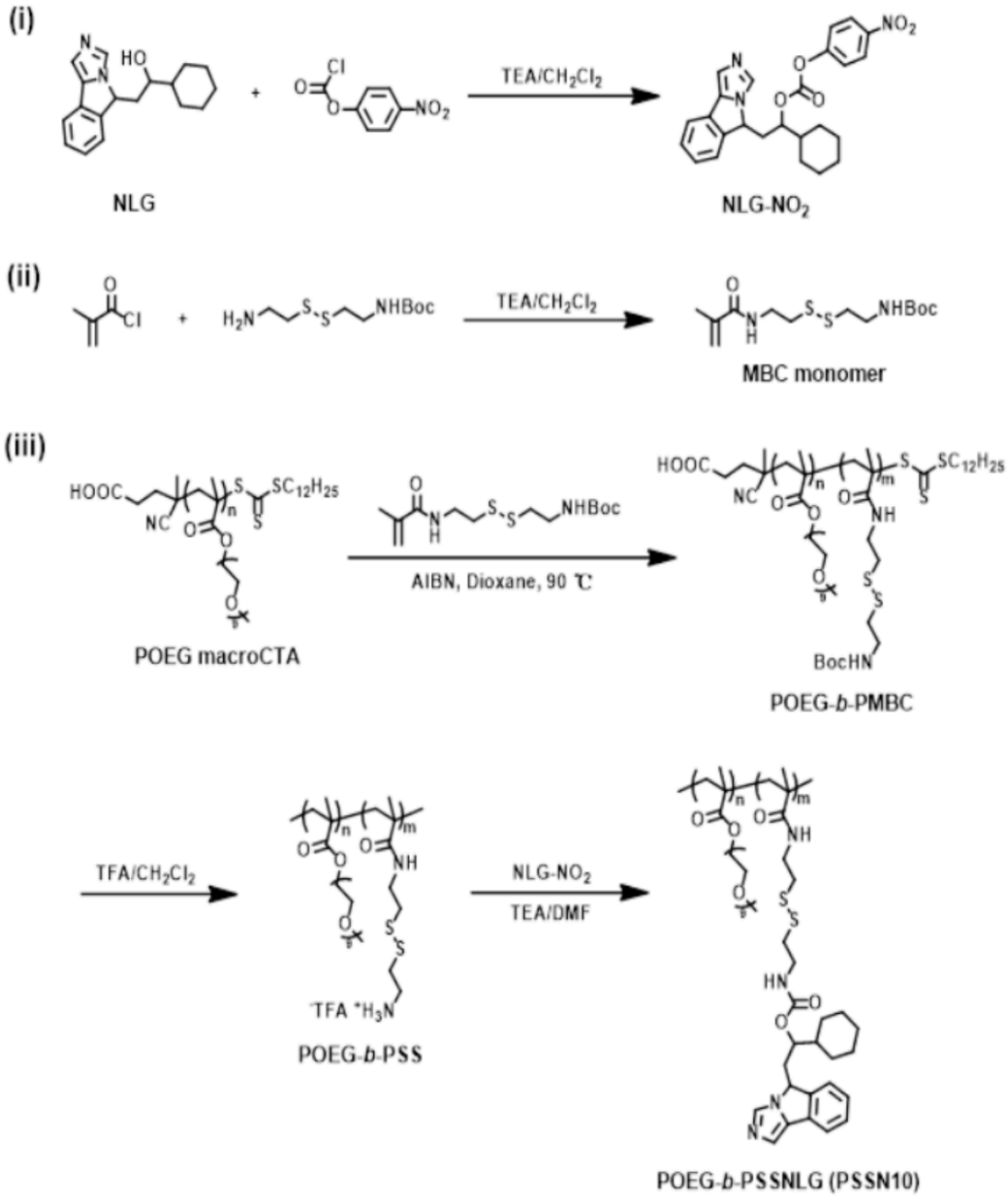

Figure 23. Synthesis scheme of PSSN10 polymers via RAFT polymerization and post-modification

5.4 RESULTS

5.4.1 Synthesis and Characterization of the PSSN10 Polymer

Figure 23 shows the synthesis scheme of PSSN10 polymer. (i) the hydroxyl group of NLG919 was activated with 4-nitrophenyl chloroformate to give NLG-NO_2. (ii) The MBC monomer was synthesized according to the literature[181]. (iii) POEG (M_n = 9 KDa) was synthesized by RAFT polymerization as reported previously[182] and further served as Macro-RAFT agent to initiate the polymerization of the MBC monomer. POEG-*b*-PMBC polymer was obtained after precipitation, followed by the deprotection of the Boc-groups in TFA/DCM solution to yield POEG-*b*-PSS polymer. The POEG-*b*-PSSNLG polymer was finally synthesized by the chemical coupling of NLG-NO_2 to the Boc-deprotected POEG-*b*-PSS polymers. The ^{1}H NMR spectrum of POEG-*b*-PSSNLG polymer was shown in Figure 24. The typical peaks at 7.72-7.17, 5.59, 2.04-0.75 ppm appeared in the ^{1}H NMR spectrum of POEG-*b*-PSSNLG, which corresponded to the protons of NLG group. By comparing the intensities of I_c (at 5.59 ppm) and I_a (at 3.39 ppm), the NLG units conjugated on each copolymer were determined to be 10, which was translated into a DLC of NLG as high as 28% (wt.). The POEG-*b*-PSSNLG prodrug polymer was denoted as PSSN10 in the following study.

5.4.2 Preparation and Characterization of Blank and DOX-loaded Micelles

PSSN10 prodrug micelles were prepared using a dialysis method. Figure 25 shows that the critical micelle concentration (CMC) of PSSN10 was 15.5 mg/L. The relatively low CMC

shall provide a good stability of PSSN10 micelles upon dilution in the blood. DLS measurements showed that PSSN10 prodrug micelles had a unimodal size distribution with an average diameter of 134.7 nm (Fig. 26b). After loading of DOX, the particle size was increased to 175.1 nm (Fig. 26c). TEM images confirmed the spherical morphology for both PSSN10 micelles and DOX/PSSN10 mixed micelles. DOX was effectively loaded into PSSN10 micelles at a DLC of 4.0% with a loading efficiency of 84.0%.

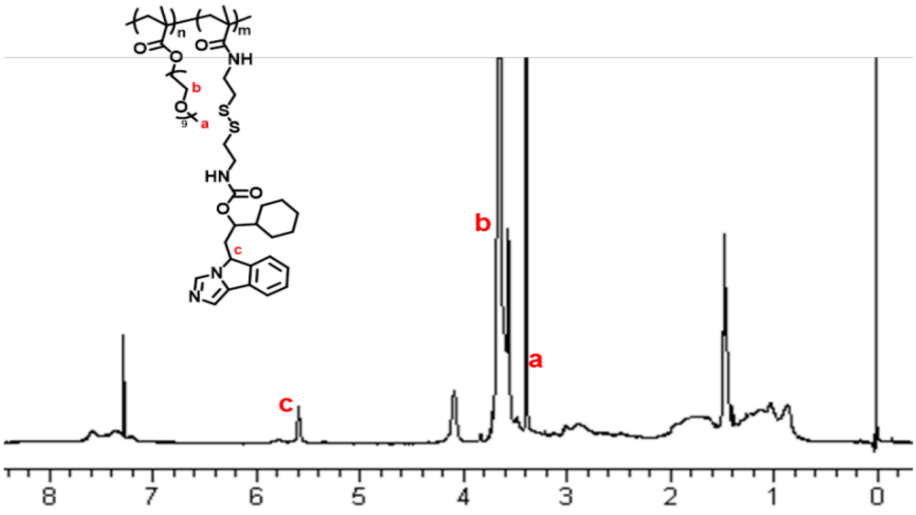

Figure 24. 1 H NMR spectrum of PSSN10 polymer in $CDCl_3$.

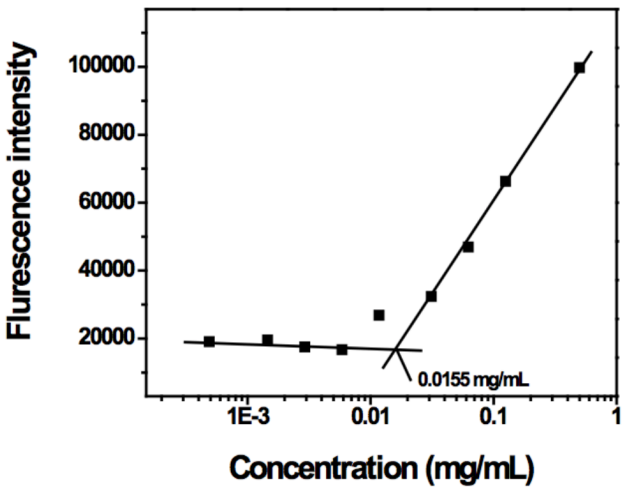

Figure 25. Plots of fluorescence intensity ratio at 650 nm versus concentrations of PSSN10 micelles

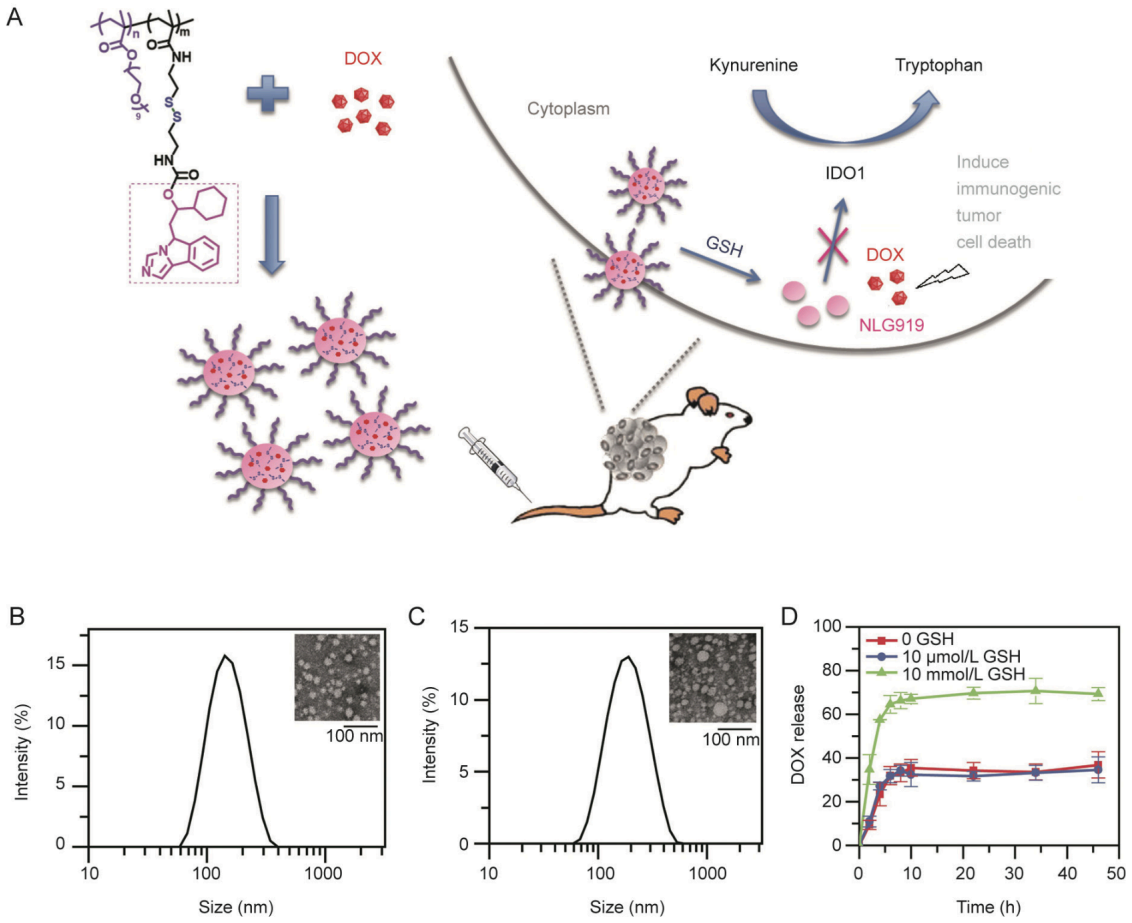

Figure 26. Schematic illustration of redox-responsive immunostimulatory PSSN10 polymeric prodrug carrier for co-delivery of NLG919 and DOX.
(a) Schematic illustration and (b) The particle size distribution of PSSN10 micelle measured by DLS (Inset: TEM image of PSSN10 micelle using negative staining. Scale bar is 100 nm.) (c) The particle size distribution of DOX/PSSN10 mixed micelle measured by DLS (Inset: TEM image of DOX/PSSN10 mixed micelle using negative staining. Scale bar is 100 nm.) (d) The *in vitro* release profiles of DOX from the DOX/PSSN10 mixed micelle in PBS with different GSH concentrations (0, 10 μM, 10 mM) at 37 °C.

The *in vitro* DOX release studies were carried out in PBS solution with different GSH concentrations (0, 10 μM, 10 mM). As shown in Fig. 26d, DOX cumulative release from DOX/PSSN10 mixed micelles was about 36 % after 24 h in the absence of GSH. No acceleration in DOX release was observed in the presence of 10 μM GSH, which mimics the slightly redox environment of extracellular compartment. However, in the presence of 10 mM

GSH, about 70% of DOX was released within 24 h, indicating that rapid release of drug could be achieved in the highly redox environment after intracellular uptake by tumor cells.

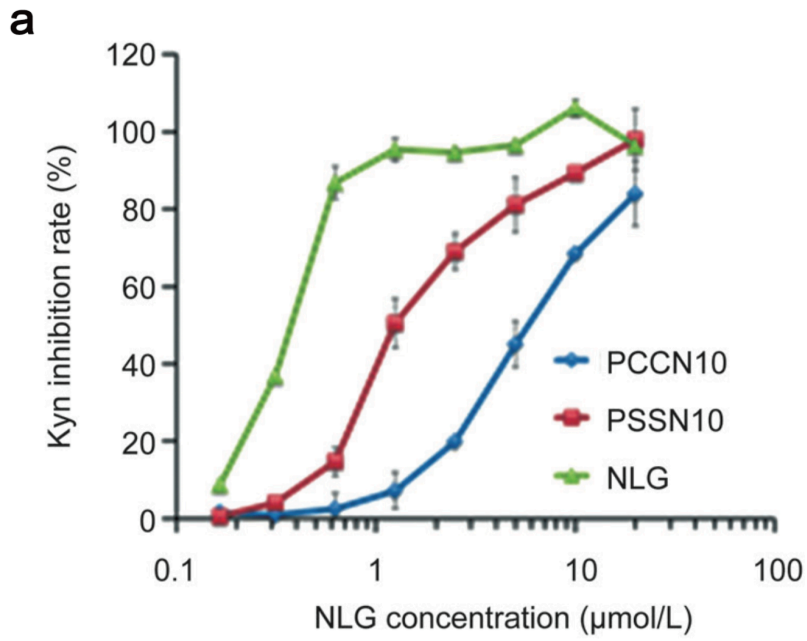

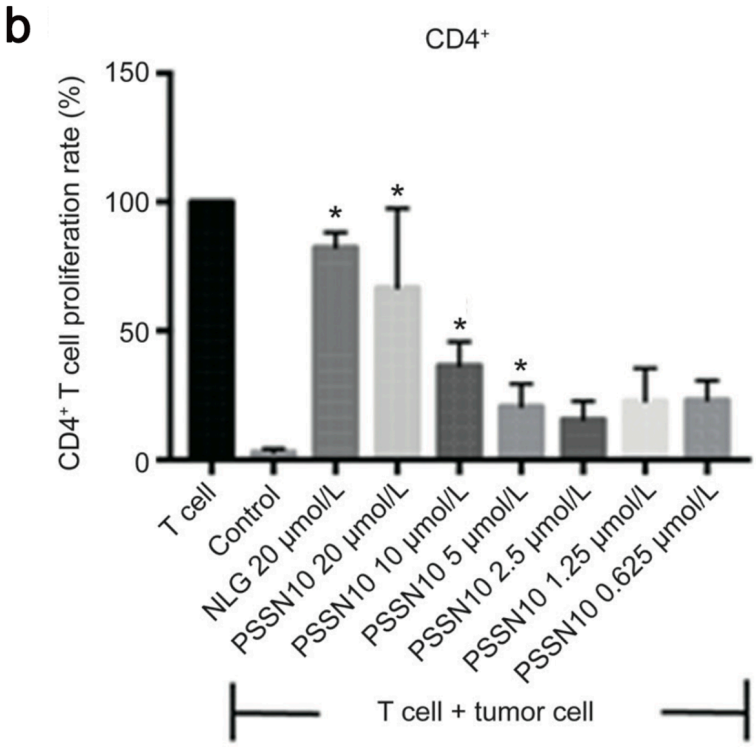

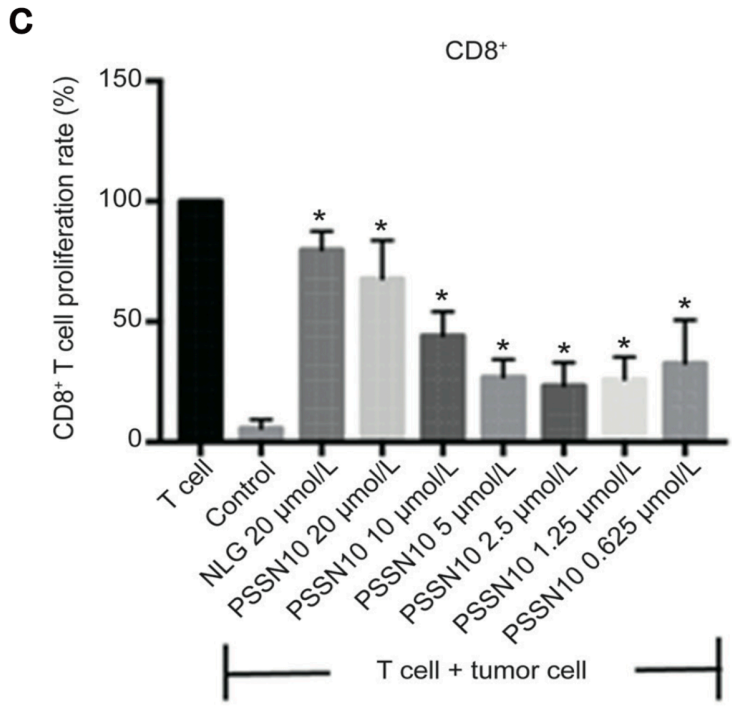

Figure 27. *In vitro* biological activities of PSSN10.
(a) *In vitro* inhibitory effect of IDO activity. HeLa cells were treated with IFN-γ together with PCCN10, PSSN10 and free NLG919. Kynurenine in supernatants was measured 2 days later. (b) The effect of PSSN10 on reversing T-cell suppression mediated by IDO-expressing mouse pancreatic cancer cells (Panc02). Panc02 cells and splenocytes were mixed and treated with IL-2, anti-CD3 antibody, IFN-γ together with PSSN10 and free NLG919 for 3 days. T-cell proliferation was measured by FACS analysis. $^{*}P < 0.05$ (vs control).

5.4.3 *In Vitro* Biological Activities of PSSN10

In order to evaluate the IDO inhibitory effect of PSSN10 prodrug carrier *in vitro*, HeLa cells were pretreated with IFN-γ to induce IDO expression, and the amount of kynurenine (Kyn) was measured following treatment with PSSN10 and NLG919. As shown in Fig. 27a, free NLG919 and PSSN10 could block the IDO function in a NLG concentration dependent manner, although PSSN10 showed less IDO inhibitory effect than free NLG919. We also synthesized PCCN10 polymers without a disulfide linkage as a control. Compared with PCCN10, PSSN10 was more active in inhibiting the IDO activity, which might be due to the

efficient cleavage of disulfide linkage from PSSN10 in response to the intracellular GSH, suggesting the importance of introducing disulfide linkage into the NLG-based prodrug polymer. Thus, subsequent studies were focused on the PSSN10 polymers.

In vitro lymphocyte-Panc02 (a murine pancreatic cancer cell line) co-culture experiment was then conducted to examine if the T-cell proliferation could be enhanced via the IDO inhibitory effect of PSSN10. Fig. 27b shows that co-culture of splenocytes isolated from BALB/c mice with IDO^+ tumor cells led to significant inhibition of the proliferation of both $CD4^+$ T cell and $CD8^+$ T cells. This inhibition was almost completely reversed by free NLG919 at 20 mM. Fig. 27b also showed that PSSN10 blocked the inhibition by the tumor cells in a concentration-dependent manner. At the same NLG concentration of 20 mM, PSSN10 showed an effect that was comparable to free NLG919.

5.4.4 Cytotoxicity and Intracellular Trafficking of DOX/PSSN10 Mixed Micelles

MTT assay was carried out in 4T1.2 and PC3 cells to evaluate the cytotoxicity of DOX/PSSN10 mixed micelles. As shown in Fig. 28a, PSSN10 alone was not effective in inhibiting the tumor cell growth. Free DOX showed a cytotoxic effect on the tumor cells in a concentration-dependent manner. DOX-loaded micelles were comparable to free DOX in the levels of cytotoxicity against tumor 4T1.2 tumor cells. Similar results were also found in the PC3 cell line (Fig. 28b).

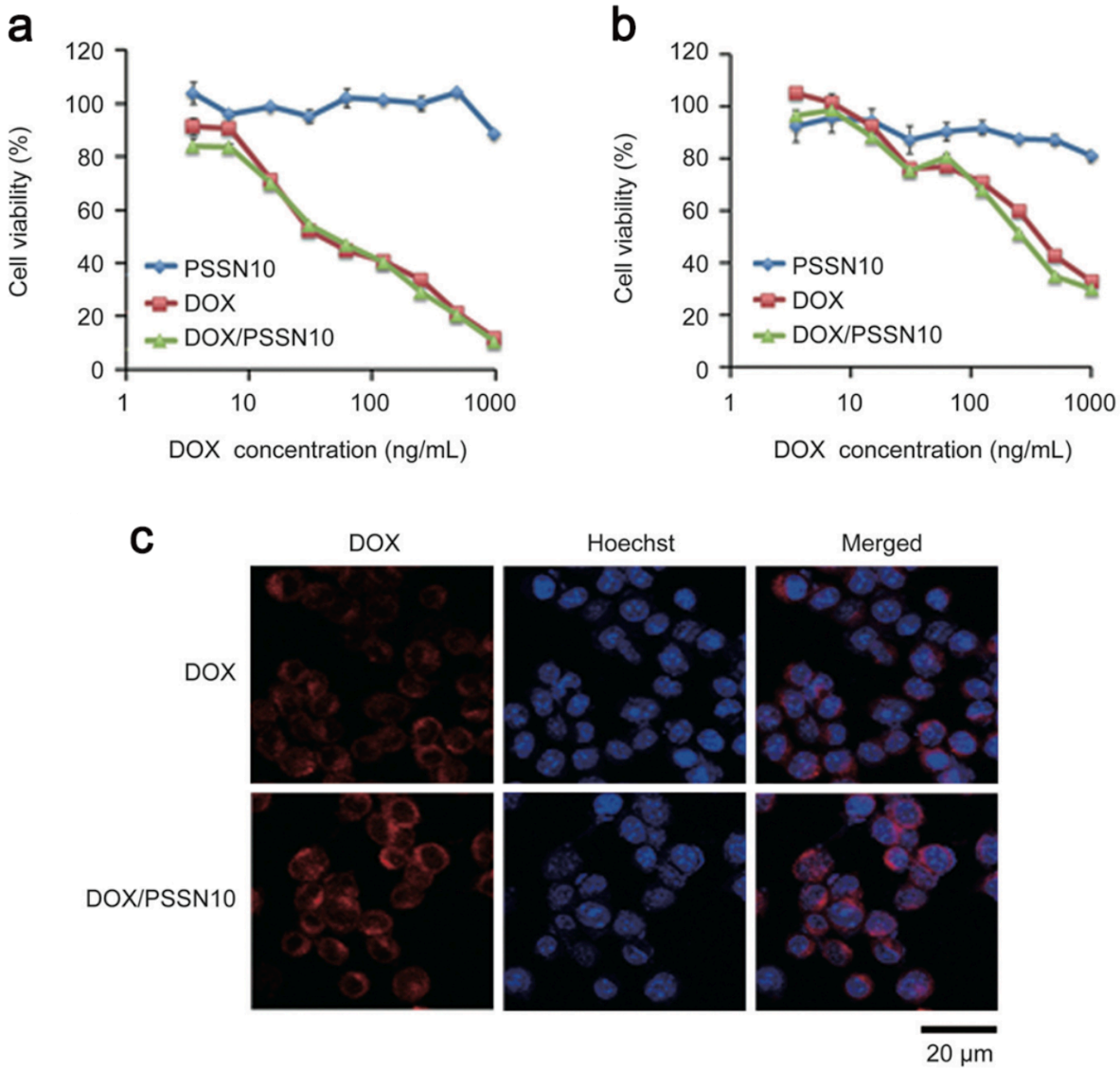

Figure 28. MTT assay of cytotoxicity of PSSN10, DOX and DOX/PSSN10 mixed micelles

Micelle cytotoxicity in (a) 4T1.2 mouse breast cancer cell line and (b) PC-3 human prostate cancer cell line. Cells were treated for 72 h and results are reported as the means ± SD for triplicate samples. (c) Confocal laser scanning microscopic images of 4T1.2 cells at 4 h following treatment with free DOX or DOX/PSSN10 mixed micelles. The nuclei were stained with Hoechst 33342.

Intracellular trafficking of DOX-loaded PSSN10 micelles was evaluated in 4T1.2 cells by confocal laser scanning microscopy with free DOX as a control (Fig. 28c). At 4 h after treatment with free DOX or DOX-loaded PSSN10 micelles, large amounts of fluorescence

signals were observed in perinuclear region of cells. Some of the DOX fluorescence signals were observed in nuclei for cells treated with DOX/PSSN10 mixed micelles, indicating the efficient intracellular delivery of DOX/PSSN10.

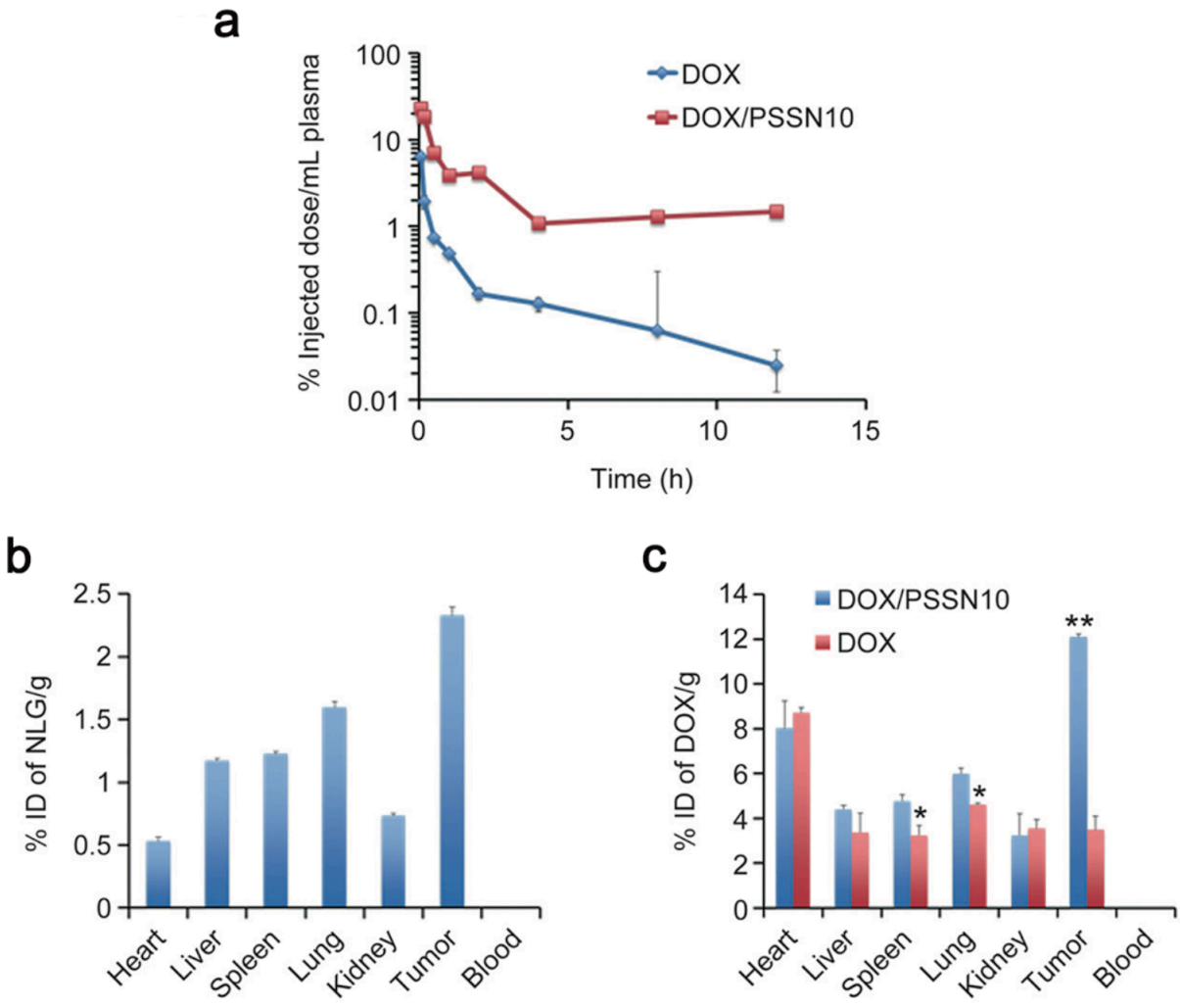

Figure 29. Pharmacokinetics and biodistribution of DOX-loaded PSSN10 micelles.
(a) Blood kinetics of DOX in BALB/c mice following *i.v.* administration of DOX-loaded PSSN10 micelles at a dose of 5 mg DOX/kg with free DOX as a control. (b) Tissue distribution of NLG in 4T1.2 tumour-bearing BALB/c mice 24 h following *i.v.* administration of DOX-loaded PSSN10 micelles. (c) Tissue distribution of DOX in 4T1.2 tumour-bearing BALB/c mice 24 h following *i.v.* administration of DOX-loaded PSSN10 or free DOX (5 mg DOX/kg). n=5, $^{*}P < 0.05$, $^{**}P < 0.01$ (DOX/PSSN10 vs DOX).

5.4.5 Plasma Pharmacokinetics and Tissue Distribution

Free DOX·HCl and DOX/PSSN10 mixed micelles (5 mg DOX/kg) were injected to BALB/c and the DOX concentrations in plasma were measured at different time points. As shown in Fig. 29a, DOX/PSSN10 remained in the blood circulation for a significantly longer time compared with free DOX. The pharmacokinetic parameters were calculated based on a noncompartment model and are outlined in Table 1. DOX/PSSN10 formulation showed significantly higher $T_{1/2}$, area under curve ($AUC_{0\text{-}inf}$) and C_{max} than those of free DOX. In contrast, the volume distribution (V_d) and clearance (CL) for DOX/PSSN10 were significantly lower than those of free DOX, which suggests a prolonged circulation time of DOX/PSSN10 formulation in the blood.

The tissue distributions of both NLG and DOX for DOX/PSSN10 mixed micelles were also investigated in BALB/c mice bearing 4T1.2 tumor. Fig. 29b shows the biodistribution of NLG at 24 h following *i.v.* administration of DOX/PSSN10 micelles. Significantly higher concentrations of NLG were detected in the tumors than those in other organs/tissues including heart, liver, spleen, lung and kidney. Besides, very little NLG was found in the blood, suggesting the good stability of the PSSN10 in the blood circulation. Fig. 29b shows the biodistribution of DOX at 24 hfollowing *i.v.* administration of DOX/PSSN10 micelles with free DOX as a control. Significantly greater amounts of DOX were detected in tumors for DOX/PSSN10 mixed micelles compared with free DOX. It is also noted that DOX/PSSN10 mixed micelles showed higher

accumulation in tumors than in other organs/tissues. These data suggest that DOX and NLG can be selectively delivered to the tumor sites via PSSN10 prodrug carrier.

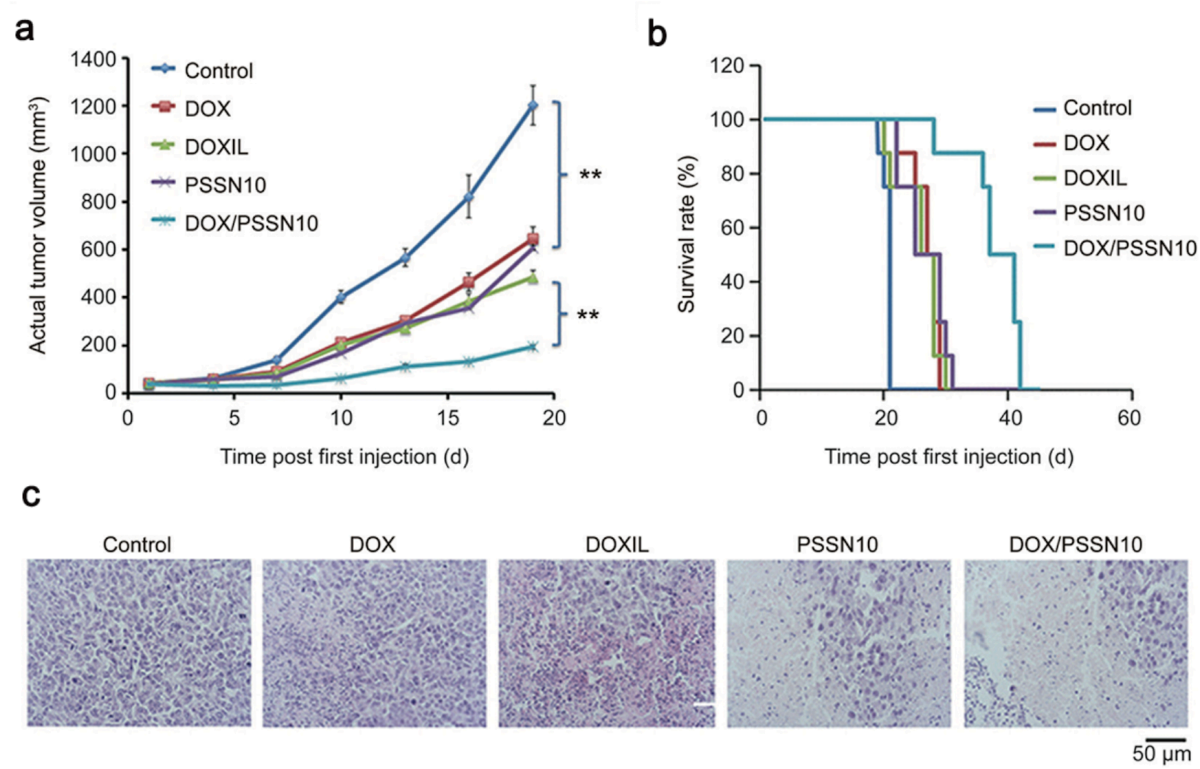

Figure 30. *In vivo* antitumor activity of PSSN10 and various DOX formulations in a syngeneic murine breast cancer model (4T1.2).
(a) Three injections were made on days 0, 3 and 6. **P < 0.01. (b) Kaplan-Meier survival of 4T1.2 tumor-bearing mice after various treatments. (c) Histological analyses of H&E stained sections of tumor tissues collected on day 19.

5.4.6 *In Vivo* Therapeutic Study

Fig. 30a shows the *in vivo* therapeutic effect of PSSN10 and DOX/PSSN10 with free DOX and DOXIL (a clinical formulation of liposomal DOX) as controls (5 mg DOX/kg). PSSN10 carrier alone showed a modest effect in inhibiting the tumor growth, which was comparable to those of DOX and DOXIL. In comparison, PSSN10 showed little cytotoxicity *in vitro* MTT study (Fig. 28a, b), which indicated that the IDO inhibitory effect instead of the

cytotoxic effect contributed to the activity of PSSN10 in inhibiting tumor growth. DOX formulated in PSSN10 micelles showed enhanced antitumor activity, which was significantly higher than that of DOXIL.

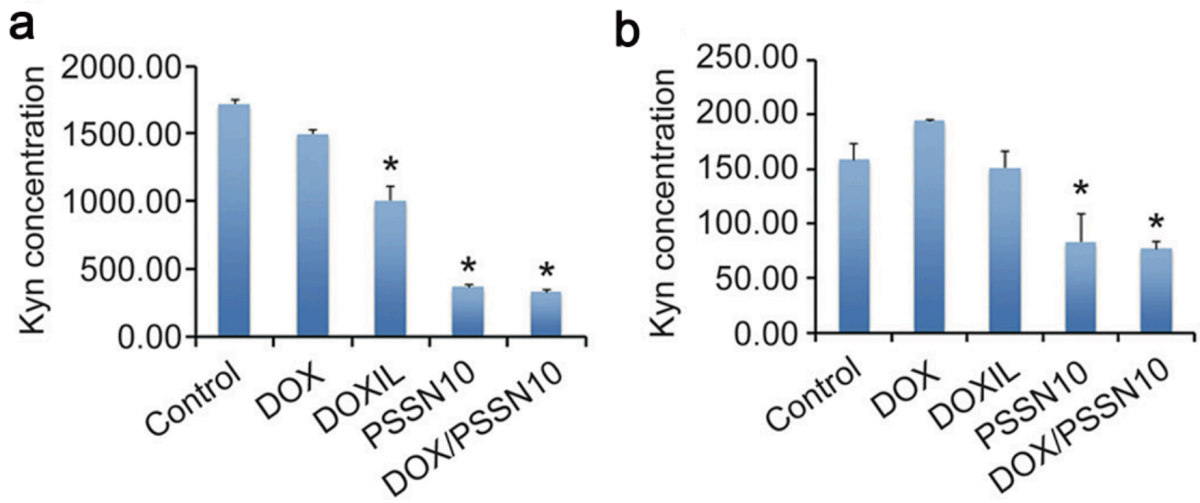

Figure 31. IDO inhibition in tumor and blood
Kynurenine concentrations in (a) tumor and (b) blood of BALB/c mice bearing s.c. 4T1.2 tumors following various treatments. *P < 0.05 (vs control).

Figure 30b shows the Kaplan-Meier survival curves of 4T1.2 tumor-bearing mice following different treatments. All formulations improved the survival rate compared to the saline control group. Among them, DOX/PSSN10 formulation resulted in the longest overall survival with a median survival of 40 days.

Fig. 30c shows the histology of tumors following different treatments. Tumors from the mice treated with DOX/PSSN10 had more necrotic/apoptotic cells compared to the tumors from other treatment groups.

5.4.7 Effect of DOX/PSSN10 Treatment on Tumor Immune Microenvironment

The Kyn concentrations, an indicator of IDO enzyme activity, in tumor tissue and blood following various treatments were measured by HPLC-MS. As shown in Fig. 31, the Kyn concentrations in both blood and tumor were significantly decreased following the treatment of PSSN10 and DOX/PSSN10, respectively. Interestingly, the levels of Kyn in the blood were also significantly decreased in the mice treated with DOXIL.

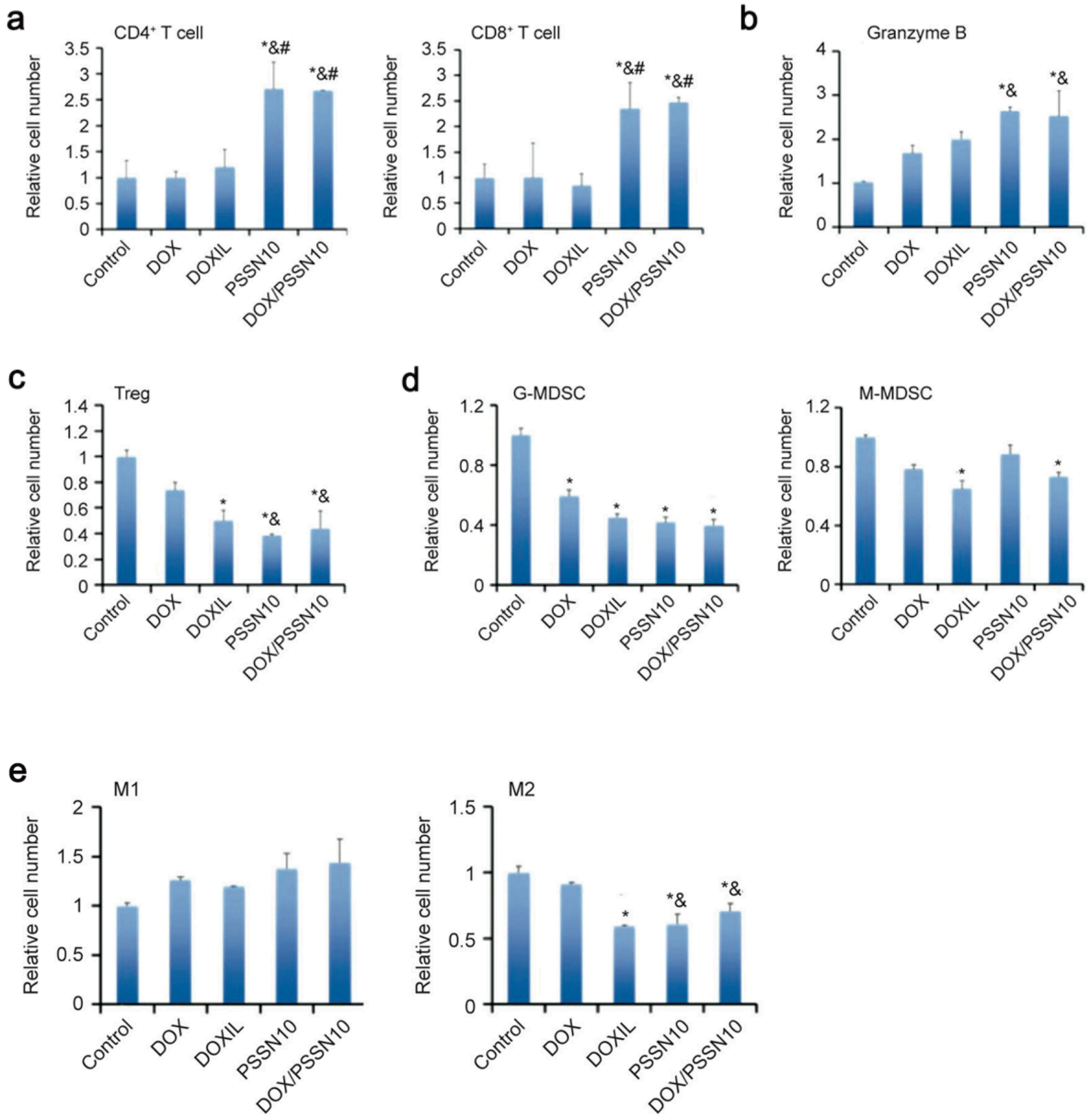

Figure 32. Flow cytometry analysis of immune cell subsets in tumor tissues.
Tumor bearing mice received various treatments at a DOX dosage of 5 mg/kg for three times at an interval of 3 days and tumoral T-cell infiltration, including (A) $CD4^+$ and $CD8^+$， (B) granzyme B-positive $CD8^+$ T cells, were measured by flow cytometry. (C) $FoxP3^+$ T regulatory cells, (D) MDSC subsets ($Gr\text{-}1^{high}CD11b^+$ granulocytic (G-MDSC) and $Gr\text{-}1^{int}CD11b^+$ monocytic (M-MDSC)) and (E) tumor-associated macrophage (TAM) populations (M1-type ($CD11b^+/F4/80^+/CD206^-$) and M2-type ($CD11b^+/F4/80^+/CD206^+$)) were also detected by flow cytometry. The bars represent means ± s.e.m. $^*P < 0.05$ (vs control); $^\&P < 0.05$ (vs DOX); $^\#P < 0.05$ (vs DOXIL).

We then further examined changes in the immune cell subpopulation in the tumor tissues that received different treatments. As shown in Fig. 32a, PSSN10 treatment led to a significant increase in relative numbers of $CD4^+$ T cells and $CD8^+$ T cells in the tumors compared with control, DOX or DOXIL groups. There was no significant difference in the relative numbers of $CD4^+$ T cells between PSSN10 and DOX/PSSN10 (Fig. 32a).

Fig. 32b shows that the relative number of granzyme B-positive $CD8^+$ T cells in tumors was increased in all treatment groups compared with control group. The relative number of granzyme B-positive $CD8^+$ T cells in tumor tissues treated with PSSN10 or DOX/PSSN10 was higher than that of DOX-treated group. No significant difference was found in the relative number of granzyme B-positive $CD8^+$ T cells between PSSN10 and DOX/PSSN10 groups.

Fig. 32c shows that the relative cell number of regulatory T cells (Treg) was reduced in all treatment groups compared with control group. Similarly, the relative cell number of granulocytic myeloid-derived suppressor cells (G-MDSC) in the tumors was reduced in all treatment groups (Figure 7D). No significant difference was found in the relative cell number of Treg (Figure 7C) or G-MDSC cells (Fig. 32d) between PSSN10 and DOX/PSSN10 groups.

There was also a slight decrease in the relative cell number of monocytic MDSC (M-MDSC) in the tumors after various treatments (Fig. 32d).

Figure. 32e shows that the relative cell number of M1 ($CD11b^{+}F4/80^{+}CD206^{-}$) tumor-associated macrophages in the tumors was slightly increased in all treatment groups. In contrast, the relative cell number of M2 ($CD11b^{+}F4/80^{+}CD206^{-}$) tumor-associated macrophages was significantly reduced following treatment with DOXIL, PSSN10 or DOX/PSSN10.

Overall, these data suggest a more immunoactive tumor microenvironment in mice treated with PSSN10 or DOX/PSSN10 in comparison with control or other treatment groups. This is consistent with the better *in vivo* IDO inhibitory effect of DOX/PSSN10 compared with that of DOXIL or other groups (Fig. 30).

5.5 DISCUSSION

Checkpoint blockade immunotherapy has been developed as a promising modality of treatment for various malignancies[189, 190]. Currently, immune checkpoint blockade is achieved with monoclonal antibodies specific for different immune checkpoint proteins [191]. Recently, there has been growing interest in developing small molecule immune checkpoint inhibitors[192, 193]. Compared to antibodies-based immunotherapeutics, small molecule checkpoint inhibitors have the advantages of excellent safety, ease of production and more efficient delivery into tumor site[193].

IDO1 is an important immune checkpoint protein, which suppresses T cell proliferation

through Trp catabolism and Kyn production. 1-Methyl-d-tryptophan (1-MT) and NLG919 are two important small molecule inhibitors with distinct mechanism for blocking IDO1-mediated tumor immune escape[194]. Compared to 1-MT, NLG919 is a more potent IDO1-selective inhibitor with an EC50 of 75 nM[195]. Some studies have shown that IDO inhibitors can improve the therapeutic efficacy of chemotherapy or work synergistically with chemotherapy[176, 177]. However, there is limited information about the combination therapy of NLG919 with a chemotherapeutic drug[196].

Our group previously developed PEG-NLG conjugate (PEG2k-Fmoc-NLG) as a prodrug nanocarrier for co-delivery of NLG919 and paclitaxel (PTX), a commonly used chemotherapeutic drug[178]. It was found that the immune-enhancing function of NLG and the tumor killing effect of PTX synergistically contributed to the increased anti-tumor efficacy. In this work, we further improved the NLG-based prodrug carrier system by increasing the number of NLG units per carrier molecule via RAFT polymerization. Compared to previous system, the NLG loading content in the new PSSN10 system is increased from 9.4 % to 19.7%, which could help to decrease the amounts of carrier materials for *in vivo* application. In addition, a disulfide linkage is introduced in the PSSN10 system, which shall promote the release of NLG from the prodrug carrier (data not shown).

PSSN10 readily formed small-sized micelles that are capable of loading various types of anticancer agents including DOX, PTX, docetaxel and curcumin (data not shown). We focused on DOX in this work as DOX can elicit caspase-dependent immunogenicity and enhance the proliferation of tumor antigen-specific $CD8^+$ T cells in tumor-draining lymph

nodes[197, 198, 199, 200]. Recent study has shown that the effectiveness of immune checkpoint blockade is dependent on a preexisting antitumor immunity[161]. In addition, it has been reported that post-chemotherapy delivery of immunotherapy was a more effective treatment mode in inhibiting tumor progression [201]. Therefore, combining PSSN10 with DOX that is capable of inducing immunogenic tumor cell death represents a rational approach of cancer immunochemotherapy.

One unique feature of our approach is the programmable release of NLG and DOX to maximize the efficacy of the combination therapy. DOX was physically loaded into PSSN10 micelles and shall be rapidly released from the micelles upon reaching the tumor site. DOX-mediated killing of tumor cells and/or the direct effect of DOX on immune cells could lead to enhanced tumor antigen presentation and improved antitumor immunity. On the other hand, NLG was covalently linked to the polymer and will be released at a relatively slower pace, which shall help to maintain or enhance the anti-tumor immune response over a prolonged period of time thorough reversing IDO-mediated immune suppression. Indeed, DOX/PSSN10 mixed micelles were significantly more effective than DOXIL or free DOX in inhibiting the tumor growth and prolonging the survival of treated mice. The superior antitumor activity of DOX/PSSN10 mixed micelles is likely due to the effective delivery of both NLG and DOX to the tumor tissue as demonstrated in the biodistribution study (Fig. 29). The synergistic action between DOX and released NLG may also play an important role.

Immunological analysis indicates that tumor tissues from mice treated with PSSN10 are more immunoactive with higher percentage of functional T cells ($CD4^+$ and $CD8^+$) and lower

percentage of Treg and MDSC compared with the tumors with no treatment or treated with DOX or DOXIL (Fig. 32). Incorporation of DOX into the PSSN10 system does not affect the function of PSSN10 in enhancing T cell proliferation and suppressing Treg and G-MDSC cells. This is somewhat different from our previous study with PTX-loaded PEG2k-Fmoc-NLG system in which incorporation of PTX led to the reduction in the percentage of total intratumoral T cells and increase in the percentage of MDSC cells compared to the PEG2k-Fmoc-NLG alone [201]. It is not clear at present whether this is due to the different drug or the dosage of the drug used in the two different studies. More studies are needed in the future to better understand the underlying mechanisms.

In conclusion, we have developed a new redox-sensitive system PSSN10 for programmable co-delivery of DOX and NLG. Our data suggest that DOX/PSSN10 had the potential to be used as an effective combination regime for cancer immunochemotherapy.

6.0 TARGETING OF MDSC TO IMPROVE NANO-IMMUNOCHEMOTHERAPY

6.1 ABSTRACT

Development of an effective treatment against advanced tumors remains a major challenge for cancer immunotherapy. We have previously developed a PEG-NLG-based chemoimmunotherapy system for targeted delivery of paclitaxel (PTX), but its efficacy is restricted by various factors, including the accumulation of myeloid-derived suppressor cells (MDSCs). In this study, we determine whether codelivery of a multi-target receptor tyrosine kinase inhibitor, sunitinib (SUN) that reduce MDSC levels can further enhance the antitumor efficacy of PTX/PEG-Fmoc-NLG micelles. To efficiently encapsulate both PTX and SUN, an improved polymeric micelle nano-delivery system (PEG_{5k}-Fmoc-NLG_2) is developed which has both a lower CMC and longer micellar stability. SUN+PTX/PEG_{5k}-Fmoc-NLG_2 micelles not only increase cytotoxic T-cell infiltration and decrease the number and percentage of MDSCs and T_{regs} in the TME, but also showed enhanced *in vivo* antitumor activity in an advanced murine breast cancer mouse model. Our findings indicated codelivery of PTX and SUN via an improved dual-functional nanocarrier (PEG_{5k}-Fmoc-NLG_2) led to reversal of the immunosuppressive phenotypes associated with PTX/PEG_{2k}-Fmoc-NLG and can be used as a novel strategy to enhance the therapeutic efficacy of existing immune-based therapies for advanced breast cancer.

6.2 BACKGROUND

Interactions between the immune system and cancerous cells play an important role in carcinogenesis and failure of the host immune system to recognize and eradicate malignant

cells may lead to tumor development. Various mechanisms are developed by tumor cells to escape from immune surveillance. Many of these mechanisms are now known on a cellular and molecular level, such as immune checkpoints, which refer to inhibitory receptors expressed on immune effector cells or immune inhibitory ligands on tumor cells. Immune checkpoint blockade for CTLA-4 and PD-1 using monoclonal antibodies (mAbs) have achieved great clinical success, which has the potential to enhance and sustain endogenous immunity, establishing durable tumor control. Despites these successes, the clinical efficacy of checkpoint blockade is still limited due to the fact that multiple suppressive mechanisms have been implicated in the resistance to checkpoint blockade, including increased expression of PD-L1 and indoleamine 2,3-dioxygenase (IDO). Another reason which results in a limitation of clinical efficacy of checkpoint blockade is the fact that the efficacy of the immune checkpoint blocked is closely associated with pre-existing antitumor immune responses. Chemotherapy drug can cause immunogenic cell death, which leads to initiation of antitumor immune responses. Checkpoint blockade can then further enhance and sustain such antitumor immunity. Therefore, combination of immunogenic chemotherapy with checkpoint blockade has a great potential of improving cancer therapy. Therefore, it is ideal to develop a strategy to induce immunogenic tumor cell death while simultaneously blocking multiple tumor immunosuppressive pathways.

Immunochemotherapy that combines a chemotherapeutic agent with an immune-modulating agent represents an attractive approach to improve cancer therapy. However, the success of immunochemotherapy is hampered by the lack of a strategy to effectively codeliver the two therapeutics to the tumors. Accordingly, we have developed a dual-functional, immunostimulatory nanomicellar carrier that is based on a prodrug conjugate (PEG_{2k}-Fmoc-NLG) of PEG with NLG919, an indoleamine 2,3-dioxygenase (IDO) inhibitor currently used for reversing tumor immune suppression. IDO is overexpressed in some

cancer cells and functions as an enzyme that catalyzes the degradation of essential amino acid tryptophan (Trp) and accumulation of its metabolites, resulting in cell cycle arrest and death of effector T cells, but increases in the number of regulatory T cells. We show that PEG2k-Fmoc-NLG alone is effective in enhancing T cell immune responses and exhibits significant antitumor activity *in vivo*. More importantly, systemic delivery of paclitaxel (PTX) using the PEG_{2k}-Fmoc-NLG nanocarrier leads to a significantly enhanced antitumor response in *in vivo* tumor mouse models. However, treatment with PTX/PEG_{2k}-Fmoc-NLG was also associated with untoward effects including upregulation of PD-1, PD-L1 and IDO-1 in tumor tissues at transcriptional level, and increased infiltration of myeloid-derived suppressor cells (MDSCs) compared to carrier alone group. This is likely due to the activation of several feedback mechanisms as well as the inflammatory response following the PTX-mediated killing of tumor cells and/or induced antitumor immunity. At the same time, the tumor cells recruit regulatory cells to attenuate antitumor immunity generated via immune checkpoints inhibition, through the liberation of immunosuppressive cytokines and alterations in the nutrient content of the microenvironment. The release of colony-stimulating factors, IL-1β, VEGF, or PGE2 by tumor cells results in the accumulation of MDSCs. MDSCs are present in TME as well as in circulation in cancer patients.

MDSC plays a major role in creating a tumor immunosuppressive microenvironment and is found to accumulate in major organs and tumor tissues in advanced tumor-bearing mice and patients. Currently, two main MDSC populations have been characterized: monocytic MDSCs and granulocytic MDSCs. Despite their similarities in morphology to monocytes and neutrophils, MDSCs are quite different by being highly immune suppressive through a number of mechanisms. MDSCs can induce immunosuppression by production of arginase I (Arg1) and inducible nitric oxide synthase (iNOS), leading to T-cell inhibition. In addition, MDSCs can also promote tumor cell proliferation, promote drug resistance, and facilitate

tumor metastasis and angiogenesis. Therefore, high numbers of tumor-infiltrating MDSCs are often related to high tumor burden and metastasis, leading to poor treatment outcome. Therapeutic targeting of MDSCs might overcome immunosuppression to enhance responses to immunotherapy.

Sunitinib is a small-molecule, multi-targeted receptor tyrosine kinase (RTK) inhibitor. It is currently approved for the treatment of gastrointestinal stromal tumors (GIST) and metastatic renal cell carcinoma. Sunitinib has shown blocking effects on a variety of receptor tyrosine kinases, including ckit, vascular endothelial growth factor receptor 2 (VEGFR2), platelet-derived growth factor receptor (PDGFR), and Flt. In addition to its direct effects on tumor cells and tumor angiogenesis, sunitinib was reported to decreases the numbers and function of MDSCs and Treg cells both systemically and in the tumor microenvironment. Sunitinib has been shown to augment tumor-infiltrating T cell IFNg production and downregulate the expression of CTLA4, PD1 and PDL1. This reduction in immune suppression provides a rationale for combining sunitinib with immunochemotherapy for the treatment of certain tumor types.

We hypothesized that incorporation of sunitinib into PTX/PEG-NLG mixed micelles shall lead to a more effective immunochemotherapy for cancer treatment by decreasing MDSC recruitment (Fig. 33). Indeed, codelivery of PTX and sunitinib via an improved dual-functional nanocarrier (PEG_{5k}-Fmoc-NLG_2) led to reversal of the immunosuppressive phenotypes associated with previous reported PTX/PEG2k-Fmoc-NLG and further enhanced antitumor activity.

6.3 EXPERIMENTAL PROCEDURES

6.3.1 Materials

Paclitaxel (PTX, 499%) was purchased from TSZ Chem (MA, USA). DOX·HCl and

Sunitinib (SUN) were purchased from LC Laboratories. α-Fmoc-ε-Boc-lysine, α, ε-Di-Boc-lysine, N, N'-dicyclohexylcarbodiimide (DCC), triethylamine (TEA) and trifluoroacetic acid (TFA) were purchased from Acros Organic (NJ, USA). Monomethoxy PEG5000, 4-dimethylaminopyridine (DMAP), Triton X-100 and other unspecified reagents were purchased from Sigma Aldrich (MO, USA). Dulbecco's Modified Eagle's Medium (DMEM) and fetal bovine serum (FBS) were purchased from Invitrogen (NY, USA).

6.3.2 Synthesis of PEG_{5K}-Fmoc-NLG_2 Conjugate

Monomethoxy PEG5000 (1 equiv.), α-Fmoc-ε-Boc-lysine (3 equiv.), DCC (6 equiv.) and DMAP (1 equiv.) were mixed in dichloromethane (DCM) and stirred at room temperature (RT) for 2 days. Then the mixture was filtered and precipitated in cold ether/ethanol twice to yield PEG_{5K}-Lys(Fmoc)-Boc. The Boc group was removed in the mixture of DCM/TFA (1:1, v/v) for 2 h at RT, followed by precipitation in cold ether/ethanol to give PEG_{5K}-Lysine(Fmoc)-NH_2. PEG_{5K}-Lys(Fmoc)-Lys(Boc_2) was then synthesized by mixing PEG_{5K}-lysine(Fmoc)-NH_2 (1 equiv.), α, ε-Di-Boc-lysine (5 equiv.), DCC (5 equiv.) and DMAP (1 equiv.) in DCM at RT for 2 days. After deprotection of Boc group in DCM/TFA (1:1, v/v), PEG_{5K}-Lys(Fmoc)-Lys(NH_2)$_2$ was obtained and then mixed with NLG919 (5 equiv.), DCC (5 equiv.) and DMAP (1 equiv.) in DCM. After stirring at RT for 2 days, the mixture was precipitated in cold ether/ethanol for three times, yielding the final product PEG_{5K}-Fmoc-NLG_2.

6.3.3 Preparation of PTX+SUN/PEG_{5K}-Fmoc-NLG_2 Micelles

PTX&SUN co-loaded PEG_{5K}-Fmoc-NLG_2 micelles were prepared through a thin-film hydration method. Briefly, PTX (5 mg/mL in DCM), SUN (5 mg/mL in ethanol), and PEG_{5K}-Fmoc-NLG_2 (50 mg/mL in DCM) were mixed at designated molar ratios in a glass

tube. After removing the organic solvent, thin-film of carrier/drug mixture was formed. Then DPBS was added to hydrate the film and a clear solution of PTX+SUN/PEG_{5K}-Fmoc-NLG_2 micelles was obtained. PTX/PEG_{5K}-Fmoc-NLG_2, SUN/PEG_{5K}-Fmoc-NLG_2, and drug-free PEG_{5K}-Fmoc-NLG_2 micelles were similarly prepared.

6.3.4 Characterization

^1H NMR spectra of synthesized materials were performed on a Varian-400 FT-NMR spectrometer (400.0 MHz) with $CDCl_3$ and DMSO-d_6 as the solvent. The critical micelle concentration (CMC) value of PEG_{5K}-Fmoc-NLG_2 micelles was measured as previously reported by using nile red as a fluorescence probe [202]. The size distribution and morphology of blank and drug-loaded micelles were detected by dynamic light scattering (DLS, Malvern Zeta Nanosizer) and transmission electron microscopy (TEM, negative staining method), respectively.

6.3.5 Cell Culture

4T1.2 mouse metastatic breast cancer cells, PANC02 murine pancreatic cell line and HeLa human cervical cancer cells were cultured in DMEM culture medium, containing 10% (v/v) fetal bovine serum and 100 IU/mL penicillin and 100 μg/mL streptomysin at 37 °C in a humidified 5% CO_2 atmosphere.

6.3.6 *In Vitro* IDO Inhibition Assay

The *in vitro* IDO inhibitory effect of PEG_{5K}-Fmoc-NLG_2 was evaluated by IDO assay. Briefly, HeLa cells were seeded at a density of 5×10^3 cells/well in a 96-well plate. After incubation for 24 h, recombinant human IFN-γ was added to each well at a concentration of 50 ng/mL. Then cells were treated with PEG_{5K}-Fmoc-NLG_2 or free NLG919 at various

concentrations of NLG919 ranging from 50 nM ~ 20 μM. After incubation for 48 h, 150 μL of the supernatants was transferred to a new 96-well plate and incubated with 75 μL of 30% trichloroacetic acid at 50 °C for 30 min to hydrolyze N-formylkynurenine to kynurenine. For colorimetric assay, supernatants were transferred to a new 96-well plate and equal volume of Ehrlich reagent (2% p-dimethylamino-benzaldehyde w/v in glacial acetic acid) was added into each well. After incubation for 10 min at RT, the mixture was measured at 490 nm by a plate reader. For HPLC-MS detection (Wastes Alliance 2695 Separation Module combined with Waters Micromass Quattro Micro TM API MS detector), the plate was centrifuged at 12,500 rpm. for 10 min and 100 μL of the supernatants was taken from each well for tryptophan and kynurenine quatification.

6.3.7 T-cell Proliferation Study

A lymphocyte-Panc02 cell co-culture experiment was performed to study the T-cell proliferation mediated by various treatments [185]. Murine Panc02 cells were stimulated by IFN-γ (50 ng/mL) to induce IDO expression and then irradiated (6,000 rad). Splenocyte suspensions were harvested from BALB/c mice and passed through the nylon wool columns. After lysing of red blood cells, splenocytes were pre-stained with 5-(and 6)-carboxyfluorescein diacetate (CFSE)). Then splenocytes (5×10^5 cells/well) and IFN-γ stimulated Panc02 cells (1×10^5 cells/well) were mixed together in a 96-well plate. Various concentrations of PEG_{5K}-Fmoc-NLG_2 and NLG919 were added to the cells. Then 100 ng/mL anti-CD3 and 10 ng/mL mouse recombinant IL-2 were added to the cocultures. After incubation for 72 h, the number of $CD8^+$ and $CD4^+$ T cells was measured by fluorescence-activated cell sorting (FACS) analysis.

6.3.8 *In Vitro* Cytotoxicity Assay

4T1.2 murine breast cancer cell lines were seeded in 96-well plates at a density of 1.5×10^3 (4T1.2) and 3×10^3 (PC3) cells/well, respectively. After incubation for 24 h, cells were treated with PTX, Carrier alone, PTX/PEG_{5k}-Fmoc-NLG_2, SUN/PEG_{5k}-Fmoc-NLG_2 or PTX+SUN/PEG_{5k}-Fmoc-NLG_2 in a gradient concentration. After treatment for 72 h, the cell viabilities were measured by MTT assay as previously reported. Untreated cells were included as a control.

6.3.9 Animals

Female BALB/c mice (6~8 weeks) were purchased from Charles River (Davis, CA). All animals were housed under pathogen-free conditions according to AAALAC guidelines. All animal-related experiments were performed in full compliance with institutional guidelines and approved by the Animal Use and Care Administrative Advisory Committee at the University of Pittsburgh.

6.3.10 Quantification of Trp/Kyn Ratio in Plasma and Tumor Tissues

The kynurenine to tryptophan concentations in plasma or tumor tissues from 4T1.2 tumor-bearing mice were examined by HPLC-MS/MS. BALB/c mice bearing 4T1.2 tumors of ~50mm^3 were treated with DPBS, PEG_{5K}-Fmoc-NLG_2, PTX/PEG_{5K}-Fmoc-NLG_2, SUN/PEG_{5K}-Fmoc-NLG_2,PTX+SUN/PEG_{5K}-Fmoc-NLG_2 (PTX dosage: 10 mg/kg; SUN dosage: 10 mg/kg) via tail vein once every 3 days for 5 times. The plasma and tumor samples were harvested at 24 h after the last treatment. Methanol was added into plasma samples at ratio of plasma/methanol 1/2.5 (v/v) and the mixture was centrifuged at 12,500 rpm. for 15 min. Supernatants were collected and analyzed by HPLC-MS for kynurenine and tryptophan quantification. Tumor samples were homogenized in water and the homogenates were mixed

with acetonitrile (1:1, v/v), centrifuged and supernatants were transferred into new tubes. Equal volumes of methanol were added to precipitate proteins and supernatants were collected for HPLC-MS detection.

6.3.11 Quantification of Tumor-infiltrating Lymphocytes

BALB/c mice bearing 4T1.2 tumors of ~50 mm^3 received various treatments via tail vein injection once every 3 days for 5 times. Tumors and spleen were harvested at 24 h following the last treatment, single cell suspensions were then prepared and stained with CD4, CD8, IFN-γ, Granzyme B, FoxP3, myloid-derived suppressor cell (CD11b and Gr-1) and macrophage (F4/80 and CD206) for FACS analysis.

6.3.12 Plasma Pharmacokinetics and Tissue Distribution

Female BALB/c mice (5 mice/group) were injected i.v. with Taxol, Sunitinib malate PTX/PEG_{5K}-Fmoc-NLG_2, SUN/PEG_{5K}-Fmoc-NLG_2 or PTX+SUN/PEG_{5K}-Fmoc-NLG_2 (PTX dosage: 10 mg/kg; SUN dosage: 10 mg/kg). Blood samples were collected at different time points (3 min, 10 min, 30 min, 1 h, 2 h, 4 h, 8 h and 12 h) and centrifuged at 12,500 rpm. for 15 min. The plasma was mixed with 350 μL acetonitrile and centrifuged at 12,000 rpm. for 5 min. The concentrations of PTX and SUN in the supernatants were determined by HPLC. The pharmacokinetic parameters were calculated based on a noncompartment model by Phoenix WinNonlin.

For tissue distribution study, Taxol, Sunitinib malate, PTX/PEG_{5K}-Fmoc-NLG_2, SUN/PEG_{5K}-Fmoc-NLG_2, PTX+SUN/PEG_{5K}-Fmoc-NLG_2 micelles (PTX dosage: 10 mg/kg; SUN dosage: 10 mg/kg) were i.v. injected into female BALB/c mice bearing 4T1.2 tumors. At 24 h post injection, mice were sacrificed and the major organs/tissues were collected, weighted and homogenized with 2 mL mixed solvent (acetonitrile: H_2O=1:1, v/v). The

mixture was centrifuged at 12,500 rpm. for 10 min, and the supernatants were collected and dried under airflow. The residues were then dissolved in 200 ml solvent (methanol to H2O=1:1, v/v) and centrifuged at 14,500 rpm. for 10 min. The collected supernatants were analyzed by HPLC for detection of PTX and SUN concentration.

6.3.13 *In Vivo* Anti-tumor Activity

For combination therapy of PTX loaded micelle and Gr-1 antibody, groups of four female Balb/C mice were administered Saline, control IgG, PTX-loaded PEG_{5k}−Fmoc−NLG_2 micelles, PTX-loaded PEG_{5k}-Fmoc-NLG_2 micelles +control IgG or PTX-loaded PEG_{5k}−Fmoc−NLG_2 micelles+Gr-1 antibody for 5 times (10 mg PTX/kg, 100ug Gr-1 antibody 100μg/mouse *i.p.*). The tumor volumes and body weights of all mice were monitored. Tumor volumes were calculated according to the formula: $(L \times W^2)/2$, in which L is the longest and W is the shortest tumor diameter (mm), and presented as relative tumor volume (the tumor volume at a given time point divided by the tumor volume prior to first treatment).

For *in vivo* antitumor activity of SUN and PTX combination, female BALB/c mice bearing 4T1.2 tumors were treated with saline, PEG_{5K}-Fmoc-NLG_2, PTX/PEG_{5K}-Fmoc-NLG_2, SUN/PEG_{5K}-Fmoc-NLG_2, PTX/SUN/PEG_{5K}-Fmoc-NLG_2 (PTX dosage: 10 mg/kg; SUN dosage: 10 mg/kg) through intravenous injection every three days for 5 times. Tumor volumes were followed as described above. At the completion of the experiment, tumor tissues were excised, fixed with 10% paraformaldehyde solution and then embedded in paraffin. The sliced tissues with a thickness of 5 μm were stained by hematoxylin and eosin (H&E) and observed by the microscope (Zeiss Axiostar Plus, USA).
The Kaplane-Meier survival of the tumor-bearing mice (n = 8) was examined within 45 days. Mice were considered to be dead either when the mice died during treatment or when the

tumor volume reached ~1000 mm^3.

The immune cell populations in the tumors following various treatments were measured by flow cytometry[188]. Cell suspensions from the spleens or tumors were filtered and red blood cells were lysed. For extracellular staining, cells were co-incubated with combinations of antibodies (CD8, CD4, CD11b, Gr-1, CD45, F4/80 and CD206). For intracellular staining, cells were fixed immediately after cell surface staining following the manufacturer's description (eBioscience), then the combinations of antibodies (IFN-γ, FoxP3 and granzyme B) were added into cells in permeabilization buffer. For IFN-γ staining, cells were stimulated with PMA (5 ng/mL) and ionomycin (500 ng/mL) in presence of 10 mg/mL BFA for 4 h followed by extracellular and intracellular staining. The data were analyzed using the FlowJo software (Tree Star Inc.).

6.4 RESULTS

6.4.1 Combination of PTX and Gr-1 Antibody Enhances Tumor Therapy

To examine the effects of PTX/PEG-Fmoc-NLG micelle in combination with Gr-1 antibody, we inoculated 4T1.2 cells into the mammary fat pad of syngeneic mice following treatment with control IgG, anti-Gr-1 antibody, PTX/PEG-Fmoc-NLG micelles, the combination of PTX/PEG-Fmoc-NLG micelles and anti-Gr-1 antibody, the combination of PTX/PEG-Fmoc-NLG micelles and control IgG, or saline for 5 times. Combined treatment of PTX formulated micelles with anti-Gr-1 antibody resulted in the best tumor inhibition effect among the 6 groups (Fig. 34a). There was no significant change in the mouse body weight (Fig. 34b).

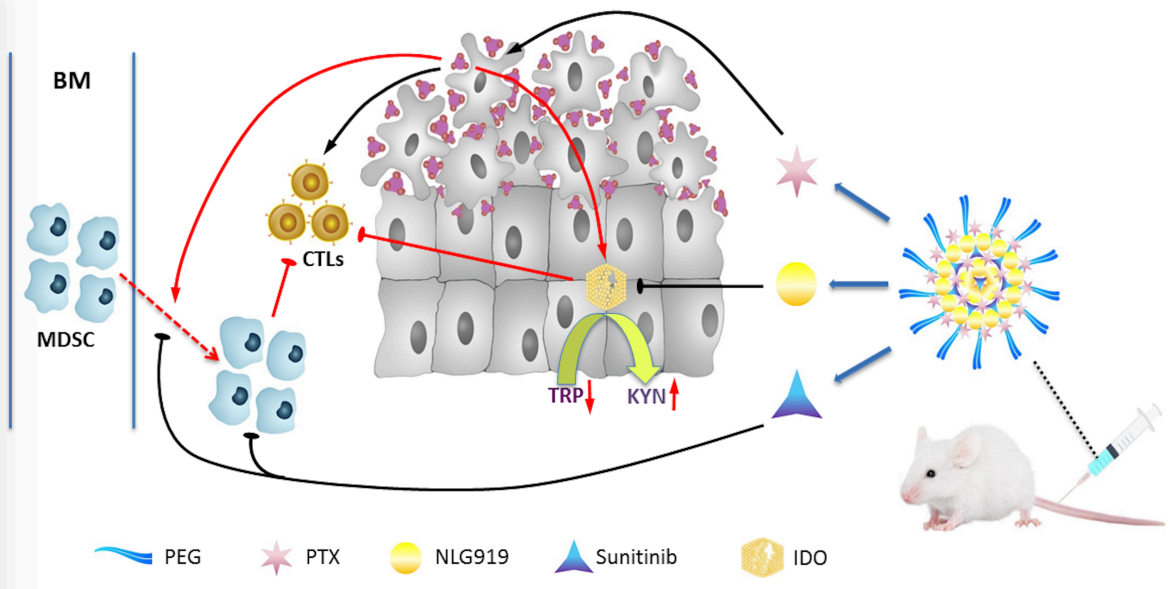

Figure 33. Schematic illustration of PTX+SUN co-loaded micelles.

6.4.2 Immune Activation With Combinational Therapy

Consistent with our previous *in vivo* experiment, PTX/PEG-Fmoc-NLG treatment significantly increased GMDSC cell percentage but the MMDSC was not significantly affected (Fig. 35a-c). With treatment of anti-Gr-1 antibody, the GMDSC cell percentage decreased significantly (Fig. 35a-b). Moreover, combined therapy of PTX micelles and anti-Gr-1 antibody enhanced the immune activation not only by increasing the number of $CD8^+$ and $CD4^+$ TILs, but also decreasing the IFN-γ^+ TILs percentage compared to PTX/PEG-Fmoc-NLG or Gr-1 antibody treatment(Fig. 35d-j). There was also a slightly increase in granzyme B^+ $CD8^+$ T cells in the tumor of the combination therapy than single therapy. This suggests that combined therapy with anti-Gr-1 antibody and PTX micelle formulation might induce tumor regression by attenuating the immunosuppressive MDSCs cells to achieve maximal anticancer efficacy.

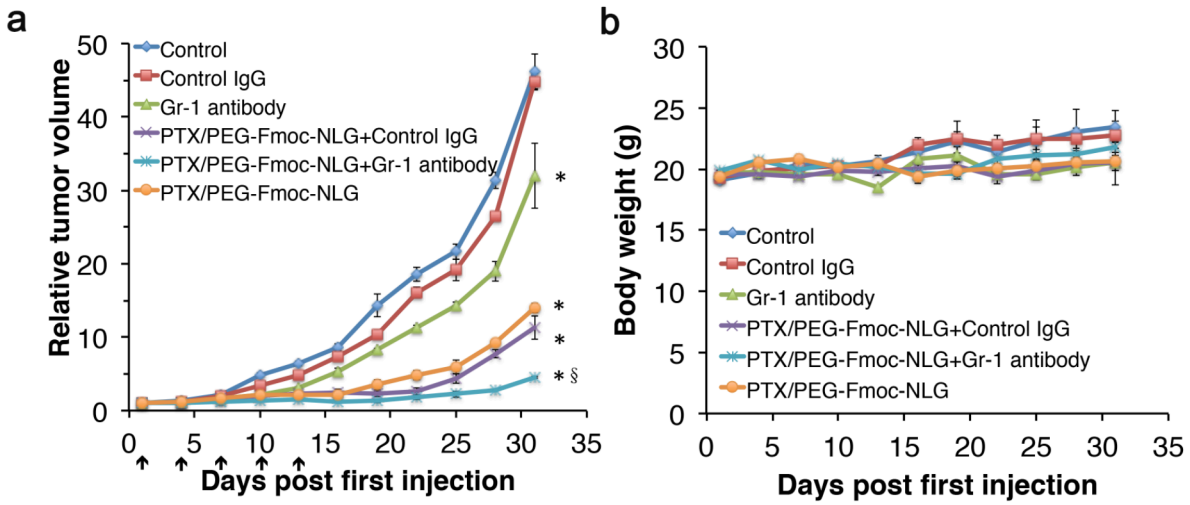

Figure 34. *In vivo* antitumor activity of PTX/PEG-Fmoc-NLG micelles in combination of Gr-1 antibody in a 4T1.2 breast cancer mouse model.

Black arrows indicate the *i.v.* treatment. A: relative tumor volume. N=5, *P<0.05, compared to control(saline), §P<0.01, compared to PTX/PEG-Fmoc-NLG. B: body weights of different treatment groups.

6.4.3 PTX Induces Chemokine Overexpression *In Vitro* and *In Vivo*

We next examined whether chemokine expression related to MDSC cell recruitment was altered following PTX treatment. As shown in Fig. 36 and Fig. 37, PTX treatment significantly increased the gene expression of a series of chemokines in 4T1.2 cells and SUN treatment decreased the gene expression. To further understand the mechanisms, we investigated the chemokine expression profiles in the TME in the tumor bearing mice after 3 treatments by RT-PCR. Figure 37 showed the PTX treatment significantly increased the chemokine expression in tumor tissues. However, all of the chemokines gene expression decreased with treatment of SUN and a combination of PTX and SUN. These data demonstrate that the upregulation of MDSCs with paclitaxel treatment might due to induction of chemokines related to MDSC recruitment and maturation and SUN treatment could

reverse this immunosuppressive status.

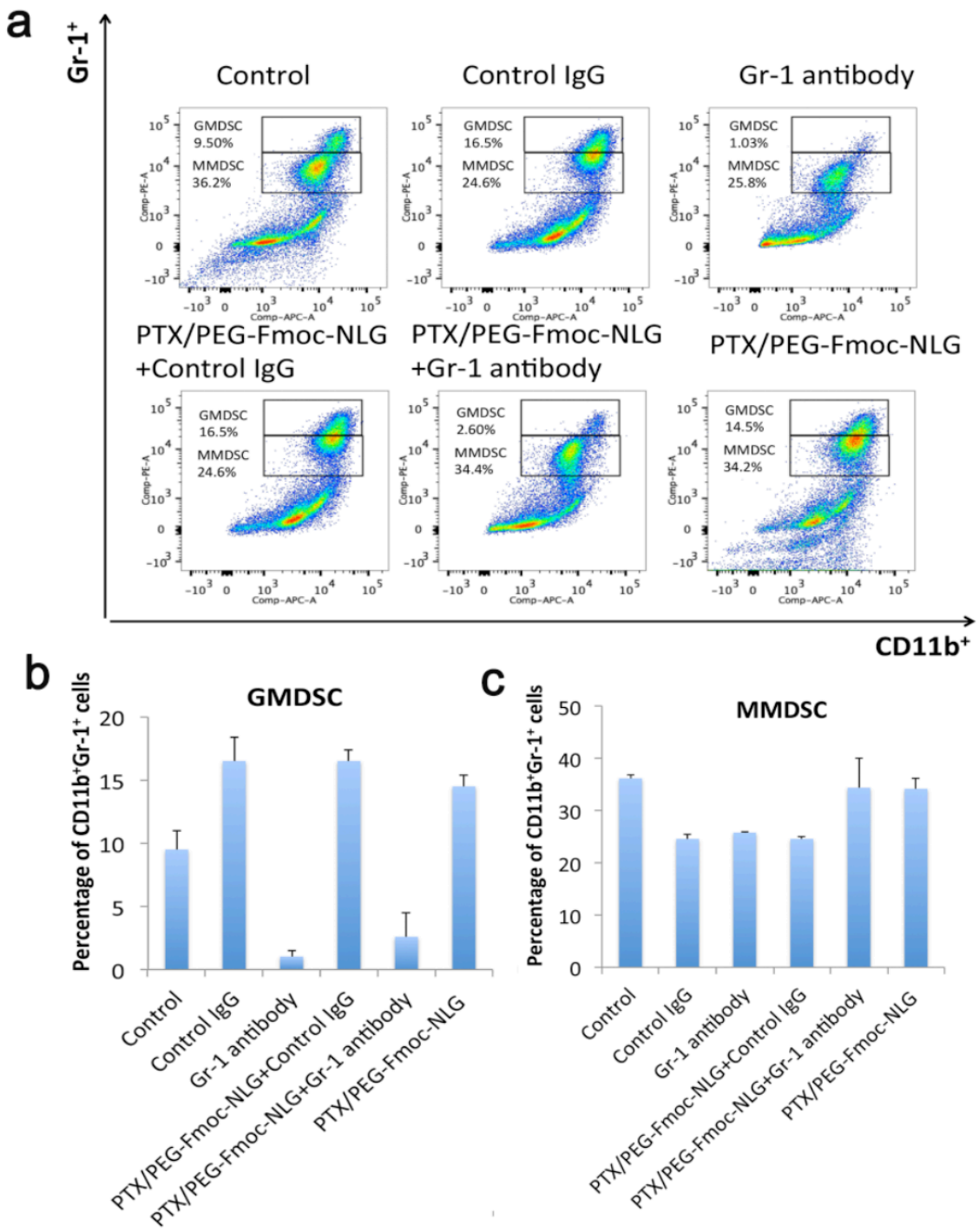

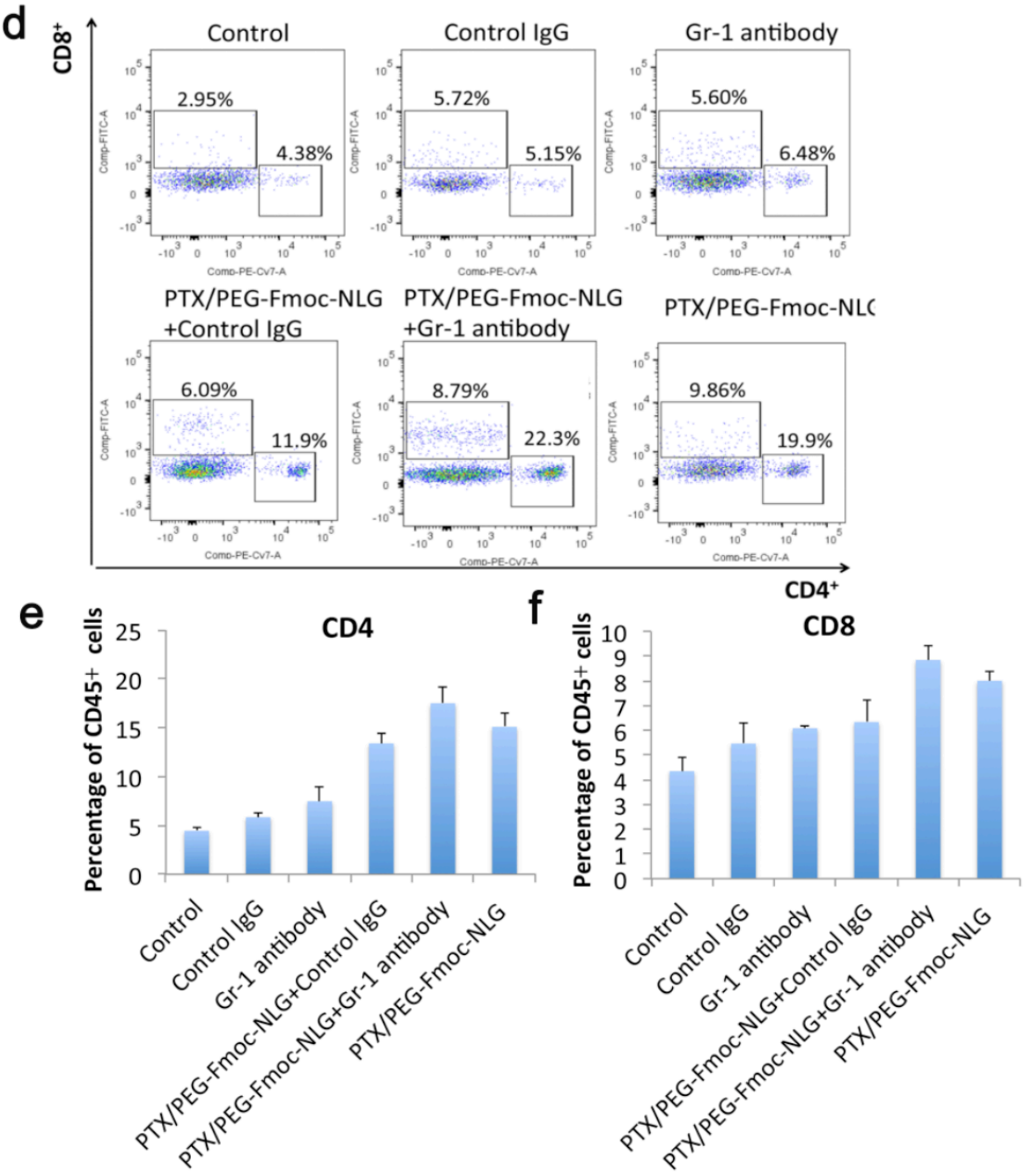
d
CD8+
Control
Control IgG
Gr-1 antibody
2.95%
4.38%
5.72%
5.15%
5.60%
6.48%
PTX/PEG-Fmoc-NLG
+Control IgG
PTX/PEG-Fmoc-NLG
+Gr-1 antibody
PTX/PEG-Fmoc-NLG
6.09%
11.9%
8.79%
22.3%
9.86%
19.9%
Comp-FITC-A
Comp-PE-Cy7-A
CD4+
e
CD4
Percentage of CD45+ cells
25
20
15
10
5
0
Control
Control IgG
Gr-1 antibody
PTX/PEG-Fmoc-NLG+Control IgG
PTX/PEG-Fmoc-NLG+Gr-1 antibody
PTX/PEG-Fmoc-NLG
f
CD8
Percentage of CD45+ cells
10
9
8
7
6
5
4
3
2
1
0
Control
Control IgG
Gr-1 antibody
PTX/PEG-Fmoc-NLG+Control IgG
PTX/PEG-Fmoc-NLG+Gr-1 antibody
PTX/PEG-Fmoc-NLG

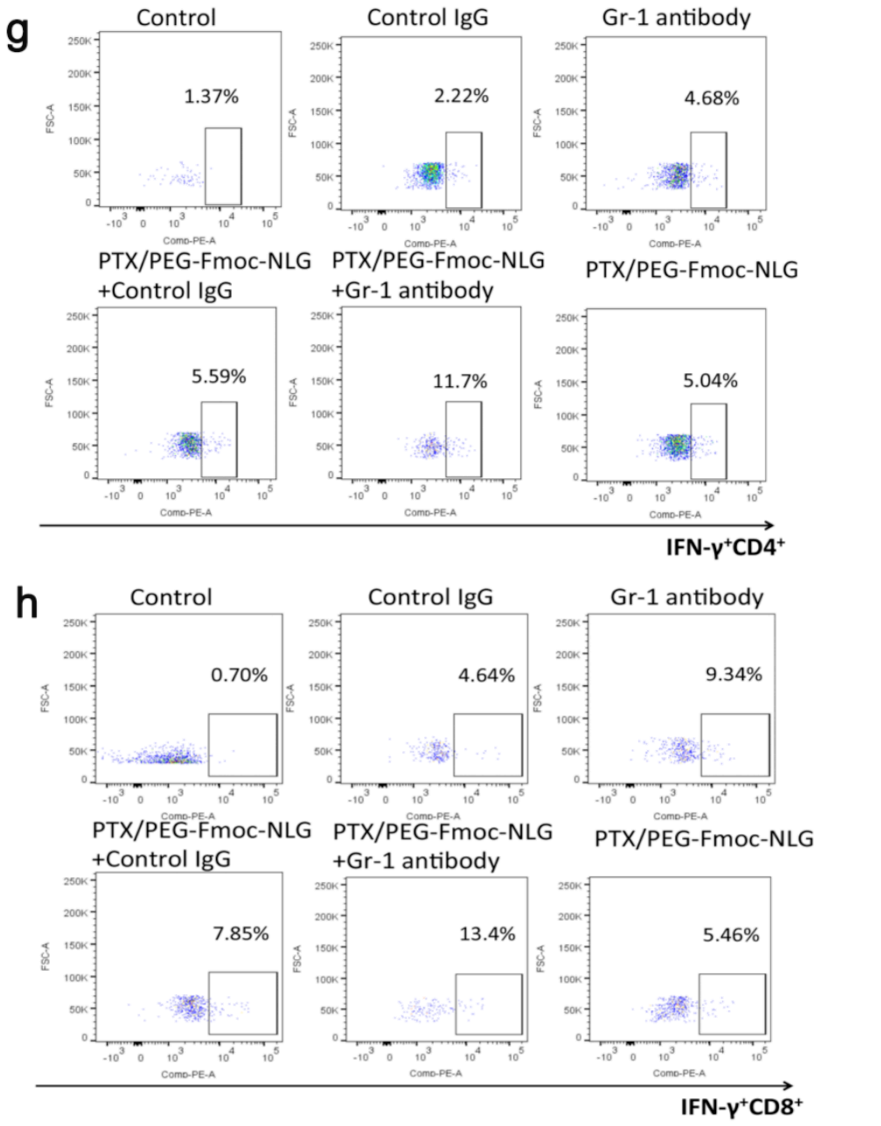
g
Control
Control IgG
Gr-1 antibody
1.37%
2.22%
4.68%
PTX/PEG-Fmoc-NLG +Control IgG
PTX/PEG-Fmoc-NLG +Gr-1 antibody
PTX/PEG-Fmoc-NLG
5.59%
11.7%
5.04%
IFN-γ+CD4+
h
Control
Control IgG
Gr-1 antibody
0.70%
4.64%
9.34%
PTX/PEG-Fmoc-NLG +Control IgG
PTX/PEG-Fmoc-NLG +Gr-1 antibody
PTX/PEG-Fmoc-NLG
7.85%
13.4%
5.46%
IFN-γ+CD8+

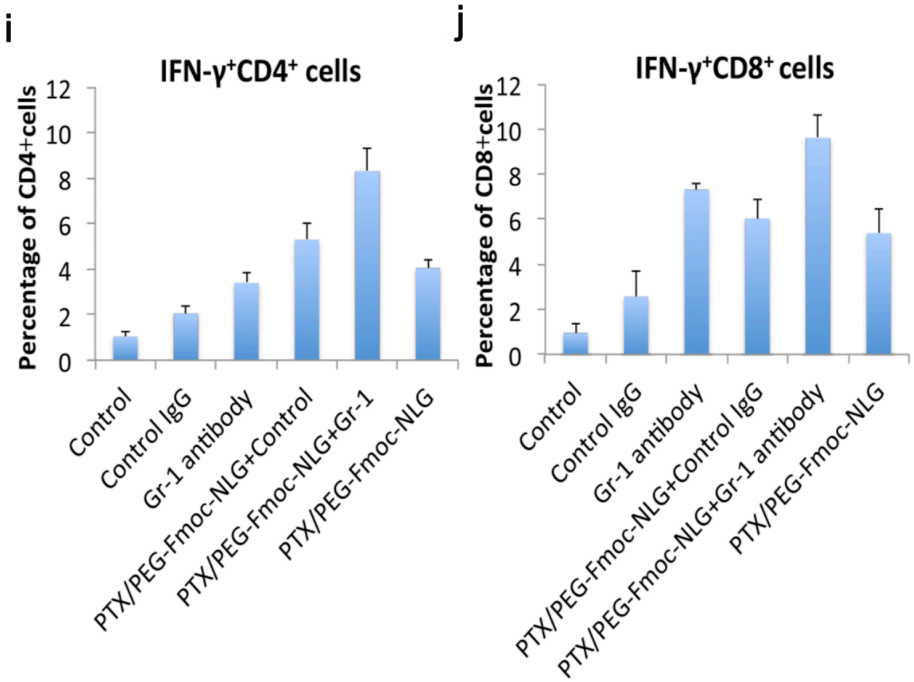
i
IFN-γ+CD4+ cells
Percentage of CD4+cells
0
2
4
6
8
10
12
Control
Control IgG
Gr-1 antibody
PTX/PEG-Fmoc-NLG+Control
PTX/PEG-Fmoc-NLG+Gr-1
PTX/PEG-Fmoc-NLG
j
IFN-γ+CD8+ cells
Percentage of CD8+cells
0
2
4
6
8
10
12
Control
Control IgG
Gr-1 antibody
PTX/PEG-Fmoc-NLG+Control IgG
PTX/PEG-Fmoc-NLG+Gr-1 antibody
PTX/PEG-Fmoc-NLG

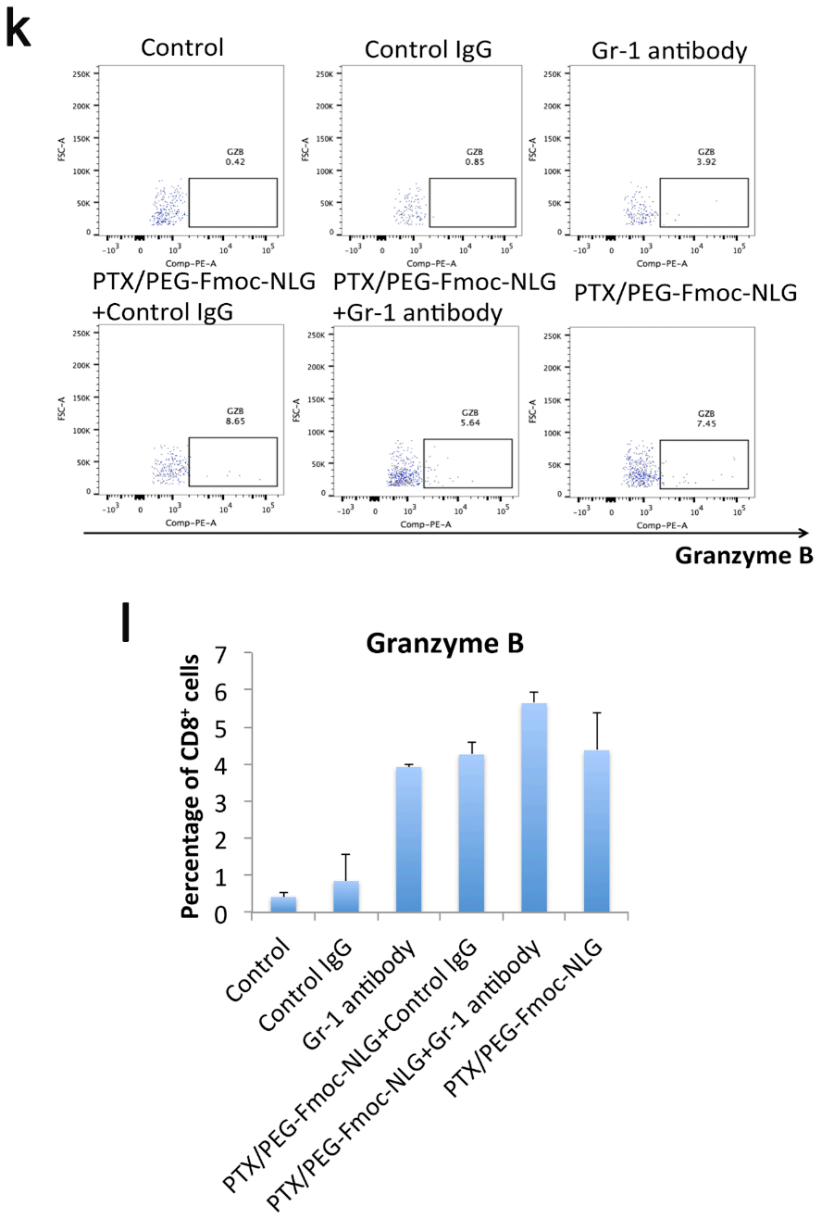

Figure 35. Flow cytometry analysis of immune cell subsets in tumor tissues with various treatments.

(a-c) Flow cytometry analysis of Gr-$1^{high}$$CD11b^{+}$ granulocytic (G-MDSC) and Gr-$1^{int}$$CD11b^{+}$ monocytic (M-MDSC) MDSC subsets. (d-l) Abundance of tumor infiltrating $CD4^{+}$ T cells(e), $CD8^{+}$ T cells(f), $IFN^{+}CD4^{+}$ T cells(i), IFN-γ^{+} $CD8^{+}$ T cells(j) and granzyme B^{+} $CD8^{+}$ T cells(l) in 4T1.2 tumor bearing mice. The bars represent means±s.e.m. (*$p<0.05$).

6.4.4 Characterization of PEG_{5K}-Fmoc-NLG_2

The self-assembly of PEG_{5k}-Fmoc-NLG_2 and the loading of hydrophobic drugs into the PEG_{5k}-Fmoc-NLG_2 micelles are illustrated in Fig. 33. The synthesis scheme of PEG_{5k}-Fmoc-NLG_2 was presented in Fig. 38. The chemical structures of PEG_{5k}-Fmoc-NLG_2

were confirmed by NMR.

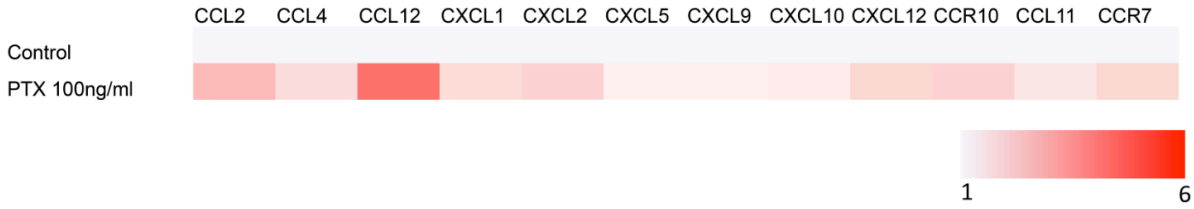

Figure 36. Expression of genes with a role in recruitment of MDSCs in 4T1.2 cells after treatment with PTX.
For each gene, expression values are normalized and plotted as log-transformed values (row-scaled and colored on a white-red scale to show the difference between samples).

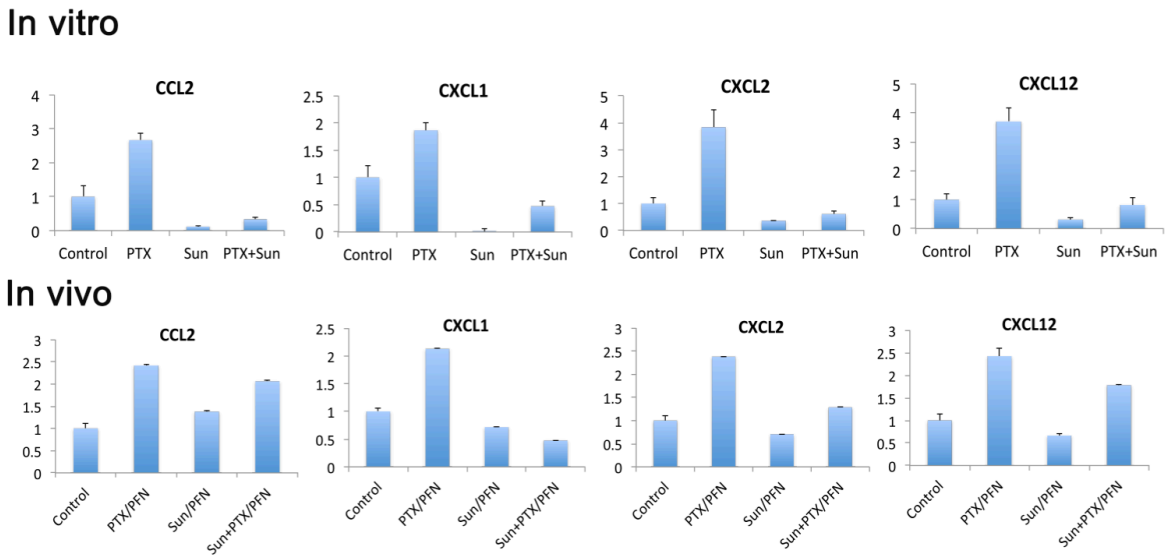

Figure 37. Expression of genes with a role in recruitment of MDSCs in 4T1.2 cells and tumor tissues after treatment with PTX, Sunitinib or combination.

6.4.5 IDO Enzyme Inhibition Effect

The IDO enzyme inhibitory activity of PEG_{5k}-Fmoc-NLG_2 was evaluated on Hela cells by examining the Trp to kynurenine (Kyn) concentration change in cell culture medium. HeLa cells were placed in a 96 well plate and stimulated with IFN-γto induce IDO expression. Cells

were treated with various concentration of carrier or free NLG drug. The amounts of Trp and Kyn in culture medium were examined by a colorimetric assay. Fig. 39 showed the free NLG919 could effectively inhibit the IDO enzyme activity by decreasing Trp/kyn conversion. The free drug had a low EC50 of 0.3 μM, the PEG_{5k}-Fmoc-NLG_2 could also maintain the IDO inhibition activity with a EC50 of 1.4 μM.

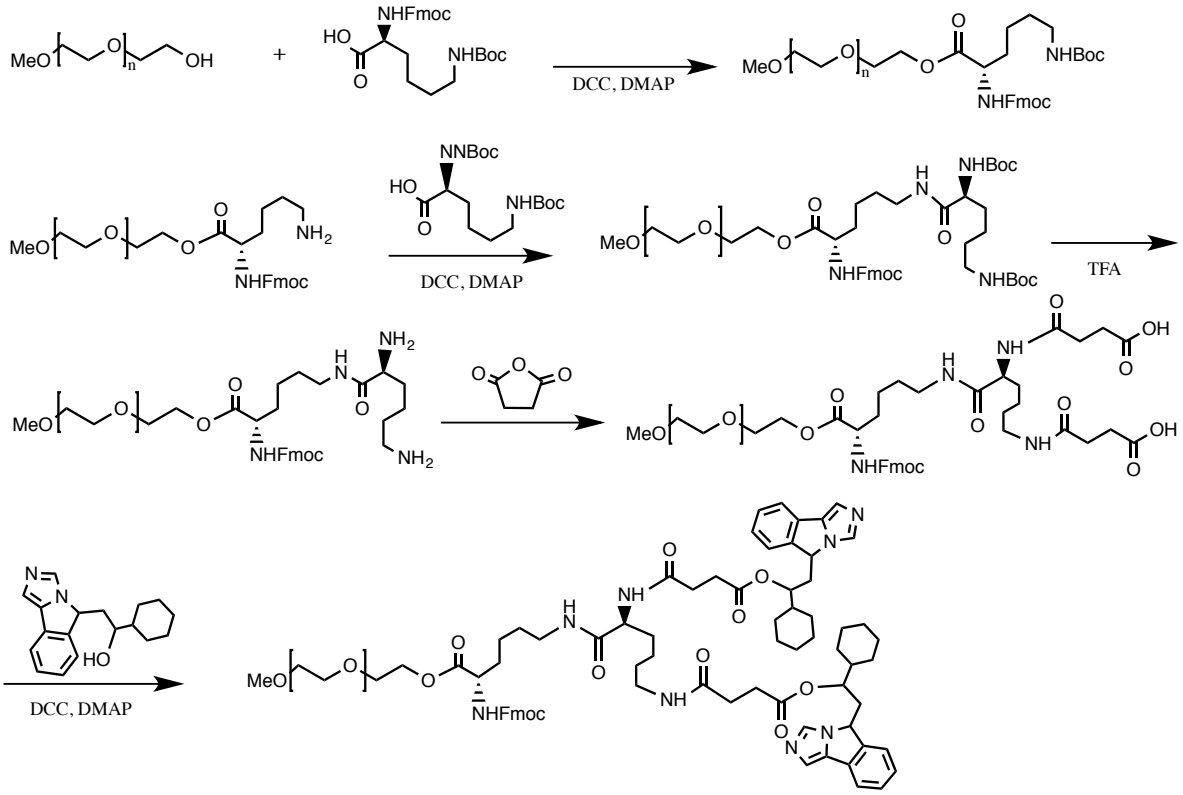

Figure 38. Synthesis scheme of PEG_{5k}-Fmoc-NLG_2.

6.4.6 Enhanced T Cell Proliferation Effect

As we showed before, T cell proliferation was greatly inhibited when lymphocytes were co-cultured with IDO expressing tumor cells. We examined whether PEG_{5k}-Fmoc-NLG_2 can lead to enhanced T-cell proliferation via inhibition of IDO expression on tumor cells in an *in vitro* lymphocyte-tumor cell co-culture study. In Fig. 40, co-culture of IDO^+ panc02 cells with splenocytes isolated from spleen of BALB/c mice led to significant inhibition of T-cell

growth. When co-cultured tumor cells were treated with NLG919 or PEG_{5k}-Fmoc-NLG_2, the T cell proliferation could be significantly restored, however, the PEG_{5k}-Fmoc-NLG_2 was slightly less effective than NLG919 free drug.

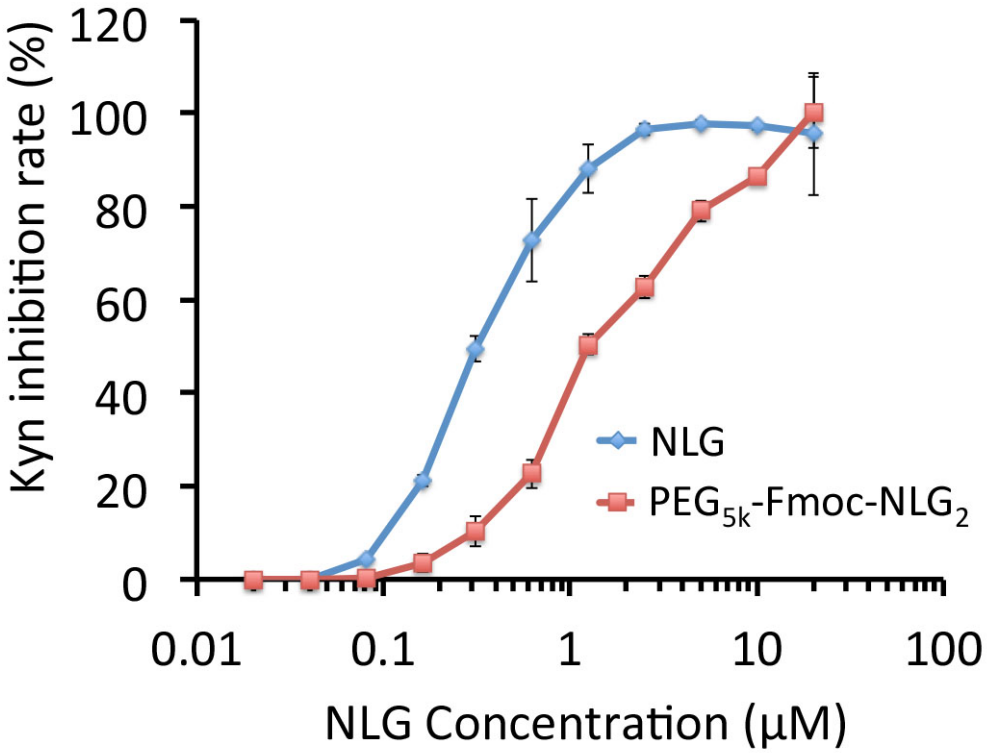

Figure 39. *In vitro* IDO inhibition assay of PEG_{5K}-Fmoc-NLG_2.
HeLa cells were stimulated with 50ng/ml of IFN-γ and treated with free NLG919 or PEG_{5K}-Fmoc-NLG_2 conjugate. Kynurenine concentration in supernatants was measure ‘d 48h after incubation by Ehrlich's reagent. Data represent means ± s.e.m.

6.4.7 Preparation and Characteristics of Drug Loaded PEG_{5k}-Fmoc-NLG_2 Micelles

This PTX+SUN formulated PEG_{5k}-Fmoc-NLG_2 nano-drug delivery system was prepared through a film hydration method. Meanwhile, PTX or SUN loaded micelles and drug free micelles were prepared as control in a similar way. The sizes and morphologies of blank and drug-formulated micelles were examined by DLS and TEM, respectively (Fig. 41). The DLS measurements showed that the mean diameter of blank micelle was 122 nm and the average

particle size of PTX/PEG_{5k}-Fmoc-NLG_2 and PTX+SUN/PEG_{5k}-Fmoc-NLG_2 were determined to be 125 nm and 126 nm, respectively (Table. 7). The co-formulation of PTX and SUN did not affect the particle size. TEM showed both blank and drug loaded micelles exhibited a spherical morphology with smooth surfaces. The observed micellar size was approximately 40 nm, which was slightly smaller than the hydrodynamic diameter obtained from the DLS experiment.

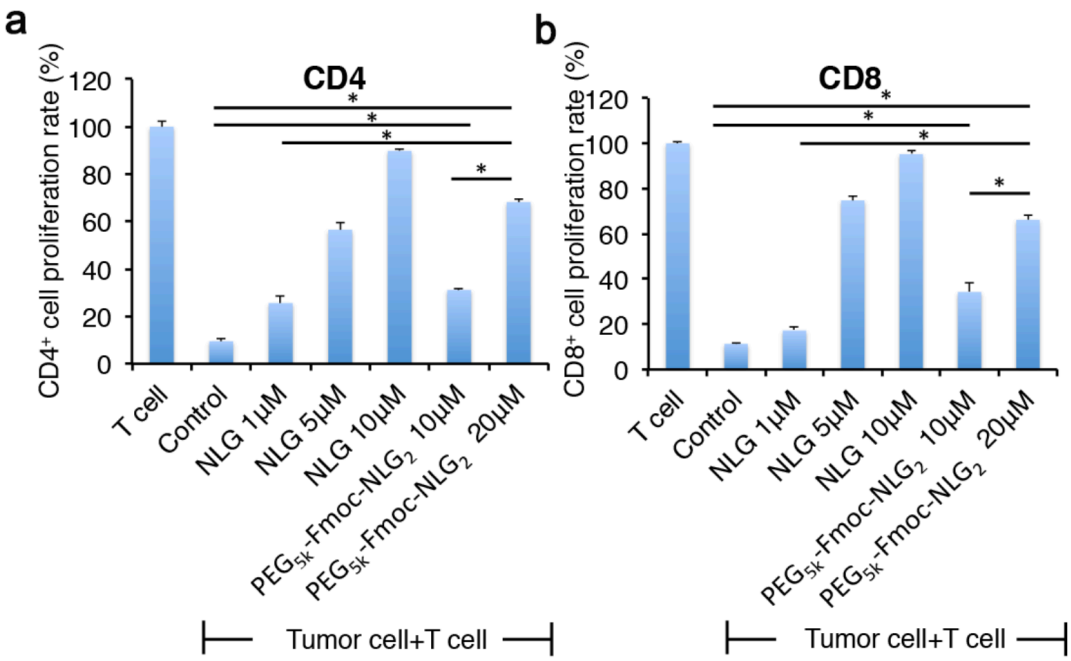

Figure 40. PEG_{5K}-Fmoc-NLG_2 reversed T cell growth inhibition mediated by IDO-expressing Panc02 cancer cells.
Panc02 cells were stimulated with 50ng/ml of IFN-γ, irradiated and co-cultured with mouse splenocytes. IL-2, anti-CD3 were used to stimulate T cell growth. Free NLG919 or PEG-NLG conjugate were added to co-cultured cells and proliferation of (A) $CD4^+$ and (B) $CD8^+$ T cells were examined by flow cytometer.

Most polymer micelles have poor physical stability after drug loading. In general, the stability of polymer micellar systems decreases as drug loading increases. PEG_{5k}-Fmoc-NLG_2 micelles were found to possess a lower CMC of 0.161μM (Fig. 42) and a higher drug loading capacity for PTX and SUN compared to previous PEG_{2k}-Fmoc-NLG system. Tab. 7 shows the PTX+SUN co-loaded PEG_{5k}-Fmoc-NLG_2 micelles could be stored

at room temperature for one week without a significant change in particle size and drug content, which was significantly higher than 48h of previous PEG_{2k}-Fmoc-NLG system, indicating excellent stability *in vitro*.

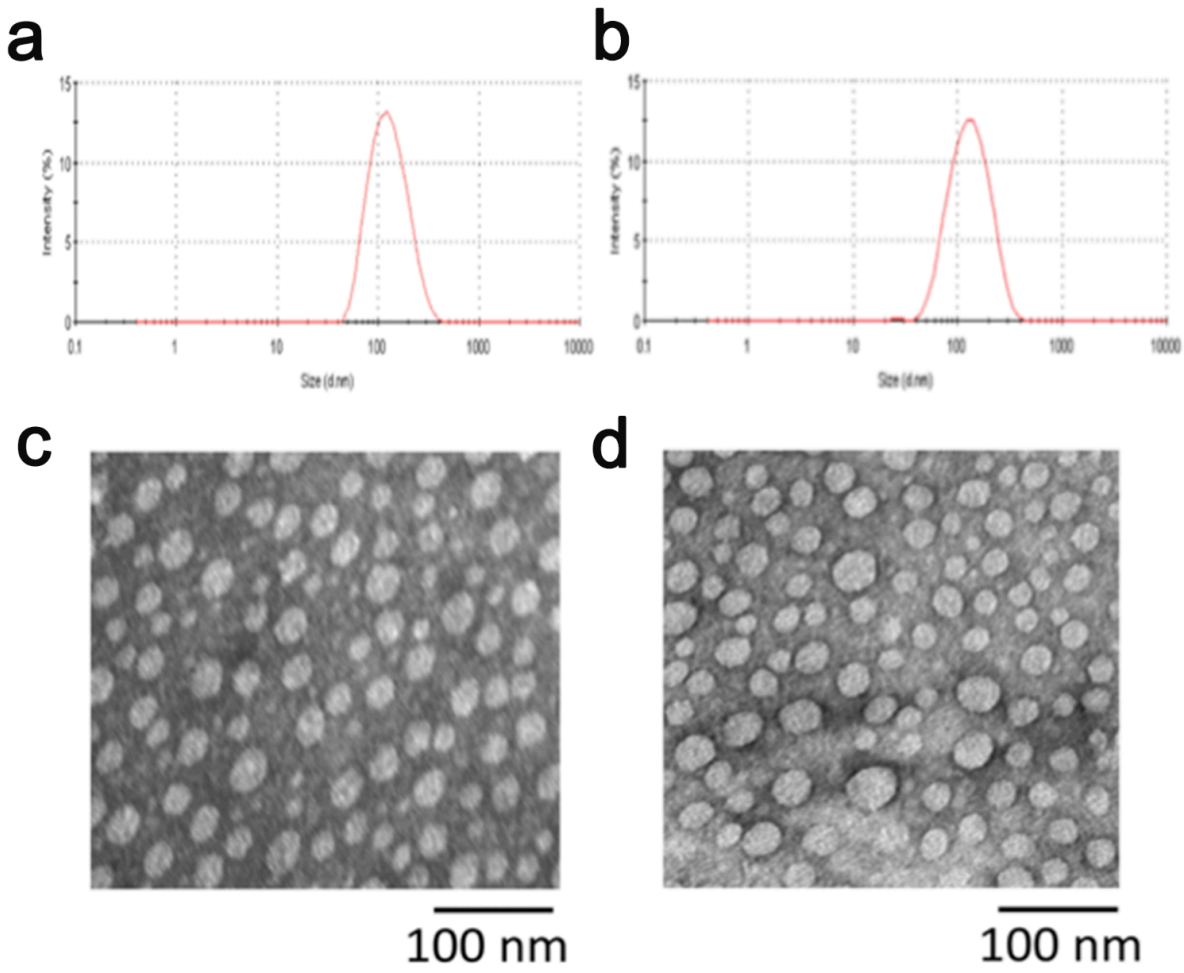

Figure 41. Size distribution and morphology of blank and PTX-loaded PEG_{5K}-Fmoc-NLG_2 micelles
Size distribution and morphology of micelles were examined by a zeta sizer and TEM at a carrier to drug ratio of 2.5:1. PTX concentration was kept at 1 mg/ml and blank micelle concentration was 20 mg/ml.

6.4.8 Release Kinetics of PTX & SUN From PEG_{5k}-Fmoc-NLG_2 Micelles

The *in vitro* release behaviors of PTX and SUN from PEG_{5k}-Fmoc-NLG_2 in PBS buffer solutions (pH 7.4) were studied through a dialysis method and are shown in Fig. 43. PTX or Sun loaded micelles, Taxol and sunitinib malate were used as controls. As shown in Fig. 43,

Taxol and SUN showed a burst release with more than 70% and 60% of drugs released, respectively, in the first 6 h. However, the PTX and SUN formulated in the micelles were exhibited significantly sustained release over free drugs. In particular, about 40% of PTX was released from micelles over 48 h, while over 80% of PTX was released from Taxol formulation. And for the SUN/micelles, only approximately 40% of cumulative release was monitored after 10 h, whereas, a burst release of SUN was recorded for the sunitinib malate with more than 80% of drug released from the dialysis bag. In addition, PTX release from PTX+SUN/PEG_{5k}-Fmoc-NLG_2 micelles was similar to that from PTX/PEG_{5k}-Fmoc-NLG_2, while SUN release from PTX+SUN/PEG_{5k}-Fmoc-NLG_2 was slightly faster compared to the single agent formulation. Overall, the PTX and SUN showed comparable release kinetics from co-formulated micelles. Importantly, this release profile of PTX and SUN from micelle formulation may benefit to the combinational treatment of chemotherapy drug, targeted therapy drug and immune therapy.

Table 7. Characterizations and Comparison of Two PEG-NLG Nanocarriers

Micelles	CMC (μM)	EC50 (μM)	Size (nm)	Stability (RT)
PEG_{2K}-Fmoc-NLG	0.737	1.25	96.9	--
PEG_{2K}-Fmoc-NLG:PTX 2.5:1	--	--	96.6	60h
PEG_{2K}-Fmoc-NLG:(PTX+Sun) 2.5:1	--	--	105	48h
PEG_{5K}-Fmoc-NLG_2	0.161	0.53	122	--
PEG_{5K}-Fmoc-NLG_2:PTX 2.5:1	--	--	125	1week
PEG_{5K}-Fmoc-NLG_2:(PTX+Sun) 2.5:1	--	--	126	96h

Drug concentrations in micelle were 1 mg/mL and blank micelle concentration was 20mg/mL. Size were measured by dynamic light scattering sizer.

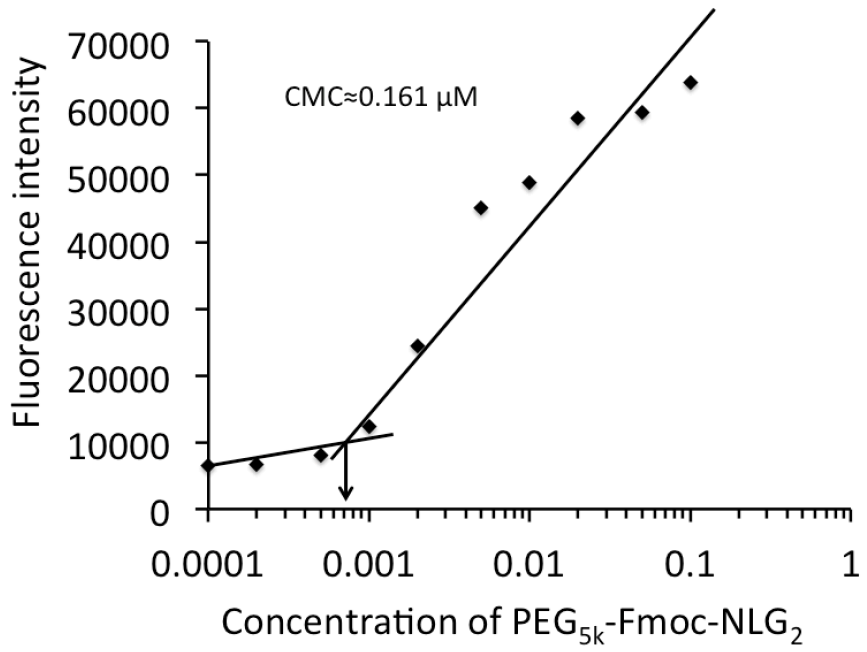

Figure 42. Measurement of CMC of PEG_{5K}-Fmoc-NLG_2 micelles.

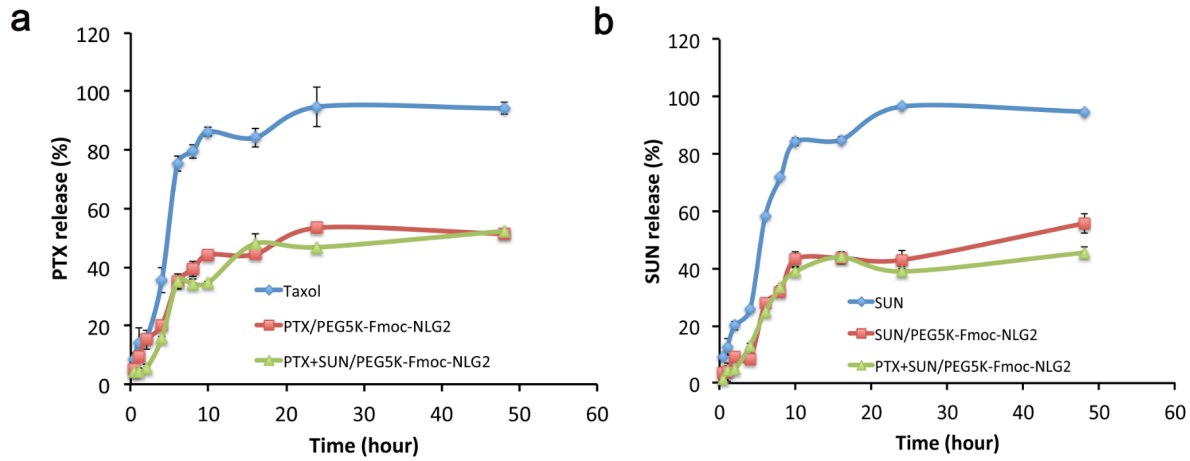

Figure 43. The *in vitro* release behaviors of PTX and SUN from PEG_{5k}-Fmoc-NLG_2 in PBS buffer.

(a) PTX release kinetics from Taxol, PTX/PEG_{5K}-Fmoc-NLG_2 or PTX+SUN/PEG_{5K}-Fmoc-NLG_2 micelles at the PTX concentration of 1mg/ml. (b) SUN release kinetics from free sunitinib, SUN/PEG_{5K}-Fmoc-NLG_2 or PTX+SUN/PEG_{5K}-Fmoc-NLG_2 micelles at the SUN concentration of 1mg/ml.

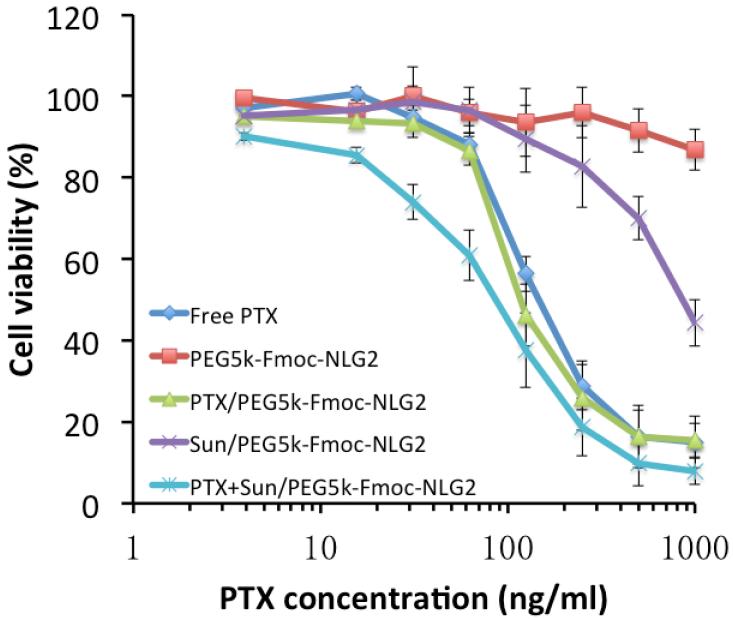

Figure 44. Cytotoxicity of micelles in 4T1.2 cells.

Cytotoxicity of PEG_{5K}-Fmoc-NLG_2 alone, free PTX, PTX/PEG_{5K}-Fmoc-NLG_2 mixed micelles, Sun/PEG_{5K}-Fmoc-NLG_2 mixed micelles and PTX+Sun/PEG_{5K}-Fmoc-NLG_2 mixed micelles were examined in a 4T1.2 mouse breast cancer cell line. Cells were incubated with various treatments for 3 days and cytotoxicity was determined by MTT assay.

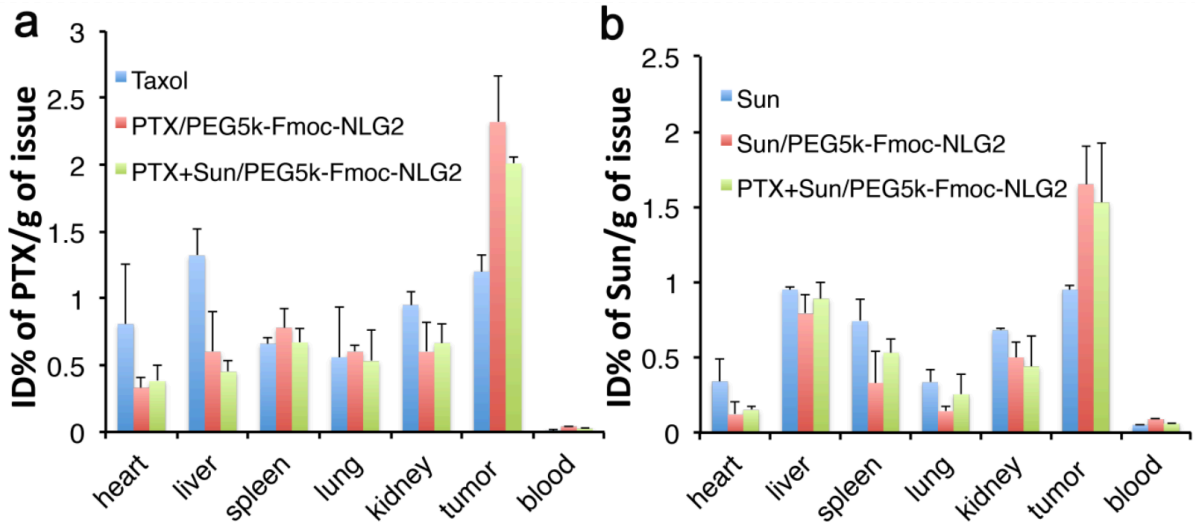

Figure 45. Biodistribution of different PTX and Sun formulations in 4T1.2 tumor-bearing mice.

Tissue and organs were harvested 24 h after i.v. administration of (a) Taxol, PTX/PEG_{5K} -Fmoc-NLG_2 mixed micelles or PTX+Sun/PEG_{5K}-Fmoc-NLG_2 mixed micelles at a PTX dose of 10 mg kg-1 or (b) Sun, Sun/PEG_{5K}-Fmoc-NLG_2 mixed micelles or PTX+Sun/PEG_{5K}

-Fmoc-NLG_2 at a Sun dose of 10 mg/kg. PTX and Sun concentrations were measured by HPLC-MS. *P<0.05 (N=3).

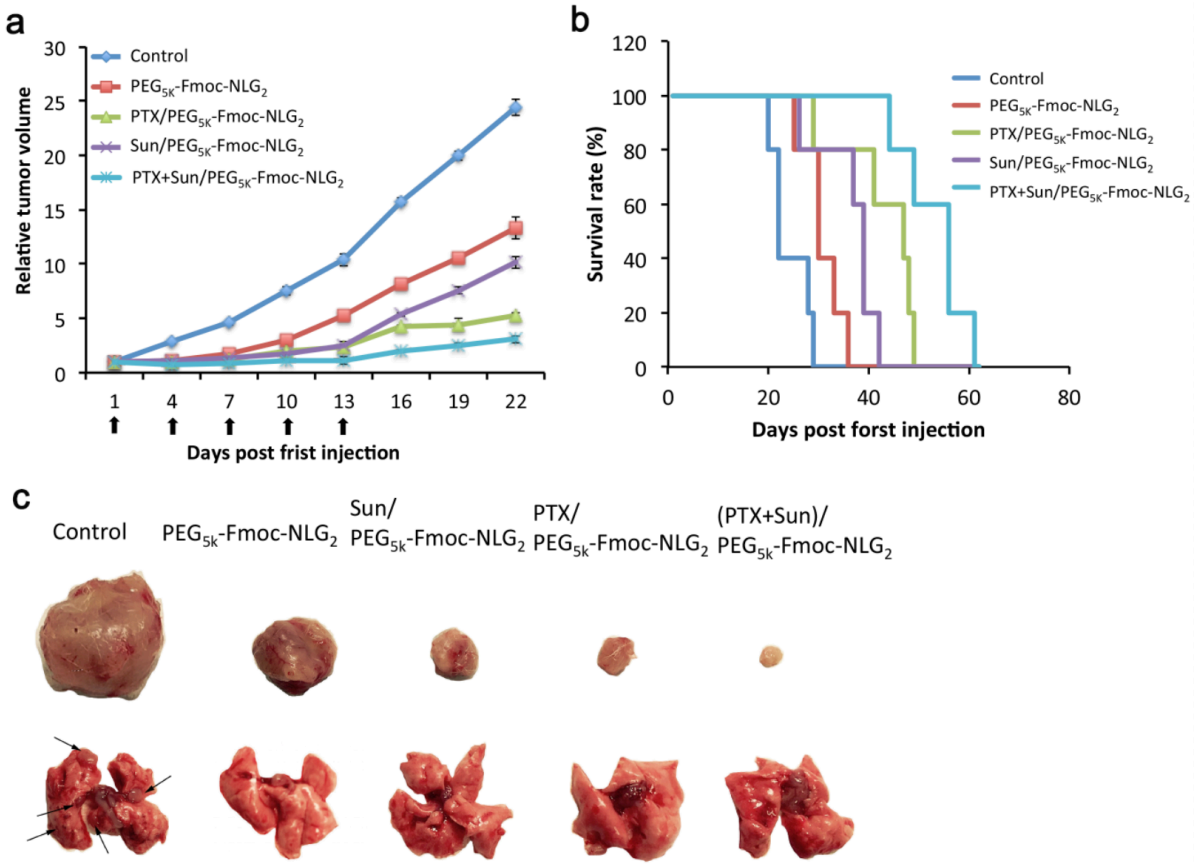

Figure 46. *In vivo* antitumor activity of PTX+Sun/PEG_{5k}-Fmoc-NLG_2 mixed micelles. (a) Enhanced *in vivo* antitumor activity of PTX+Sun/PEG_{5k}-Fmoc-NLG_2 mixed micelles compared to Sun formulated PEG_{5k}-Fmoc-NLG_2 ($^{\#}P < 0.05$, N = 5), PTX formulated in PEG_{5k}-Fmoc-NLG_2 micelles ($^{\&}P < 0.05$, N = 5) or PEG_{5k}-Fmoc-NLG_2 blank micelles. $^{*}P < 0.05$ (vs control, N = 5). Data represent means ± s.e.m. (b) Survival rate of various treatment groups. (c) Tumors and lungs were harvested by the end of five treatments. Lung metastases were indicated by the black arrows.

6.4.9 *In Vitro* Cytotoxicity

The cytotoxicity of blank and drug loaded PEG_{5k}-Fmoc-NLG_2 micelles against 4T1.2 were determined using an MTT assay and compared with free PTX or SUN (Fig. 44). The PEG_{5k}-Fmoc-NLG_2 carrier alone exhibited negligible cytotoxicity at various polymer concentrations ranged from 0.07 to 17.5 μg/mL for 72 h, which indicated good biocompatibility of nanocarriers. The IC50 of SUN/PEG_{5k}-Fmoc-NLG_2 and sunitinib malate

was 5.14 and 7.78 μM, respectively. The slightly enhanced cytotoxicity of SUN loaded micelle could be attributed to the enhanced delivery of drug to the 4T1.2 cells by micelle delivery system. As expected, the PTX/PEG_{5k}-Fmoc-NLG_2 ($IC50=10^3$ ng/mL) also showed enhanced cytotoxicity compared to free PTX (IC50=112 ng/ml). Moreover, the PTX+Sun/PEG_{5k}-Fmoc-NLG_2 showed the best *in vitro* antitumor activity with a low IC50 of 95ng/ml, this could due to the combined cell killing effect of PTX and SUN towards tumor cells.

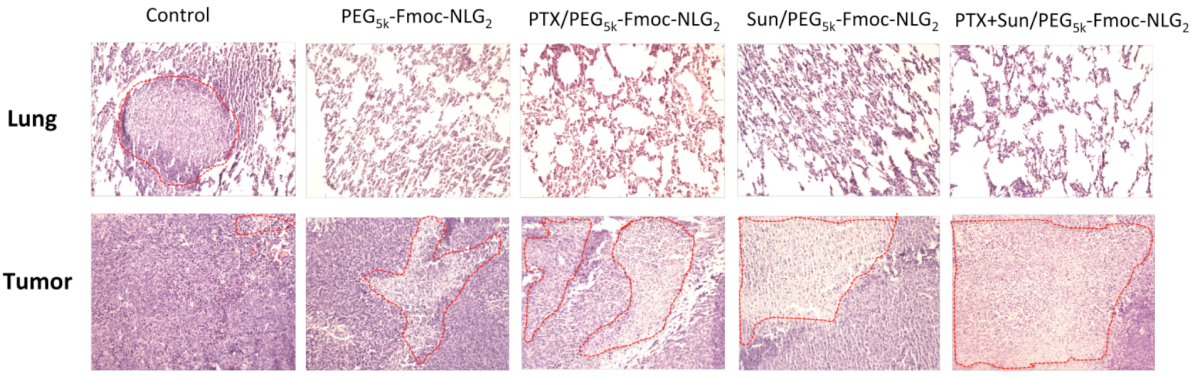

Figure 47. Histological analyses (H&E) of lung and tumor tissues
Tissues were collected at day 19 in the *in vivo* therapeutic study.

6.4.10 *In Vivo* Biodistribution and Blood Kinetics of PTX+SUN Formulated Micelles

The distribution, accumulation and elimination of administrated drugs in main organs and tumors could directly affect their therapeutic efficacy. To test whether PEG_{5k}-Fmoc-NLG_2 could specifically deliver SUN and PTX into tumors, *in vivo* biodistribution studies were performed in 4T1.2 tumor-bearing mice. Groups of 3 mice were treated intravenously with SUN+PTX/PEG_{5k}-Fmoc-NLG_2, PTX/PEG_{5k}-Fmoc-NLG_2, SUN/PEG_{5k}-Fmoc-NLG_2, Taxol or sunitinib malate at the same dosage of SUN and PTX (10mg/kg), major organs and tumor tissues were collected after 24h and PTX or SUN concentrations were measured by HPLC. As shown in Fig. 45, SUN+PTX/PEG_{5k}-Fmoc-NLG_2 showed higher drug accumulation in

tumors while lower distribution in other organs including lung, liver and kidney compared to Taxol or sunitinib malate. The single drug formulation did not show significant difference compared to co-loaded micelles. It can be concluded that PEG_{5k}-Fmoc-NLG_2 can selectively deliver both SUN and PTX to tumors, which favored the reduction of systemic toxicity.

6.4.11 *In Vivo* Antitumor Efficacy

The antitumor activity of PTX+SUN/PEG_{5k}-Fmoc-NLG_2 was evaluated in a 4T1.2 murine tumor metastasis model. Various formulations were given intravenously and tumor growth was followed during the therapeutic period (Fig. 46). As shown in Fig. 46a, all treatment groups including carrier alone group exhibited antitumor effect at day 19 compared to control group (saline treatment). PTX+SUN/PEG_{5k}-Fmoc-NLG_2 exhibited the best antitumor activity compared to PTX/PEG_{5k}-Fmoc-NLG_2 and Sun/PEG_{5k}-Fmoc-NLG_2, the antitumor effect still remained after stopping treatment on day 14. The tumor inhibition indexes of, carrier alone, PTX/PEG_{5k}-Fmoc-NLG_2, SUN/PEG_{5k}-Fmoc-NLG_2 and PTX+SUN/PEG_{5k}-Fmoc-NLG_2 group were 53.4%, 67.4%, 43.8% and 80.9% compared with saline group, respectively, which could be attributed to direct tumor killing effect of PTX/SUN and the subsequent immune stimulation effect by SUN and NLG. Fig. 46b displayed the body weights of mice, no significant fluctuation of the body weights was shown in all treatment groups, suggesting that no obvious systematic toxicity of the micelle formulations. The pathological H&E staining examinations of tumor tissue and lung tissue were carried out at day 19 (Fig. 47). Consistent with the lung tissue harvested by the end of therapeutic study, there are obvious lung metastasis nodules in the control group (Fig. 46c, Fig. 47). Administration of carrier alone, PTX/PEG_{5k}-Fmoc-NLG_2, SUN/PEG_{5k}-Fmoc-NLG_2 all caused some tumor cell death and nuclei breakdown in the tumor tissues and the PTX+SUN/PEG_{5k}-Fmoc-NLG_2 group showed a higher percentage of tumor cell death. This demonstrated that the

PTX+SUN/PEG_{5k}-Fmoc-NLG_2 treatment resulted in the most effective apoptosis of tumor cells (Fig. 47). Nevertheless, the detailed mechanisms of cell apoptosis are still unclear and need further investigation.

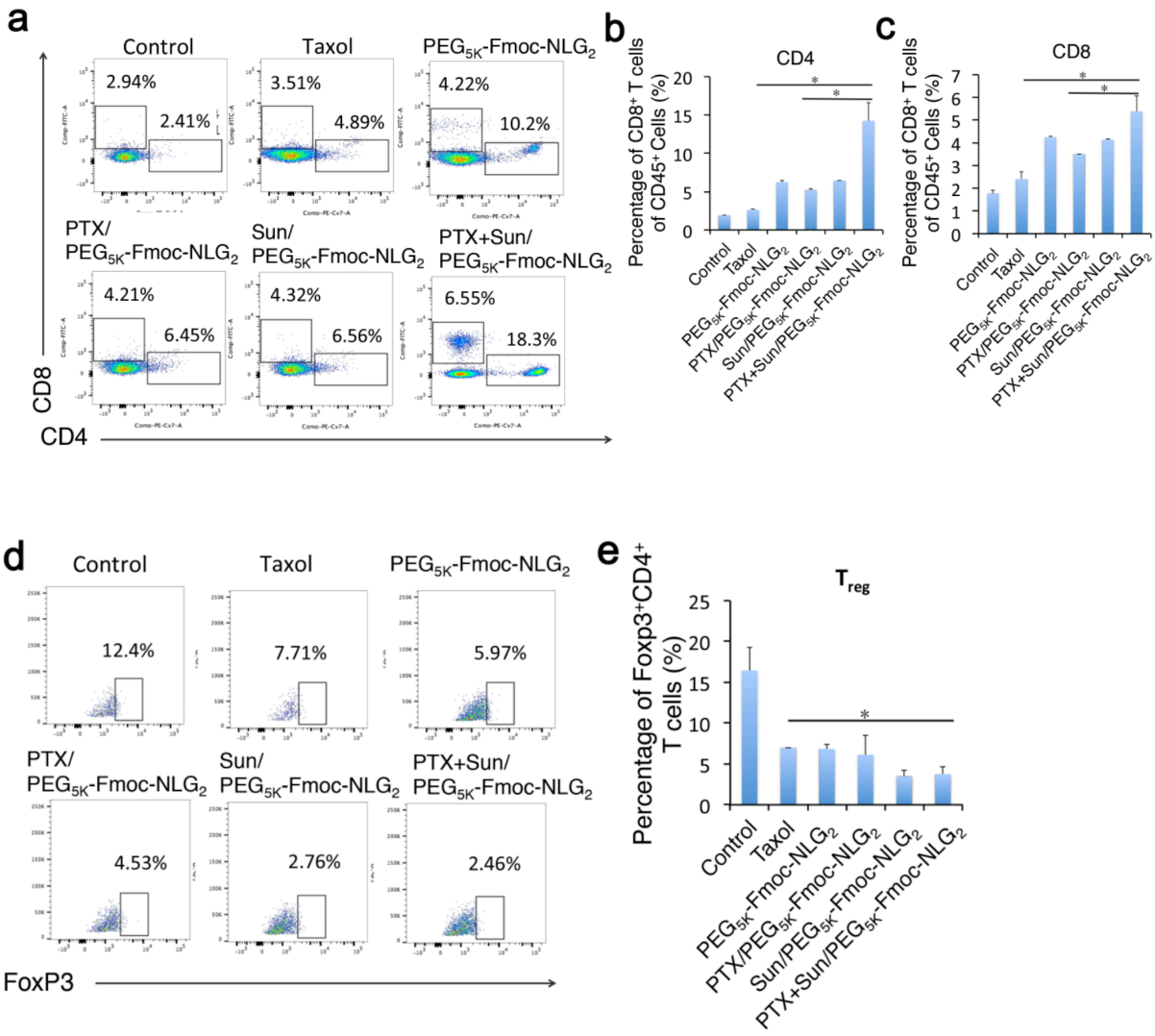

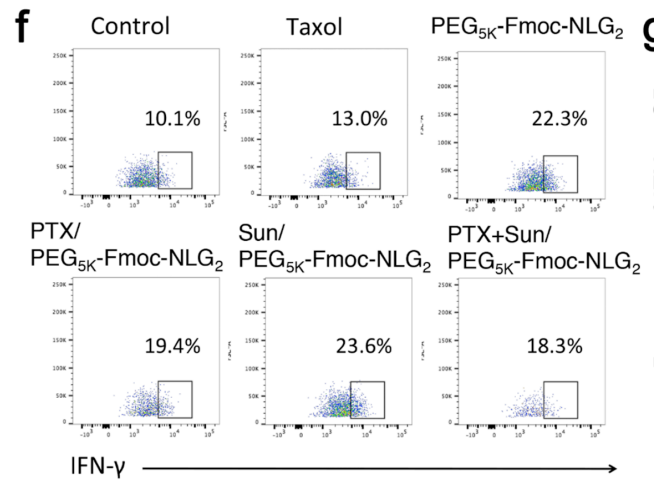
f
Control
Taxol
PEG5K-Fmoc-NLG2
10.1%
13.0%
22.3%
PTX/ PEG5K-Fmoc-NLG2
Sun/ PEG5K-Fmoc-NLG2
PTX+Sun/ PEG5K-Fmoc-NLG2
19.4%
23.6%
18.3%
IFN-γ

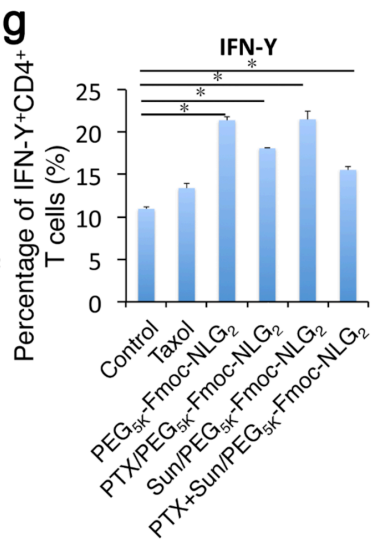
g
IFN-Y
Percentage of IFN-Y+CD4+ T cells (%)
0
5
10
15
20
25
Control
Taxol
PEG5K-Fmoc-NLG2
PTX/PEG5K-Fmoc-NLG2
Sun/PEG5K-Fmoc-NLG2
PTX+Sun/PEG5K-Fmoc-NLG2

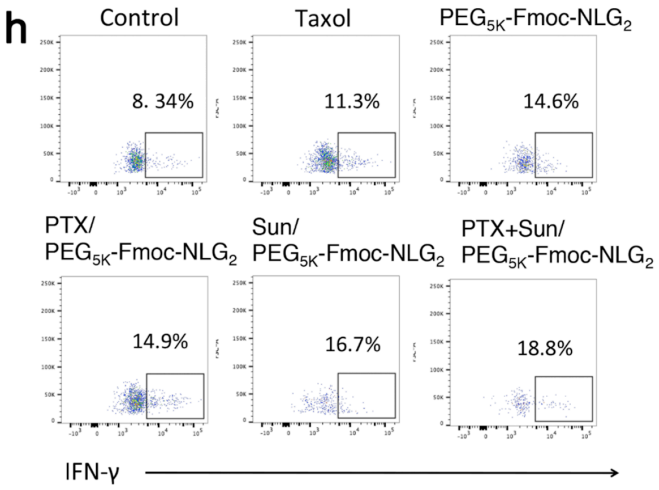
h
Control
Taxol
PEG5K-Fmoc-NLG2
8. 34%
11.3%
14.6%
PTX/ PEG5K-Fmoc-NLG2
Sun/ PEG5K-Fmoc-NLG2
PTX+Sun/ PEG5K-Fmoc-NLG2
14.9%
16.7%
18.8%
IFN-γ

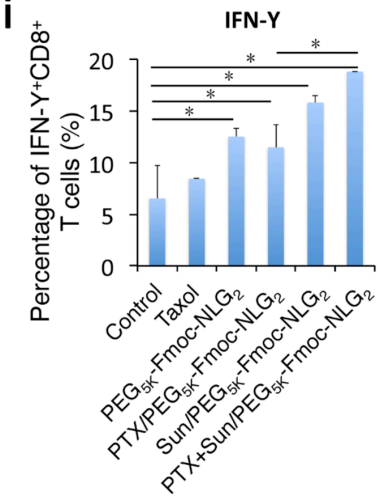
i
IFN-Y
Percentage of IFN-Y+CD8+ T cells (%)
0
5
10
15
20
Control
Taxol
PEG5K-Fmoc-NLG2
PTX/PEG5K-Fmoc-NLG2
Sun/PEG5K-Fmoc-NLG2
PTX+Sun/PEG5K-Fmoc-NLG2

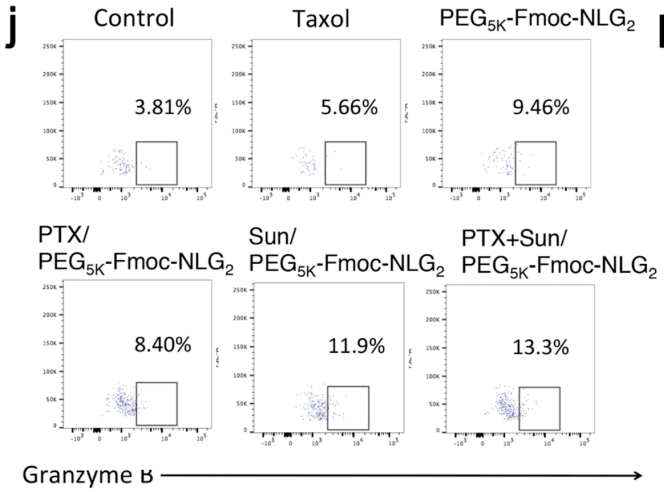
j
Control
Taxol
PEG5K-Fmoc-NLG2
3.81%
5.66%
9.46%
PTX/ PEG5K-Fmoc-NLG2
Sun/ PEG5K-Fmoc-NLG2
PTX+Sun/ PEG5K-Fmoc-NLG2
8.40%
11.9%
13.3%
Granzyme B

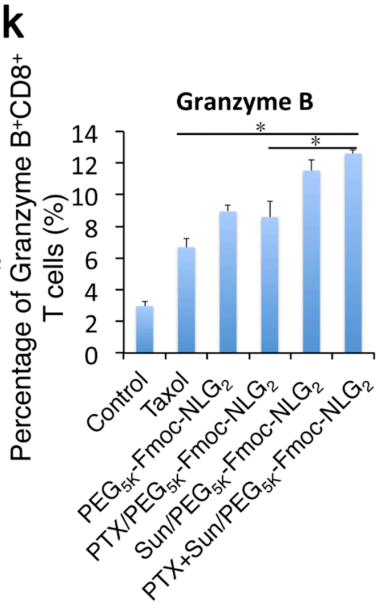
k
Granzyme B
Percentage of Granzyme B+CD8+ T cells (%)
0
2
4
6
8
10
12
14
Control
Taxol
PEG5K-Fmoc-NLG2
PTX/PEG5K-Fmoc-NLG2
Sun/PEG5K-Fmoc-NLG2
PTX+Sun/PEG5K-Fmoc-NLG2

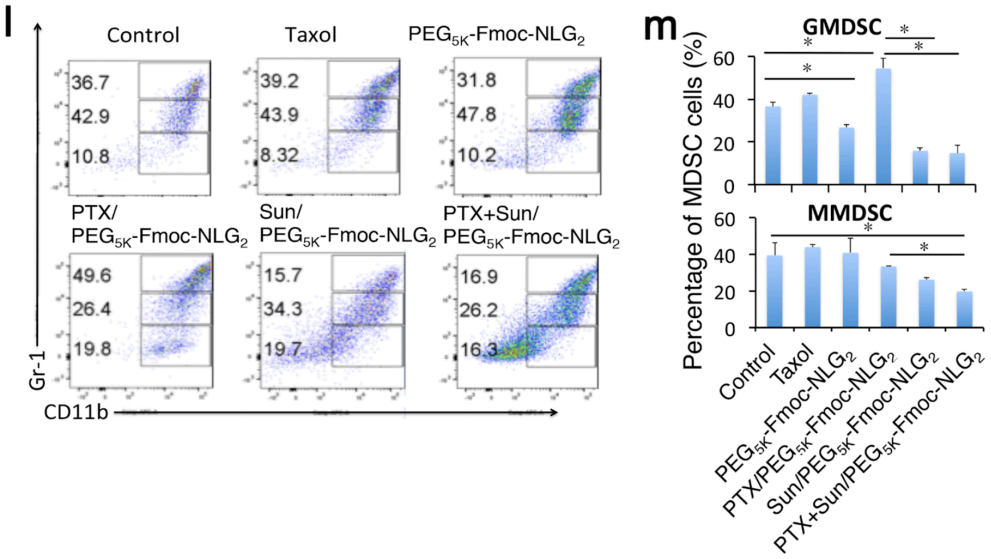

Figure 48. Flow cytometry analysis of immune cell subsets in tumor tissues.
4T1.2 tumor bearing mice were received various treatments of Taxol, PEG_{5K}-Fmoc-NLG_2, PTX/PEG_{5K}-Fmoc-NLG_2 mixed micelles, Sun/PEG_{5K}-Fmoc-NLG_2 mixed micelles or PTX+Sun/PEG_{5K}-Fmoc-NLG_2 mixed micelles at a PTX dosage of 10 mg/kg and sunitinib dosage of 10 mg/kg for three times at an interval of 3 days and tumoral T-cell infiltration, including (a-c) $CD4^+$ and $CD8^+$, (d-e) $FoxP3^+$ T regulatory cells, (f-g)IFN-γ^+CD4^+ T cells, (h-i)IFN-γ^+CD8^+ T cells and (j-k) granzyme B-positive $CD8^+$ T cells, were measured by flow cytometry. (l-m) MDSC subsets ($Gr\text{-}1^{high}CD11b^+$ granulocytic (G-MDSC) and $Gr\text{-}1^{int}CD11b^+$ monocytic (M-MDSC)) were also detected by flow cytometry. The bars represent means ± s.e.m. $^*P < 0.05$.

6.4.12 The Change of Immune Cell Populations in the TME

Tumor tissues from mice received various treatments were harvested and analyzed for their tumor infiltrating immune cell populations using flow cytometry. Antitumor cytotoxic $CD8^+$ T cells and $CD4^+$ T helper cells are of paramount importance in immune defense against tumors. Figure. 48a-c showed infiltration of more $CD4^+$ and $CD8^+$ T cells in the tumors treated with PEG_{5k}-Fmoc-NLG_2 compared to control group and the combination treatment of PTX+SUN/PEG_{5k}-Fmoc-NLG_2 yielded the highest percentages of $CD8^+$ T cells in the TME among all of the groups ($p<0.001$ vs. PBS; $p<0.05$ vs. Taxol and PTX/PEG_{5k}-Fmoc-NLG_2). All treatment groups showed a decrease of $Foxp3^+CD4^+$ cells (Fig. 48d-e). It is interesting to note that the PTX+SUN/PEG_{5k}-Fmoc-NLG_2 exhibited a dramatically increased IFN-γ^+CD8^+

T cell infiltration but not IFN-γ^+CD4^+ T compared to carrier alone, Taxol or the PTX/PEG_{5k}-Fmoc-NLG_2 micelles (Fig. 48f-i). The percentage of granzymeB^+CD8^+ cells also greatly elevated in the combinational treatment group compared to Taxol or PTX/PEG_{5k}-Fmoc-NLG_2 (Fig. 48j-k). For the immune suppressive cell populations, the myeloid-derived suppressor cells (MDSCs) play important roles in tumor immune escape and similarly as we observed before, an increase in MDSCs cells in the tumor was observed in Taxol or PTX/PEG_{5k}-Fmoc-NLG_2 treatment group (Fig. 48l-m). To combat this unfavorable upregulation, we treated the mice with SUN/PEG_{5K}-Fmoc-NLG_2, both the intratumoral GMDSCs and MMDSCs were significantly decreased and when combined with PTX treatment, the percentage of MDSCs remained as low as those of SUN monotherapy, indicating the strong ability of SUN to reverse the tumor's immune suppression.

6.5 DISCUSSION

Previous we developed a PEG_{2k}-Fmoc-NLG based dual-functional carrier for efficient delivery of PTX. This carrier was synthesized by conjugating one molecule of NLG to a hydrophilic motif PEG (MW = 2000), it could significantly inhibit the murine 4T1.2 breast cancer and effectively induce the antitumor immune response in tumor site, however, the percentage of immunosuppressive MDSC cells was significantly increased in the PTX/PEG_{2k}-Fmoc-NLG groups and there was also a slight decrease in tumor infiltrating $CD4^+$ and $CD8^+$ T cells compared to carrier alone. Meanwhile, the tumoral expression of other immune checkpoint proteins such as PD-L1 and PD1 were significantly upregulated in tumor with PTX treatment. We subsequently showed that selective depletion of MDSCs with anti-Gr-1 antibody in combination with chemoimmunotherapy significantly improved

antitumor efficacy in a murine mouse model, providing evidence that MDSCs upregulation contribute to tumor immune evasion and relapse (Fig. 34). Induction of MDSCs is a fundamental immune escape mechanism employed by the tumor-bearing host in response to chemotherapy treatment such as doxorubicin and cyclophosphamide[203, 204]. The increased MDSCs in tumor might due to a series of inflammatory cytokines, chemokines and growth factors induced by PTX, which promoted the immature myeloid cells proliferation and expansion. As shown in Figs. 36 and 37, CCL2, CXCL1, CXCL2 and CXCL12 were among chemokine mediators induced by PTX/PEG-Fmoc-NLG treatment, candidate effector molecules that may promote the proliferation and recruitment of MDSCs. We tried to knockdown one of the critical chemokine gene in the tumor cells, however, it could not reverse the immune-inhibitory MDSC increase exerted by PTX/PEG-Fmoc-NLG. This inspired us to find a combinational therapy that can affect all these chemokines and decrease MDSCs accumulation in tumor area.

It has been reported that the tyrosine kinase inhibitor SUN decreased tumor growth and improved survival in B16F10 melanoma and treatment of tumor-bearing mice with SUN lead to reduced vessel density and decreased accumulation of $CD11b^{+}Gr1^{+}$ myeloid derived suppressor cells in tumors. The ability of SUN reversing immune suppressive tumor microenvironment might due to inhibition of differentiation of dendritic cells (DCs) by inhibiting tyrosine kinases (VEGFR, PDGFR-α and –β, Fms-like TK-3 and kit) or prevent the accumulation of MDSCs by inhibition of STAT3 and c-Kit or directly induce the apoptosis of MDSCs. In this study, either SUN alone or co-treated with PTX significantly decreased the chemokine expression both *in vitro* and *in vivo* (Fig. 37). In order to co-delivery SUN with PTX, we developed a more advanced drug delivery system PEG_{5k}-Fmoc-NLG_2 with increased amount of NLG, which not only contributed to the carrier/drug interaction but the anticancer effect of carrier. The PEG_{5k}-Fmoc-NLG_2 had a lower CMC value compared to

PEG_{2K}-conjugates (Fig. 42). Our data indicated that the PEG_{5k}-Fmoc-NLG_2 conjugates were significantly more effective than the PEG_{2k}-Fmoc-NLG system in micelle stability and drug loading capability (Tab. 7). The PTX loaded PEG_{5k}-Fmoc-NLG_2 showed 3 times longer stable time than the previous system with no significant change of the micelle size. This might due the increase in the hydrophobic core, which contributes to the loading of hydrophobic drug through hydrophobic interaction and π–π interaction. Another modification in the carrier was increasing the PEG chain to 5000kd, which significantly increased the *in vivo* circulation time of micelles as we reported before[31]. It has been demonstrated that the new delivery system can well accommodate both PTX and SUN in one formulation and achieve enhanced *in vitro* cytotoxity and *in vivo* antitumor activity.

In addition to the simplicity in codelivery, our system could provide a programmable release of various drug components via both physical encapsulation (for PTX and SUN) and chemical conjugation (for NLG). PTX/SUN and NLG shall have different temporal release kinetics upon codelivery to tumors. PTX/SUN has a much faster rate of release compared to that of NLG. The relatively rapid release of PTX and SUN will lead to the first round of antitumor response that will be further potentiated by the immune response that follows. The immune response could result from enhanced antigen presentation following PTX- and SUN-mediated killing of tumor cells and/or direct effect of SUN and PTX on immune cells. More importantly, addition of SUN effectively reverses some of the untoward effects that are associated with delivery of PTX via PEG-NLG-based nanocarrier. Meanwhile, the slow release of active NLG919 from the prodrug will help to sustain or enhance the magnitude of immune response by reversing IDO-mediated immune suppression. As a result, our approach has led to significantly improved antitumor activity as shown in Fig. 46a. It is also demonstrated that the SUN+PTX/PEG-Fmoc-NLG significantly increased tumoral infiltrating $CD8^+$ T cells, while reducing intra-tumor MDSCs and T_{regs}, creating a more

immunogenic microenvironment for antitumor therapy.

Our results showed that combining the targeted therapy SUN treatment, chemotherapy treatment of PTX and immunocheckpoint inhibition of NLG919 exerted potent complementary antitumor effects mediated by direct tumor cell killing effect, dendritic cell activation, a reduction in MDSC and reversing immunosuppressive environment, resulting in enhanced recruitment of cytotoxic T-cells and significant antitumor activity.

6.6 CONCLUSION

In this report, we found that tumor-targeted codelivery of PTX and SUN in PEG_{5k}-Fmoc-NLG_2 micelles changed the chemokine profile of the tumor which led to decreased percentage of MDSCs and increased cytotoxic T cell infiltration in the TME, thereby abrogating tumor-associated immune suppression. Our studies provide evidence in an *in vivo* animal model that targeted co-delivery of tyrosine kinase inhibitors and small molecule chemotherapy drug to tumors can be used as a novel strategy to enhance the therapeutic efficacy for advanced tumors.

7.0 TARGETED CODELIVERY OF DOXORUBICIN AND IL-36γ EXPRESSION PLASMID FOR AN OPTIMAL CHEMO-GENE COMBINAITON THERAPY AGAINST CANCER LUNG METASTASIS

7.1 ABSTRACT

Cancer metastasis is the main cause for the high mortality in breast cancer patients. Co-delivery of chemodrugs and gene therapeutics in a single system is a promising strategy for effective anti-metastatic therapy. In this work we developed two novel copolymers (POEG-*st*-Pmor and POEG-*st*-Ppipe) for targeted co-delivery of IL-36γ expression plasmid and doxorubicin (Dox) to lung metastasis of breast cancer. Both polymers readily formed micelles that were effective in loading Dox and simultaneously forming complexes with IL-36γ plasmid. Interestingly, particles co-loaded with Dox and plasmid or siRNA were significantly smaller and more stable than the particles loaded with Dox only. Intravenous delivery of the co-loaded nanoparticles led to effective delivery of both Dox and siRNA/plasmid to lungs as well as distant s.c. solid tumors. Gene transfection in both lungs and s.c. tumors was significantly higher with our two polymers compared to PEI. In the tumor therapy study, the Dox+IL-36γ plasmid/POEG-*st*-Pmor polymer could not only bring improved anti-metastatic effect but synergistically enhance the type I immune response by increasing the IFN-γ positive $CD4^+$ and $CD8^+$ T cells and simultaneously decreasing the immunosuppressive myeloid-derived suppressor cell (MDSCs) in the lung. POEG-*st*-Pmor and POEG-*st*-Ppipe may represent a simple and effective delivery system for an optimal chemo-gene combination therapy.

7.2 INTRODUCTION

Cancer metastasis, which refers to the spread of cancer cells from the primary tumor site to distant tissues or organs, is the main cause of breast cancer-related deaths[205, 206]. Lung, liver, bone and brain are major organs for breast cancer metastases and more than 60% of breast cancer patients show metastasis in lungs at late stages[207, 208]. Although surgery may be effective in treating the primary tumor, chemotherapy is necessary for advanced lung metastases[209, 210]. Despite recent advancements in chemotherapy, the five-year survival rate of metastatic breast cancer remains low (~20%) with serious side effects, mainly due to off-target toxicity[211]. Therefore, the development of therapies to achieve efficient targeting of metastasis is highly demanded, which will likely achieve enhanced therapeutic efficacy and reduced systemic toxicities.

Current lung metastasis targeted delivery largely relies on the size-driven systems such as nanoparticles, micelles and liposomes[212, 213, 214]. Although these nanoscale carriers show promising results, drawbacks such as poor stability, complex formulation strategy and potential toxicity remain unresolved. Most current nanocarriers can improve therapeutic effect through enhancement of permeation and retention (EPR) effect in primary tumors with vasculature pore sizes above 100 mm[3,126]. However, small metastatic tumors are usually less vascularized, which limits the access of nanoparticles to these lesions[215]. Thus, drug delivery systems with well-defined carrier structures, sufficient *in vivo* stability and high targeting efficiency are urgently needed to overcome the current problems. It has been reported that small ligands such as linear tertiary amines on the carriers may benefit lung targeted drug delivery since the lung is proven to be a site for accumulation of numerous basic amines[216, 217]. These studies have inspired us to explore the potential of tertiary amine-derived carriers as targeting systems for treatment of lung metastasis.

We herein developed two multifunctional delivery systems that are based on an amphiphilic polymer with morpholine or piperazine attached to the pendant side chains (POEG-*st*-Pmor and POEG-*st*-Ppipe) for codelivery of small molecule chemotherapy drugs and nucleic acids (siRNA and plasmid). The hydrophobic anticancer drugs are expected to be incorporated into the hydrophobic core through hydrophobic-hydrophobic interaction and π-π stacking. Morpholine or piperazine is incorporated into the polymer to introduce positives charges to form complexes with nucleic acids. The positively charged morpholine and piperazine groups in the polymers can also facilitate the accumulation of the carrier in the lung due to the presystemic extraction and the interaction of positively charged tertiary amine with negatively charged cell membrane in the lung. Doxorubicin (Dox) and IL-36γ plasmid were selected as the model drug and DNA for the combination therapy. Dox is a first-line chemotherapeutic drug in the treatment of a broad range of cancers including breast, ovary, bladder, and lung cancers, and breast cancer metastasis[218, 219]. Interleukin cytokine is reported to have a synergistic effect in combination with conventional antitumor treatments such as chemotherapy[220, 221]. Interleukin 36 (α, β, γ) belongs to IL-1 family of cytokines and the three isoforms share the same receptor complex[222]. IL-36γ is reported to promote the differentiation of type 1 effector lymphocytes, including $CD8^+$, NK, and γδT cells *in vitro*[222]. The tumoral expression of IL-36γ exerts strong antitumor immune responses *in vivo* and transforms the tumor microenvironment in favor of tumor eradication[222]. We hypothesized that codelivery of Dox and IL-36γ plasmid via our multifunctional carriers represents a simple and effective approach for the treatment of lung metastasis. We first examined the biophysical properties of the nanocarrier co-loaded with Dox and IL-36γ plasmid. The efficiency of delivery and transfection was then examined both *in vitro* and *in vivo*. Finally, the antitumor effect of Dox+ IL-36γ/polymer as well as the underlying mechanism was investigated.

7.3 EXPERIMENTAL PROCEDURES

7.3.1 Materials and Reagents

Doxorubicin (>99%) was purchased from LC Laboratories (MA, USA). Dicyclohexylcarbodiimide (DCC) was purchased from Alfa Aesar (MA, USA). 4-(Dimethylamino) pridine (DMAP) was purchased from Calbiochem−Novabiochem Corporation (CA, USA). Vinylbenzyl chloride, 4-Cyano-4-[(dodecylsulfanylthio carbonyl)sulfanyl]pentanoic acid, oligo(ethylene glycol) methacry-late OEGMA (average Mn = 500), 2,2-Azobis(isobutyronitrile) (AIBN), trypsin-EDTA solution, 3-(4,5-dimethylthiazol-2-yl)-2,5-di phenyl tetrazolium bromide (MTT) and Dulbecco's Modified Eagle's Medium (DMEM) were all purchased from Sigma-Aldrich (MO, U.S.A.). Opti-MEM medium was purchased from Invitrogen (Carlsbad, USA). AIBN was purified by recrystallization in anhydrous ethanol. Fetal bovine serum (FBS) and penicillin-streptomycin solution were purchased from Invitrogen (NY, U.S.A.).

7.3.2 Synthesis of VBMor and VBPipe-Boc Monomer

Vinylbenzyl chloride (167.2 mg, 1.1 mM), morpholine (95.8 mg, 1.1 mM) or piperazine-Boc (94.7 mg, 1.1mM), and K_2CO_3 (0.69 g, 5 mM) were dissolved in 6 mL DMF and stirred at 50°C for 6 h. After cooling down to room temperature, 20 mL water was added to the mixture, followed by three times extraction with 50 mL CH_2Cl_2. After evaporation of CH_2Cl_2, the crude product was purified by column chromatography with petroleum ether/ethyl acetate (v/v, 4/1~2/1) as the elution liquid. VBMor or VBPipe-Boc monomer was obtained with a 71% or 75% yield, respectively.

7.3.3 Synthesis of POEG-*st*-Pmor, POEG-*st*-P(pipe-Boc) and POEG-*st*-Ppipe Polymer

VBMor monomer (228.8 mg, 1.13 mmol) or VBpipe-Boc monomer (341.2 mg, 1.13 mmol), OEG500 (100 mg, 0.20 mmol), AIBN (1 mg, 0.0062 mmol), 4-Cyano-4-[(dodecylsulfanylthiocarbonyl) sulfanyl] pentanoic acid (6 mg, 0.015 mmol), and 1 mL of dried tetrahydrofuran were added into a Schlenk tube, and deoxygenated by free-pump-thawing for three times. Then the mixture was filled with N_2 and immersed into an oil bath thermostated at 80 °C to start the polymerization. After 24 h, the reaction was quenched by immersing the tube into liquid nitrogen and the mixture was precipitated in hexane for 3 times. The product POEG-*st*-Pmor or POEG-*st*-P(pipe-Boc) was obtained after vacuum drying. POEG-*st*-Ppipe polymer was further synthesized by Boc deprotection of POEG-*st*-P(pipe-Boc) precursor in a mixture of CH_2Cl_2/TFA (1: 1, v/v).

7.3.4 Preparation and Characterization of IL-36γ Plasmid/Dox-co-formulated Micelles

Dox-loaded POEG-*st*-Pmor and POEG-*st*-Ppipe micelles were prepared by the dialysis method. Briefly, 10 mg of polymer was dissolved in 5 mL of DMSO and mixed with 100 μL of Dox DMSO solution (10 mg/ml). To remove free Dox from the Dox-incorporated micelles, the solution was dialyzed against PBS using dialysis membrane with a MW cutoff of 3500. The solution was lyophilized and resolubilized in 1mL PBS. Drug-free micelles were prepared similarly. For plasmid DNA complexation, polymeric micelles were diluted to different concentrations in water and mixed with plasmid DNA solution to obtain the desired N/P ratios. This mixture was allowed to incubate at RT for 20 min prior to further characterization.

7.3.5 *In Vitro* Characterization of Polymers

The particle size and zeta potential of POEG-*st*-Pmor and POEG-*st*-Ppipe polymers were determined by dynamic light scattering (Nano-ZS 90, Malvern Instruments, Malvern, UK). The morphology of POEG-*st*-Pmor and POEG-*st*-Ppipe polymers was observed under a transmission electron microscope (TEM). The micelles were placed on a copper grid covered with nitrocellulose. The samples were negatively stained with phosphotungstic acid and dried at room temperature before measurement.

Drug loading capacity (DLC) and Drug loading efficiency (DLE) were determined as described before. The amount of Dox loaded in the micelles was determined by high performance liquid chromatography (HPLC, Shimadzu LC-20AD, Japan). The DLC of Dox/micelles were calculated using the equation： DLC=Drug incorporated/(input polymer+Drug)×100%

7.3.6 Critical Micelle Concentration

The critical micellar concentration (CMC) was determined using Nile Red as a fluorescence probe [223]. Micelles of various concentrations (0.0001 to 1 mg/mL) were first prepared. Two μl of a Nile Red solution in acetone (0.97 mg/mL) were then added to each sample and acetone was evaporated prior to fluorescence measurements using a microplate reader. Fluorescence from emission wavelength ranging from 560 to 750nm was recorded with an excitation wavelength of 550 nm.

7.3.7 *In Vitro* Drug Release Study

The *in vitro* Dox release kinetics for the POEG-*st*-Pmor and POEG-*st*-Ppipe micelles was determined by a dialysis method. Briefly, 0.5ml of Dox-loaded micelles and micelles co-loaded with Dox and IL-36γ plasmid at a Dox concentration of 0.5 mg/mL were placed

into a dialysis bag (MW cutoff 3500), respectively. The dialysis bag was incubated in 100 mL PBS with gentle shaking at 37 °C. Two ml of PBS solution outside of the dialysis bag was collected at different time points and equal amount of fresh PBS was added back. The concentrations of released Dox were determined by HPLC [224].

7.3.8 Gel Retardation Assay

Plasmid/polymer complexes were prepared at different N/P ratios, ranging from 0.1 to 20 (plasmid DNA concentration was fixed at 5 mg/ml). The resulting complexes were then electrophoresed on a 1% agarose gel in TAE buffer at 120 mV for 30 min, and visualized using a UV illuminator with ethidium bromide staining. Free plasmid DNA was used as a control.

7.3.9 Cell Culture

The murine breast cancer cell line 4T1.2 was cultured in DMEM medium supplemented with 10% FBS and 1% penicillin/streptomycin at 37 $^{\circ}$C in 5% CO_2 atmosphere.

7.3.10 *In Vitro* Cytotoxicity

The cytotoxicity of Dox-formulated POEG-*st*-Pmor and POEG-*st*-Ppipe micelles, IL-36γ plasmid-complexed micelles and Dox+IL-36γ plasmid-co-loaded micelles were assessed in 4T1.2 breast cancer cells and compared to free Dox. Briefly, 4T1.2 cells (2000 cells/well) were seeded in 96-well plates for overnight and were treated with various concentrations of Dox formulations for 72h. MTT solution was added to each well and MTT formazan was solubilized by DMSO after 2h of incubation. The absorbance in each well was measured by a microplate reader at a wavelength of 570 nm. Cell viability was calculated as [(ODtreat −

ODblank)/(ODcontrol − ODblank) × 100%]. The cytotoxicity of POEG-*st*-Pmor and POEG-*st*-Ppipe micelles alone was similarly tested in 4T1.2 cells as described above.

7.3.11 Stability of the Micelles in BSA

BSA was used to simulate the physiological environment to investigate the stability of POEG-*st*-Pmor and POEG-*st*-Ppipe micelle complexes under the mimicked physiological conditions. Plasmid DNA/micelle complexes and plasmid DNA+Dox/micelle complex were prepared as described above and incubated with BSA (30 mg/ml). pDNA/PEI complexes were used as a control. Sizes of complexes were followed at different time point as an indication of stability.

7.3.12 Intracellular Localization of Micelle Complexes

4T1.2 cells (1×10^4 cells/well) were seeded in 6 well plates and incubated for 24 h. FAM-siRNA/POEG-*st*-Pmor micelle complexes, Dox+FAM-siRNA/POEG-*st*-Pmor micelles, FAM-siRNA/POEG-*st*-Ppipe micelles, and Dox+FAM-siRNA/POEG-*st*-Ppipe micelles (siRNA concentration: 10 pmol/well) were then added and incubated with the cells for 2h. After removing the cell culture medium, cells were washed with cold PBS for three times. To label the cell nucleus, cells were treated with Hoechst (0.1 μg/mL) for 15 min. Cell were then washed with cold PBS for three times before observation under a confocal scanning microscope.

7.3.13 *In Vitro* Plasmid Transfection

4T1.2 cells were seeded in a 96-well plate and incubated for 24 h until cells were 80% confluent. Cells were then transfected with EGFP plasmid/POEG-*st*-Pmor micelle complexes (N/P=20), EGFP plasmid/POEG-*st*-Ppipe micelle complexes (N/P=20) or EGFP plasmid/PEI

(N/P=20) complexes in serum-free opti-DMEM medium. After 4 h incubation, transfection medium was removed and 100 μL of fresh complete medium were added to each well. PBS group was used as a control. After 48h, the transfected cells were observed under a fluorescence microscope (OLYMPUS America, Melville, NY).

7.3.14 *In Vivo* Fluorescence Imaging

Female Balb/C mice bearing 4T1.2 tumor (~400 mm^3) in the mammary fat pad were used to investigate the biodistribution and *in vivo* transfection efficiency of our micellar carriers.

AF647 siRNA was used to examine the biodistribution of nucleic acids-loaded POEG-*st*-Pmor and POEG-*st*-Ppipe *in vivo*. At 24 h after injection of the AF647 siRNA-loaded nanomicelles through tail vain, major organs and tissues (lung, liver and tumors) were collected, embedded in OCT, and frozen in liquid nitrogen. The specimens were cryosectioned into 20 μm sections. The signals of AF647-labeled siRNA in tissues were examined under a confocal microscope.

The *in vivo* transfection efficiency of POEG-*st*-Pmor and POEG-*st*-Ppipe micellar carriers was evaluated with EGFP plasmid as a reporter gene. Linear PEI was used to as control. Various formulations were injected i.v. into tumor-bearing mice at a dose of 50 μg plasmid per mouse, and one day later, the mice were injected with 1 μg of Hoechst one hour before sacrifice. The fluorescence signal of GFP in the cryosections was examined under a confocal microscope.

7.3.15 Breast Cancer Lung Metastasis Mouse Model

Female Balb/c mice at 4-6 weeks of age were injected with 2×10^5 4T1.2 cells through the tail vein. Five days after tumor cell injection, mice were randomly divided into 6 groups. POEG-*st*-Pmor was chosen as a representative carrier system for codelivery of IL-36γ

plasmid and Dox. Animals were treated intravenously with free POEG-*st*-Pmor micelles, IL-36γ plasmid/POEG-*st*-Pmor micelles, Dox+control plasmid/POEG-*st*-Pmor micelles and Dox+IL-36γ plasmid/POEG-*st*-Pmor micelles every three days for three times. The PBS treatment group was used as control. Dox dosage was 5 mg/kg and plasmid dosage was 50μg per mouse. Lung tissues were harvested and weighted 11 days after the first injection. Pulmonary metastases were enumerated by intra-tracheal injection of India ink solution. India ink-injected lungs were washed in Feket's solution (300 ml 70% EtOH, 30 ml 37% formaldehyde and 5 ml glacial acetic acid) and white tumor nodules against a dark blue lung background were counted.

7.3.16 Histopathological Analysis

The lung tissues were harvested and fixed in 10% formalin after the above treatments. The fixed samples were then embedded in paraffin and the tissue sections were stained with hematoxylin/eosin and analyzed for the presence of metastases under microscope. The total number of metastases per lung section was counted in different treatment groups.

7.3.17 Analysis of Tumor-infiltrating Lymphocytes and Myeloid-derived Suppressor Cells

Lung tissues were collected in serum free RPMI medium and cut mechanically with scissors. Liberase TL (0.3mg/ml) and DNase I (0.3 mg/ml) were used to digest the lung tissue and tumor nodules. Tissues were further grinded and filtered through a 40-mm cell strainer. TILs and MDSC cells were further purified and stained with fluorescence-labeled antibody for flow cytometry analysis using a FACS flow cytometer.

7.4 RESULT

7.4.1 Synthesis of POEG-st-Pmor and POEG-st-Ppipe Polymers

The synthesis scheme and proton NMR spectrums for POEG-*st*-Pmor and POEG-*st*-Ppipe polymers were shown in Fig. 49 and Fig. 50. First, VBMor and VBPipe-Boc monomers were synthesized by reacting vinylbenzyl chloride with morpholine and piperazine-Boc, respectively. Then, statistical copolymers POEG-*st*-Pmor and POEG-*st*-P(pipe-Boc) were prepared via reversible addition-fragmentation chain-transfer (RAFT) polymerization of OEG500 monomer and VBMor or VBPipe-Boc monomer, espectively. The structures and molecular weights of POEG-*st*-Pmor and POEG-*st*-P(pipe-Boc) polymers were characterized by ^{1}H NMR and gel permeation chromatography (GPC). The average degree of polymerization (DP) of the OEG500 monomer was calculated to be 9 according to the conversion of OEG500 monomer at the end of the polymerization. The DP of the VBMor and VBPipe-Boc monomer was determined to be 50 and 45 respectively, by comparing the intensities of I_a and I_c (Fig. 51 and 52 of the Supporting Information). The average molecular weight M_n determined by GPC is 9,260 for POEG-*st*-Pmor and 14,200 for POEG-*st*-P(pipe-Boc), and the polydispersity is 1.13 and 1.25, respectively, which indicated the successful synthesis of POEG-*st*-Pmor and POEG-*st*-P(pipe-Boc) copolymers with well-defined structures. POEG-*st*-Ppipe polymer was obtained by TFA-mediated Boc deprotection of POEG-*st*-P(pipe-Boc) precursor in CH_2Cl_2. The molecular structure of POEG-*st*-Ppipe polymer was further confirmed by ^{1}H NMR (Fig. 53). The strong peaks at 1.42 ppm (Boc groups) disappeared, indicating the successful removal of Boc groups.

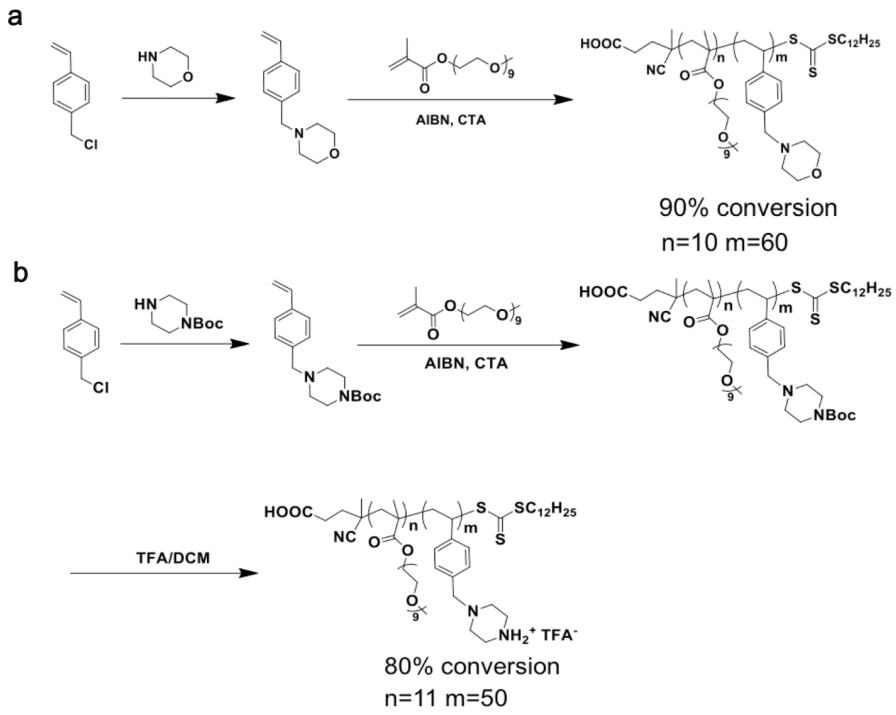

Figure 49. Synthesis scheme of (a) POEG-*st*-Pmor and (b) POEG-*st*-Ppipe polymers.

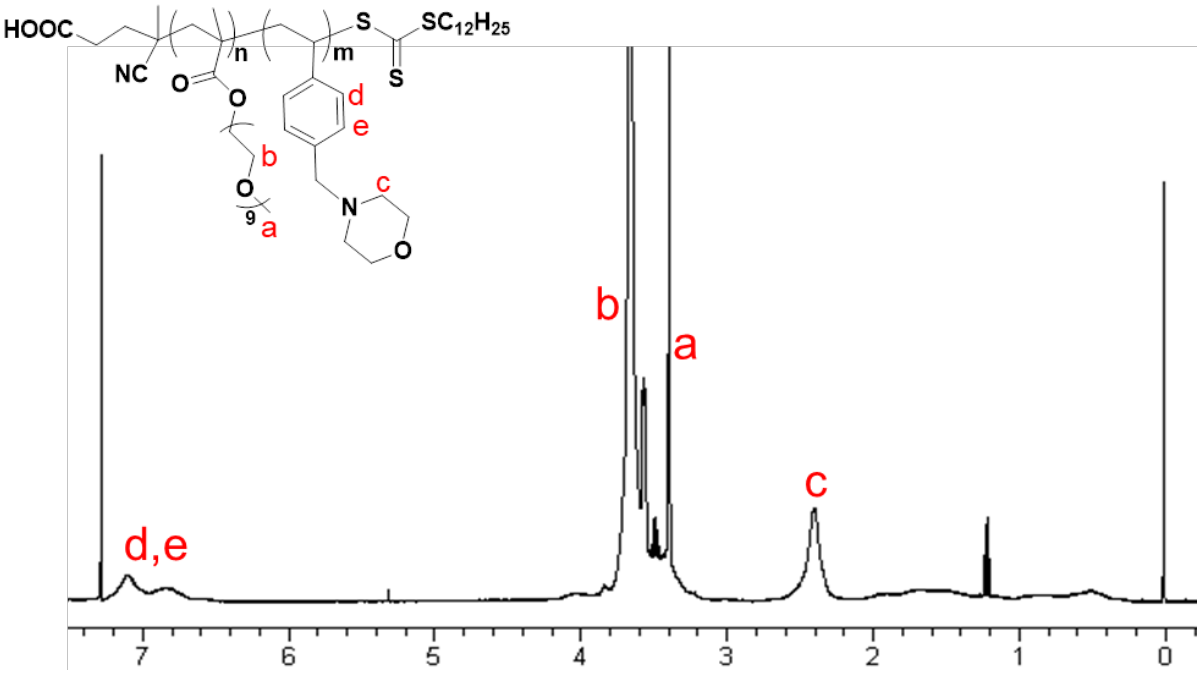

Figure 50. ^{1}H NMR of POEG-*st*-Pmor polymer

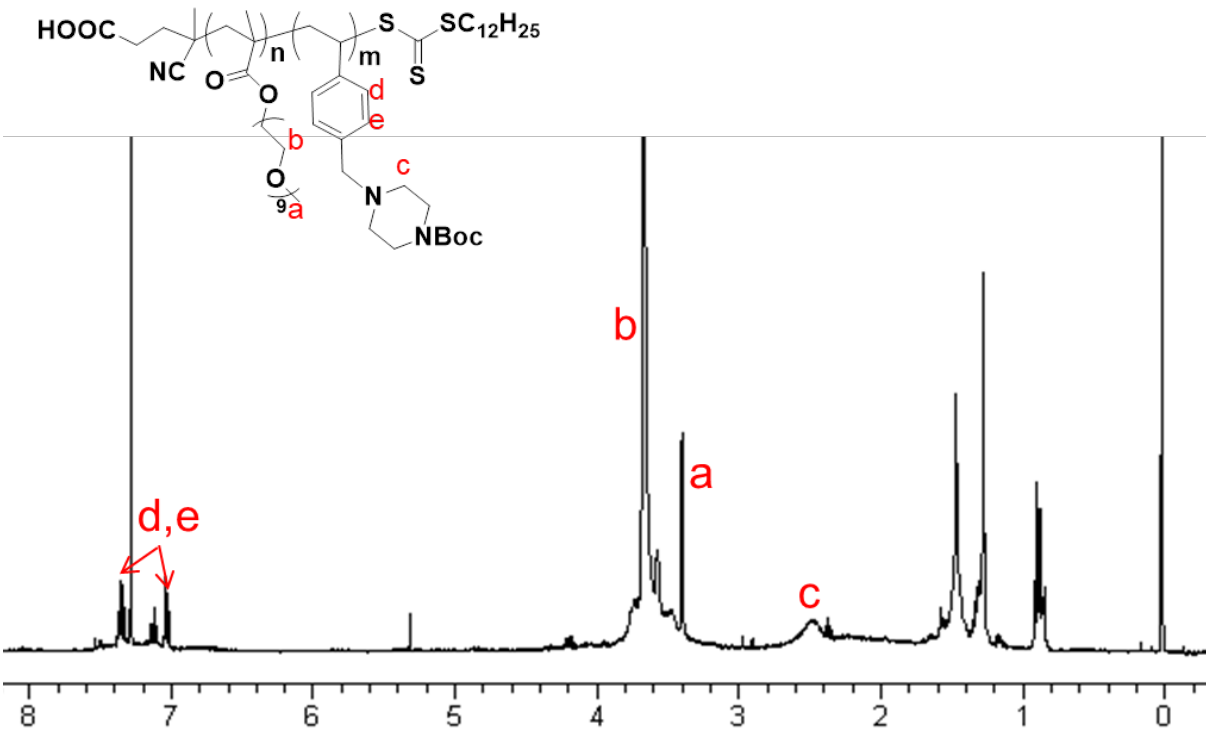

Figure 51.^{1}H NMR of POEG-*st*-P(pipe-Boc) polymer

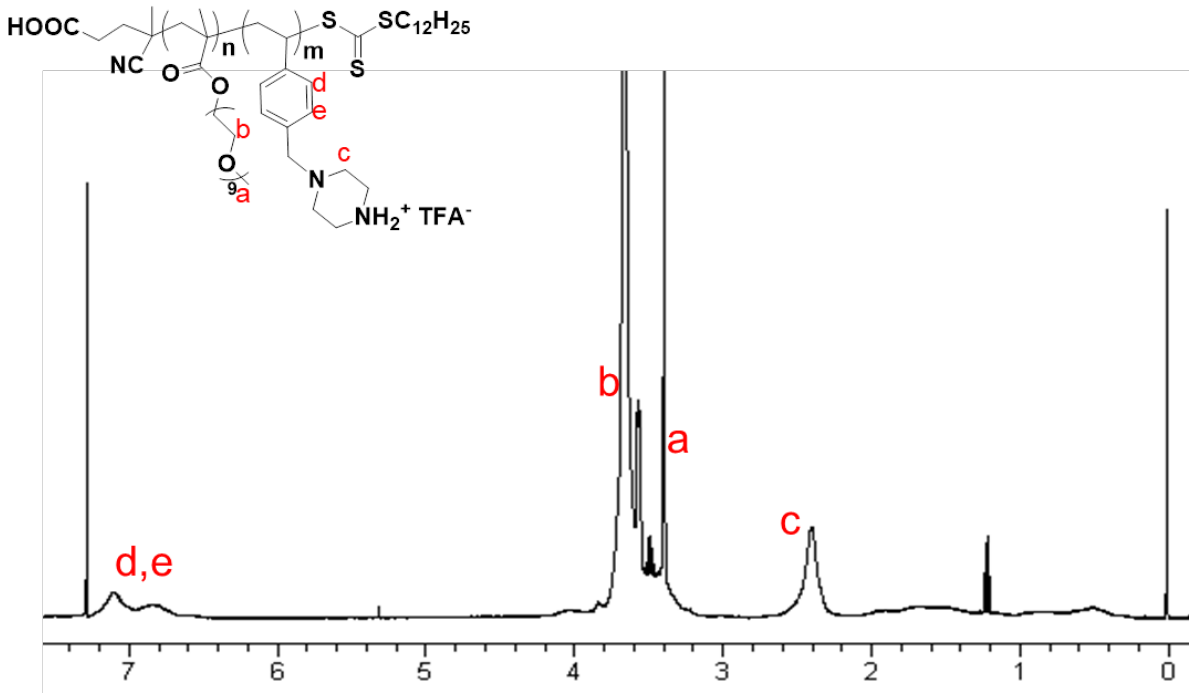

Figure 52. ^{1}H NMR of POEG-*st*-Ppipe polymer

7.4.2 Characterization of Micellar Nanoparticles

POEG-*st*-Pmor and POEG-*st*-Ppipe micelles were prepared via a dialysis method. As shown in Fig. 53, both micelles had sizes around 200 nm (Fig. 53, Tab. 9) as tested with a zetasizer and TEM. The critical micelle concentrations (CMC) of both polymers were determined using nile red as a fluorescence probe. Both POEG-*st*-Pmor and POEG-*st*-Ppipe polymers have a low CMC around 0.04 mg/ml (Fig. 54).

The Dox-loaded POEG-*st*-Pmor and POEG-*st*-Ppipe micelles were similarly prepared as blank micelles and both carriers could load Dox at a carrier/drug mass ratio starting from 10:1 with sizes ranging from 160 to 190 nm (Fig. 53, Tab. 8) and could remain stable for two weeks and one week at room temperature, respectively. Then we tested whether the POEG-*st*-Pmor and POEG-*st*-Ppipe could from stable complexes with plasmid DNA. A gel retardation assay was performed to assess the pDNA binding ability of the pMor- and pPipe-based polymers. Plasmid DNA/carrier complexes were fabricated at various N/P ratios from 0.1:1 to 30:1. As shown in Fig. 55a, b, complete complexation of plasmid DNA by POEG-*st*-Pmor or POEG-*st*-Ppipe polymer was achieved at an N/P ratio of 5/1 or greater. The surface zeta potentials of the POEG-*st*-Pmor and POEG-*st*-Ppipe blank micelles were 26.4 mV and 36.8 mV, respectively before the addition of IL-36γ plasmid (Fig. 56 and Tab. 8). At the N/P ratios of below 1, the complexes were negatively charged and the particle sizes were similar to the sizes of the micelles alone. There was a significant increase in the sizes of the complexes at an N/P ratio of 3. At this ratio, the particle charges were close to neutral. Interestingly, further increases in the N/P ratios led to a significant decrease in the particle sizes and the particles became more positively charged with continuous increases in the N/P ratios. Specifically, when the micelles were mixed with IL-36γ plasmid at an N/P ratio of 20:1, the average size of the complexes decreased to 70-80 nm (Tab. 8, Fig. 56). Nonetheless, DNA/micelle complexes were less positively charged compared to free micelles with a

surface zeta potential of 10.3 and 17.8 mV for plasmid/POEG-*st*-Pmor and plasmid/POEG-*st*-Ppipe complexes, respectively (Tab. 8).

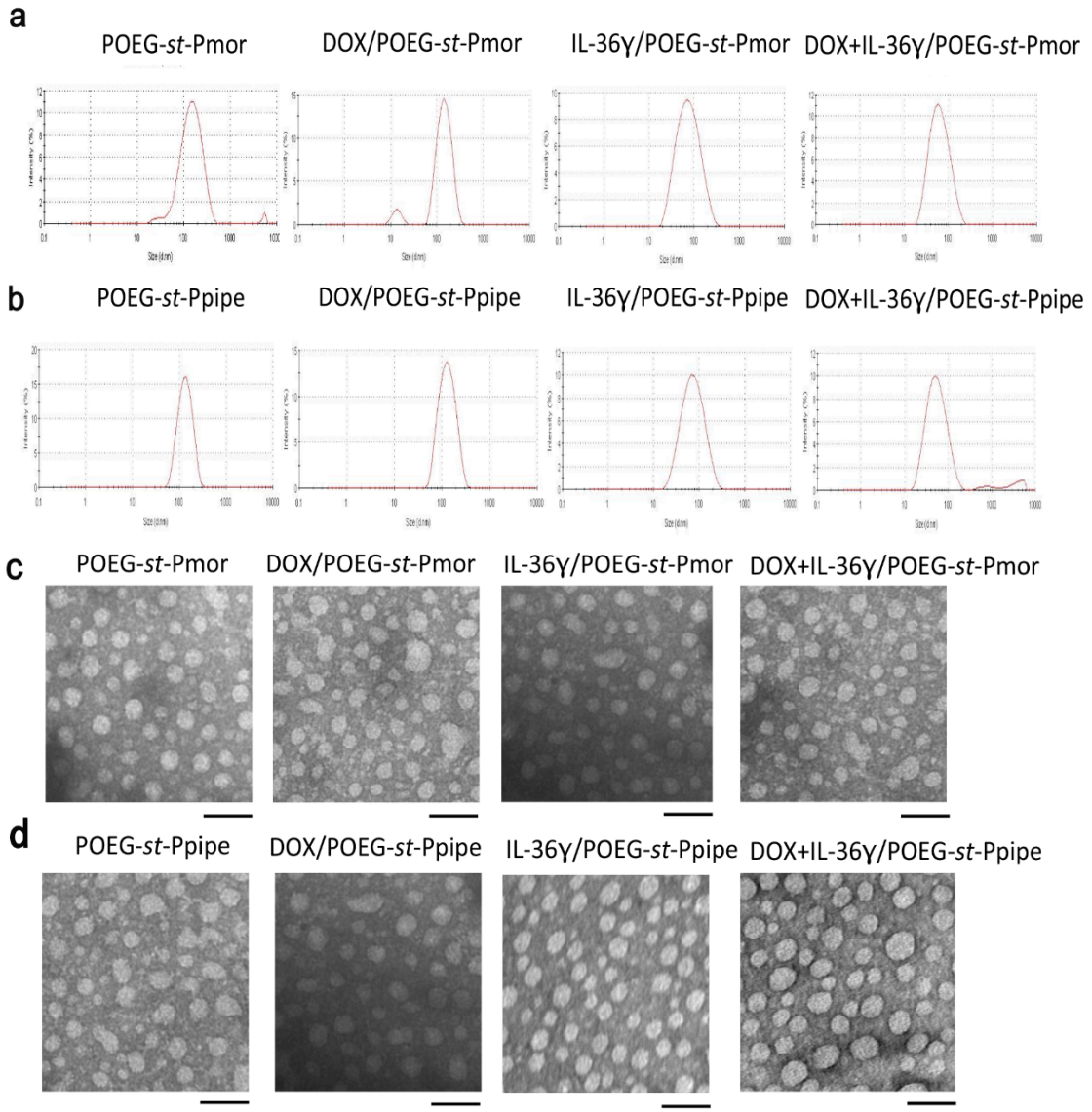

Figure 53. Particle size distribution and TEM images of micelles
(a-b)Particle size distribution and (c-d) TEM images of Blank micelles, Dox-loaded micelles, IL-36γ plasmid complexed micelles and micelles co-loaded with IL-36γ plasmid and DOX. Scale bars: 100 nm.

We then went on to further explore the possibility of co-delivery of pDNA and Dox by POEG-*st*-Pmor and POEG-*st*-Ppipe micelles. As shown in Fig. 53 and Tab. 8, the size distribution and zeta-potential were not significantly affected when Dox was added to the

pDNA/polymer complexes at a drug concentration of 1 mg/mL and a carrier/drug ratio of 20/1 (m/m).

7.4.3 Stability of the Complexes in BSA

The colloidal stability of DNA/micelle complexes was tested in BSA solution (30mg/mL). PEI/DNA complexes were used as a control (N/P=20, zeta potential=18.3 mV). As shown in Fig. 57, exposure of PEI/DNA complexes to BSA led to a rapid increase in the particle sizes. At 5 h post-incubation, the sizes of PEI/DNA complexes increased from 149 to 261 nm. It is also apparent that both POEG-*st*-Pmor/DNA and POEG-*st*-Ppipe/DNA complexes were resistant to BSA-induced aggregation and showed minimal changes in sizes throughout the entire 18 h of observation.

7.4.4 *In Vitro* Dox Release

The profile of Dox release from the Dox-loaded micelles was examined by a dialysis method with Dox.HCl solution as a control (Fig. 58). Free Dox exhibited a burst release with more than 80% of drug released at the first 4 hours. However, Dox formulated in POEG-*st*-Pmor and POEG-*st*-Ppipe micelles showed a significantly slower kinetics of release with less than 25% of Dox being released outside of dialysis bag at the first 4 hours, and only 35% and 31% of Dox released at 24h for POEG-*st*-Pmor and POEG-*st*-Ppipe micelles, respectively. The micelles co-loaded with Dox and plasmid exhibited an even slower Dox release profile compared to micelles loaded with Dox alone at later time points.

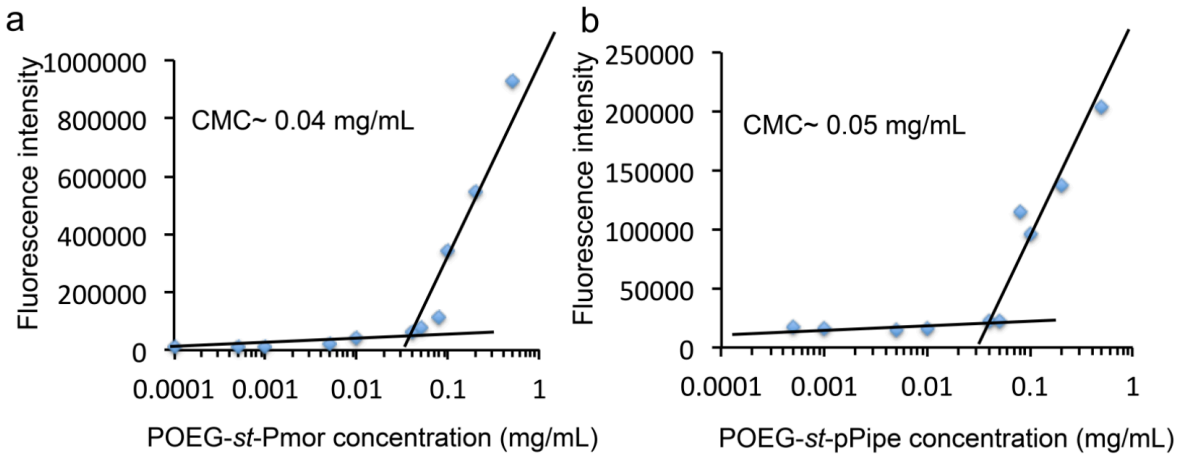

Figure 54. The CMC values of POEG-*st*-Pmor and POEG-*st*-Ppipe polymers.
CMC of (a) POEG-*st*-Pmor and (b) POEG-*st*-Ppipe polymers determined from the plot of nile red fluorescence intensity.

7.4.5 Cytotoxicity of Bank Micelles and Dox+IL36γ Plasmid/micelle Complexes

The *in vitro* cytotoxicity of Dox+IL36γ plasmid/micelle complexes was evaluated with 4T1.2 breast cancer cells via MTT assay. Cells were treated with various treatments for 72 h and the final concentrations of Dox ranged from 4 to 1000 ng/mL (Fig. 59a). The free Dox and the Dox-loaded micelles showed a dose-dependent cell killing profile. The Dox/POEG-*st*-Pmor and Dox/POEG-*st*-Ppipe had lower IC50s (60ng/ml and 110ng/ml, respectively) compared to free Dox (IC50=130ng/ml) (Fig. 59a). Incorporation of IL36γ plasmid into Dox-loaded micelles led to slightly increased cytotoxicity on 4T1.2 cells. POEG-*st*-Pmor or POEG-*st*-Ppipe alone showed minimal cytotoxicity to 4T1.2 cells at the polymer concentration as high as 20μg/mL (Fig. 59b).

Table 8. Biophysical Characteristics of Blank Micelles and the Micelles Co-loaded With IL-36γ Plasmid and DOX

Micelles	Mass ratio (mg: mg)	N/P ratio	Size (nm)	Zeta potential (mV)	Stability
POEG-*st*-Pmor	--	--	184	26.4	--
IL-36γ/POEG-*st*-Pmor	--	20	95.0	10.3	--
	10:1	--	178	27.1	2 weeks
DOX/POEG-*st*-Pmor	20:1	--	174	24.7	4 weeks
	30:1	--	162	26.0	1 month
DOX+IL-36γ/POEG-*st*-Pmor	20:1	20	84.4	10.4	1 month
POEG-*st*-Ppipe	--	--	167	36.8	--
IL-36γ/POEG-*st*-Ppipe	--	20	88.4	17.8	--
	10:1	--	194	26.5	1 weeks
DOX/POEG-*st*-Ppipe	20:1	--	180	33.7	2 weeks
	30:1	--	189	34.0	3 weeks
DOX+IL-36γ/POEG-*st*-Ppipe	20:1	20	69.9	18.4	3 weeks

Drug concentrations in micelle were 1 mg/mL and blank micelle concentration was 20 mg/mL. Size and zeta potential were measured by dynamic light scattering sizer.

7.4.6 Cellular Internalization of Nanomicelles

The cellular uptake of siRNA/micelle complexes was investigated by confocal laser scanning microscopy. The siRNA/micelle complexes were prepared at an N/P ratio of 20:1 to ensure complete siRNA binding to the micelles. 4T1.2 mouse breast cancer cells were incubated for 4 h with micelle complexes carrying Dox and/or FAM-labeled siRNA and then observed under a confocal microscope. As shown in Fig. 60, Dox-loaded POEG-*st*-Pmor and POEG-*st*-Ppipe micelles showed more Dox cellular uptake compared to free Dox at the same Dox concentration. The signals for free Dox were largely found in nucleus while the signals for the micellar Dox were mainly located outside the nucleus. This might be due to the different cellular uptake routes of free Dox and Dox micelles.

Fig. 61 showed even more uptake of micellar Dox following complexation with FAM-siRNA. Moreover, both Dox+FAM-siRNA/POEG-*st*-Pmor and Dox+FAM-siRNA/POEG-*st*-Ppipe showed substantial yellow fluorescence signals in a

merged channel likely due to the overlap of Dox (red) and FAM-siRNA (green), suggesting co-localization of Dox and FAM-siRNA.

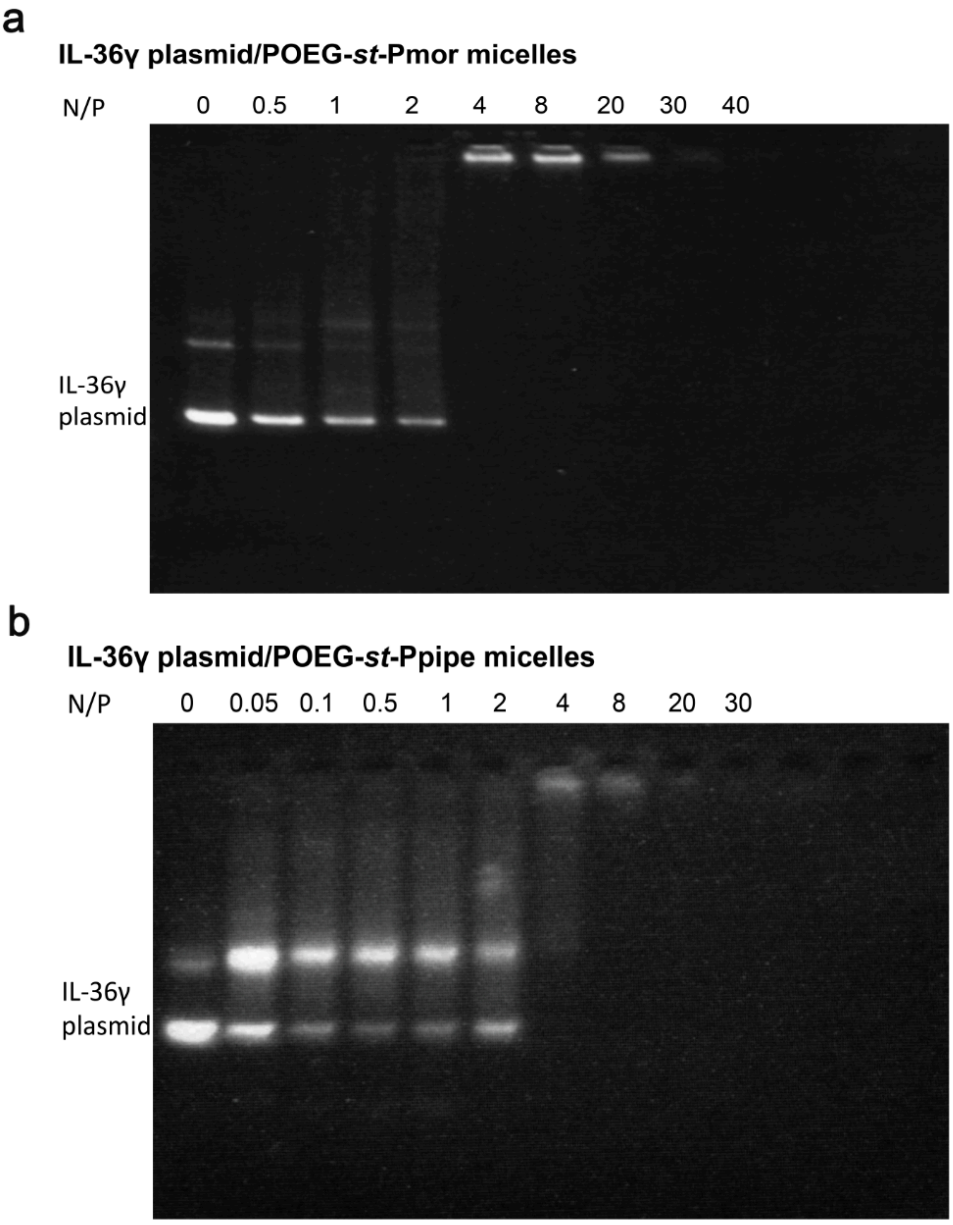

Figure 55. Gel retardation assay of IL-36γ plasmid/polymer complexes at different N/P ratios.

Samples were incubated for 20 min at room temperature before being loaded onto a 1% (w/v) agarose gel (100 V, 30 min). Representative gel images of plasmid/POEG-*st*-Pmor polymer (a) and plasmid/POEG-*st*-Ppipe polymer (b) are shown from three independent experiments.

7.4.7 *In Vitro* Transfection with EGFP Plasmid

The above results indicate that POEG-*st*-Pmor and POEG-*st*-Ppipe micelles were effective in delivering nucleic acids into cancer cells. To further assess the capability of the micelle complexes to enter cells, release plasmids, leading to expression of biologically active protein, we performed *in vitro* transfection with EGFP plasmid. Fig. 62 shows that 4T1.2 tumor cells were effectively transfected with EGFP plasmid complexed with POEG-*st*-Pmor or POEG-*st*-Ppipe micelles. 4T1.2 cells were also effectively transfected with branched PEI, a control carrier.

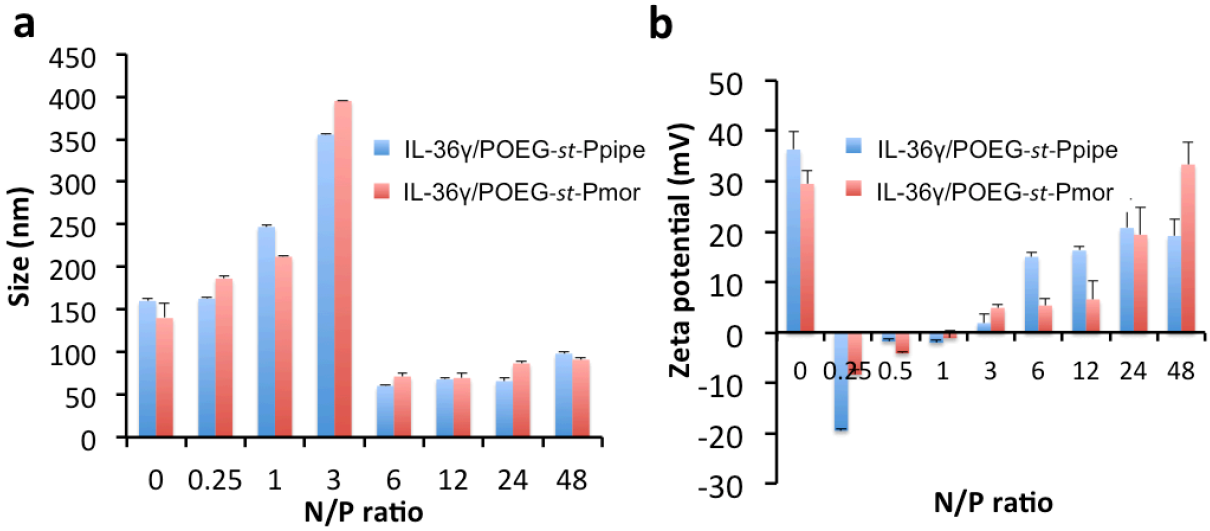

Figure 56. Particle sizes and zeta potentials of IL-36γ plasmid/POEG-*st*-Pmor and IL-36γ plasmid/POEG-*st*-Ppipe complexes.
Particle sizes (a) and zeta potentials (b) of IL-36γ plasmid/POEG-*st*-Pmor and IL-36γ plasmid/POEG-*st*-Ppipe complexes formed at different N/P ratios. Data are expressed as means ± s.e.m. (n=3).

7.4.8 *In Vivo* Distribution of AF647-siRNA-loaded Nanomicelles

To gain insight into the distribution of siRNA/micelle complexes, confocal examination of the tissue sections was performed at 24 h following i.v. administration of AF647-siRNA/micelle complexes. As shown in Fig. 63, substantial amounts of fluorescence

(AF647) signals were detected in s.c. tumor tissues for both POEG-*st*-Pmor and POEG-*st*-Ppipe formulations. We also observed significant amounts of AF647 signals in lungs but much fewer signals in liver. In contrast, AF647-siRNA/PEI complexes were largely found in lungs with little accumulation in the tumors.

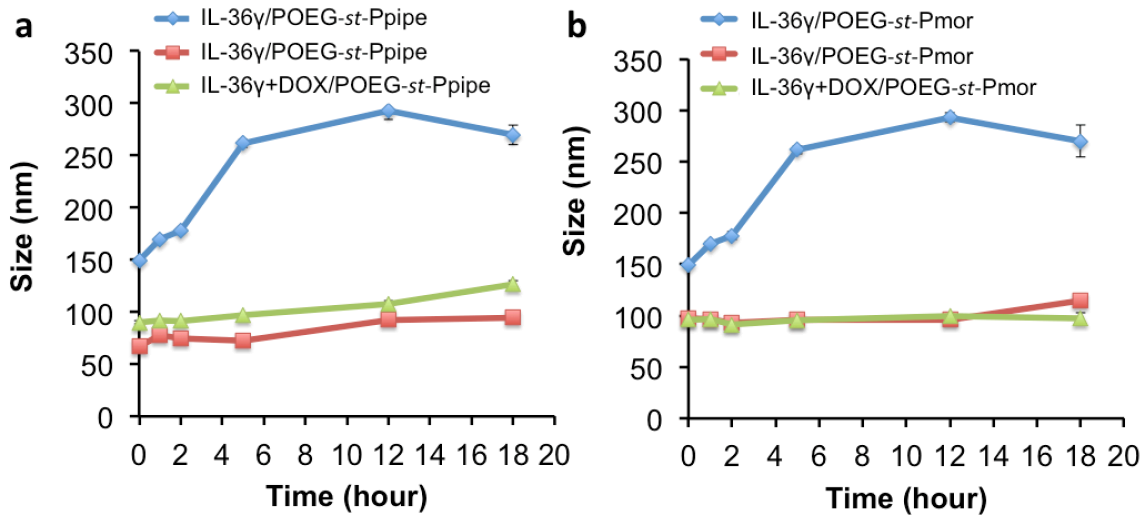

Figure 57. The BSA stability of DOX+ IL-36γ plasmid coloaded micelles.
The stability of (a) DOX+ IL-36γ plasmid/POEG-*st*-Pmor and (b) DOX+IL-36γ plasmid/POEG-*st*-Ppipe was examined by incubating complexes (1 mg DOX/mL in PBS, pH 7.4) with bovine serum albumin (BSA, 30mg/mL) at 37°C. Changes in sizes of the complexes were followed by DLS. Data are means ± s.e.m. (n=3).

7.4.9 *In Vivo* Transfection Efficiency

EGFP was used as a reporter gene with linear PEI as a control carrier. Gene expression in tissue sections was examined with a confocal microscope. As shown in Fig. 64a, there were significantly more EGFP signals in tumors with POEG-*st*-Pmor or POEG-*st*-Ppipe formulation compared to linear PEI. In agreement with previous reports, lungs could be effectively transfected by linear PEI (Fig. 64b). However, more and stronger signals of EGFP were observed in lungs transfected with POEG-*st*-Pmor or POEG-*st*-Ppipe formulation (Fig. 64b). Liver was hardly transfected with either of our formulations or control linear PEI.

These results suggest that POEG-*st*-Pmor and POEG-*st*-Ppipe polymers are suitable for *in vivo* gene delivery to both lungs and distant solid tumors (Fig. 64c).

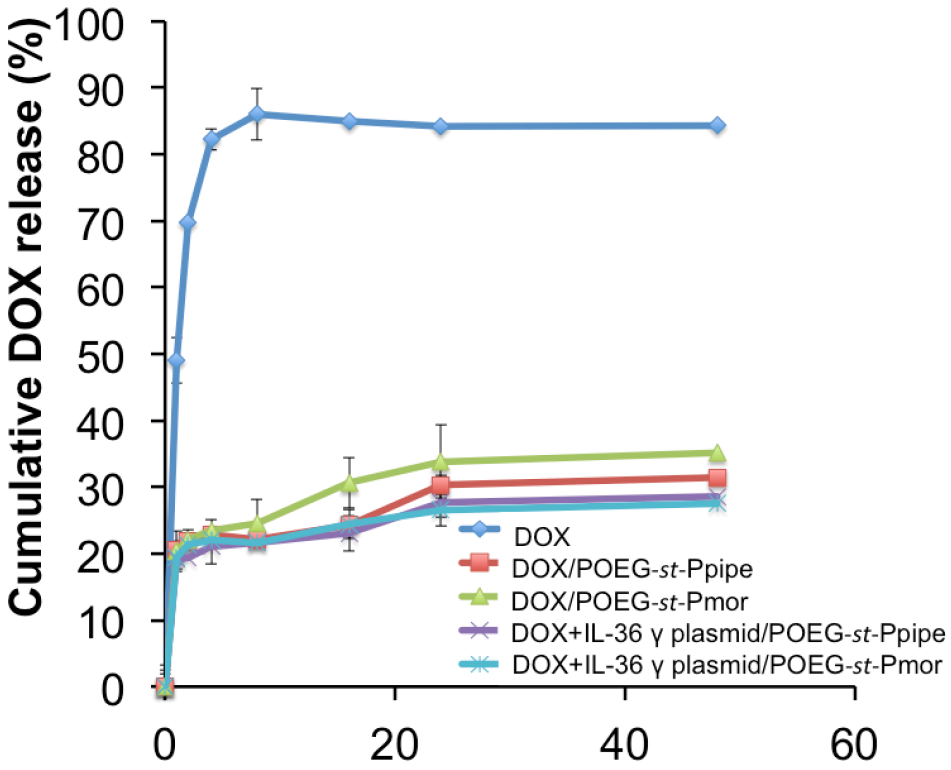

Figure 58. *In vitro* drug release profiles.
In vitro drug release of DOX from (A) DOX+IL-36γ plasmid/POEG-*st*-Pmor and (B) DOX+IL-36γ plasmid/POEG-*st*-Ppipe in PBS at 37°C. Data are mean ± s.e.m. (n=3).

7.4.10 Anti-tumor Activity of Micelles Co-loaded With Dox and IL-36γ Plasmid

Next we investigated the anti-tumor activity of Dox+IL-36γ plasmid/POEG-*st*-Pmor complexes *in vivo*. A mouse model of breast cancer lung metastasis (4T1.2) was generated in female Balb/c mice and various treatments were given to each group of mice via tail vein injection (Fig. 65a). As shown in Fig. 65b, the carrier alone did not show therapeutic activity compare to control group. Free Dox showed a modest inhibition of lung metastasis and micelles co-loaded with Dox and IL-36γ plasmid showed the best anti-metastasis effect

compared to free Dox, Dox+control plasmid/micelles and IL-36γ plasmid/micelles. The H&E staining of lung tissues showed clear tumor cell infiltration from all of the groups except for the co-delivery group (Fig. 65c). The group with more tumor nodules had more lung weights (Fig. 65d&e). Body weights were also monitored during the treatment period. No significant decrease of body weight was observed, indicating the safety of the formulation (Figure. 65f).

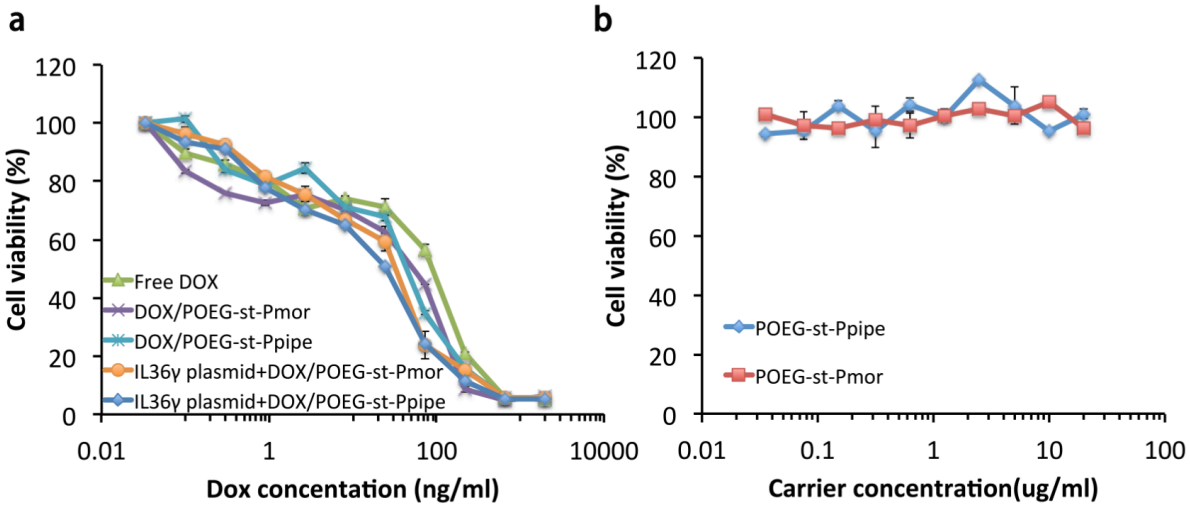

Figure 59. *In vitro* cytotoxicity study.
(a) *In vitro* cytotoxicity of DOX+IL-36γ plasmid/POEG-*st*-Pmor and DOX+IL-36γ plasmid/POEG-*st*-Ppipe in 4T1.2 cells. (b) *In vitro* cytotoxicity of drug-free micelles. Cells were treated for 72 h, and cytotoxicity was determined by MTT assay. Values were reported as means ± s.e.m. from triplicate samples.

7.4.11 Immune Cell Infiltration Profile in Tumor-bearing Lungs

Following demonstration of the significant antitumor activity of Dox+IL-36γ plasmid/POEG-*st*-Pmor, we examined the immune cell infiltration in the tumor-bearing lungs to elucidate a role of immune response in the overall antitumor activity. As shown in Fig.66a&c, there was a significant increase of cytotoxic $CD8^+$ T cells in the lung tissues treated with free Dox, IL-36γ plasmid/POEG-*st*-Pmor or the combination of both compared to untreated control group. Although there was no significant difference in the total number

of T cells between Dox+IL-36γ plasmid/POEG-*st*-Pmor and Dox+control plasmid/POEG-*st*-Pmor, the numbers of IFN-γ^+ $CD4^+$ and IFN-γ^+ $CD8^+$ T cells were significantly increased in the combination treatment group compared to either of the other treatment groups. We also examined the immunosuppressive myeloid-derived suppressor cells (MDSCs) in lung tissues. The granulocytic MDSCs (GMDSCs) express high levels of Gr-1 and monocytic MDSCs (MMDSCs) express intermediate level of Gr-1 and both of them are positive for CD11b. The numbers of GMDSC were significantly decreased in all treatment groups except the carrier alone group (Fig. 66h-j). Surprisingly, there was a significant increase in the number of $Foxp3^+$ $CD4^+$ T cells (regulatory T cells (Treg)) in the mice treated with IL-36γ plasmid, alone or in combination with Dox (Fig. 66k-l).

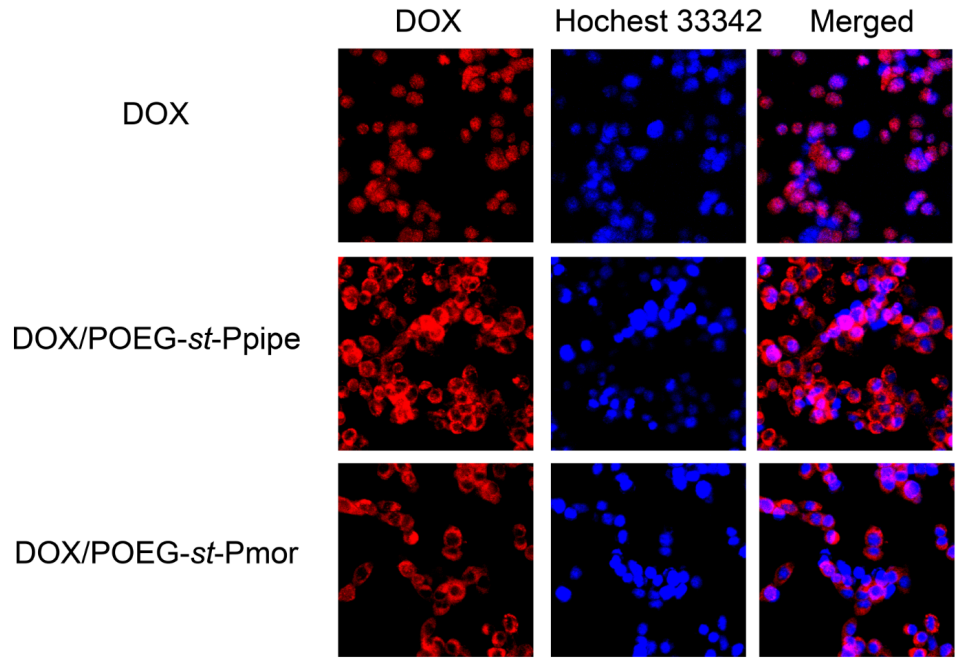

Figure 60. Cellular uptake of free DOX, DOX-loaded POEG-*st*-Pmor micelles and DOX-loaded POEG-*st*-Ppipe micelles in 4T1.2 cancer cells.
Photos were taken at 2h of incubation. Cell nuclei were stained with Hoechst 33342.

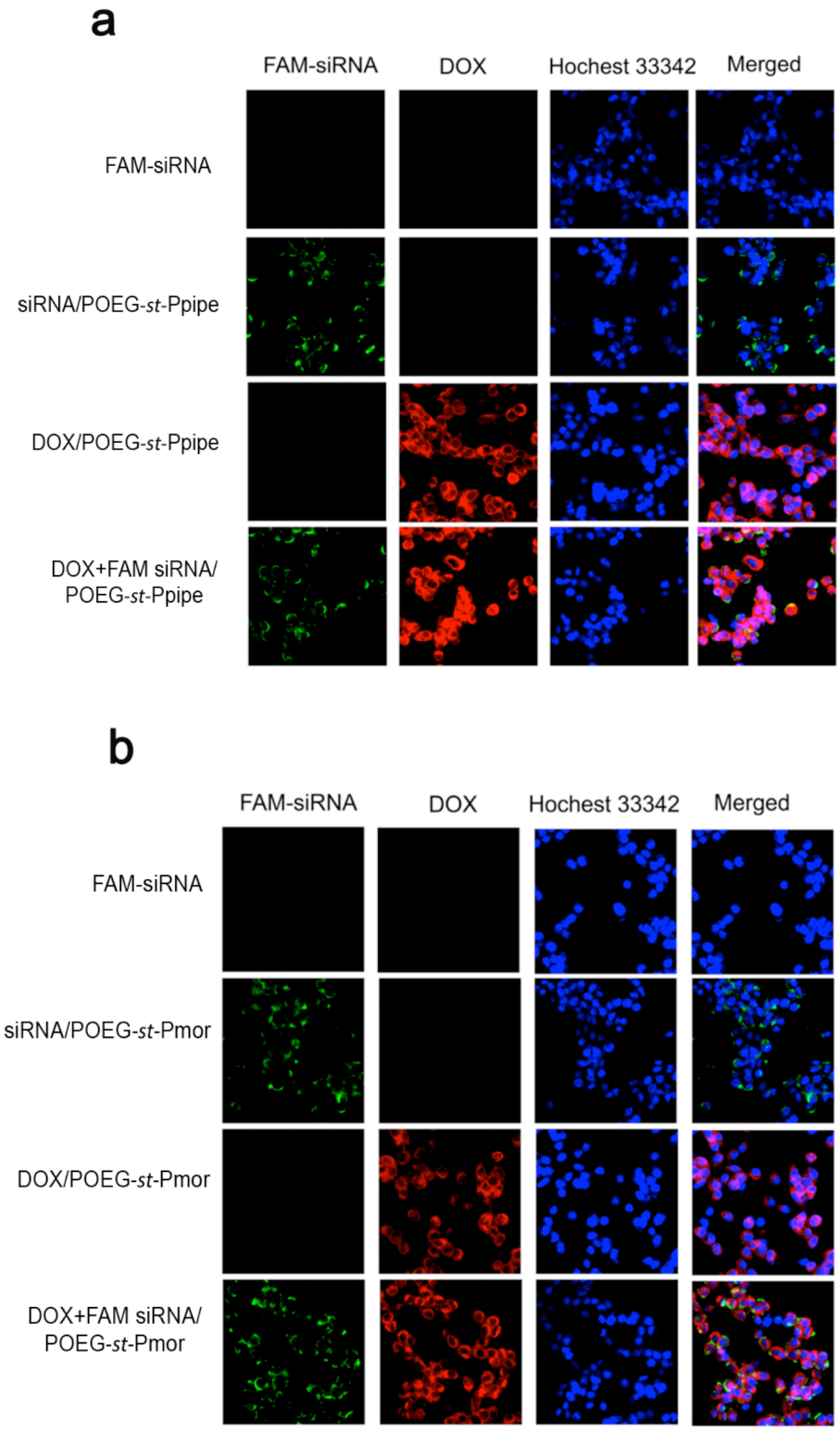

Figure 61. Internalization and colocalization of (a) DOX+siRNA^{FAM}/POEG-*st*-Pmor and (b) DOX+siRNA^{FAM}/POEG-*st*-Ppipe in 4T1.2 cancer cells.

From left to right: fluorescein-labeled siRNA (green); DOX (red); nuclear staining with Hoechst 33342 (blue); an overlay of siRNA, DOX and Hoechst.

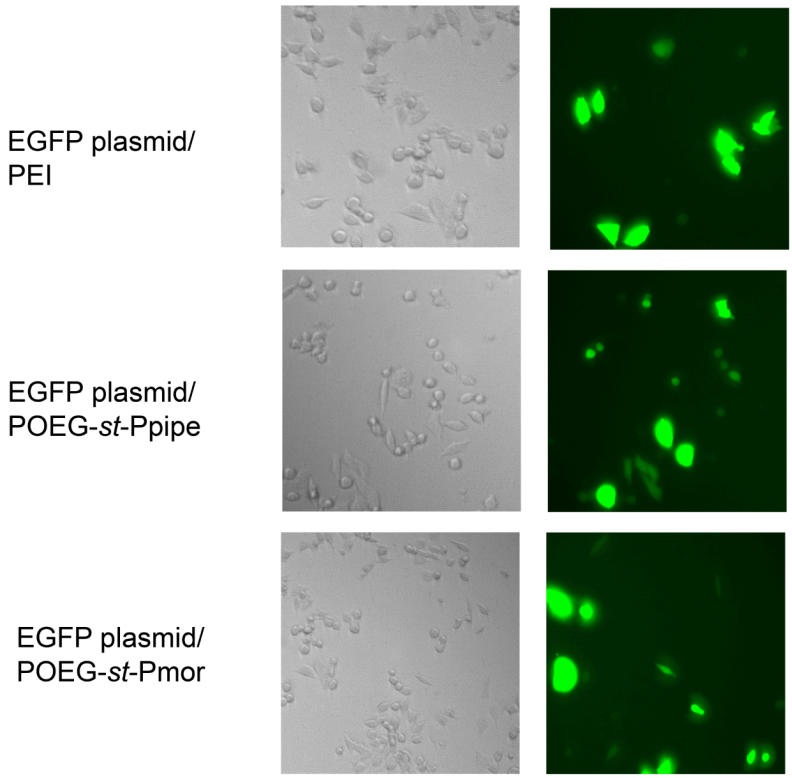

Figure 62. EGFP transfection *in vitro*

Expression of EGFP 48 h following transfection of 4T1.2 cells with pEGFP-C1 complexed with PEI, POEG-*st*-Pmor, and POEG-*st*-Ppipe, respectively.

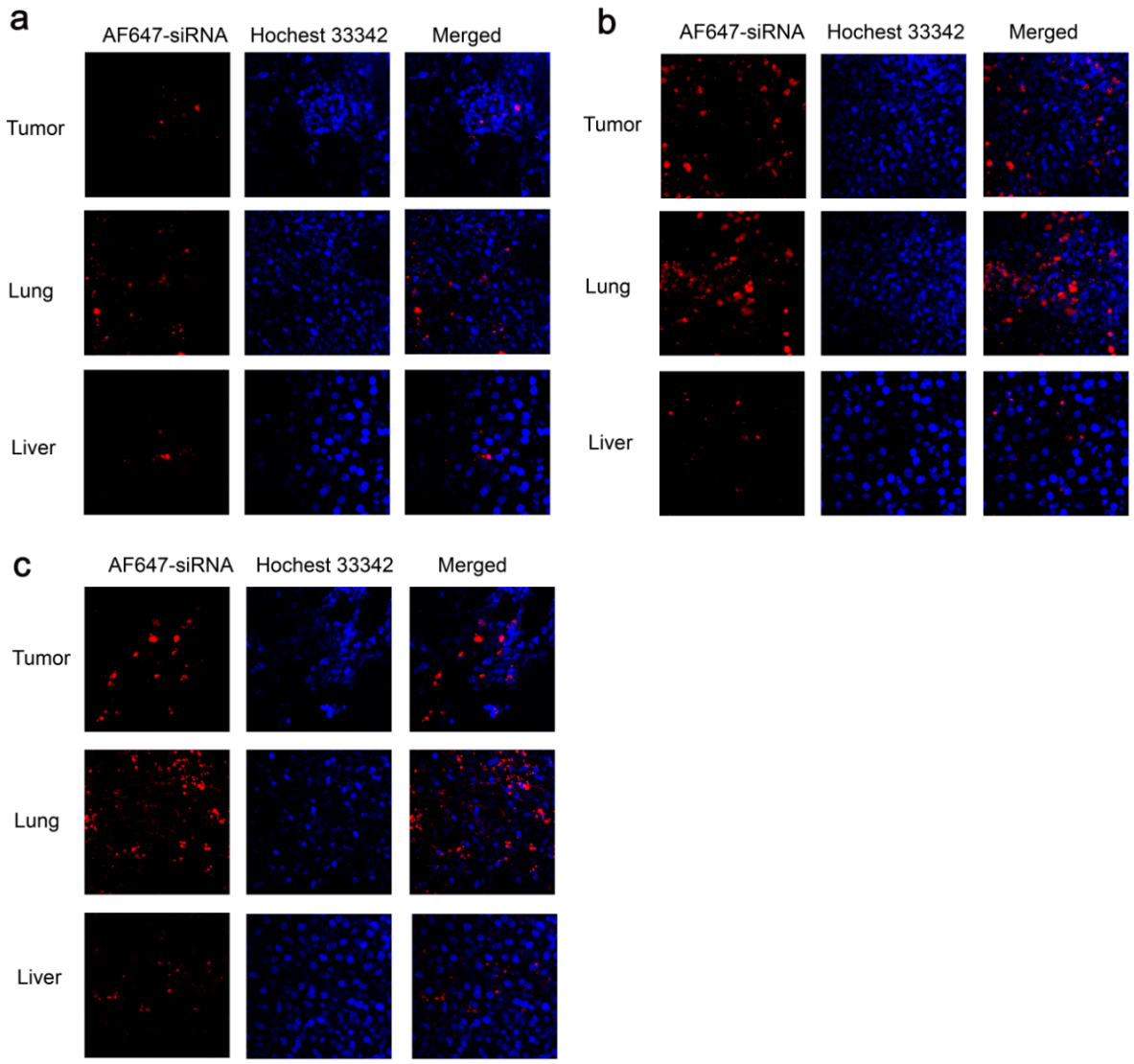

Figure 63. *In vivo* siRNA distribution in tumors, lung, and liver.
In vivo siRNA distribution in tumors, lung, and liver 24 h following i.v. injection of (a) siRNA/PEI, (b) siRNA/POEG-*st*-Pmor, and (c) siRNA/POEG-*st*-Ppipe. Cell nucleus was stained by hoechst.

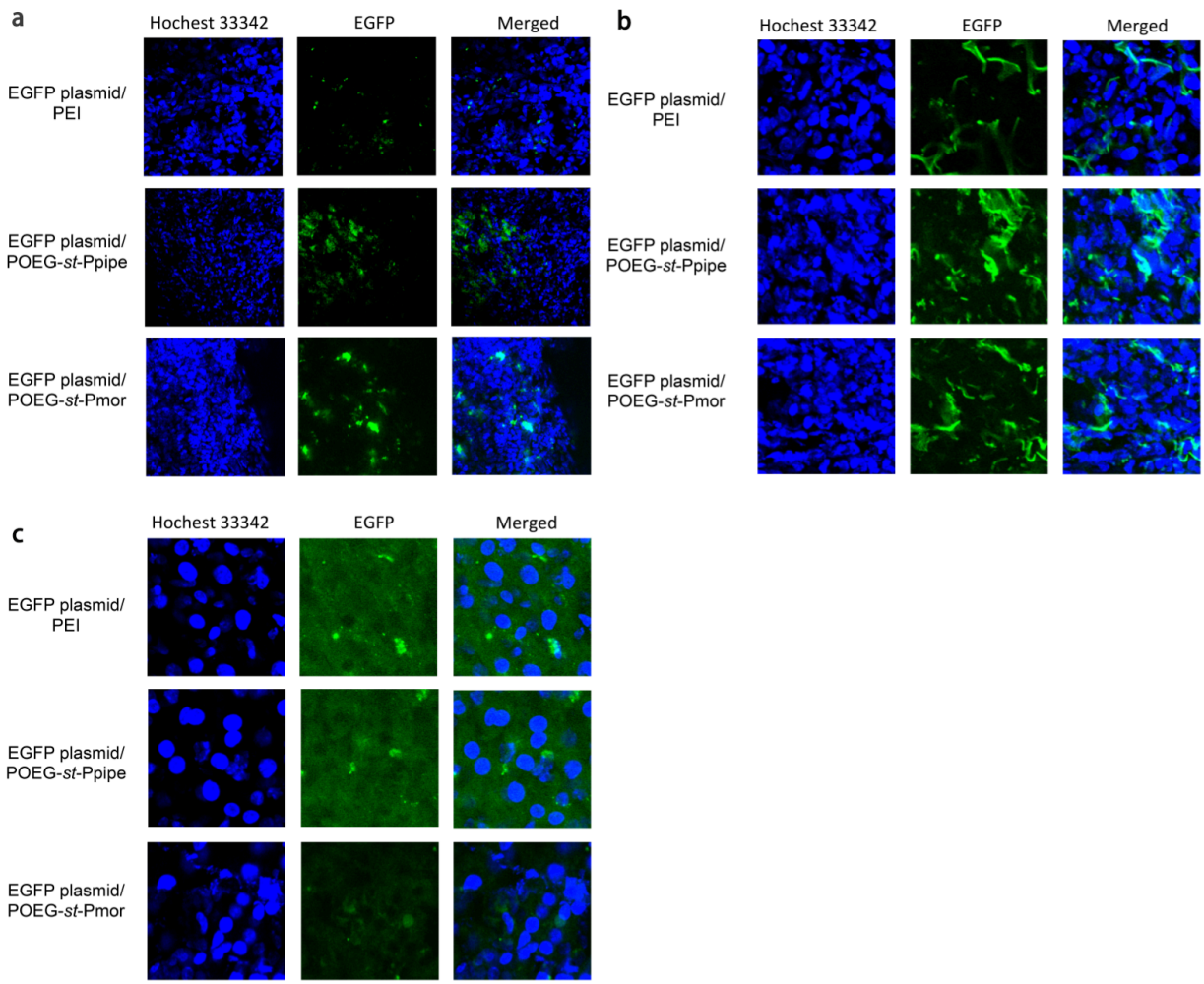

Figure 64. *In vivo* GFP expression in liver, lung and tumor tissues.
Balb/c mice bearing 4T1.2 tumor were i.v. injected with EGFP plasmid/PEI, EGFP plasmid/POEG-*st*-Pmor and EGFP plasmid/POEG-*st*-Ppipe. GFP expression in (a) tumor, (b) lung, and (c) liver was examined 24 h later.

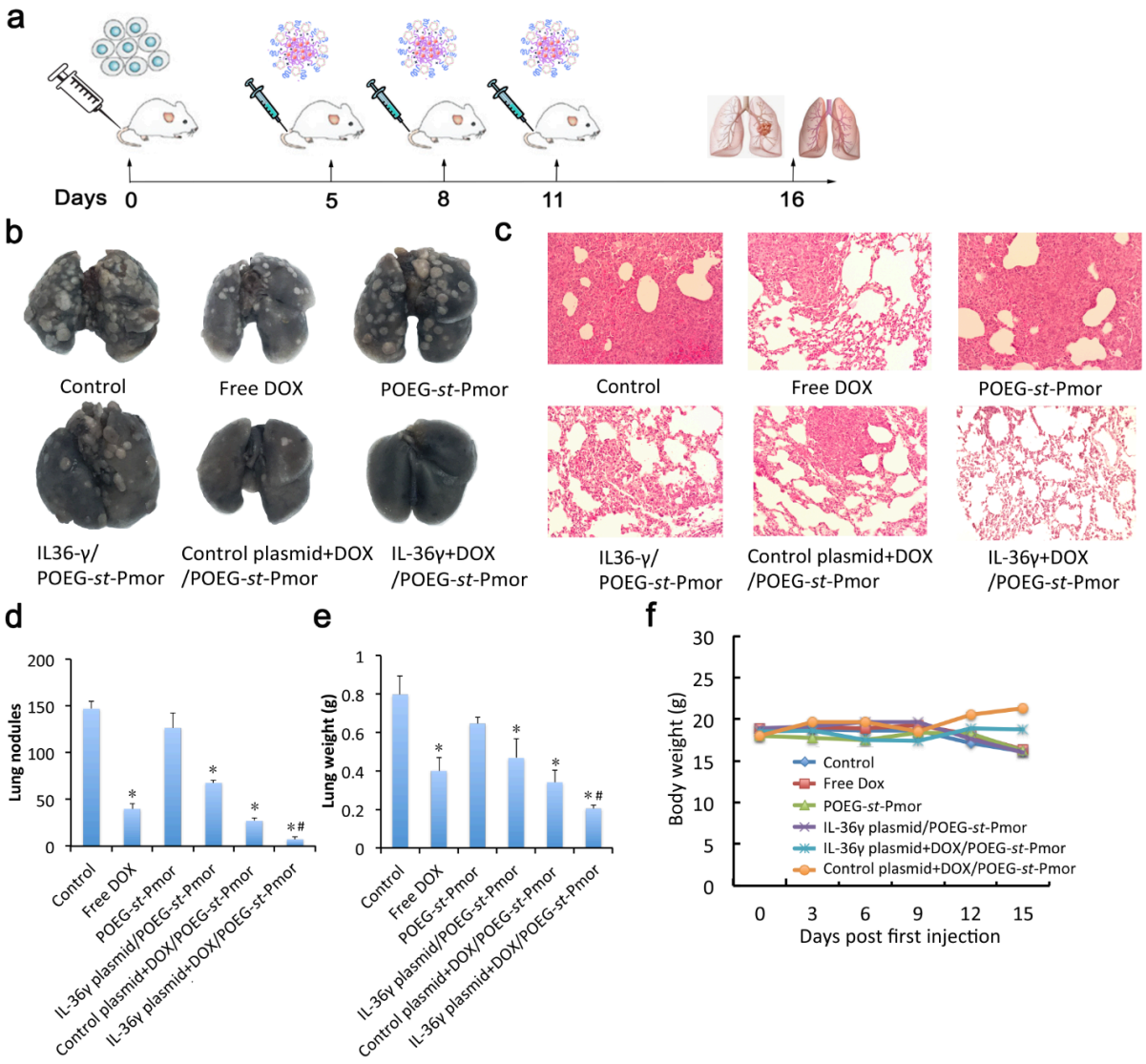

Figure 65. Synergistic antitumor activity of IL36γplasmid and DOX codelivered by POEG-*st*-Pmor micelles in a mouse model of breast cancer (4T1.2) lung metastasis.

(a) experimental scheme for the establishment of lung metastasis and treatment. (b) representative gross images of lungs collected from mice receiving various treatments. (c) H&E staining of lung tissues. (d) quantification of tumor nodules. (e) mouse lung weights (n = 5). (f) changes in mouse body weights during the treatment period. Data are presented as the means ± SEM. *$p < 0.05$ versus control.

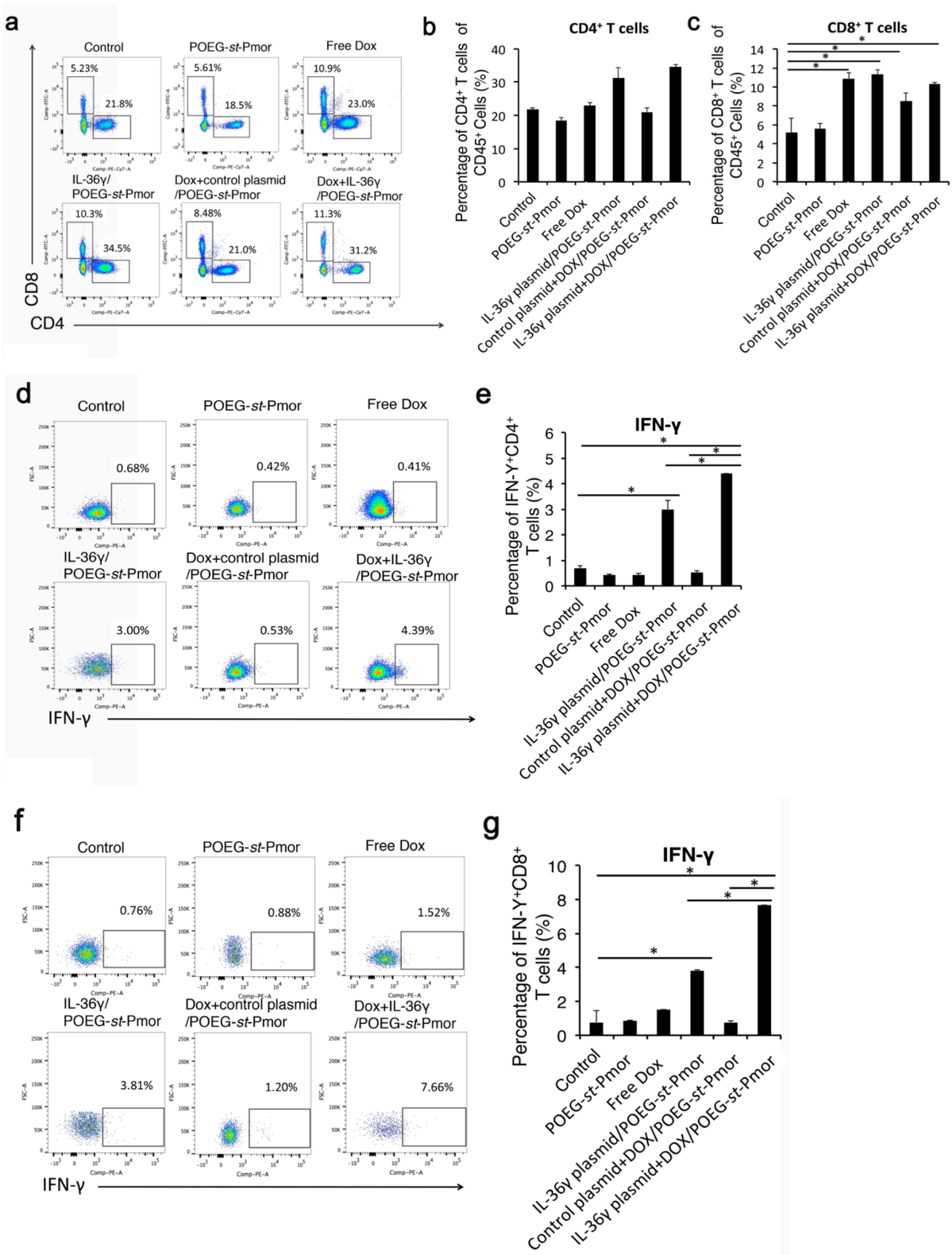
a
Control
POEG-st-Pmor
Free Dox
5.23%
21.8%
5.61%
18.5%
10.9%
23.0%
IL-36γ/
POEG-st-Pmor
Dox+control plasmid
/POEG-st-Pmor
Dox+IL-36γ
/POEG-st-Pmor
10.3%
34.5%
8.48%
21.0%
11.3%
31.2%
CD8
CD4
b
CD4⁺ T cells
Percentage of CD4⁺ T cells of CD45⁺ Cells (%)
Control
POEG-st-Pmor
Free Dox
IL-36γ plasmid/POEG-st-Pmor
Control plasmid+DOX/POEG-st-Pmor
IL-36γ plasmid+DOX/POEG-st-Pmor
c
CD8⁺ T cells
Percentage of CD8⁺ T cells of CD45⁺ Cells (%)
d
Control
POEG-st-Pmor
Free Dox
0.68%
0.42%
0.41%
IL-36γ/
POEG-st-Pmor
Dox+control plasmid
/POEG-st-Pmor
Dox+IL-36γ
/POEG-st-Pmor
3.00%
0.53%
4.39%
IFN-γ
e
IFN-γ
Percentage of IFN-γ⁺CD4⁺ T cells (%)
f
Control
POEG-st-Pmor
Free Dox
0.76%
0.88%
1.52%
IL-36γ/
POEG-st-Pmor
Dox+control plasmid
/POEG-st-Pmor
Dox+IL-36γ
/POEG-st-Pmor
3.81%
1.20%
7.66%
IFN-γ
g
IFN-γ
Percentage of IFN-γ⁺CD8⁺ T cells (%)

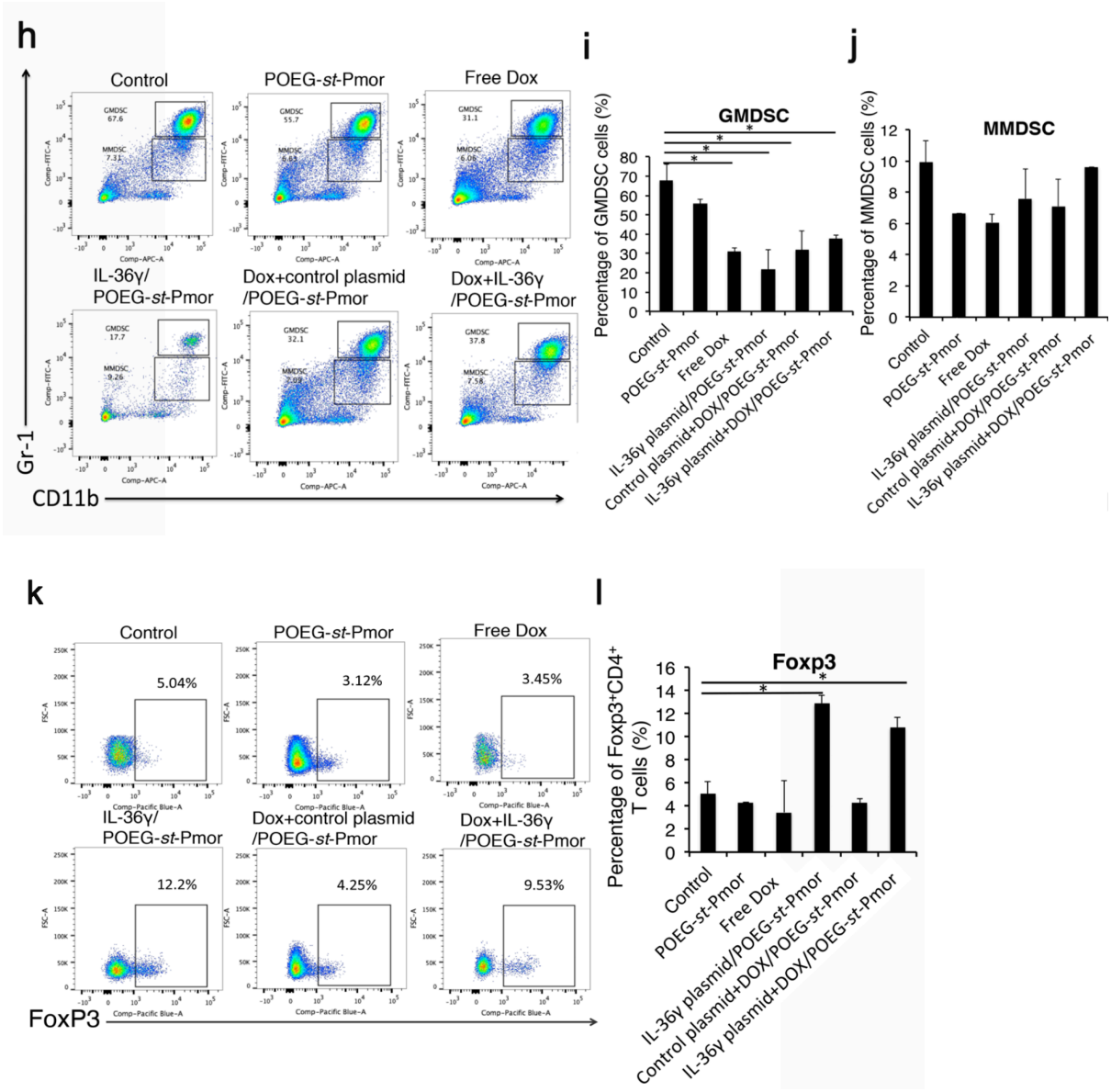

Figure 66. Flow analysis of infiltration of immune cells in tumor-bearing lungs following various treatments.

Balb/c mice were injected with $2*10^5$ 4T1.2 cells via tail vein. 5 days later, mice were treated with POEG-*st*-Pmor carrier, free Dox, IL-36γplasmid/POEG-*st*-Pmor, Dox+control plasmid/POEG-*st*-Pmor and Dox+IL-36γplasmid/POEG-*st*-Pmor, respectively for three times. (a-c) T lymphocyte subsets isolated from lung tissues with 4T1.2 metastasis were analyzed by flow cytometry. The percentage of $CD4^+$ and $CD8^+$ T cells in the lung tissues with various treatments was determined by flow cytometry analysis. (d-g) IL-36γplasmid/micelles increased the $IFN\gamma^+$ $CD4^+$ and $IFN\gamma^+$ $CD8^+$ T cells in tumor-bearing lungs. (h-j) MDSC subsets (GMDSC and MMDSC) were stained with CD11b and Gr-1 antibody and determined by flow cytometry. The results are shown as the means ± s.e.m of 3 mice in each group. *P< 0.05. (k-l) flow analysis of $Foxp3^+$ T regulatory cells in mouse lungs.

7.5 DISCUSSION

Most delivery systems developed so far are designed for delivery of either small molecule drugs or nucleic acid-based therapeutics. In this study, we have developed a simple micellar system that is highly effective in codelivery of small molecules and nucleic acids (siRNA and plasmids). In addition to providing a platform for any new combination therapy that involves both small molecule drugs and nucleic acid therapeutics, our approach also resolves the issue of instability that is associated with most micellar carriers. Micelles are formed through the self-assembly of amphiphilic monomers, which is a reversible and dynamic process. Micelles tend to fall apart when they are diluted in the blood upon systemic administration. This can be further aggravated by the lipid exchange as a result of interactions with lipoproteins in the blood. A number of strategies have been reported to cross-link the monomers to stabilize the micelles. Some of the approaches involve a complicated procedure and/or modification of the structure of the monomer. In our system, the multivalent charge-charge interactions between the cationic polymer and nucleic acids (both siRNA and plasmid DNA) serve as a simple approach to cross-link the micelles. As a result, micelles that are co-loaded with small molecules and plasmid or siRNA are likely to be more stable than free micelles or the micelles that are loaded with small molecule alone. This is supported by the data from Dox release study: Dox formulated in the co-loaded nanoparticles exhibited a slower kinetics of release compared to the formulation that is loaded with Dox only (Fig. 58). Interestingly, the size of the co-loaded micelles (~80 nm) is also significantly smaller that of free micelles (~180 nm) or the micelles loaded with Dox alone (~170 nm) (Tab. 8). This might be

attributed to a decreased repulsion among the positively monomers as a result of charge neutralization following complexation with siRNA or plasmid DNA. More studies are needed to better understand the underlying mechanism.

The complexes of DNA with either POEG-*st*-Pmor or POEG-*st*-Ppipe polymer were significantly more stable than PEI/DNA complexes following exposure to BSA (30 mg/mL). This is likely due to the dynamic shielding of the complexes by PEG despite the fact that both complexes remain positively charged. The improved stability of the two complexes in the presence of serum proteins may contribute to the efficient delivery of siRNA to distant s.c. tumors (Fig. 63). A more effective accumulation in the lung (Fig. 63) is likely due to the interaction of tertiary amine moiety with negatively charged cell membrane in the lung. Amine-containing basic compounds have been reported to be predominantly accumulate in the lung due to the specific binding to acidic phospholipids on the cell membrane, which is abundantly distributed in lung tissue. Therefore our carriers are suitable for codelivery of nucleic acid therapeutics and small molecule drugs to both distant solid tumors and lung metastatic lesions.

POEG-*st*-Pmor and POEG-*st*-Ppipe were comparable to PEI in transfecting tumor cells *in vitro* (Fig. 62). However, they were more effective than PEI in transfecting either lungs or tumor tissues *in vivo* (Fig. 63&64). The higher efficiency of POEG-*st*-Pmor and POEG-*st*-Ppipe polymers might be due to the improved stability of POEG-*st*-Pmor and POEG-*st*-Ppipe complexes in blood circulation due to the PEG shielding. It is also possible that POEG-*st*-Pmor and POEG-*st*-Ppipe form more stable complexes with DNA compared to

PEI due to an additional mechanism of polymer/DNA interaction through the π-π interactions between the benzene rings in DNA and our polymers.

POEG-*st*-Pmor polymer was chosen to further examine the therapeutic effect of codelivery of Dox and IL-36γ as both POEG-*st*-Pmor and POEG-*st*-Ppipe polymers showed similar biophysical properties (Tab. 8) and comparable efficiency in codelivery (Fig. 62, 63&64). POEG-*st*-Pmor alone was not active in the 4T1.2 lung metastasis model. Delivery of Dox or IL-36γ alone via POEG-*st*-Pmor polymer showed a modest activity in inhibiting the lung metastasis. Combination of the two led to a significant improvement in antitumor activity as shown by both smallest number of tumor nodules in the lung and the lowest weights of the tumor-bearing lungs (Fig. 65b,d&e). Flow study showed that codelivery of IL-36γ and Dox was most effective in activating T cell response, suggesting that the synergistic effect of Dox and IL-36γ combination on the immune system may play a role in the improved antitumor activity. Interestingly, the T_{reg} cells were also increased following treatment with IL-36γ, alone or in combination with Dox (Figure 66k-l). This may be due to high amounts of IFN-γ accumulated locally, which may trigger the induction of Foxp3 expression in T cells[225]. Combination of IL-36γ/Dox codelivery with other therapies that can block the conversion of $CD4^+CD25^-$ T cells to $CD4^+$ T_{regs} may help to further enhance the outcome of treatment.

7.6 CONCLUSION

In this study, we developed and systematically evaluated the potential of POEG-*st*-Pmor and POEG-*st*-Ppipe nanocarriers for codelivery of Dox and IL36γ plasmid. Stable and nanosized micelles co-loaded with plasmid/siRNA and Dox could be readily prepared and were highly effective in delivery to lungs as well as distant s.c. tumors. Significantly improved antitumor activity was demonstrated with codelivery of Dox and L36γ plasmid in comparison with other control groups in a 4T1.2 lung metastasis model. POEG-*st*-Pmor and POEG-*st*-Ppipe may represent a simple and effective deliver system for an optimal chemo-gene combination therapy.

8.0 SUMMARY AND PERSPECTIVES

New drug candidates often face the problems of poor bioavailability and undesirable side effects in the transition to clinic. Further, therapeutic effect of the newly emerging gene therapy using DNA and proteins is completely dependent on the delivery efficiency. Nanomedicines have been investigated for the targeted delivery of anticancer reagents to the critical site of action with improved therapeutic efficacy. Many different nanomedicines are well designed for longer stability, increased solubility, enhanced pharmacokinetics/biodistribution, decreased toxicity, and improved efficacy of drugs. Basically, the nanomedicines can be divided to liposomes, polymeric conjugates, polymeric nanoparticles, polymeric micelles and other types. Polymeric micelles present a promising delivery system for hydrophobic drugs, which possess a unique core-shell structure. The hydrophobic core incorporates water-soluble drugs via hydrophobic interaction and the hydrophilic outer layers play an important role in systemic administration, particular in enhancing circulation time and interaction with targeted cells.

During my graduate study, I worked on several projects to develop multi-functional polymeric micelle system for the targeted delivery of anticancer agents. I firstly discovered significant synergistic effect between curcumin and FTS in treatment of prostate cancers and we demonstrated curcumin could be effectively loaded into PEG-FTS micellar system and achieved enhanced antitumor activity both *in vitro* and *in vivo*. In a metastatic 4T1.2 breast cancer mouse model, tumor growth was significantly inhibited by curcumin/PEG_{5K}-FTS_2(L) mixed micelles compared to curcumin formulated in Cremophor/EL. In order to further

improve the drug loading and formulation stability of the PEG-FTS_2, a drug-interactive Fmoc motif was incorporated into the carrier system. As a result, curcumin-loaded PEG_{5K}-Fmoc-FTS_2 micelles were more effective in inhibiting tumor cell colony formation and the curcumin/PEG_{5K}-Fmoc-FTS_2 demonstrated superior antitumor activity compared to curcumin/Cremophr EL and curcumin/PEG_{5K}-FTS_2 in 4T1.2 mouse model.

In order to counteract undesirable upregulation of immunecheckpoint proteins during the treatment and further improve the antitumor efficacy by stimulating anticancer immune response, efforts were also made to develop a novel micellar nanocarrier based on PEG-derivatized NLG919 prodrug. The prodrug not only well retained the IDO enzyme inhibition effect in an *in vitro* kynurenine inhibition assay and T cell proliferation study, but could be used as nanocarrier for delivery of chemotherapy drugs. Pharmacokinetics and biodistribution studies showed that PTX formulated PEG-Fmoc-NLG mixed micelles were able to retain PTX in the bloodstream for a longer time period than Taxol formulation and efficiently deliver the drug to tumor sites. More importantly, PTX loaded PEG-Fmoc-NLG led to superior antitumor activity in breast cancer and melanoma cancer models. Then we further improved the PEG-NLG carrier system by increasing the number of NLG content in the carrier (from 9.4% to 19.7%) via RAFT polymerization. The new polymer could not only decrease the amounts of carrier materials in *in vivo* application by increase the drug loading capacity and micelle stability but increase NLG release by introducing a disulfide linkage into the PSSN10 system. However, there were many untoward immunesuppressive mechanisms were activated during the PTX/PEG-NLG treatment including upregulation of MDSCs or other immunecheckpoints. A multi-target receptor tyrosine kinase inhibitor, SUN

that reduces MDSC levels was introduced to an improved PEG_{5k}-Fmoc-NLG_2 micelle system that was capable for loading both SUN and PTX. SUN+PTX/PEG_{5k}-Fmoc-NLG_2 micelles not only decreased the number and percentage of MDSCs and T_{regs} in the TME, but also showed enhanced *in vivo* antitumor activity in an advanced murine breast cancer mouse model.

Our improved vectors worked well for most of the hydrophobic chemotherapeutics, but could not simultaneously deliver genes that could target to most of the disease target. Multifunctional nanocarriers PEG-pMor and PEG-pPipe were carefully designed and synthesized for targeted co-delivery of IL-36γ plasmid DNA and Dox to lung metastasis of breast cancer. The Dox+IL-36γ plasmid/PEG-pMor polymers could not only decrease the tumor lung metastases but also synergistically enhance the antitumor immune response by increasing the functional lymphocyte infiltration and simultaneously decreasing MDSC cell accumulation in lung.

Although all these micelle systems allowed for passive accumulation inside tumors with leaky vasculature, the majority of these nanoparticles were still cleared by the RES system, resulting in short half lives and unwanted micelle deposition in the liver and spleen. Development of multifunctional micelles, either through conjugation of targeting ligands on the micelle surface or a triggered release mechanism, can lessen these problems by increasing particle/drug exposure to the tumor.

Targeting ligands are designed to conjugate to the out layer of the micelles in order to induce specific targeting and uptake of the micelle by tumor cells. Small organic molecules such as folic acid targeting on receptor over-expressed on cancer cells, peptide ligands such

as cRGD peptide targeting the avb3 integrin, or the tumor specific antibodies are now widely used as targeting ligand for micelle system to improve the drug accumulation in tumor sites.

Another strategy for improve current micelle system is to trigger site-specific drug release by modifying micelle structures. After reaching the targeted site, efficient drug release from micelle carriers becomes critically important to ensure drug bioavailability, and hence achieve the desired cytotoxic effect. The incorporation of pH sensitive linkage using acid-labile bonds or adding pH-sensitive components for effective protonation in the structure of micelle will help with the accumulation of drug in tumor site.

In addition, more investigations on the structure-activity relationship of polymeric micellar are needed to improve the drug-carrier interaction. Investigations of new combinational therapy strategies are necessary to offer better antitumor activity in designing drug delivery system. These studies shall lead to the development of further improved micellar systems to advance the treatment of cancers.

BIBLIOGRAPHY

1. Siegel RL, Miller KD, Jemal A. Cancer statistics, 2016. *CA: a cancer journal for clinicians* **66**, 7-30 (2016).
2. Early Breast Cancer Trialists' Collaborative G. Effects of radiotherapy and of differences in the extent of surgery for early breast cancer on local recurrence and 15-year survival: an overview of the randomised trials. *The Lancet* **366**, 2087-2106 (2005).
3. Yap TA, Carden CP, Kaye SB. Beyond chemotherapy: targeted therapies in ovarian cancer. *Nature reviews Cancer* **9**, 167 (2009).
4. Sawyers C. Targeted cancer therapy. *Nature* **432**, 294 (2004).
5. van Zutphen S, Reedijk J. Targeting platinum anti-tumour drugs: Overview of strategies employed to reduce systemic toxicity. *Coordination chemistry reviews* **249**, 2845-2853 (2005).
6. Lytton-Jean AKR, Kauffman KJ, Kaczmarek JC, Langer R. Cancer nanotherapeutics in clinical trials. In: *Nanotechnology-Based Precision Tools for the Detection and Treatment of Cancer* (ed^(eds). Springer (2015).
7. Cho K, Wang XU, Nie S, Shin DM. Therapeutic nanoparticles for drug delivery in cancer. *Clinical cancer research* **14**, 1310-1316 (2008).
8. Chidambaram M, Manavalan R, Kathiresan K. Nanotherapeutics to overcome conventional cancer chemotherapy limitations. *Journal of pharmacy & pharmaceutical sciences* **14**, 67-77 (2011).
9. Kanapathipillai M, Brock A, Ingber DE. Nanoparticle targeting of anti-cancer drugs that alter intracellular signaling or influence the tumor microenvironment. *Advanced drug delivery reviews* **79**, 107-118 (2014).
10. Hockel M, Vaupel P. Tumor hypoxia: definitions and current clinical, biologic, and molecular aspects. *Journal of the National Cancer Institute* **93**, 266-276 (2001).
11. Iyer AK, Khaled G, Fang J, Maeda H. Exploiting the enhanced permeability and retention effect for tumor targeting. *Drug discovery today* **11**, 812-818 (2006).
12. Schiffelers RM*, et al.* Cancer siRNA therapy by tumor selective delivery with ligand-targeted sterically stabilized nanoparticle. *Nucleic acids research* **32**, e149-e149 (2004).
13. Cheng J*, et al.* Formulation of functionalized PLGA–PEG nanoparticles for in vivo targeted drug delivery. *Biomaterials* **28**, 869-876 (2007).
14. Tobio M, Gref R, Sanchez A, Langer R, Alonso MJ. Stealth PLA-PEG nanoparticles as protein carriers for nasal administration. *Pharmaceutical research* **15**, 270-275 (1998).
15. Letchford K, Burt H. A review of the formation and classification of amphiphilic block copolymer nanoparticulate structures: micelles, nanospheres, nanocapsules and polymersomes. *European journal of pharmaceutics and biopharmaceutics* **65**, 259-269 (2007).
16. Mukerjee P, Mysels KJ. Critical micelle concentrations of aqueous surfactant systems. (ed^(eds). National Standard reference data system (1971).

17. Oerlemans C, Bult W, Bos M, Storm G, Nijsen JFW, Hennink WE. Polymeric micelles in anticancer therapy: targeting, imaging and triggered release. *Pharmaceutical research* **27**, 2569-2589 (2010).
18. Sezgin Z, Yüksel N, Baykara T. Preparation and characterization of polymeric micelles for solubilization of poorly soluble anticancer drugs. *European journal of pharmaceutics and biopharmaceutics* **64**, 261-268 (2006).
19. Matsumura Y, Kataoka K. Preclinical and clinical studies of anticancer agent‐incorporating polymer micelles. *Cancer science* **100**, 572-579 (2009).
20. Deng C, Jiang Y, Cheng R, Meng F, Zhong Z. Biodegradable polymeric micelles for targeted and controlled anticancer drug delivery: promises, progress and prospects. *Nano Today* **7**, 467-480 (2012).
21. Kim T-Y*, et al.* Phase I and pharmacokinetic study of Genexol-PM, a cremophor-free, polymeric micelle-formulated paclitaxel, in patients with advanced malignancies. *Clinical cancer research* **10**, 3708-3716 (2004).
22. Danhier F, Feron O, Préat V. To exploit the tumor microenvironment: passive and active tumor targeting of nanocarriers for anti-cancer drug delivery. *Journal of Controlled Release* **148**, 135-146 (2010).
23. Zhong Y, Meng F, Deng C, Zhong Z. Ligand-directed active tumor-targeting polymeric nanoparticles for cancer chemotherapy. *Biomacromolecules* **15**, 1955-1969 (2014).
24. Kedar U, Phutane P, Shidhaye S, Kadam V. Advances in polymeric micelles for drug delivery and tumor targeting. *Nanomedicine: Nanotechnology, Biology and Medicine* **6**, 714-729 (2010).
25. Wei H, Cheng S-X, Zhang X-Z, Zhuo R-X. Thermo-sensitive polymeric micelles based on poly (N-isopropylacrylamide) as drug carriers. *Progress in Polymer Science* **34**, 893-910 (2009).
26. Na K, Lee KH, Lee DH, Bae YH. Biodegradable thermo-sensitive nanoparticles from poly (L-lactic acid)/poly (ethylene glycol) alternating multi-block copolymer for potential anti-cancer drug carrier. *European journal of pharmaceutical sciences* **27**, 115-122 (2006).
27. Musacchio T, Laquintana V, Latrofa A, Trapani G, Torchilin VP. PEG-PE micelles loaded with paclitaxel and surface-modified by a PBR-ligand: synergistic anticancer effect. *Molecular pharmaceutics* **6**, 468-479 (2008).
28. Nakajima TE*, et al.* Synergistic antitumor activity of the novel SN‐38‐incorporating polymeric micelles, NK012, combined with 5‐fluorouracil in a mouse model of colorectal cancer, as compared with that of irinotecan plus 5‐fluorouracil. *International journal of cancer* **122**, 2148-2153 (2008).
29. Lu J*, et al.* Targeted delivery of doxorubicin by folic acid-decorated dual functional nanocarrier. *Molecular pharmaceutics* **11**, 4164-4178 (2014).
30. Huang Y*, et al.* PEG-derivatized embelin as a dual functional carrier for the delivery of paclitaxel. *Bioconjugate chemistry* **23**, 1443-1451 (2012).
31. Zhang X*, et al.* PEG-farnesyl thiosalicylic acid telodendrimer micelles as an improved formulation for targeted delivery of paclitaxel. *Molecular pharmaceutics* **11**, 2807-2814 (2014).

32. Zhao M, Huang Y, Chen Y, Xu J, Li S, Guo X. PEG-Fmoc-Ibuprofen Conjugate as a Dual Functional Nanomicellar Carrier for Paclitaxel. *Bioconjugate chemistry* **27**, 2198-2205 (2016).
33. Chen Y, Zhang X, Lu J, Huang Y, Li J, Li S. Targeted delivery of curcumin to tumors via PEG-derivatized FTS-based micellar system. *The AAPS journal* **16**, 600-608 (2014).
34. Jansen B*, et al.* Novel Ras antagonist blocks human melanoma growth. *Proceedings of the National Academy of Sciences* **96**, 14019-14024 (1999).
35. Laheru D*, et al.* Integrated preclinical and clinical development of S-trans, trans-Farnesylthiosalicylic Acid (FTS, Salirasib) in pancreatic cancer. *Investigational new drugs* **30**, 2391-2399 (2012).
36. Laheru D*, et al.* Integrated development of S-trans, trans-farnesylthiosalicyclic acid (FTS, salirasib) in advanced pancreatic cancer. *Journal of Clinical Oncology* **27**, 4529-4529 (2009).
37. Wolfson E, Schmukler E, Schokoroy ST, Kloog Y, Pinkas‐Kramarski R. Enhancing FTS (Salirasib) efficiency via combinatorial treatment. *Biology of the Cell* **107**, 130-143 (2015).
38. Yang M*, et al.* Chemotherapy induces tumor immune evasion by upregulation of programmed cell death ligand 1 expression in bone marrow stromal cells. *Molecular Oncology* **11**, 358-372 (2017).
39. Igney FH, Krammer PH. Immune escape of tumors: apoptosis resistance and tumor counterattack. *Journal of leukocyte biology* **71**, 907-920 (2002).
40. Rosenberg SA, Yang JC, Restifo NP. Cancer immunotherapy: moving beyond current vaccines. *Nature medicine* **10**, 909 (2004).
41. Pardoll DM. The blockade of immune checkpoints in cancer immunotherapy. *Nature reviews Cancer* **12**, 252 (2012).
42. Rosenberg SA. A new era for cancer immunotherapy based on the genes that encode cancer antigens. *Immunity* **10**, 281-287 (1999).
43. Mellman I, Coukos G, Dranoff G. Cancer immunotherapy comes of age. *Nature* **480**, 480 (2011).
44. Couzin-Frankel J. Cancer immunotherapy. (ed^(eds). American Association for the Advancement of Science (2013).
45. Gajewski TF, Schreiber H, Fu Y-X. Innate and adaptive immune cells in the tumor microenvironment. *Nature immunology* **14**, 1014-1022 (2013).
46. Sato E*, et al.* Intraepithelial CD8+ tumor-infiltrating lymphocytes and a high CD8+/regulatory T cell ratio are associated with favorable prognosis in ovarian cancer. *Proceedings of the National Academy of Sciences of the United States of America* **102**, 18538-18543 (2005).
47. Schreiber RD, Old LJ, Smyth MJ. Cancer immunoediting: integrating immunity's roles in cancer suppression and promotion. *Science* **331**, 1565-1570 (2011).
48. Mahmoud SMA*, et al.* Tumor-infiltrating CD8+ lymphocytes predict clinical outcome in breast cancer. *Journal of clinical oncology* **29**, 1949-1955 (2011).
49. Blattman JN, Greenberg PD. Cancer immunotherapy: a treatment for the masses. *Science* **305**, 200-205 (2004).

50. Sheikh NA*, et al.* Sipuleucel-T immune parameters correlate with survival: an analysis of the randomized phase 3 clinical trials in men with castration-resistant prostate cancer. *Cancer Immunology, Immunotherapy* **62**, 137-147 (2013).
51. Schlom J. Therapeutic cancer vaccines: current status and moving forward. *Journal of the National Cancer Institute* **104**, 599-613 (2012).
52. Belardelli F. Role of interferons and other cytokines in the regulation of the immune response. *Apmis* **103**, 161-179 (1995).
53. Medzhitov R, Janeway CA. Innate immunity: impact on the adaptive immune response. *Current opinion in immunology* **9**, 4-9 (1997).
54. Cooper MA, Fehniger TA, Caligiuri MA. The biology of human natural killer-cell subsets. *Trends in immunology* **22**, 633-640 (2001).
55. Vähä-Koskela MJV, Heikkilä JE, Hinkkanen AE. Oncolytic viruses in cancer therapy. *Cancer letters* **254**, 178-216 (2007).
56. Pol J, Kroemer G, Galluzzi L. First oncolytic virus approved for melanoma immunotherapy. (ed^(eds). Taylor & Francis (2016).
57. Yee C*, et al.* Adoptive T cell therapy using antigen-specific CD8+ T cell clones for the treatment of patients with metastatic melanoma: in vivo persistence, migration, and antitumor effect of transferred T cells. *Proceedings of the National Academy of Sciences* **99**, 16168-16173 (2002).
58. Lipson EJ, Drake CG. Ipilimumab: an anti-CTLA-4 antibody for metastatic melanoma. *Clinical Cancer Research* **17**, 6958-6962 (2011).
59. Benson DM*, et al.* The PD-1/PD-L1 axis modulates the natural killer cell versus multiple myeloma effect: a therapeutic target for CT-011, a novel monoclonal anti–PD-1 antibody. *Blood* **116**, 2286-2294 (2010).
60. Topalian SL, Drake CG, Pardoll DM. Targeting the PD-1/B7-H1 (PD-L1) pathway to activate anti-tumor immunity. *Current opinion in immunology* **24**, 207-212 (2012).
61. Hamid O*, et al.* Safety and tumor responses with lambrolizumab (anti–PD-1) in melanoma. *N Engl J Med* **2013**, 134-144 (2013).
62. Platten M, Wick W, Van den Eynde BJ. Tryptophan catabolism in cancer: beyond IDO and tryptophan depletion. *Cancer research* **72**, 5435-5440 (2012).
63. Munn DH*, et al.* Expression of indoleamine 2, 3-dioxygenase by plasmacytoid dendritic cells in tumor-draining lymph nodes. *Journal of Clinical Investigation* **114**, 280 (2004).
64. Munn DH, Mellor AL. Indoleamine 2, 3-dioxygenase and tumor-induced tolerance. *Journal of Clinical Investigation* **117**, 1147 (2007).
65. Moon YW, Hajjar J, Hwu P, Naing A. Targeting the indoleamine 2, 3-dioxygenase pathway in cancer. *Journal for immunotherapy of cancer* **3**, 1186 (2015).
66. Mellman I, Coukos G, Dranoff G. Cancer immunotherapy comes of age. *Nature* **480**, 480-489 (2011).
67. Sharma P, Allison JP. Immune checkpoint targeting in cancer therapy: toward combination strategies with curative potential. *Cell* **161**, 205-214 (2015).

68. Nowak AK, Robinson BWS, Lake RA. Synergy between chemotherapy and immunotherapy in the treatment of established murine solid tumors. *Cancer research* **63**, 4490-4496 (2003).
69. Mantovani A, Allavena P, Sica A, Balkwill F. Cancer-related inflammation. *Nature* **454**, 436-444 (2008).
70. Postow MA, Callahan MK, Wolchok JD. Immune checkpoint blockade in cancer therapy. *Journal of clinical oncology* **33**, 1974-1982 (2015).
71. Hamanishi J*, et al.* Safety and antitumor activity of anti–PD-1 antibody, nivolumab, in patients with platinum-resistant ovarian cancer. *Journal of Clinical Oncology* **33**, 4015-4022 (2015).
72. Mautino MR*, et al.* NLG919, a novel indoleamine-2, 3-dioxygenase (IDO)-pathway inhibitor drug candidate for cancer therapy. (ed^(eds). AACR (2013).
73. Liu X*, et al.* Selective inhibition of IDO1 effectively regulates mediators of antitumor immunity. *Blood* **115**, 3520-3530 (2010).
74. Bissell MJ, Hines WC. Why don't we get more cancer? A proposed role of the microenvironment in restraining cancer progression. *Nature medicine* **17**, 320-329 (2011).
75. Hanahan D, Weinberg RA. Hallmarks of cancer: the next generation. *cell* **144**, 646-674 (2011).
76. Niidome T, Huang L. Gene therapy progress and prospects: nonviral vectors. *Gene therapy* **9**, 1647 (2002).
77. Izquierdo M. Short interfering RNAs as a tool for cancer gene therapy. *Cancer gene therapy* **12**, 217-227 (2005).
78. Yazawa K, Fujimori M, Amano J, Kano Y, Taniguchi Si. Bifidobacterium longum as a delivery system for cancer gene therapy: selective localization and growth in hypoxic tumors. *Cancer gene therapy* **7**, 269 (2000).
79. Wang Y, Gao S, Ye W-H, Yoon HS, Yang Y-Y. Co-delivery of drugs and DNA from cationic core–shell nanoparticles self-assembled from a biodegradable copolymer. *Nature materials* **5**, 791-796 (2006).
80. Chen AM*, et al.* Co‐delivery of doxorubicin and Bcl‐2 siRNA by mesoporous silica nanoparticles enhances the efficacy of chemotherapy in multidrug‐resistant cancer cells. *Small* **5**, 2673-2677 (2009).
81. Saad M, Garbuzenko OB, Minko T. Co-delivery of siRNA and an anticancer drug for treatment of multidrug-resistant cancer. *Nanomedicine* **3**, 761-776 (2008).
82. Khan M, Ong ZY, Wiradharma N, Attia ABE, Yang YY. Advanced materials for co‐delivery of drugs and genes in cancer therapy. *Advanced healthcare materials* **1**, 373-392 (2012).
83. Kakizawa Y, Kataoka K. Block copolymer micelles for delivery of gene and related compounds. *Advanced drug delivery reviews* **54**, 203-222 (2002).
84. Jhaveri AM, Torchilin VP. Multifunctional polymeric micelles for delivery of drugs and siRNA. *Frontiers in pharmacology* **5**, (2014).
85. Felgner JH*, et al.* Enhanced gene delivery and mechanism studies with a novel series of cationic lipid formulations. *Journal of Biological Chemistry* **269**, 2550-2561 (1994).

86. Duvoix A*, et al.* Chemopreventive and therapeutic effects of curcumin. *Cancer letters* **223**, 181-190 (2005).
87. Kawamori T*, et al.* Chemopreventive effect of curcumin, a naturally occurring anti-inflammatory agent, during the promotion/progression stages of colon cancer. *Cancer research* **59**, 597-601 (1999).
88. Aggarwal BB*, et al.* Curcumin suppresses the paclitaxel-induced nuclear factor-κB pathway in breast cancer cells and inhibits lung metastasis of human breast cancer in nude mice. *Clinical Cancer Research* **11**, 7490-7498 (2005).
89. Mukhopadhyay A, Bueso-Ramos C, Chatterjee D, Pantazis P, Aggarwal BB. Curcumin downregulates cell survival mechanisms in human prostate cancer cell lines. *Oncogene* **20**, 7597 (2001).
90. Kunnumakkara AB, Anand P, Aggarwal BB. Curcumin inhibits proliferation, invasion, angiogenesis and metastasis of different cancers through interaction with multiple cell signaling proteins. *Cancer letters* **269**, 199-225 (2008).
91. Chen Y-R, Tan T-H. Inhibition of the c-Jun N-terminal kinase (JNK) signaling pathway by curcumin. *Oncogene* **17**, (1998).
92. Lev-Ari S*, et al.* Celecoxib and curcumin synergistically inhibit the growth of colorectal cancer cells. *Clinical Cancer Research* **11**, 6738-6744 (2005).
93. Lev-Ari S*, et al.* Curcumin augments gemcitabine cytotoxic effect on pancreatic adenocarcinoma cell lines. *Cancer investigation* **25**, 411-418 (2007).
94. Notarbartolo M, Poma P, Perri D, Dusonchet L, Cervello M, D'Alessandro N. Antitumor effects of curcumin, alone or in combination with cisplatin or doxorubicin, on human hepatic cancer cells. Analysis of their possible relationship to changes in NF-kB activation levels and in IAP gene expression. *Cancer letters* **224**, 53-65 (2005).
95. Rotblat B, Ehrlich M, Haklai R, Kloog Y. The Ras inhibitor farnesylthiosalicylic acid (Salirasib) disrupts the spatiotemporal localization of active Ras: a potential treatment for cancer. *Methods in enzymology* **439**, 467-489 (2008).
96. Marom M, Haklai R, Ben-Baruch G, Marciano D, Egozi Y, Kloog Y. Selective inhibition of Ras-dependent cell growth by farnesylthiosalisylic acid. *Journal of Biological Chemistry* **270**, 22263-22270 (1995).
97. Kloog Y, Cox AD. RAS inhibitors: potential for cancer therapeutics. *Molecular medicine today* **6**, 398-402 (2000).
98. McLaughlin SK*, et al.* The RasGAP gene, RASAL2, is a tumor and metastasis suppressor. *Cancer cell* **24**, 365-378 (2013).
99. Min J*, et al.* An oncogene-tumor suppressor cascade drives metastatic prostate cancer by coordinately activating Ras and nuclear factor-[kappa] B. *Nature medicine* **16**, 286-294 (2010).
100. Gana-Weisz M, Halaschek-Wiener J, Jansen B, Elad G, Haklai R, Kloog Y. The Ras inhibitor S-trans, trans-farnesylthiosalicylic acid chemosensitizes human tumor cells without causing resistance. *Clinical cancer research* **8**, 555-565 (2002).
101. Downward J. Targeting RAS signalling pathways in cancer therapy. *Nature reviews Cancer* **3**, 11 (2003).

102. Haklai R, Elad-Sfadia G, Egozi Y, Kloog Y. Orally administered FTS (salirasib) inhibits human pancreatic tumor growth in nude mice. *Cancer chemotherapy and pharmacology* **61**, 89-96 (2008).
103. Biran A, Brownstein M, Haklai R, Kloog Y. Downregulation of survivin and aurora A by histone deacetylase and RAS inhibitors: a new drug combination for cancer therapy. *International journal of cancer* **128**, 691-701 (2011).
104. Mologni L, Brussolo S, Ceccon M, Gambacorti-Passerini C. Synergistic effects of combined Wnt/KRAS inhibition in colorectal cancer cells. *PloS one* **7**, e51449 (2012).
105. Anand P, Kunnumakkara AB, Newman RA, Aggarwal BB. Bioavailability of curcumin: problems and promises. *Molecular pharmaceutics* **4**, 807-818 (2007).
106. Kraitzer A, Kloog Y, Haklai R, Zilberman M. Composite fiber structures with antiproliferative agents exhibit advantageous drug delivery and cell growth inhibition in vitro. *Journal of pharmaceutical sciences* **100**, 133-149 (2011).
107. Zhang X*, et al.* PEG-farnesylthiosalicylate conjugate as a nanomicellar carrier for delivery of paclitaxel. *Bioconjugate chemistry* **24**, 464-472 (2013).
108. Zhang X*, et al.* Reduction-sensitive dual functional nanomicelles for improved delivery of paclitaxel. *Bioconjugate chemistry* **25**, 1689-1696 (2014).
109. Gao X, Huang L. Potentiation of cationic liposome-mediated gene delivery by polycations. *Biochemistry* **35**, 1027-1036 (1996).
110. Kinkade CW*, et al.* Targeting AKT/mTOR and ERK MAPK signaling inhibits hormone-refractory prostate cancer in a preclinical mouse model. *The Journal of clinical investigation* **118**, 3051 (2008).
111. Smalley KSM, Eisen TG. Farnesyl thiosalicylic acid inhibits the growth of melanoma cells through a combination of cytostatic and pro‐apoptotic effects. *International journal of cancer* **98**, 514-522 (2002).
112. Aoki H, Takada Y, Kondo S, Sawaya R, Aggarwal BB, Kondo Y. Evidence that curcumin suppresses the growth of malignant gliomas in vitro and in vivo through induction of autophagy: role of Akt and extracellular signal-regulated kinase signaling pathways. *Molecular pharmacology* **72**, 29-39 (2007).
113. Kurzrock R, Li L. Liposome-encapsulated curcumin: in vitro and in vivo effects on proliferation, apoptosis, signaling, and angiogenesis. *Journal of Clinical Oncology* **23**, 4091-4091 (2005).
114. Yallapu MM, Jaggi M, Chauhan SC. Curcumin nanoformulations: a future nanomedicine for cancer. *Drug discovery today* **17**, 71-80 (2012).
115. Lin Y-L*, et al.* A Lipo-PEG-PEI complex for encapsulating curcumin that enhances its antitumor effects on curcumin-sensitive and curcumin-resistance cells. *Nanomedicine: Nanotechnology, Biology and Medicine* **8**, 318-327 (2012).
116. Liu L*, et al.* Curcumin loaded polymeric micelles inhibit breast tumor growth and spontaneous pulmonary metastasis. *International journal of pharmaceutics* **443**, 175-182 (2013).
117. Gong C*, et al.* Improving antiangiogenesis and anti-tumor activity of curcumin by biodegradable polymeric micelles. *Biomaterials* **34**, 1413-1432 (2013).

118. Gou M*, et al.* Curcumin-loaded biodegradable polymeric micelles for colon cancer therapy in vitro and in vivo. *Nanoscale* **3**, 1558-1567 (2011).
119. Ma Z, Haddadi A, Molavi O, Lavasanifar A, Lai R, Samuel J. Micelles of poly (ethylene oxide) - b - poly (ε - caprolactone) as vehicles for the solubilization, stabilization, and controlled delivery of curcumin. *Journal of Biomedical Materials Research Part A* **86**, 300-310 (2008).
120. Yang R, Zhang S, Kong D, Gao X, Zhao Y, Wang Z. Biodegradable polymer-curcumin conjugate micelles enhance the loading and delivery of low-potency curcumin. *Pharmaceutical research* **29**, 3512-3525 (2012).
121. Wang K*, et al.* Novel micelle formulation of curcumin for enhancing antitumor activity and inhibiting colorectal cancer stem cells. *International journal of nanomedicine* **7**, 4487 (2012).
122. Song L, Shen Y, Hou J, Lei L, Guo S, Qian C. Polymeric micelles for parenteral delivery of curcumin: preparation, characterization and in vitro evaluation. *Colloids and Surfaces A: Physicochemical and Engineering Aspects* **390**, 25-32 (2011).
123. Wang Y-J*, et al.* Stability of curcumin in buffer solutions and characterization of its degradation products. *Journal of pharmaceutical and biomedical analysis* **15**, 1867-1876 (1997).
124. Pan M-H, Huang T-M, Lin J-K. Biotransformation of curcumin through reduction and glucuronidation in mice. *Drug metabolism and disposition* **27**, 486-494 (1999).
125. Mohanty C, Sahoo SK. The in vitro stability and in vivo pharmacokinetics of curcumin prepared as an aqueous nanoparticulate formulation. *Biomaterials* **31**, 6597-6611 (2010).
126. Maeda H, Wu J, Sawa T, Matsumura Y, Hori K. Tumor vascular permeability and the EPR effect in macromolecular therapeutics: a review. *Journal of controlled release* **65**, 271-284 (2000).
127. Cabral H*, et al.* Accumulation of sub-100 nm polymeric micelles in poorly permeable tumours depends on size. *Nature nanotechnology* **6**, 815-823 (2011).
128. Von Hoff DD*, et al.* Increased survival in pancreatic cancer with nab-paclitaxel plus gemcitabine. *The New England journal of medicine* **369**, 1691-1703 (2013).
129. Loi S*, et al.* Prognostic and predictive value of tumor-infiltrating lymphocytes in a phase III randomized adjuvant breast cancer trial in node-positive breast cancer comparing the addition of docetaxel to doxorubicin with doxorubicin-based chemotherapy: BIG 02-98. *J Clin Oncol* **31**, 860-867 (2013).
130. Yu Y*, et al.* Inhibition of Spleen Tyrosine Kinase Potentiates Paclitaxel-Induced Cytotoxicity in Ovarian Cancer Cells by Stabilizing Microtubules. *Cancer cell* **28**, 82-96 (2015).
131. Zitvogel L, Apetoh L, Ghiringhelli F, Andre F, Tesniere A, Kroemer G. The anticancer immune response: indispensable for therapeutic success? *J Clin Invest* **118**, 1991-2001 (2008).

132. Vincent J*, et al.* 5-Fluorouracil selectively kills tumor-associated myeloid-derived suppressor cells resulting in enhanced T cell-dependent antitumor immunity. *Cancer research* **70**, 3052-3061 (2010).
133. Vanneman M, Dranoff G. Combining immunotherapy and targeted therapies in cancer treatment. *Nature reviews Cancer* **12**, 237-251 (2012).
134. John J*, et al.* Differential effects of Paclitaxel on dendritic cell function. *BMC immunology* **11**, 14 (2010).
135. Bracci L, Schiavoni G, Sistigu A, Belardelli F. Immune-based mechanisms of cytotoxic chemotherapy: implications for the design of novel and rationale-based combined treatments against cancer. *Cell death and differentiation* **21**, 15-25 (2014).
136. Spranger S, Koblish HK, Horton B, Scherle PA, Newton R, Gajewski TF. Mechanism of tumor rejection with doublets of CTLA-4, PD-1/PD-L1, or IDO blockade involves restored IL-2 production and proliferation of CD8(+) T cells directly within the tumor microenvironment. *Journal for immunotherapy of cancer* **2**, 3 (2014).
137. Curran MA, Montalvo W, Yagita H, Allison JP. PD-1 and CTLA-4 combination blockade expands infiltrating T cells and reduces regulatory T and myeloid cells within B16 melanoma tumors. *Proceedings of the National Academy of Sciences of the United States of America* **107**, 4275-4280 (2010).
138. Topalian SL*, et al.* Safety, activity, and immune correlates of anti-PD-1 antibody in cancer. *The New England journal of medicine* **366**, 2443-2454 (2012).
139. Lipson EJ*, et al.* Durable cancer regression off-treatment and effective reinduction therapy with an anti-PD-1 antibody. *Clinical cancer research : an official journal of the American Association for Cancer Research* **19**, 462-468 (2013).
140. Pardoll DM. The blockade of immune checkpoints in cancer immunotherapy. *Nature reviews Cancer* **12**, 252-264 (2012).
141. Hodi FS*, et al.* Biologic activity of cytotoxic T lymphocyte-associated antigen 4 antibody blockade in previously vaccinated metastatic melanoma and ovarian carcinoma patients. *Proceedings of the National Academy of Sciences of the United States of America* **100**, 4712-4717 (2003).
142. Phan GQ*, et al.* Cancer regression and autoimmunity induced by cytotoxic T lymphocyte-associated antigen 4 blockade in patients with metastatic melanoma. *Proceedings of the National Academy of Sciences of the United States of America* **100**, 8372-8377 (2003).
143. Brahmer JR*, et al.* Phase I study of single-agent anti-programmed death-1 (MDX-1106) in refractory solid tumors: safety, clinical activity, pharmacodynamics, and immunologic correlates. *J Clin Oncol* **28**, 3167-3175 (2010).
144. Moffett JR, Namboodiri MA. Tryptophan and the immune response. *Immunology and cell biology* **81**, 247-265 (2003).

145. Uyttenhove C, *et al.* Evidence for a tumoral immune resistance mechanism based on tryptophan degradation by indoleamine 2,3-dioxygenase. *Nature medicine* **9**, 1269-1274 (2003).
146. Mellor AL, Munn DH. Tryptophan catabolism and T-cell tolerance: immunosuppression by starvation? *Immunology today* **20**, 469-473 (1999).
147. Muller AJ, DuHadaway JB, Donover PS, Sutanto-Ward E, Prendergast GC. Inhibition of indoleamine 2,3-dioxygenase, an immunoregulatory target of the cancer suppression gene Bin1, potentiates cancer chemotherapy. *Nat Med* **11**, 312-319 (2005).
148. Zhang P, *et al.* A PEG-Fmoc conjugate as a nanocarrier for paclitaxel. *Biomaterials* **35**, 7146-7156 (2014).
149. Lu J, *et al.* An improved D-alpha-tocopherol-based nanocarrier for targeted delivery of doxorubicin with reversal of multidrug resistance. *J Control Release* **196**, 272-286 (2014).
150. Lu J, *et al.* The self-assembling camptothecin-tocopherol prodrug: An effective approach for formulating camptothecin. *Biomaterials* **62**, 176-187 (2015).
151. Li J, *et al.* miR-122 regulates collagen production via targeting hepatic stellate cells and suppressing P4HA1 expression. *J Hepatol* **58**, 522-528 (2013).
152. Hou DY, *et al.* Inhibition of indoleamine 2,3-dioxygenase in dendritic cells by stereoisomers of 1-methyl-tryptophan correlates with antitumor responses. *Cancer research* **67**, 792-801 (2007).
153. Koblish HK, *et al.* Hydroxyamidine inhibitors of indoleamine-2,3-dioxygenase potently suppress systemic tryptophan catabolism and the growth of IDO-expressing tumors. *Molecular cancer therapeutics* **9**, 489-498 (2010).
154. Holmgaard RB, Zamarin D, Munn DH, Wolchok JD, Allison JP. Indoleamine 2,3-dioxygenase is a critical resistance mechanism in antitumor T cell immunotherapy targeting CTLA-4. *The Journal of experimental medicine* **210**, 1389-1402 (2013).
155. Handke N, *et al.* Elaboration of glycopolymer-functionalized micelles from an N-vinylpyrrolidone/lactide-based reactive copolymer platform. *Macromolecular bioscience* **13**, 1213-1220 (2013).
156. Zhang P, *et al.* Effective co-delivery of doxorubicin and dasatinib using a PEG-Fmoc nanocarrier for combination cancer chemotherapy. *Biomaterials* **67**, 104-114 (2015).
157. Mocellin S, Provenzano M, Rossi CR, Pilati P, Nitti D, Lise M. Use of quantitative real-time PCR to determine immune cell density and cytokine gene profile in the tumor microenvironment. *Journal of immunological methods* **280**, 1-11 (2003).
158. Maeda H, Wu J, Sawa T, Matsumura Y, Hori K. Tumor vascular permeability and the EPR effect in macromolecular therapeutics: a review. *J Control Release* **65**, 271-284 (2000).
159. Zitvogel L, Apetoh L, Ghiringhelli F, Kroemer G. Immunological aspects of cancer chemotherapy. *Nat Rev Immunol* **8**, 59-73 (2008).
160. Sharon E, Streicher H, Goncalves P, Chen HX. Immune checkpoint inhibitors in clinical trials. *Chin J Cancer* **33**, 434-444 (2014).

161. Pardoll DM. The blockade of immune checkpoints in cancer immunotherapy. *Nature Reviews Cancer* **12**, 252-264 (2012).
162. Perkins D*, et al.* Regulation of CTLA-4 expression during T cell activation. *The Journal of Immunology* **156**, 4154-4159 (1996).
163. Contardi E*, et al.* CTLA‐4 is constitutively expressed on tumor cells and can trigger apoptosis upon ligand interaction. *Int J Cancer* **117**, 538-550 (2005).
164. Topalian SL, Drake CG, Pardoll DM. Immune checkpoint blockade: a common denominator approach to cancer therapy. *Cancer Cell* **27**, 450-461 (2015).
165. Blank C, Mackensen A. Contribution of the PD-L1/PD-1 pathway to T-cell exhaustion: an update on implications for chronic infections and tumor evasion. *Cancer Immunol Immunother* **56**, 739-745 (2007).
166. Okazaki T, Honjo T. The PD-1–PD-L pathway in immunological tolerance. *Trends Immunol* **27**, 195-201 (2006).
167. Ribas A. Releasing the brakes on cancer immunotherapy. *N Engl J Med* **373**, 1490-1492 (2015).
168. Da Silva C, Rueda F, Löwik C, Ossendorp F, Cruz LJ. Combinatorial prospects of nano-targeted chemoimmunotherapy. *Biomaterials* **83**, 308-320 (2016).
169. Apetoh L, Ladoire S, Coukos G, Ghiringhelli F. Combining immunotherapy and anticancer agents: the right path to achieve cancer cure? *Ann Oncol* **26**, 1813-1823 (2015).
170. Xiao Y, Freeman GJ. The microsatellite instable subset of colorectal cancer is a particularly good candidate for checkpoint blockade immunotherapy. *Cancer discovery* **5**, 16-18 (2015).
171. Curti A, Trabanelli S, Salvestrini V, Baccarani M, Lemoli RM. The role of indoleamine 2, 3-dioxygenase in the induction of immune tolerance: focus on hematology. *Blood* **113**, 2394-2401 (2009).
172. Hwu P, Du MX, Lapointe R, Taylor MW, Young HA. Indoleamine 2, 3-dioxygenase production by human dendritic cells results in the inhibition of T cell proliferation. *The Journal of Immunology* **164**, 3596-3599 (2000).
173. Munn DH, Mellor AL. IDO in the tumor microenvironment: inflammation, counter-regulation, and tolerance. *Trends Immunol* **37**, 193-207 (2016).
174. Smith C*, et al.* IDO is a nodal pathogenic driver of lung cancer and metastasis development. *Cancer discovery* **2**, 722-735 (2012).
175. Nayak A*, et al.* A Phase I study of NLG919 for adult patients with recurrent advanced solid tumors. *Journal for immunotherapy of cancer* **2**, 1 (2014).
176. Awuah SG, Zheng Y-R, Bruno PM, Hemann MT, Lippard SJ. A Pt (IV) Pro-drug Preferentially Targets Indoleamine-2, 3-dioxygenase, Providing Enhanced Ovarian Cancer Immuno-Chemotherapy. *J Am Chem Soc* **137**, 14854-14857 (2015).
177. Muller AJ, DuHadaway JB, Donover PS, Sutanto-Ward E, Prendergast GC. Inhibition of indoleamine 2, 3-dioxygenase, an immunoregulatory target of the cancer suppression gene Bin1, potentiates cancer chemotherapy. *Nat Med* **11**, 312-319 (2005).

178. Chen Y XR, Huang Y, Zhao W, Li J, Zhang X, Wang P, Venkataramanan R, Fan J, Xie W, Ma X, Lu B, Li S. An immunostimulatory dual-functional nanocarrier that improves cancer immunochemotherapy. *Nat Commun* **Just Accepted**, (2016).
179. Casares N, *et al.* Caspase-dependent immunogenicity of doxorubicin-induced tumor cell death. *The Journal of experimental medicine* **202**, 1691-1701 (2005).
180. Sun J, *et al.* Preparation of functional water-soluble low-cytotoxic poly(methacrylate)s with pendant cationic l-lysines for efficient gene delivery. *Macromol Biosci* **13**, 35-47 (2013).
181. Sun P, Zhou D, Gan Z. Novel reduction-sensitive micelles for triggered intracellular drug release. *J Control Release* **155**, 96-103 (2011).
182. Sun J, *et al.* A prodrug micellar carrier assembled from polymers with pendant farnesyl thiosalicylic acid moieties for improved delivery of paclitaxel. *Acta Biomater* **43**, 282-291 (2016).
183. Sun J, Luo T, Sheng R, Li H, Wang Z, Cao A. Intracellular plasmid DNA delivery by self-assembled nanoparticles of amphiphilic PHML-b-PLLA-b-PHML copolymers and the endocytosis pathway analysis. *J Biomater Appl* **31**, 606-621 (2016).
184. Liu X, *et al.* Selective inhibition of IDO1 effectively regulates mediators of antitumor immunity. *Blood* **115**, 3520-3530 (2010).
185. Hou D-Y, *et al.* Inhibition of indoleamine 2, 3-dioxygenase in dendritic cells by stereoisomers of 1-methyl-tryptophan correlates with antitumor responses. *Cancer Res* **67**, 792-801 (2007).
186. Lu J, *et al.* An improved d-α-tocopherol-based nanocarrier for targeted delivery of doxorubicin with reversal of multidrug resistance. *J Control Release* **196**, 272-286 (2014).
187. Koblish HK, *et al.* Hydroxyamidine inhibitors of indoleamine-2, 3-dioxygenase potently suppress systemic tryptophan catabolism and the growth of IDO-expressing tumors. *Mol Cancer Ther* **9**, 489-498 (2010).
188. Broz ML, *et al.* Dissecting the tumor myeloid compartment reveals rare activating antigen-presenting cells critical for T cell immunity. *Cancer Cell* **26**, 638-652 (2014).
189. Haanen JB, Robert C. Immune checkpoint inhibitors. In: *Immuno-Oncology* (ed^(eds). Karger Publishers (2015).
190. Brahmer JR, Pardoll DM. Immune checkpoint inhibitors: making immunotherapy a reality for the treatment of lung cancer. *Cancer immunology research* **1**, 85-91 (2013).
191. Weber J. Immune checkpoint proteins: a new therapeutic paradigm for cancer-preclinical background: CTLA-4 and PD-1 blockade. In: *Seminars in Oncology* (ed^(eds) (2010).
192. Cheng T, Liu Z, Wang R. A knowledge-guided strategy for improving the accuracy of scoring functions in binding affinity prediction. *BMC Bioinformatics* **11**, 1 (2010).
193. Barakat K. Do We Need Small Molecule Inhibitors for the Immune Checkpoints? *Journal of Pharmaceutical Care & Health Systems* **2014**, (2014).

194. Muller AJ, Malachowski WP, Prendergast GC. Indoleamine 2, 3-dioxygenase in cancer: targeting pathological immune tolerance with small-molecule inhibitors. *Expert Opin Ther Targets* **9**, 831-849 (2005).
195. Qian S, Zhang M, Chen Q, He Y, Wang W, Wang Z. IDO as a drug target for cancer immunotherapy: recent developments in IDO inhibitors discovery. *RSC Advances* **6**, 7575-7581 (2016).
196. Murphy AG, Zheng L. Small molecule drugs with immunomodulatory effects in cancer. *Human vaccines & immunotherapeutics* **11**, 2463-2468 (2015).
197. Ma Y, *et al.* Contribution of IL-17–producing γδ T cells to the efficacy of anticancer chemotherapy. *The Journal of experimental medicine* **208**, 491-503 (2011).
198. Galluzzi L, Senovilla L, Zitvogel L, Kroemer G. The secret ally: immunostimulation by anticancer drugs. *Nat Rev Drug Discovery* **11**, 215-233 (2012).
199. Kim J-E, *et al.* Cancer cells containing nanoscale chemotherapeutic drugs generate antiovarian cancer-specific CD4+ T cells in peritoneal space. *J Immunother* **35**, 1-13 (2012).
200. Rios-Doria J, *et al.* Doxil synergizes with cancer immunotherapies to enhance antitumor responses in syngeneic mouse models. *Neoplasia* **17**, 661-670 (2015).
201. Lake RA, Robinson BW. Immunotherapy and chemotherapy—a practical partnership. *Nat Rev Cancer* **5**, 397-405 (2005).
202. Sun J, *et al.* A prodrug micellar carrier assembled from polymers with pendant farnesyl thiosalicylic acid moieties for improved delivery of paclitaxel. *Acta Biomaterialia* **43**, 282-291 (2016).
203. Ding Z-C, Munn DH, Zhou G. Chemotherapy-induced myeloid suppressor cells and antitumor immunity: The Janus face of chemotherapy in immunomodulation. *Oncoimmunology* **3**, e954471 (2014).
204. Ding Z-C, *et al.* Immunosuppressive myeloid cells induced by chemotherapy attenuate antitumor CD4+ T-cell responses through the PD-1–PD-L1 axis. *Cancer research* **74**, 3441-3453 (2014).
205. Chaffer CL, Weinberg RA. A perspective on cancer cell metastasis. *Science* **331**, 1559-1564 (2011).
206. Liotta LA, Steeg PS, Stetler-Stevenson WG. Cancer metastasis and angiogenesis: an imbalance of positive and negative regulation. *Cell* **64**, 327-336 (1991).
207. Chambers AF, Groom AC, MacDonald IC. Metastasis: dissemination and growth of cancer cells in metastatic sites. *Nature Reviews Cancer* **2**, 563-572 (2002).
208. Minn AJ, *et al.* Genes that mediate breast cancer metastasis to lung. *Nature* **436**, 518-524 (2005).
209. Leo F, *et al.* Lung metastases from melanoma: when is surgical treatment warranted? *British journal of cancer* **83**, 569-572 (2000).
210. Bacci G, *et al.* High grade osteosarcoma of the extremities with lung metastases at presentation: treatment with neoadjuvant chemotherapy and simultaneous resection of primary and metastatic lesions. *Journal of surgical oncology* **98**, 415-420 (2008).

211. Andre F, *et al.* Breast cancer with synchronous metastases: trends in survival during a 14-year period. *Journal of Clinical Oncology* **22**, 3302-3308 (2004).
212. Pashkevich MA, Sigal BM, Plevritis SK. Modeling the transition of lung cancer from early to advanced stage. *Cancer Causes & Control* **20**, 1559-1569 (2009).
213. Murphy EA, *et al.* Nanoparticle-mediated drug delivery to tumor vasculature suppresses metastasis. *Proceedings of the National Academy of Sciences* **105**, 9343-9348 (2008).
214. Bisht S, *et al.* Systemic administration of polymeric nanoparticle-encapsulated curcumin (NanoCurc) blocks tumor growth and metastases in preclinical models of pancreatic cancer. *Molecular cancer therapeutics* **9**, 2255-2264 (2010).
215. Ackerman NB. The blood supply of experimental liver metastases. IV. Changes in vascularity with increasing tumor growth. *Surgery* **75**, 589-596 (1974).
216. Hoet PHM, Nemery B. Polyamines in the lung: polyamine uptake and polyamine-linked pathological or toxicological conditions. *American Journal of Physiology-Lung Cellular and Molecular Physiology* **278**, L417-L433 (2000).
217. Zhou M, *et al.* Tertiary amine mediated targeted therapy against metastatic lung cancer. *Journal of Controlled Release* **241**, 81-93 (2016).
218. Gao Z-G, Tian L, Hu J, Park I-S, Bae YH. Prevention of metastasis in a 4T1 murine breast cancer model by doxorubicin carried by folate conjugated pH sensitive polymeric micelles. *Journal of controlled release* **152**, 84-89 (2011).
219. Xiao J, Duan X, Yin Q, Zhang Z, Yu H, Li Y. Nanodiamonds-mediated doxorubicin nuclear delivery to inhibit lung metastasis of breast cancer. *Biomaterials* **34**, 9648-9656 (2013).
220. Sampath P, *et al.* Paracrine immunotherapy with interleukin-2 and local chemotherapy is synergistic in the treatment of experimental brain tumors. *Cancer research* **59**, 2107-2114 (1999).
221. Ramakrishnan R, Gabrilovich DI. Mechanism of synergistic effect of chemotherapy and immunotherapy of cancer. *Cancer immunology, immunotherapy* **60**, 419-423 (2011).
222. Wang X, *et al.* IL-36γ transforms the tumor microenvironment and promotes type 1 lymphocyte-mediated antitumor immune responses. *Cancer cell* **28**, 296-306 (2015).
223. Chen Y, *et al.* An immunostimulatory dual-functional nanocarrier that improves cancer immunochemotherapy. *Nature Communications*, (2016).
224. Zhang X, *et al.* Targeted delivery of anticancer agents via a dual function nanocarrier with an interfacial drug-interactive motif. *Biomacromolecules* **15**, 4326-4335 (2014).
225. Wang Z, *et al.* Role of IFN-γ in induction of Foxp3 and conversion of CD4+ CD25− T cells to CD4+ Tregs. *Journal of Clinical Investigation* **116**, 2434 (2006).